HSJ1 and Motor Neuropathy

Heather Louise Smith

A Thesis submitted for the degree of

Doctor of Philosophy

University College London

Institute of Ophthalmology

2015

Declaration

I, Heather Louise Smith, confirm that the work presented in this thesis is my own. Where information has been derived from other sources, I confirm that this has been indicated in the thesis.

Acknowledgments

I would like to thank my supervisor, Professor Michael Cheetham, for his guidance over the past few years and for allowing me to pursue some of my own research interests. I would also like to thank Professor Alison Hardcastle for her valuable input and advice on the project. A special thanks goes to Naheed Kanuga, for her endless patience and for always having the time to help. I would also like to thank all lab members for their help and assistance and for providing an enjoyable environment to work in. Finally, I would like to thank my family and friends for their encouragement and constant support.

Abstract

Homo sapiens DnaJ 1 (HSJ1) is a neuronal DnaJ protein that functions to target misfolded and aggregated proteins for degradation. The accumulation of misfolded and aggregated protein can be toxic to cells, causing neurodegeneration; therefore, proteins that function in protein quality control, such as HSJ1, play a critical role in maintaining protein homeostasis and promoting cell survival.

The protective nature of HSJ1 is highlighted by the ability of the HSJ1a isoform to combat protein aggregation in cell and mouse models of neurodegenerative diseases, such as amyotrophic lateral sclerosis (ALS), a disease caused by the progressive loss of motor neurons. Based on the anti-aggregation function of HSJ1a towards ALS-associated proteins, I sought to determine whether HSJ1a could also protect against mutant ubiquilin-2 aggregation, a protein recently implicated in X-linked ALS. I identified wild-type ubiquilin-2 as a binding partner of HSJ1a and demonstrated that HSJ1a retained the ability to bind to ubiquilin-2 mutants, suggesting HSJ1a could potentially modulate mutant ubiquilin-2 aggregation in cells.

Recently, three mutations in *HSJ1* have been identified in autosomal recessive cases of hereditary motor neuropathies, diseases caused by the degeneration of lower motor neurons. I sought to determine the pathogenicity of the most recently identified variant, HSJ1-Y5C. Using a combination of the heterologous expression of HSJ1-Y5C in SK-N-SH neuroblastoma cells and the examination of endogenous HSJ1-Y5C in patient fibroblasts, I characterised the Y5C substitution as a disease-causing, loss of function mutation that reduces the half-life of HSJ1, leading to a loss of protein. To investigate how the loss of HSJ1 function causes motor neuron degeneration, I examined the cellular phenotype of motor neurons in *Hsj1* knockout mice. I demonstrated that a significant 12% of motor neurons degenerate between P15 and P20. Prior to motor neuron loss, motor neurons appear chromatolytic and signs of impaired protein homeostasis are observed, with an increase in protein ubiquitylation, a possible increase in autophagosome formation and activation of the IRE1 and PERK branches of the unfolded protein response. The activation of these cellular stress responses suggests that HSJ1 is a critical component of the protein quality control network in motor neurons.

Table of contents

List of figures

List of tables

Abbreviations

AARS	Alanyl-tRNA synthetase
AAV	Adeno-associated virus
AD	Alzheimer's disease
ADP	Adenosine diphosphate
ALS	Amyotrophic lateral sclerosis
AMC	7-amino-4-methylcoumarin
AMPK	Adenosine monophosphate-activated protein kinases
APS	Ammonium persulphate
ARSACS	Autosomal recessive spastic ataxia of Charlevoix-Saguenay
ATF4	Activating transcription factor 4
ATF6	Activating transcription factor 6
ATG	Autophagy-related genes
ATP	Adenosine triphosphate
ATP7A	ATPase copper transporting alpha polypeptide
Aβ	Amyloid β
BAK	BCL2-antagonist/killer 1
BAX	BCL2-associated X protein
BCA	Bicinchroninic acid
BCL2	B cell CLL/lymphoma 2
BIM	BCL2-like 11
BSA	Bovine serum albumin
BSCL2	Berardinelli-seip congential lipodystrophy 2
CFTR	Cystic fibrosis transmembrane conductance regulator
CHIP	C-terminus of Hsp70 interacting protein
CHOP	C/EBP homologous protein
CHX	Cycloheximide
CMA	Chaperone-mediated autophagy
CMT	Charcot Marie Tooth
CNS	Central nervous system

CRISPR	Clustered regularly interspaced short palindromic repeat system
DAPI	4’,6-diamidino-2-phenylindole
DCTN1	Dynactin 1
DM	n-Dodecyl-β-D-maltoside
DMEM	Dulbecco’s Modified Eagle medium
DNAJB2	DnaJ homolog subfamily B member 2
DUBs	Deubiquitinases
DYNC1H1	Dynein cytoplasmic 1 heavy chain 1
E. coli	*Escherichia coli*
E1	Ubiquitin-activating enzyme
E2	Ubiquitin-conjugating enzyme
E3	Ubiquitin-ligase enzyme
EDEM1	ER degradation enhancer, mannosidase α-like 1
eIF2α	Eukaryotic initiation factor 2
ER	Endoplasmic reticulum
ERAD	Endoplasmic reticulum-associated degradation
FCS	Fetal calf serum
FF	Fast-fatigable
FR	Fast-fatigue resistant
FUS	Fused in sarcoma
GARS	Glycyl-tRNA synthetase
GDAP1	Ganglioside-induced differentiation-associated protein 1
GFP	Green fluorescent protein
HBSS	Hank’s balanced salt solution
HD	Huntington’s disease
HECT	Homologous to E6-AP C-terminus
HMN	Hereditary motor neuropathy
HMSN	Hereditary motor and sensory neuropathy
Hop	Hsp70 and Hsp90 organising protein
HSF1	Heat shock transcription factor 1
HSJ1	*Homo sapiens* DnaJ 1

HSN	Hereditary sensory neuropathy
Hsp	Heat-shock protein
HSP	Hereditary spastic paraplegia
HSPB1	Heat shock protein B1
HSPB8	Heat shock protein B8
HSR	Heat shock response
IGHMBP2	Immunoglobulin μ-binding protein 2
iPSC	Induced pluripotent stem cell
IRE1	Inositol-requiring enzyme 1
KIF1B	Kinesin family member 1B
LB	Luria-Bertani
LC3	Light chain 3
LIR	LC3-interacting region
LRSAM1	Leucine-rich repeats and sterile alpha motif-containing 1
MC4R	Melanocortin receptor 4
MFN2	Mitofusin 2
MN	Motor neuron
MOI	Multiplicity of infection
MPZ	Myelin protein zero
mTORC1	Mammalian target of rapamycin complex 1
N2a	Neuroblastoma 2a
NBD	N-terminal ATPase domain
NCV	Nerve conduction velocity
NEF	Nucleotide exchange factor
NFL	Neurofilament light chain
NMD	Nonsense mediated decay
NMJ	Neuromuscular junction
OMM	Outer mitochondrial membrane
PBS	Phosphate buffered saline
PCR	Polymerase chain reaction
PD	Parkinson’s disease

PDB	Protein data bank
PERK	Protein kinase RNA-like ER kinase
PFA	Paraformaldehyde
PI3K	Phosphoinositide 3-kinase
PIC	Protease inhibitor cocktail
PMP22	Peripheral myelin protein 22
PNS	Peripheral nervous system
PolyQ	Polyglutamine
PPI	Peptidylprolyl isomerise
PUMA	p53 upregulated modulator of apoptosis
RAB7	RAS-associated protein 7
RER	Rough endoplasmic reticulum
RING	Really interesting new gene
ROS	Reactive oxygen species
S	Slow
SBD	Substrate binding domain
SCA3	Spinocerebellar ataxia type 3
SD	Standard deviation
SDS	Sodium dodecyl sulphate
SDS-PAGE	SDS polyacrylamide gel electrophoresis
SFM	Serum free media
SMA	Spinal muscular atrophy
SMN1	Survival motor neuron 1
SOD1	Superoxide dismutase 1
TALEN	Transcription activator-like effector nucleases
TBS	Tris buffered saline
TDP-43	TAR DNA binding protein
TPR	Tetratricopeptide repeat
TRIM2	Tripartite motif containing 2
TRPV4	Transient receptor potential cation channel subfamily V member 4
UBA	Ubiquitin binding domain

UIM	Ubiquitin-interacting motif
ULK1	Unc-54-like autophagy activating kinase 1
UPR	Unfolded protein response
UPS	Ubiquitin proteasome system
VCP	Valosin containing protein
VP	Virus particle
WT	Wild-type
XBP1	X-box binding protein 1
ZFN	Zinc finger nuclease

Chapter 1 – Introduction

1.1 The nervous system

The nervous system is the main control centre of the body, functioning to detect, interpret and respond to internal and external stimuli. The nervous system can be divided into the central nervous system (CNS) and the peripheral nervous system (PNS). The CNS consists of the brain, brainstem, spinal cord and the retina, whilst the PNS encompasses the motor and sensory neurons that extended from the CNS and connect to the muscles and organs of the body.

1.1.1 Motor neurons

Motor neurons are large polarised cells that function to convey electrical impulses (action potentials) from the CNS to muscle fibres, stimulating muscle contraction. Structurally, they can be divided into four distinct regions; the dendrites, the cell body, the axon and the synaptic terminal (Lodish *et al.* 2000). The dendrites branch outwards from the cell body and are specialised to receive chemical signals from the synaptic terminals of other neurons. Dendrites then convert the chemical signal into an action potential, which is propagated along the axon, away from the cell body and towards the synaptic terminal. In humans, motor neuron axons can reach up to one metre in length. To ensure the efficient propagation of action potentials over long distances, axons are insulated with a myelin sheath.

Motor neurons are divided into upper motor neurons or lower motor neurons depending upon their location in the CNS (Figure 1.1). Upper motor neurons originate from the cerebral cortex region of the brain. Their axons descend via the corticobulbar and corticospinal tracts to the brainstem and the spinal cord, respectively, where they innervate lower motor neurons. The axons of lower motor neurons project outwards from the brainstem and spinal cord and innervate skeletal muscle fibres (Figure 1.2) (Purves *et al.* 2001).

Lower motor neurons can be divided into three subtypes (α, β or γ) according to the type of muscle fibre they innervate (Kuffler *et al.* 1951). α-motor neurons innervate extrafusal muscle fibres. Extrafusal muscle fibres are the most numerous muscle fibres and are responsible for muscle contraction. γ-motor neurons innervate intrafusal muscle fibres, which are located in the muscle spindle, a specialised sensory receptor embedded in extrafusal muscle fibres. The muscle spindle senses position and movement and contributes to fine motor control. In contrast to α- and γ-motor neurons, β-motor neurons are able to innervate both extrafusal and intrafusal muscle fibres.

An α-motor neuron and the muscle fibres it innervates form a motor unit. Motor units can be further divided into fast-fatigable (FF), fast-fatigue resistant (FR) or slow (S) (Burke *et al.* 1973). FF motor units stimulate large muscles and achieve the greatest force of the three types, however, the muscle fibres fatigue quickly. FR motor units stimulate moderately sized muscle groups. They do not react as fast as FF motor units but they can be sustained for much longer. S motor units exert low force and are required for sustained muscle contraction, such as the maintenance of posture.

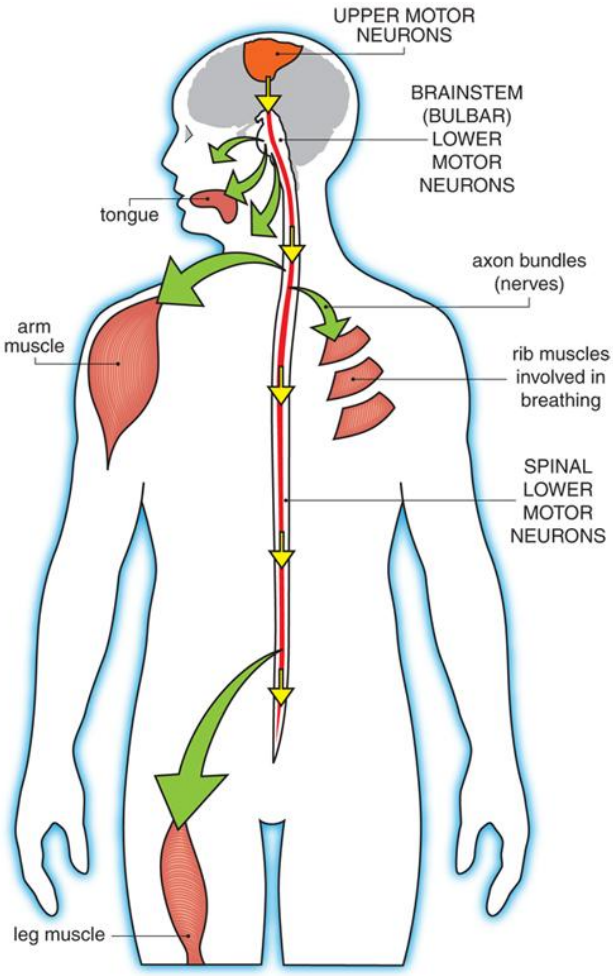

Figure 1.1 The location of upper motor neurons and lower motor neurons in the CNS. Upper motor neurons are located in the cerebral cortex of the brain. Lower motor neurons are located in the brainstem and spinal cord. Lower motor neurons project outward from the brainstem and spinal cord to directly innervate skeletal muscle fibres. Figure from http://mdna.org/disease.

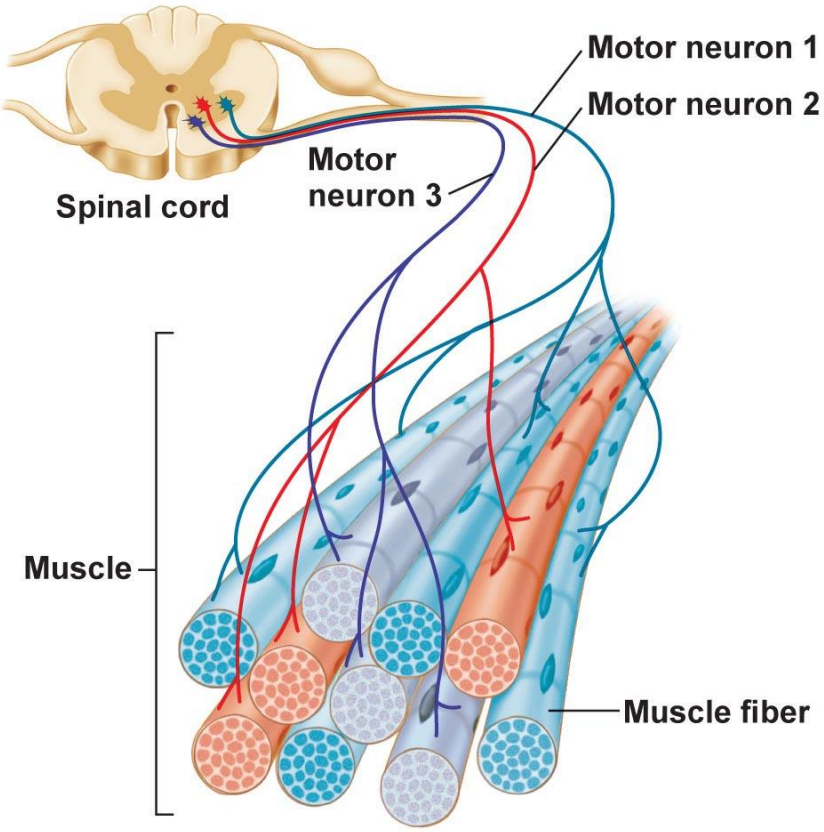

Figure 1.2 Lower motor neurons project from the spinal cord and directly innervate skeletal muscle fibres. A single motor neuron can branch to innervate multiple muscle fibres. Figure from Pearson Education Inc. 2011.

1.1.2 The neuromuscular junction

The neuromuscular junction mediates synaptic transmission between a motor neuron and a muscle fibre. The arrival of an action potential at the pre-synaptic terminal of a motor neuron triggers the opening of voltage-dependent calcium channels, resulting in an influx of calcium. The influx of calcium causes synaptic vesicles to dock and fuse with the pre-synaptic membrane, resulting in the release of the neurotransmitter acetylcholine into the synaptic cleft. Acetylcholine binds to acetylcholine receptors on the plasma membrane of the muscle fibre, which serve as ligand-gated ion channels. Acetylcholine binding triggers the opening of the channel and the influx of sodium ions, inducing depolarisation and subsequent muscle contraction (Takamori 2012).

1.2 Motor neuron disorders

Motor neuron disorders are a heterogeneous group of neurological diseases caused by the progressive degeneration of upper and/or lower motor neurons. Examples of motor neuron disorders are discussed briefly below.

1.2.1 Amyotrophic lateral sclerosis

Amyotrophic lateral sclerosis (ALS) is caused by the progressive loss of upper and lower motor neurons. Clinically, the disease is characterised by muscle weakness and atrophy, with muscles in the hands, arms and legs typically the first to be affected (Talbot 2009). ALS is a fatal disease, with death usually occurring 2-5 years after symptom onset due to respiratory failure. The disease affects around 2 in every 100,000 individuals, with the majority of cases being sporadic (Al-Chalabi *et al.* 2014). Of the familial cases, 40% are caused by the intronic hexanucleotide repeat expansion of the *C9orf72* gene (Renton *et al.* 2014). Mutations in the enzyme superoxide dismutase 1 (SOD1) are the second most common cause of familial ALS, accounting for 12% of cases, followed by mutations in the RNA-binding proteins TAR DNA binding protein (TDP-43) and fused in sarcoma (FUS), each accounting for 4% of cases (Renton *et al.* 2014). Mutations are most commonly inherited in an autosomal dominant manner, although autosomal recessive and X-linked inheritance have also been reported.

1.2.2 Hereditary spastic paraplegia

Hereditary spastic paraplegia (HSP) is an inherited disorder caused by the degeneration of upper motor neuron axons in the corticospinal tract, causing progressive spasticity and weakness of the lower limbs. The disease affects around 3 in every 100,000 individuals, with symptom onset varying from early childhood to late adulthood (Lo Giudice *et al.* 2014).

HSP can be divided into uncomplicated or complicated, depending on the presence of additional clinical features. The disease can be inherited in an autosomal dominant, autosomal recessive or X-linked manner. Autosomal dominant uncomplicated HSP is the most prevalent subtype and over 20 causative genes for this subtype have been identified to date (Fink 2014). The causative genes encode proteins with a diverse range of function, including axonal transport, mitochondrial function and myelin formation (Fink 2014).

1.2.3 Spinal muscular atrophy

Spinal muscular atrophy (SMA) is an inherited disorder caused by the degeneration of lower motor neurons in the spinal cord. The disease affects around 1 in 100,000 individuals and patients typically present with weakness and atrophy of the proximal limb muscles. SMA is classified according to the age of onset and the severity of symptoms (Crawford *et al.* 1996, Hamilton *et al.* 2013). Type I is the most severe form of the disease and has the earliest age of onset, with symptoms usually presenting at birth. Type II typically presents in early childhood and is less severe, although still disabling. Type III and type IV present in adolescence and adulthood, respectively, and are the least severe forms of the disease. The majority of cases display autosomal recessive inheritance, although autosomal dominant and X-linked inheritance has also been reported. 95% of patients have a loss of function mutation in the survival motor neuron gene (*SMN1*) (Lefebvre *et al.* 1995), which encodes a protein with a key role in RNA splicing (Li *et al.* 2014).

1.3 Inherited peripheral neuropathies

Inherited peripheral neuropathies are a clinically heterogeneous group of disorders caused by the degeneration of the motor and/or sensory neurons of the peripheral nervous system. Inherited peripheral neuropathies can be divided into three main subtypes; hereditary motor and sensory neuropathy (HMSN), distal hereditary motor neuropathy (dHMN) and hereditary sensory neuropathy (HSN).

1.3.1 Charcot Marie Tooth disease

HMSN, also known as Charcot Marie Tooth disease (CMT), is the one of the most commonly inherited neurological disorders, affecting around 1 in 2500 individuals (Vallat *et al.* 2013, El-Abassi *et al.* 2014). Symptom onset typically occurs in the second decade of life, although onset in the third decade is not uncommon. Although both motor and sensory neurons are affected, motor symptoms predominate. The clinical phenotype of CMT is characterised by progressive muscle weakness and wasting of the distal lower limbs. The muscles in the feet are typically the first to be affected, leading to foot deformities and foot

drop. Gradually the muscles of the lower legs become affected, causing gait disturbances, with frequent stumbling and falling. Tendon reflexes are reduced or absent. As with the motor deficits, sensory deficits are more pronounced distally, with decreased sensation to touch, vibration and pain (Vallat *et al.* 2013, El-Abassi *et al.* 2014).

CMT can be divided into a demyelinating form (CMT1) and an axonal form (CMT2). CMT1 is the more prevalent subtype, accounting for around 80% of cases (Murphy *et al.* 2012). CMT1 and CMT2 are clinically indistinguishable and nerve conduction studies (NCS) are required to differentiate between the two forms (Harding and Thomas 1980). NCS are performed on the upper limbs, usually on the median motor nerve and the sural sensory nerve. A reduction in nerve conduction velocity (NCV) indicates demyelination, with a velocity less than 38 m/s characteristic of CMT1. Patients with CMT2 display a normal NCV, with speeds above 45 m/s.

The majority of CMT1 and CMT2 cases have an autosomal dominant pattern of inheritance, although autosomal recessive and X-linked inheritance has also been reported. To date, over 30 causative genes for CMT1 and CMT2 have been identified (Table 1.1). A molecular diagnosis can be established in 50-70% of patients; with 90% of such patients having mutations in one of four genes; *PMP22*, *MFN2*, *GJB1* or *MPZ* (Saporta *et al.* 2011). Most types of CMT1 map to genes that encode proteins associated with myelin proteins and Schwann cell function, whereas CMT2 causative genes encode proteins that are typically associated with axonal structure and function (Rossor *et al.* 2013, Jerath *et al.* 2015).

1.3.2 CMT2 and dHMN

Patients that lack the sensory component of CMT are classified as having dHMN. Clinically, it is difficult to differentiate between dHMN and CMT2, as it is not uncommon for CMT2 patients to present without significant sensory symptoms. NCS are therefore required to determine whether sub-clinical sensory deficits are present and distinguish between the two diseases. As with CMT2, dHMN is usually associated with an autosomal dominant pattern of inheritance. Ten causative genes for dHMN have been identified to date (Table 1.2), however a large proportion of patients remain without a genetic diagnosis (Rossor *et al.* 2012). Interestingly, mutations in the same gene have been identified to cause both dHMN and CMT2. dHMN and CMT2 causative genes encode proteins with a range of cellular functions, including protein folding and degradation (*HSPB1, HSPB8, LRSAM1, TRIM2, DNAJB2*), axonal transport (*DCTN1, DYNC1H1, NEFL, RAB7, KIF1B*), mitochondrial dynamics (*MFN2, GDAP1*) protein translation (*IGHMBP2, AARS, GARS*) and ion channel function (*ATP7A, TRPV4*) (Figure 1.3). Potential pathogenic mechanisms are discussed below, with impairments in protein folding and degradation discussed in section 1.8.

AD CMT1	**Gene**	**Protein**
CMT1A	*PMP22*	Peripheral myelin protein 22
CMT1B	*MPZ*	Myelin protein zero
CMT1C	*LITAF*	Lipopolysaccharide-induced tumor necrosis factor
CMT1D	*EGR2*	Early growth response 2
CMT1E	*PMP22*	Peripheral myelin protein 22
CMT1F	*NEFL*	Neurofilament light chain
AR CMT1		
AR CMT1A	*GDAP1*	Ganglioside-induced differentiation-associated protein 1
AR CMT1B1	*MTMR2*	Myotubularin-related protein 2
AR CMT1B2	*MTMR13*	Myotubularin-related protein 13
AR CMT1B3	*SBF1*	SET binding factor 1
AR CMT1C	*SH3TC2*	SH3 domain and tetratricopeptides repeats 2
AR CMT1D	*NDRG1*	N-myc downstream-regulated gene 1 protein
AR CMT1E	*EGR2*	Early growth response 2
AR CMT1F	*PRX*	Periaxin
AR CMT1G	*HK1*	Hexokinase 1
AR CMT1H	*FGD4*	Frabrin
AR CMT1J	*FIG4*	FIG4 homolog, SCA domain containing lipid phosphatase
AD CMT2		
CMT2A1	*KIF1B*	Kinesin family member 1B
CMT2A2	*MFN2*	Mitofusin 2
CMT2B	*RAB7*	RAS-associated protein 7
CMT2C	*TRPV4*	Transient receptor potential cation channel subfamily V member 4
CMT2D	*GARS*	Glycyl-tRNA synthetase
CMT2E	*NEFL*	Neurofilament light chain
CMT2F	*HSPB1*	Heat shock protein B1
CMT2I	*MPZ*	Myelin protein zero
CMT2J	*MPZ*	Myelin protein zero
CMT2K	*GDAP1*	Ganglioside-induced differentiation-associated protein 1
CMT2L	*HSPB8*	Heat shock protein B8
CMT2M	*DNM2*	Dynamin 2
CMT2N	*AARS*	Alanyl-tRNA synthetase
CMT2O	*DYNC1H1*	Dynein cytoplasmic 1 heavy chain 1
CMT2P	*LRSAM1*	Leucine-rich repeats and sterile alpha motif-containing 1
CMT2Q	*DHTKD1*	Dehydrogenase E1 and transketolase domain-containing 1
AR CMT2		
AR CMT2	*HINT1*	Histidine triad nucleotide-binding protein 1
AR CMT2	*TRIM2*	Tripartite motif containing 2
AR CMT2	*DNAJB2*	DnaJ homolog subfamily B member 2

Table 1.1 Identified causative genes in CMT1 and CMT2. AD – autosomal dominant, AR – autosomal recessive **(**Reilly *et al.* 2011, Rossor *et al.* 2013, Baets *et al.* 2014, Tazir *et al.* 2014, Brennan *et al.* 2015, Jerath *et al*. 2015).

	Gene	Protein
AD dHMN	*BSCL2*	Berardinelli-seip congential lipodystrophy 2 (seipin)
	DCTN1	Dynactin 1
	DYNC1H1	Dynein cytoplasmic 1 heavy chain 1
	GARS	Glycyl-tRNA synthetase
	HSPB1	Heat shock protein B1
	HSPB8	Heat shock protein B8
	TRPV4	Transient receptor potential cation channel subfamily V member 4
AR dHMN	*IGHMBP2*	Immunoglobulin μ-binding protein 2
	DNAJB2	DnaJ homolog subfamily B member 2
X-linked dHMN	*ATP7A*	ATPase copper transporting alpha polypeptide

Table 1.2 Identified causative genes in dHMN. AD – autosomal dominant, AR – autosomal recessive (Rossor *et al.* 2012, Drew *et al.* 2011).

1.3.3 Mechanisms of disease pathogenesis in CMT2 and dHMN

1.3.3.1 Impaired axonal transport

Axonal transport is responsible for the movement of organelles, proteins and lipids between the cell body and the synaptic terminal of a neuron. The process is bi-directional, with anterograde transport moving cargo from the cell body to the synaptic terminal and retrograde transport moving cargo from the synaptic terminal back to the cell body (Gentil *et al.* 2012, Jerath *et al.* 2015). The platform for transportation is provided by the cytoskeleton, which runs along the entire length of the axon. The neuronal cytoskeleton consists of three components; microtubules, actin filaments and neurofilaments. Cargo is attached to the microtubules via the kinesin and dynein motor proteins, which function in anterograde and retrograde transport, respectively (Gentil *et al.* 2012, Jerath *et al.* 2015).

Motor neurons place a substantial demand on the axonal transport system due to their long axons and high synaptic activity. The system is, therefore, under considerable pressure to supply the synaptic terminal with the proteins, lipids and organelles required for synaptic function, whilst returning elements that require degradation back to the cell body. Such a high dependence on an efficient transport system makes motor neurons particularly vulnerable to impairments in the trafficking process. Five of the dHMN/CMT2 causative genes identified to date encode proteins that function in axonal transport, with four of the genes encoding motor proteins or motor protein adaptors (*KIF1B, DYNC1H1, DCTN1* and *RAB7*). Although the mechanisms of pathogenesis remain to be fully characterised, accumulating evidence suggests that the mutations result in a loss of function phenotype. Mutations in KIF1B, a member of the kinesin family, were reported to cause a decrease in ATPase activity and motility (Zhao *et al.* 2001). *Kif1b*$^{+/-}$ mice show defects in synaptic vesicle trafficking, supporting the hypothesis that a loss of KIF1B function reduces the anterograde transport of cargo (Zhao *et al.* 2001). Mutations in *DYNC1H1*, *DCTN1* and *RAB7* were reported to impair the retrograde transport system. *DYNC1H1* encodes a component of dynein, whereas both *DCTN1* and *RAB7* encode dynein adaptor proteins. In transfected cells, mutant DCTN1 exhibited a reduced binding affinity for microtubules, whilst mutant RAB7 showed impaired GTPase activity (Puls *et al.* 2003, McCray *et al.* 2010). Whilst the consequences of the impaired activity remain to be determined, it is likely that the mutant proteins impair the attachment of specific cargo to microtubules, preventing their retrograde transport.

In addition to the identification of mutations in motor proteins and motor protein adaptors, mutations have also been identified in *NEFL*, encoding neurofilament light chain (NFL), a component of neurofilaments. Mutations in NFL were found to promote the aggregation of

the protein, reducing the incorporation of NFL into neurofilaments and destabilising the cytoskeletal network (Brownlees *et al.* 2002, Zhai *et al.* 2007). The destabilisation of the cytoskeleton was found to impair the trafficking of mitochondria in motor neurons (d'Ydewalle *et al.* 2012). Collectively, the identification of *KIF1B*, *DYNC1H1*, *DCTN1*, *RAB7* and *NEFL* as dHMN/CMT2 causative genes highlights defective axonal transport as a common mechanism of motor neuron degeneration.

1.3.3.2 Mitochondrial dysfunction

Mitochondria are fundamental for neuronal function and survival. They primarily function to produce adenosine triphosphate (ATP), the energy currency of the cell; however, they also play important roles in calcium storage, cell signalling and apoptosis (Sheng 2014). Motor neurons have a high rate of ATP consumption; the exocytosis of synaptic vesicles and the restoration of ion gradients following the propagation of an action potential are both ATP-dependent processes. To meet this demand, motor neurons have a large number of mitochondria that are strategically localised to regions where demand for ATP and calcium buffering are high, such as the synaptic terminals (Sheng 2014).

Mitochondria are dynamic organelles that undergo fission and fusion events (Scorrano 2013). Mitochondrial fission is important for the trafficking of the organelle and the removal of damaged parts of the network, whereas the fusion of mitochondria is proposed to enable the mixing of mitochondrial content, a process that is postulated to be crucial for maintaining mitochondrial homeostasis. Interestingly, 20% of autosomal dominant cases of CMT2 are caused by mutations in mitofusin 2 (MFN2), an outer mitochondrial membrane GTPase that functions in mitochondrial fusion (Verhoeven *et al.* 2006). In addition to mediating fusion, MFN2 is also important in the formation of endoplasmic reticulum (ER) - mitochondria contact sites, enabling the movement of calcium between the two organelles (de Brito *et al.* 2008). The protein is also proposed to function in the axonal transport of mitochondria, interacting with Miro/Milton, a complex that serves as an adaptor to dock mitochondria to motor proteins (Misko *et al.* 2010). Over 50 patient mutations in *MFN2* have been identified to date, with the majority of mutations missense mutations (Cartoni *et al.* 2009). In patient nerve biopsies, mitochondria appear small and fragmented, suggesting an impairment in the fusion process (Baloh *et al.* 2007). Furthermore, the mitochondria were observed to accumulate in the distal regions of the motor neuron axon, which may also suggest an impairment in the retrograde transport of mitochondria (Baloh *et al.* 2007). Indeed, mitochondrial trafficking was markedly reduced in cells expressing mutant MFN2 constructs (Misko *et al.* 2010). Cytosolic calcium levels were also increased (de Brito *et al.* 2010). MFN2 mutations therefore appear to cause a variety of mitochondrial defects.

Mutations in ganglioside-induced differentiation-associated protein 1 (GDAP1) have also been identified to cause autosomal dominant cases of CMT2. GDAP1 is an outer mitochondrial membrane protein and is proposed to have a role in mitochondrial fission and fusion (Pareyson *et al.* 2015). Interestingly, the expression of GDAP1 mutants resulted in mitochondria appearing fragmented, indicative of either a reduced rate of fusion or an increased rate of fission. The fragmented mitochondria showed an increase in toxic reactive oxygen species (ROS) production (Niemann *et al.* 2009). Impairments in either the fusion or fission of mitochondria therefore appear to have deleterious effects on motor neuron survival.

1.3.3.3 Ion channel dysfunction

Copper is an essential element, acting as a cofactor for numerous enzymes. Its intracellular levels, however, are tightly regulated due to its ability to act as a potential generator of toxic free radicals. Copper-transporting ATPase 1 (ATP7A) forms part of a network to regulate copper metabolism (La Fontaine *et al.* 2007). ATP7A resides in the trans-Golgi network where it functions to transport copper into the Golgi compartment for incorporation into copper-dependent enzymes. The protein translocates to the plasma membrane in response to an increase in intracellular copper levels, where it mediates the removal of copper from the cell (Kim *et al.* 2008). Missense mutations in *ATP7A* have been identified in two families with X-linked dHMN (Kennerson *et al.* 2010). The expression of mutant ATP7A in HeLa and N2a cells led to a greater accumulation of the transporter at the plasma membrane compared to the wild-type protein, suggesting an impairment in the endocytic recycling of ATP7A back to the trans-Golgi compartment (Kennerson *et al.* 2010). The prolonged retention of ATP7A at the plasma membrane has been proposed to lead to a chronic deficiency of copper-dependent enzymes.

Mutations in transient receptor vallanoid 4 (*TRPV4*), encoding a cation channel, have also been identified in autosomal dominant cases of CMT2 (Auer-Grumbach *et al.* 2010, Deng *et al.* 2010, Landoure *et al.* 2010). Mutant TRPV4 expressed in N2a cells displayed increased calcium channel activity, leading to an increase in the levels of intracellular calcium (Fecto *et al.* 2011). Interestingly, elevated levels of intracellular calcium retard the mobility of mitochondria and it has been suggested that mutant TRPV4 may indirectly interfere with axonal transport of mitochondria, although this hypothesis remains to be confirmed experimentally (Gentil *et al.* 2012).

1.3.3.4 Impaired protein translation

Aminoacyl tRNA synthetases are ubiquitous enzymes that function in protein translation, catalysing the attachment of an amino acid to its cognate tRNA molecule. Once tRNA is charged, the ribosome transfers the amino acid from the tRNA into the growing polypeptide chain, in accordance to the mRNA codon sequence. Interestingly, mutations in glycyl-tRNA synthetase (*GARS*) and alanyl-tRNA synthetase (*AARS*) have been identified in autosomal dominant cases of dHMN and CMT2, respectively (Antonellis *et al.* 2003, Latour *et al.* 2010, Wallen *et al.* 2013). Investigations into the mechanism of pathogenesis suggest that the mutations result in a loss of function phenotype. In yeast complementation studies, the majority of AARS and GARS mutants resulted in a loss of complementation, suggesting an impairment in tRNA charging (Antonellis *et al.* 2006). However, a proportion of AARS and GARS mutants were able to rescue yeast viability, implying that impaired tRNA charging does not underlie the pathogenesis of all disease-associated mutations (Antonellis *et al.* 2006). In human spinal cord tissue, wild-type GARS localises to puncta in the axons of motor neurons (Antonellis *et al.* 2006). In transfected motor neuron cell lines, mutant GARS failed to localise to axons (Antonellis *et al.* 2006, Jordanova *et al.* 2006). The lack of axonal localisation of the protein has been proposed to deplete tRNA charging in the axon, impairing local axonal translation and potentially decreasing the levels of axonal proteins that are critical for axonal function (Wallen *et al.* 2013).

Mutations in immunoglobulin μ-binding protein 2 (*IGHMBP2*) have been identified to underlie autosomal recessive cases of dHMN. Although the precise function of IGHMBP2 remains unknown, the protein has been identified as an ATP-dependent helicase, unwinding both DNA and RNA (Guenther *et al.* 2009). The protein has been reported to interact with the ribosome, suggesting a possible function in protein translation (Guenther *et al.* 2009). The majority of mutations in IGHMBP2 are missense mutations that lie in close proximity to the helicase domain (Grohmann *et al.* 2001, Guenther *et al.* 2007). The characterisation of patient mutations using *in vitro* assays revealed that mutant IGHMBP2 has reduced ATPase and helicase activity (Guenther *et al.* 2009), suggesting that mutations in IGHMBP2 could potentially impair protein translation.

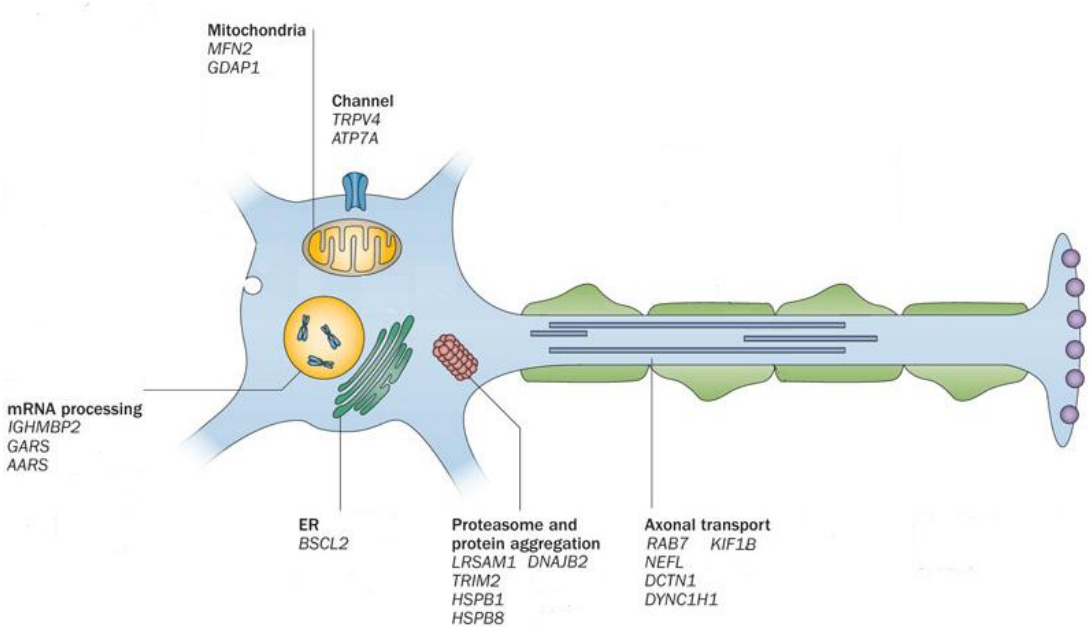

Figure 1.3 Examples of CMT2 and dHMN causative genes. Schematic of a motor neuron highlighting the cellular processes that may be impaired in CMT2 and dHMN; axonal transport (*DCTN1*, *DYNC1H1*, *KIF1B*, *NEFL*, *RAB7*), mitochondrial function (*GDAP1*, *MFN2*), ion channel activity (*ATP7A*, *TRPV4*), protein translation, (*AARS*, *GARS*, *IGHMBP2*), protein folding and protein degradation (*DNAJB2*, *HSPB1*, *HSPB8*, *LRSAM1*, *TRIM2*) and ER homeostasis (*BSCL2*). Figure adapted from Rossor *et al.* 2013.

1.4 Protein folding

Proteins are central players in the majority of cellular processes. They are synthesised as linear polypeptide chains, yet they must fold to their native three-dimensional structure in order to achieve functionality. In 1973, Anfinsen demonstrated that the three-dimensional structure of a protein is encoded in its amino acid sequence. Each amino acid residue can adopt a number of different conformations, generating a large number of possible three-dimensional structures. Taking this into consideration, Levinthal argued that protein folding simply cannot occur through the random sampling of all possible conformations until the native structure is reached. Instead, he postulated the existence of a protein folding pathway (Levinthal 1969). The current model of protein folding is highly complex and the principles that guide the folding process remain to be fully characterised. However, the model is based on the principle that folding occurs through a free energy funnel (Figure 1.4), with proteins seeking the most thermodynamically favourable conformation with the lowest free energy (Hartl *et al.* 2011, Kim *et al.* 2013). Folding is proposed to be initiated by the spontaneous collapse of the polypeptide chain into a compact state, referred to as a molten globule, a process mediated by hydrophobic interactions among non-polar residues. The burial of non-polar residues in the interior of the protein is thermodynamically favourable and decreases the free energy of the protein. Following hydrophobic collapse, folding to the native state relies on the formation of native hydrogen bonds and van der Waals forces. Such interactions further decrease the free energy of the protein and subsequently the free energy funnel narrows, representing the restricted conformational space that needs to be searched en route to the native state (Hartl *et al.* 2011, Kim *et al.* 2013).

1.5 Protein quality control

In the crowded cellular environment, partially folded proteins with exposed hydrophobic amino acid residues are susceptible to the formation of non-native interactions that can lead to protein misfolding and aggregation. If allowed to accumulate, misfolded and aggregated proteins can cause toxicity (cytotoxicity), leading to numerous diseases such as diabetes, cardiovascular disease and neurodegenerative diseases (Mukherjee *et al.* 2015, Del Monte *et al.* 2014, Hipp *et al.* 2014). Cells have therefore adopted an intrinsic network of protein quality control that promotes efficient folding and either the re-folding or degradation of misfolded and aggregated protein. The protein quality control machinery includes molecular chaperones, the ubiquitin proteasome system (UPS) and autophagy. The mechanisms by which these three systems function to maintain protein homeostasis (proteostasis) are discussed in the following section.

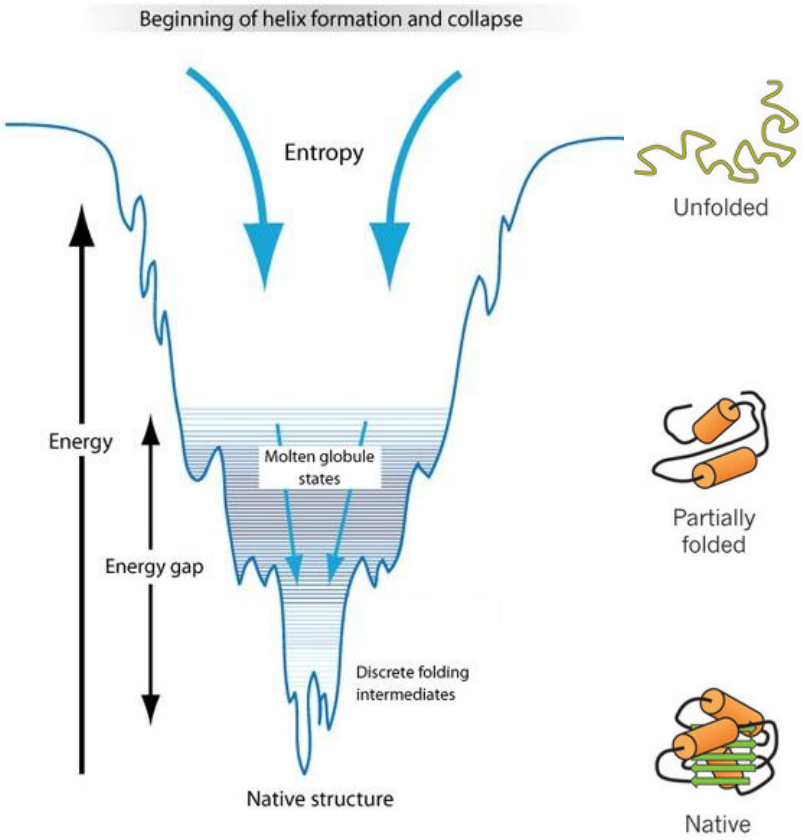

Figure 1.4 Protein folding free-energy funnel. Hydrophobic collapse of the polypeptide chain into a molten globule is thermodynamically favourable. The formation of native interactions further decreases the free energy of the protein and limits the free-energy landscape that needs to be searched en route to the native state. The free-energy landscape is often rugged; proteins must cross kinetic barriers during folding. Failure to do so can result in partially folded intermediates becoming kinetically trapped. Figure adapted from www.learner.org/proteinfoldingfunnel and Hartl *et al.* 2011.

1.5.1 Molecular chaperones

Molecular chaperones are defined as proteins that interact with, stabilise or assist another protein to gain its native and functionally active conformation, without being present in the final structure (Ellis 1987). Members of the molecular chaperone family are often referred to as heat-shock proteins (Hsp) due to their upregulation under stress conditions that typically destabilise proteins, such as elevated temperature and oxidative stress. Molecular chaperones are often classified according to their molecular weight and families include Hsp90, Hsp70, Hsp60, Hsp40 (DnaJ) and the small Hsp (Figure 1.5). Molecular chaperones display large functional diversity and in addition to their fundamental roles in *de novo* folding, and the refolding of misfolded proteins, chaperones also regulate critical cellular processes such as protein trafficking, protein degradation and macromolecular complex assembly and disassembly (Hartl *et al.* 2011).

1.5.1.1 Hsp90 (HSPC)

Hsp90 (HSPC) is an ATP-dependent chaperone that functions in the activation and stabilisation of client proteins. Client proteins include protein kinases, cell cycle regulators, cell surface receptors and transcription factors; therefore, Hsp90 plays a critical role in cellular processes such as signal transduction, cell cycle progression, apoptosis and protein degradation (Kim *et al.* 2013). The activation of Hsp90 clients is driven by a cycle of substrate binding and release, mediated by a series of conformational changes and an ATP-induced transition between an open and a closed conformation. Hsp90 exists as a homodimer (Figure 1.5), with each subunit consisting of three domains; an N-terminal ATP-binding domain (N-domain), a middle domain that binds the substrate (M-domain) and a C-terminal dimerisation domain (C-domain). In the absence of nucleotide Hsp90 adopts a V-shaped open conformation. The binding of ATP to the N-domain induces a conformational change that closes a lid over the nucleotide binding pocket. Following lid closure, the N-domains dimerise, forming a compact structure with a closed conformation. The formation of the closed dimer induces ATP hydrolysis, subsequently promoting the N-domains to dissociate and the return of Hsp90 to the open conformation, with the release of the substrate (Pearl *et al.* 2006).

The reaction cycle of Hsp90 is regulated by various co-chaperones. The co-chaperones exhibit specific binding preferences for different Hsp90 conformations and affect different stages of the cycle, such as client binding and ATP hydrolysis (Li *et al.* 2014). Co-chaperones therefore usually co-operate in a sequential cycle to facilitating the maturation of Hsp90 clients. Many co-chaperones contain a tetratricopeptide repeat (TPR) domain that recognises a docking site at the C-terminal of Hsp90 formed by a conserved EEVD motif

(Scheufler *et al.* 2000). Such TPR domain-containing co-chaperones include Hop, which stabilises the open conformation of Hsp90 and facilitates substrate binding by acting as an adaptor protein between Hsp70 and Hsp90, enabling client transfer (Chen *et al.* 1998). Alternatively, CHIP, an E3 ubiquitin ligase, is a TPR domain-containing co-chaperone that mediates the attachment of ubiquitin chains to the client and thereby signals for its degradation (Bozaykut *et al.* 2014).

1.5.1.2 Hsp70 (HSPA)

Hsp70 (HSPA) functions in a wide array of cellular processes including the folding of newly synthesised protein, the refolding of misfolded and aggregated protein, transport of proteins across membranes, and protein degradation (Kim *et al.* 2013). These functions rely on the ability of Hsp70 to interact with hydrophobic stretches exposed in client proteins and subsequently undergo an ATP-dependent cycle of substrate binding and release (Figure 1.6). Hsp70 is composed of a 44 kDa N-terminal ATPase domain (NBD) and a C-terminal substrate binding domain (SBD), divided into an 18 kDa β-sandwich subdomain that forms a hydrophobic binding pocket and a 10 kDa α-helical subdomain that acts as a lid (Figure 1.6) (Hartl *et al.* 2011). The NBD and SBD are connected by a flexible linker that enables the NBD to allosterically control the conformation of the SBD. In the ATP-bound state the binding pocket and lid are in an open conformation. The SBD has a low substrate affinity and fast substrate exchange rates. The hydrolysis of ATP to ADP drives the SBD into a high affinity state for substrate binding through the closing of the lid, enabling stable binding of the client protein. The release of ADP and the rebinding of ATP triggers the opening of the lid and the subsequent unloading of the bound substrate (Mayer *et al.* 2010).

The Hsp70 reaction cycle contains two rate limiting steps; ATP hydrolysis, due to low basal ATPase activity, and the dissociation of ADP. Hsp70 therefore requires the action of cofactors to facilitate the reaction cycle between ATP and ADP bound states. The ATPase activity of Hsp70 is stimulated by members of the DnaJ family via their conserved J domain (Liberek *et al.* 1991). The dissociation of ADP requires the opening of the nucleotide binding cleft, a process catalysed by nucleotide exchange factors (NEFs) (Gassler *et al.* 2001).

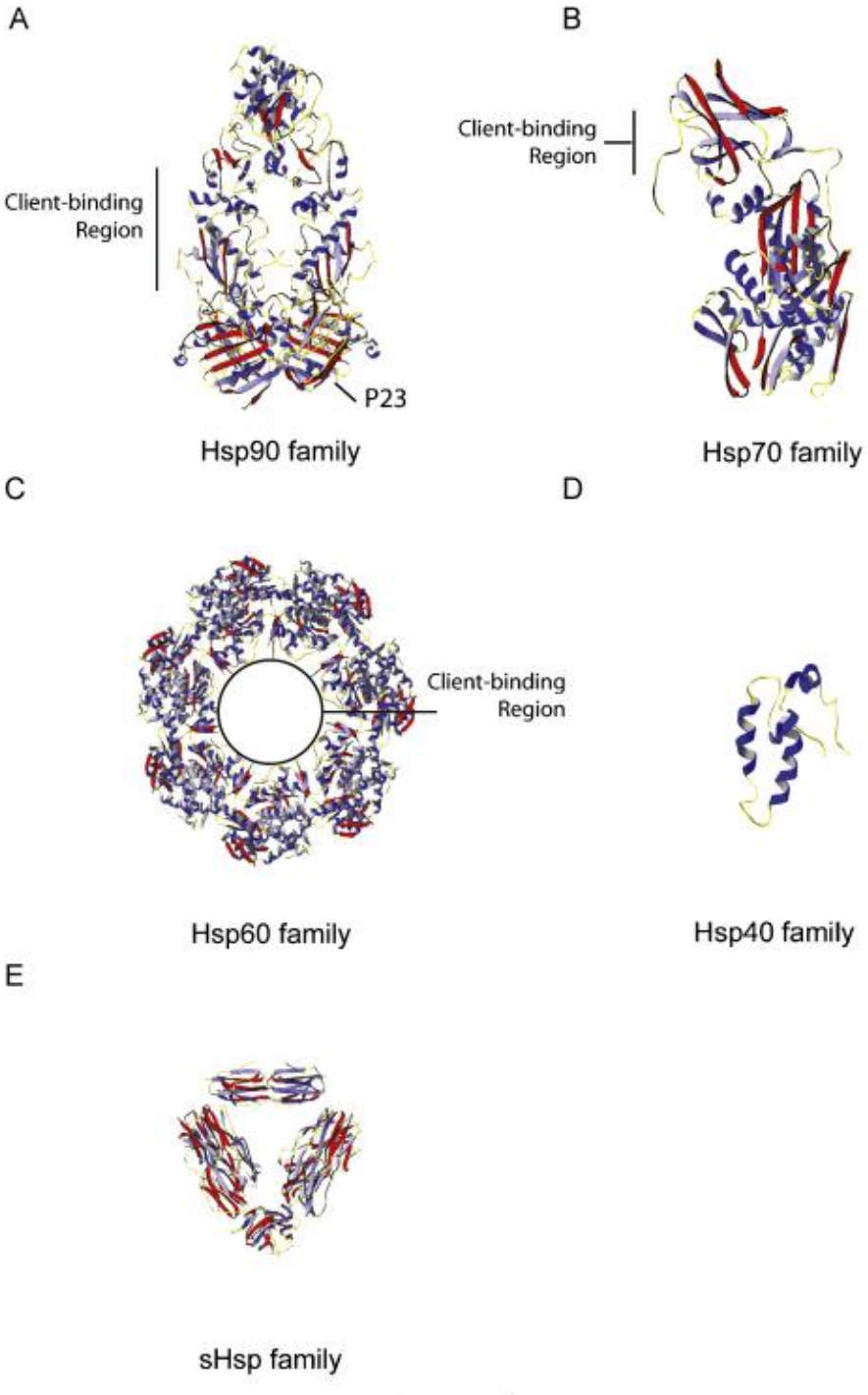

Figure 1.5 Ribbon diagrams showing the structure of representatives from the major molecular chaperone families. A: Yeast Hsp90 with its co-chaperone p23 (PDB 2CG9). **B:** Amino acids 1-554 of bovine Hsc70 (PDB 1YUW). **C:** Bacterial GroEL viewed from above (PDB 1GR1). **D:** J domain of human DnaJ protein HDJ-1 (PDB 1HDJ). **E:** Small Hsp family member Hsp16.3 from *Mycobacterium tuberculosis*. Figure adapted from Kosmaoglou *et al.* 2008.

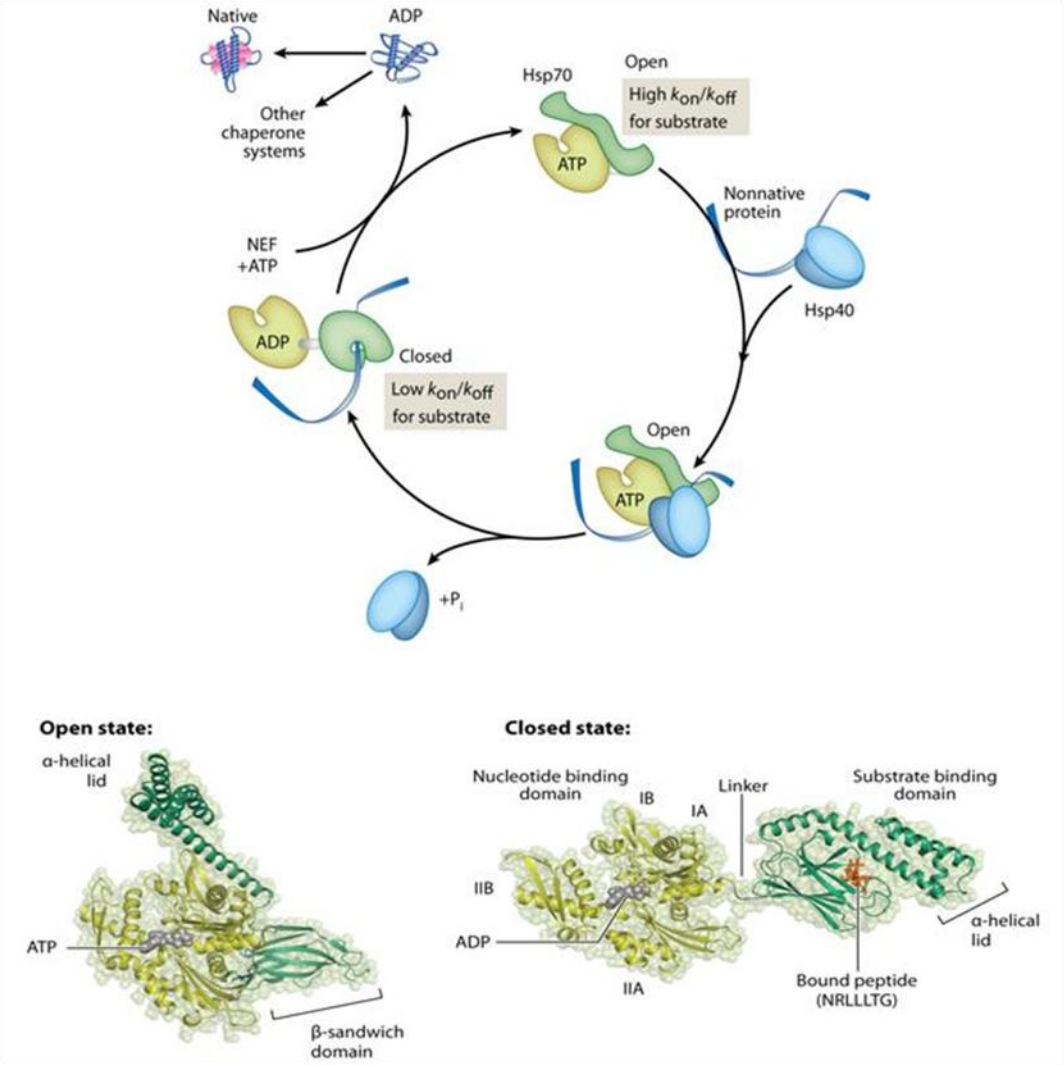

Figure 1.6 Hsp70 reaction cycle and structure. Hsp40 (DnaJ) delivers unfolded or misfolded clients to the SBD of Hsp70. The conserved J domain of DnaJ stimulates the ATPase activity of Hsp70, promoting lid closure and the tight binding of the substrate. NEFs induce the dissociation of ADP leading to the opening of the lid and the release of the substrate. A cycle of binding and release promotes protein folding. Figure from Kim *et al.* 2013.

1.5.1.3 DnaJ (Hsp40/DNAJ)

As mentioned above, members of the DnaJ family are important regulators of Hsp70 activity. All DnaJ proteins contain a J domain, a conserved region of 70 amino acids that folds into four α-helices. Helix II and helix III form an antiparallel two-helix bundle, with a loop connecting the two helices containing a histidine-proline-aspartate (HPD) motif (Figure 1.7) (Kampinga *et al.* 2010). The HPD motif is critical for lowering the activation energy of ATP hydrolysis by Hsp70, although the exact mechanism by which this occurs remains elusive. It has been established that interactions between the J domain and both the NBD and the flexible linker of Hsp70 are crucial for stimulating ATPase activity. However, the C-terminal lid of Hsp70 has also been shown to be critical for modulating DnaJ binding, suggesting that a complex interaction between the J domain and Hsp70 is required to efficiently stimulate ATPase activity (Gao *et al.* 2012).

The human genome encodes 49 DnaJ proteins, which can be divided into three classes according to their domain composition (Cheetham *et al.* 1998, Kampinga *et al.* 2009). Class I proteins share all domains present in *Escherichia coli* DnaJ, with an N-terminal J domain, a glycine-phenylalanine (GF) rich region, a zinc binding domain and a C-terminal domain. Class II proteins contain an N-terminal J domain and a GF rich region, whereas class III proteins share only the J domain. The diversification of domains outside the J domain has enabled DnaJ proteins to adopt specialised functions. For example, domains that target DnaJ proteins to precise intracellular locations promote the interaction of Hsp70 with specific clients. Furthermore, client binding domains enable DnaJ proteins to deliver clients directly to the SBD of Hsp70 (Kampinga *et al.* 2010).

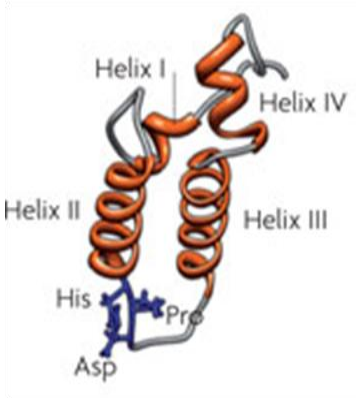

Figure 1.7 Structure of the J domain from *E. coli* DnaJ. The J domain contains four helices, with a loop between helix II and helix III containing a HPD motif. The HPD motif is critical for lowering the activation energy of Hsp70 ATPase activity. PDB 1XBL. Figure from Kampinga *et al.* 2010.

1.5.1.4 Hsp60 (HSPD/HSPE)

Hsp60, also called chaperonins, are large double ring complexes that enclose a central cavity (Figure 1.5). Substrate proteins, typically folding intermediates, are encapsulated in the central cavity, thereby shielding exposed hydrophobic residues from aggregation and allowing the substrate to fold in a protected environment (Kusmierczyk *et al.* 2001, Yébenes *et al.* 2011). Chaperonins can be divided to two subgroups. Group I chaperonins (HSPD) are present in bacteria (GroEL) and the mitochondrial matrix (Hsp60). They contain 7 subunits per ring and require co-chaperones that act as lids over the complexes (GroES in bacteria and Hsp10 in mitochondria). Group II chaperonins (HSPE) are found in archaea (thermosome) and in the cytosol of eukaryotes (TRiC) and they typically have 8 subunits per ring (Yébenes *et al.* 2011).

The GroEL chaperonin in *E. coli* has been the most extensively studied (Hartl *et al.* 2009). Each subunit consists of an equatorial ATP binding domain, a hinge domain and an apical substrate binding domain. The apical domain forms the entrance to the GroEL cavity and exposes hydrophobic residues to mediate substrate binding. Following substrate binding to one of the rings, ATP binds to each of the 7 subunits, inducing conformational changes, enabling the association of GroES and the subsequent encapsulation of the substrate. Upon GroES binding, the GroEL cavity enlarges, creating an environment for productive protein folding. The hydrolysis of ATP to ADP triggers the dissociation of the GroES lid and the release of the substrate (Horwich *et al.* 2007, Hartl *et al.* 2011, Yébenes *et al.* 2011). Multiple folding cycles may be required before the substrate reaches its native state.

1.5.1.5 Small Hsp (HSPB)

Small heat shock proteins differ from the other members of the molecular chaperone family in that they are ATP independent. The human genome encodes 10 small Hsps (termed HSPB1-10) and they range in size from 12-42 kDa. They share a conserved 100 amino acid α-crystallin domain that is flanked by variable N-terminal and C-terminal extensions. These extensions mediate substrate recognition as well as enabling the formation of oligomers. Small Hsps are able to bind to unfolded or misfolded protein and prevent their aggregation until the protein can be transferred to Hsp70 (Carra *et al.* 2012).

1.5.2 The ubiquitin proteasome system

The ubiquitin proteasome system (UPS) mediates the degradation of short-lived, damaged and misfolded proteins. Such proteins are targeted for degradation through the covalent attachment of ubiquitin, a modification that enables substrates to be recognised by the proteasome, a proteolytic machine localised in the cytosol and nucleus of eukaryotic cells (Inobe *et al.* 2014).

The conjugation of ubiquitin to protein substrates requires the co-ordinated action of three enzymes (Komander 2009). First, an ubiquitin-activating enzyme (E1) activates ubiquitin in an ATP-dependent manner. The E1 enzyme catalyses the formation of a high-energy thioester bond between an active site cysteine residue and the C-terminal glycine residue of ubiquitin (Gly76). Following activation, ubiquitin is transferred from E1 to an active site cysteine residue of an ubiquitin-conjugating enzyme (E2). The final step in the cascade is mediated by an ubiquitin ligase enzyme (E3) that binds to both the E2 and the substrate and promotes the transfer of ubiquitin, catalysing the formation of an isopeptide bond between the glycine residue of ubiquitin and a lysine residue of the substrate. E3 ubiquitin ligases contain one of two domains; a HECT (homologous to E6-AP C-terminus) domain or a RING (really interesting new gene) domain (Bernassola *et al.* 2008, Deshaies *et al.* 2009). HECT domain E3 ubiquitin ligases bind ubiquitin during the transfer process whereas RING domain E3 ubiquitin ligases catalyse the direct transfer of ubiquitin from the E2 to the substrate. The human genome encodes over 600 E3 ubiquitin ligases. Their abundance and selectivity suggests that E3 ubiquitin ligases are responsible for the substrate specificity of the UPS (Metzger *et al.* 2012).

Ubiquitin has seven lysine residues that can be used in the formation of polyubiquitin chains (K6, K11, K27, K29, K33, K48 and K63). The different linkages generate distinct topologies that can be recognised by specific ubiquitin-binding proteins (Komander 2012). K48-linked ubiquitin chains are the primary signal for proteasomal degradation, with at least four ubiquitin molecules required for recognition by the proteasome (Thrower *et al.* 2000) The functional significance of K6, K11, K27, K29 and K33-linked ubiquitin chains remains to be fully characterised, however there is evidence to suggest that K6, K11, K27, K29 and K63-linked chains can also target a protein for proteasomal degradation (Komander 2012).

The 26S proteasome is a 2.5 mDa protein complex that consists of a 20S core particle and a 19S regulatory particle (Figure 1.8). The 20S core particle is composed of four stacked heptameric rings that form a central chamber, with two outer α-rings and two inner β-rings (Inobe *et al.* 2014, Gu *et al.* 2014). Subunits β1, β2 and β5 of each β-ring have proteolytic activity, displaying caspase-like, trypsin-like and chymotrypsin-like peptidase activity,

respectively. Access to the proteolytic sites is restricted by the two outer α-rings, which gate the central chamber. Gate opening and the translocation of the substrate into the proteolytic chamber is regulated by the 19S particle. The 19S regulatory particle can be divided into a base and a lid complex (Lander *et al.* 2012). The base structure consists of a ring of six AAA ATPase subunits (Rpt1-6) (Tomko *et al.* 2010). Three of the ATPase subunits contain C-terminal tails with a specific HbYX motif. These C-terminal tails bind to pockets in the 20S α-ring, tethering the two particles and subsequently promoting gate opening (Smith *et al.* 2007, Gillette *et al.* 2008). Both the base and the lid structures contain subunits that bind to polyubiquitin chains. Once the ubiquitylated substrate is bound to the 19S regulatory particle, the ubiquitin chain is cleaved by Rpn11, a subunit of the lid complex (Verma *et al.* 2002). The ATPase subunits of the base subsequently unfold the polypeptide chain through cycles of ATP hydrolysis. Only once the chain is unfolded can it proceed into the proteolytic chamber, where the substrate is cleaved into small peptides. Upon their exit from the proteasome, the small peptides are digested by cytosolic endopeptidases and aminopeptidases.

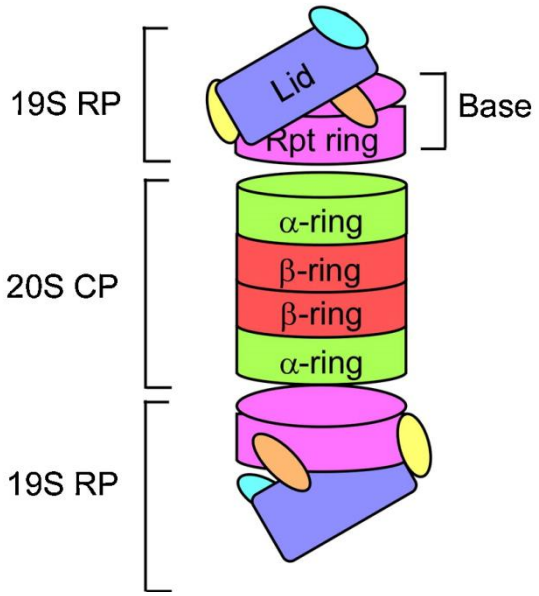

Figure 1.8 Schematic representation of the 26S proteasome. The 26S proteasome is composed of a 20S core particle and a 19S regulatory particle. The 20S particle is composed of four stacked heptameric rings. Subunits of the β-rings have proteolytic activity. The α-rings act as a gate to the proteolytic chamber. Gate opening is regulated by the 19S particle, which is composed of a lid and a base sub-complex. Figure from Lee *et al.* 2013.

1.5.3 Autophagy

Autophagy mediates the lysosomal degradation of cellular components. Unlike the UPS, which degrades short-lived proteins, autophagy typically degrades long-lived proteins and is capable of degrading large structures such as protein aggregates and damaged organelles. There are three types of autophagy; macroautophagy, microautophagy and chaperone-mediated autophagy (CMA) (Lee *et al.* 2013). In CMA, cytosolic proteins containing a pentapeptide KFERQ motif are recognised by Hsc70 and targeted to the lysosome through an interaction with the integral lysosomal membrane protein, LAMP2A. In microautophagy, cytosolic material is directly engulfed into the lysosome through the invagination of the membrane. In macroautophagy, cytosolic components are engulfed by vesicles, which subsequently fuse with the lysosome. The molecular machinery of macroautophagy (herein referred to as autophagy) has been extensively characterised in yeast, with the identification of approximately 30 autophagy-related genes (ATG), many of which have mammalian orthologues (Mizushima 2011).

Autophagy requires the formation of a double membrane vesicle called an autophagosome (Rubinsztein *et al.* 2012). Autophagosome formation is initiated by the extension of an enveloping membrane (isolation membrane), a process dependent on the activation of the ULK1 complex, composed of ULK1, ATG13, ATG101 and FIP200. The activity of the induction complex is regulated by two kinases; mammalian target of rapamycin complex (mTORC1) and adenosine monophosphate-activated protein kinase (AMPK) (Kim *et al.* 2011). Under nutrient-rich conditions, mTORC1 phosphorylates ULK1 and ATG13, maintaining the complex in an inactive state. Under starvation conditions, mTORC1 is inhibited, resulting in the dephosphorylation of the ULK1 complex, which in turn facilitates the binding of AMPK. AMPK then activates the complex via a series of phosphorylation events. In addition to requiring the activation of the ULK1 complex, isolation membrane formation also requires the activation of the phosphoinositide 3-kinase (PI3K) complex, whose components include Beclin1 and the P13K Vps34. Vsp34 is responsible for the formation of phosphatidylinositol 3-phosphate, which is essential for the nucleation, expansion and curvature of the isolation membrane.

The elongation of the isolation membrane into an autophagosome is mediated by two ubiquitin-like conjugation reactions (Rubinsztein *et al.* 2012). ATG12 is conjugated to ATG5 via the concerted action of ATG7 and ATG10, E1-like and E2-like enzymes, respectively. The conjugate then interacts with ATG16L. The ATG12-ATG5-ATG16L complex is proposed to serve as a platform for protein-protein interactions at the autophagosome membrane. The second ubiquitin-like conjugation reaction involves the

conversion of LC3-I to LC3-II. LC3 is synthesised as pro-LC3; the protein is subsequently cleaved at its C-terminus by ATG4, exposing a conserved glycine residue (LC3-I). ATG7 and ATG3 facilitate the binding of phosphatidylethanolamine to the exposed glycine residue, forming LC3-II. The lipidated form is recruited into the autophagosome membrane and promotes the maturation of the vesicle, with the subsequent engulfment of cytosolic cargo. Upon maturation, the autophagosome fuses with lysosomes, allowing the degradation of the cargo by lysosomal hydrolytic enzymes.

Autophagy adaptor proteins, such as p62, NBR1 and NIX, mediate the selective recruitment of cargo into the autophagosome (Johansen *et al.* 2011). The adaptor proteins contain two critical domains, an LC3-interacting region (LIR) and an ubiquitin binding domain (UBA). The UBA domain binds to ubiquitylated substrates, typically with K63-linked ubiquitin chains. Once bound to the cargo, the adaptor can then bind to LC3-II via the LIR, thereby targeting the ubiquitylated substrate for engulfment by the autophagosome.

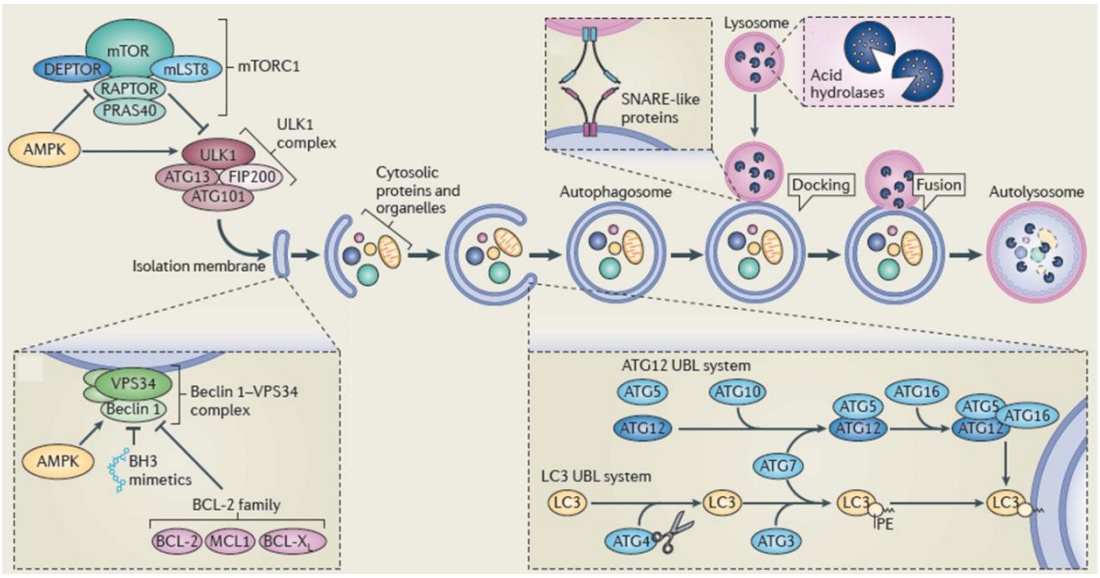

Figure 1.9 The autophagy pathway. Autophagosome formation requires the activation of the ULK1 complex and the Vps34 PI3K complex. These complexes function to initiate the formation of an isolation membrane. The isolation membrane is extended into an autophagosome through two ubiquitylation-like (UBL) reactions. ATG7 and ATG10 conjugate ATG12 to ATG5. The conjugate then associates with ATG16L. The second ubiquitylation-like reaction requires the conversion of pro-LC3 to LC3-I by ATG4. ATG7 and ATG3 then catalyse the attachment of phosphatidylethanolamine (PE) to LC3-I, forming LC3-II. As the autophagosome forms, cargo becomes engulfed in the vesicle. Upon formation, the autophagosome fuses with the lysosome, enabling the cargo to be degraded by acidic hydrolases. Figure from Mariño *et al.* 2014.

1.5.4 ER-associated degradation

The ER is responsible for the folding and post-translational modification of newly synthesised membrane and secretory proteins. The high rate of protein folding in the ER places a burden on the organelle and a significant fraction of proteins fail to reach their native conformation (Matus *et al.* 2011). Misfolded proteins in the ER are targeted to the proteasome for degradation in a process termed ER-associated degradation (ERAD). The process can be divided into four stages; the recognition of misfolded substrates, their retrotranslocation to the cytosol, protein ubiquitylation, and finally targeting to the proteasome (Ruggiano *et al.* 2014).

The ERAD pathway is co-ordinated by a membrane complex consisting of multiple components (Olzmann *et al.* 2013). Components of the complex can interact with misfolded proteins directly or alternatively, misfolded proteins can be recruited to the complex by molecular chaperones, such as the ER luminal Hsp70 protein BiP, or EDEM1, a lectin that exhibits chaperone-like activity. Once recruited to the ERAD machinery, the misfolded protein must be retrotranslocated across the lipid bilayer to the cytosol. The identity of the retrotranslocation channel remains unknown, however, a series of candidates have been proposed. One possible candidate is the Sec61 translocon, which facilitates the import of newly synthesised polypeptide chains into the ER (Schäfer *et al.* 2009). It is possible that the translocon may function in a bidirectional manner, enabling both the import and export of polypeptide chains. Members of the Derlin family have also been proposed to function as retrotranslocation channels, along with Hrd1 and gp78, integral membrane E3 ubiquitin ligases (Carvalho *et al.* 2010). The function of Hrd1 and gp78 as retrotranslocation channels could couple protein export with protein ubiquitylation. Protein ubiquitylation is a pre-requisite for the binding of p97/VCP, a cytosolic AAA ATPase that drives the extraction of the polypeptide chains from the ER membrane in an ATP-dependent manner (Stolz *et al.* 2011). Upon the extraction from the membrane, the ubiquitylated ERAD substrate is recognised by molecular chaperones and ubiquitin-binding proteins and is targeted to the proteasome for degradation.

1.6 Cell stress responses

1.6.1 The unfolded protein response

The accumulation of misfolded proteins in the ER can activate an unfolded protein response (UPR), a dynamic signalling pathway that aims to restore proteostasis by increasing the folding and degradative capacity of the organelle (Walters and Ron 2011). The UPR is orchestrated by three transmembrane proteins; inositol-requiring enzyme 1 (IRE1), protein

kinase RNA-like ER kinase (PERK) and activating transcription factor 6 (ATF6). Under resting conditions, the three transmembrane proteins are maintained in an inactive state through their association with BiP. Upon the accumulation of misfolded proteins, BiP dissociates and the UPR is activated (Figure 1.10).

IRE1 is a type I transmembrane protein that contains a cytosolic serine/threonine kinase domain and an endoribonuclease domain. The dissociation of BiP leads to the dimerisation and autophosphorylation of IRE1, activating the endoribonuclease activity of the protein. The endoribonuclease activity of IRE1 catalyses the unconventional splicing of X-box binding protein 1 (XBP1) mRNA, with the excision of a 26-nucleotide intron that subsequently shifts the coding reading-frame. Spliced XBP1 is stable and is translated to XBP1s, an active transcription factor that upregulates ER chaperones and ERAD machinery, thus increasing the folding and degradative capacity of the ER (Walters and Ron 2011, Deegan *et al.* 2013).

PERK is a type I transmembrane protein with a cytosolic serine/threonine kinase domain. Upon its activation, the kinase domain catalyses the phosphorylation of eukaryotic initiation factor 2 (eIF2α), leading to the inhibition of general translation and thereby reducing the entry of newly synthesised proteins into the ER. Phosphorylated eIF2α results in the selective translation of activating transcription factor 4 (ATF4), a transcription factor that upregulates ER chaperones as well as proteins involved in autophagy, amino acid metabolism and oxidative stress (Walters and Ron 2011, Deegan *et al.* 2013).

ATF6 is a type II transmembrane protein and a member of the leucine zipper protein family. The dissociation of BiP unmasks two Golgi localisation signals, promoting the translocation of ATF6 to the cis-Golgi compartment. At the Golgi, the 90 kDa protein is cleaved by a site 1 protease and a site 2 protease, generating a 50 kDa N-terminal fragment that contains the leucine zipper DNA-binding domain. Following cleavage, the active fragment translocates to the nucleus where it acts as a transcription factor, upregulating ER chaperones, ERAD machinery and XBP1 (Walters and Ron 2011, Deegan *et al.* 2013).

If the adaptive responses of the UPR are unable to restore proteostasis, the UPR activates an apoptotic signalling pathway, leading to programmed cell death (Szegezdi *et al.* 2006). One mechanism by which apoptosis is induced is though the PERK branch. ATF4 upregulates the pro-apoptotic transcription factor CHOP. CHOP downregulates the anti-apoptotic protein BCL2 whilst upregulating the transcription of pro-apoptotic BH3-only proteins such as BIM and PUMA (Puthalakath *et al.* 2007). BH3-only proteins translocate to the outer mitochondrial membrane (OMM) where they activate BAK/BAX, the regulators of apoptosis. Once activated, BAK/BAX form homo-oligomers in the OMM, initiating

membrane permeabilisation, the release of cytochrome c and the subsequent activation of caspases, cysteine proteases that play an essential role in apoptosis.

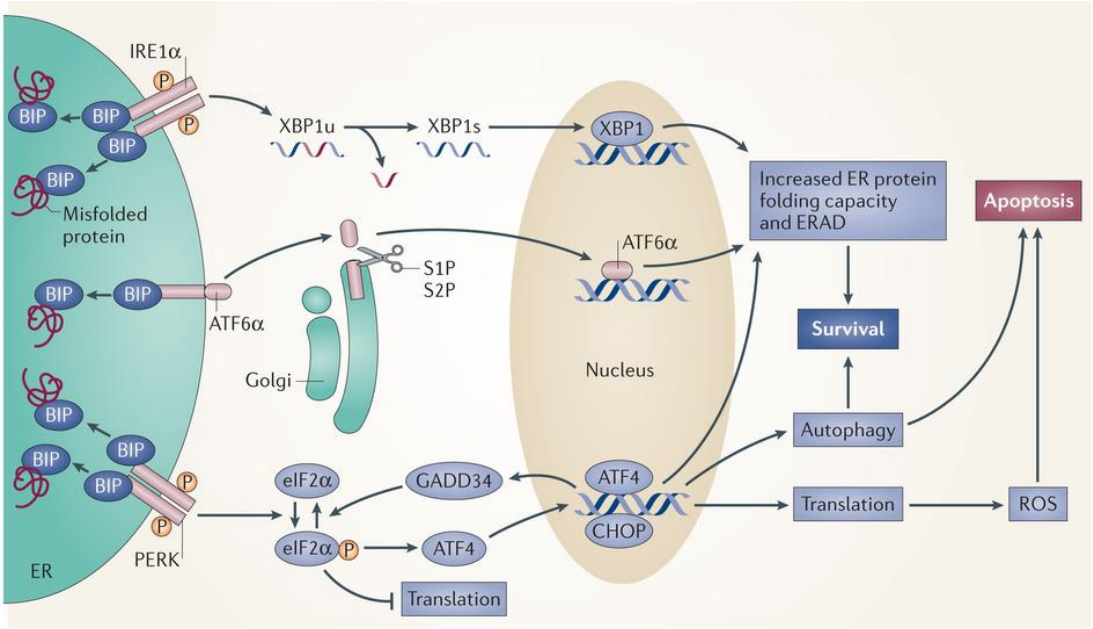

Figure 1.10 The three branches of the unfolded protein response. The accumulation of misfolded protein in the ER results in the dissociation of BiP from the three transmembrane proteins, leading to their activation. PERK phosphorylates eIF2α causing an inhibition of general translation. Phosphorylated eIF2α results in the selective translation of the transcription factor ATF4, which upregulates UPR target genes. IRE1 activation leads to the unconventional splicing of XBP1 mRNA. Spliced XBP1 is stable and is translated to XBP1s, an active transcription factor. The dissociation of BiP from ATF6 exposes Golgi localisation signals. Upon translocation, ATF6 is cleaved by site 1 and site 2 proteases, producing an active transcription factor. The active 50 kDa fragment translocates to the nucleus and upregulates target genes. If the UPR fails to restore homeostasis, an apoptotic signalling cascade is induced. Figure from Wang *et al.* 2014.

1.6.2 The heat shock response

The heat shock response (HSR) is a highly conserved stress pathway that functions to up-regulate heat shock proteins upon exposure to cell stressors, such as elevated temperature, oxidative stress and altered pH (Morimoto 2011). In mammals, the HSR is co-ordinated by heat shock transcription factor 1 (HSF1), a transcription factor with an N-terminal DNA binding domain and a C-terminal oligomerisation domain (McMillan *et al.* 1998). Under normal conditions, HSF1 is retained in a complex with Hsp90 or Hsp70, maintaining the transcription factor in a monomeric repressed state (Zou *et al.* 1998, Shi *et al.* 1998). Upon cell stress, Hsp90 and Hsp70 preferentially bind to non-native proteins, thereby releasing HSF1, enabling its trimerisation and subsequent activation. Activated HSF1 translocates to the nucleus and binds to heat shock elements in the promoter region of genes encoding heat shock proteins, leading to their elevated transcription (Vihervaara *et al.* 2014). The rapid expression of molecular chaperones promotes the recovery from stress-induced damage to proteins.

1.7 Impaired protein quality control in neurodegenerative diseases

Whilst the degeneration of upper and/or lower motor neurons defines motor neuron disorders, the selective degeneration of other neuronal populations in the brain, brainstem and spinal cord defines other neurological diseases. Collectively, these diseases are referred to as neurodegenerative diseases. ALS, Alzheimer's disease (AD), Huntington's disease (HD) and Parkinson's disease (PD) are four of the most widely studied neurodegenerative diseases, with particular focus on dissecting the molecular mechanisms that underlie neuronal degeneration in each disease (Bettens *et al.* 2013, Walker *et al.* 2007, Kailia and Lang 2015, Kiernan *et al.* 2011).

HD is a hereditary disease, whereas AD, ALS and PD are predominantly sporadic. Clinically and pathologically, sporadic cases of AD, ALS and PD are often indistinguishable from the hereditary forms of the disease (representing 5-10% of cases), suggesting common mechanisms of disease pathogenesis. The identification and characterisation of causative genes for hereditary cases can therefore advance our understanding of the molecular mechanism that underlie neuronal degeneration in both forms of the disease.

1.7.1 Protein aggregates are a hallmark of neurodegenerative diseases

Ubiquitylated protein aggregates are a pathological hallmark of many neurodegenerative diseases. Impairments in proteostasis may therefore be a common underlying mechanism of disease pathogenesis. Indeed, many of the causative mutations identified in hereditary cases

lead to the misfolding and aggregation of the disease-related protein, for example, amyloid-β (Aβ) in AD, SOD1 in ALS, huntingtin in HD and α-synuclein in PD (Hardy *et al.* 1992, Goedert *et al.* 1989, Rosen *et al.* 1993, DiFiglia *et al.* 1997, Spillantini *et al.* 1998, Ross *et al.* 2004, Soto *et al.* 2008). The chronic production of misfolded protein can overwhelm the protective capabilities of the protein quality control network, with the over-burdening of available chaperones and degradation machineries (Hartl *et al.* 2011). The functional depletion of protein quality control components leads to further protein misfolding and aggregation, promoting the collapse of proteostasis and driving disease progression.

The large aggregates observed pathologically are thought to represent the end point of the aggregation process, which begins with the formation of small soluble oligomers, followed by the formation of protofibrils then mature fibrils (Lim and Yue 2015). Soluble oligomers and protofibrils are suggested to pose the most toxic potential to the cell; these toxic species expose hydrophobic surfaces that can mediate aberrant interactions with other proteins and cellular membranes (Walsh *et al.* 2002, Winner *et al.* 2011). The aggregation of soluble oligomers into larger insoluble deposits is suggested to be a protective response, reducing the exposed surface area that can form aberrant interactions (Arrasate *et al.* 2004). Although larger aggregates may not be considered the most toxic species, it is unlikely that they are completely harmless. Large aggregates may contribute to cytotoxicity through their ability to physically obstruct axonal transport (Goldstein 2012). Neurons rely heavily on axonal transport in order to efficiently sustain their function. Neurons are therefore vulnerable to aggregate formation and thus place a high demand on the protein quality control machinery to maintain proteostasis.

1.7.2 Molecular chaperones are protective in neurodegenerative disease

Molecular chaperones are important therapeutic targets in neurodegenerative diseases. Their manipulation could re-balance the protein quality control network, restoring proteostasis and potentially slowing disease progression. The first demonstration that molecular chaperones could act as potent modulators of protein aggregation and neurodegeneration was provided by Cummings *et al.* (1998) using a cellular model of polyglutamine (polyQ) disease. They showed that the overexpression of DnaJA1 was able to reduce the aggregation of polyglutamine expanded ataxin-1. Since this first report, the effect of other DnaJ proteins on polyQ aggregation has been studied. DnaJB2a was identified as a particularly effective suppressor of polyQ aggregation in cells and will be discussed in more detail is section 1.8.4 (Westhoff *et al.* 2005). A comparative study by Hageman *et al.* (2010) revealed that members of the DnaJB subfamily were more effective than members of the DnaJA subfamily at reducing the formation of high molecular weight species and insoluble

aggregates in cells expressing mutant polyQ. Interestingly, within the DnaJB subfamily, members were found to exhibit differential anti-aggregation properties; DnaJB6b and DnaJB8 were found to suppress polyQ aggregation to a greater extent than DnaJB1 and DnaJB2b (Hageman *et al*. 2010). All four DnaJB proteins were found to reduce polyQ aggregation by facilitating its degradation via the proteasome (Bailey *et al.* 2002, Westhoff *et al.* 2005, Hageman *et al*. 2010); however, unlike DnaJB1 and DnaJB2b, the ability of DnaJB6b and DnaJB8 to reduce polyQ aggregation was almost completely independent of J domain activity. Instead, the anti-aggregation properties were found to be dependent on the C-terminal serine-rich region (Hageman *et al*. 2010), a region unique to DnaJB6 and DnaJB8 that functions in substrate recognition and the formation of oligomers. Small Hsps have also been shown to suppress polyQ aggregation. As with members of the DnaJB family, members of the small Hsp family also exhibited different anti-aggregation properties; the overexpression of HSPB6, HSPB7, HSPB8 or HSPB9 reduced polyQ aggregation in cells, whereas the overexpression of HSPB1, HSPB2, HSPB3, HSPB4, HSPB5 or HSPB10 had little or no effect (Vos *et al.* 2010). HSPB7 was identified as the strongest suppressor of polyQ inclusion formation, acting to target polyQ for autophagy-mediated degradation. This corresponded with a reduction in polyQ-mediated cytotoxicity (Vos *et al.* 2010).

The anti-aggregation properties of molecular chaperones have also been examined in other models of neurodegenerative disease. Hsp70 has been particular well studied in models of PD. The overexpression of Hsp70 has been shown to suppress α-synuclein aggregation both *in vitro* and *in vivo*. In a cell model, the overexpression of Hsp70 reduced the levels of high molecular weight and detergent insoluble α-synuclein, as well as reducing total α-synuclein levels. This corresponded with a reduction in α-synuclein-mediated cytotoxicity (Klucken *et al.* 2004). Consistent with the *in vitro* observations, the overexpression of Hsp70 in a transgenic mouse model reduced α-synuclein aggregation (Klucken et al. 2004). Further studies in mice and *Drosophila melanogaster* revealed that the Hsp70-mediated reduction in α-synuclein aggregation corresponded with an increase in dopaminergic neuron survival, enabling the preservation of striatal dopamine levels (Auluck *et al.* 2002, Cleren *et al.* 2005). The mechanism by which Hsp70 suppresses α-synuclein aggregation was proposed to rely on the inhibition of fibril formation, with Hsp70 binding to protofibrils and preventing their elongation and further nucleation (Huang *et al.* 2006).

Hsp70 is also protective in cell models of ALS, ameliorating mutant SOD1 aggregation and toxicity in primary motor neuron cultures (Takeuchi *et al.* 2002, Patel *et al.* 2004). Members of the small Hsp family are also protective *in vitro*, with HSPB1 protecting against mutant SOD1-induced cell death and HSPB8 reducing mutant SOD1 aggregation by stimulating the

autophagy-mediated degradation of the protein (Patel *et al.* 2004, Crippa *et al.* 2010). Although Hsp70 and HSPB1 showed promising effects *in vitro*, their upregulation *in vivo* has proved less successful. The overexpression of Hsp70 was unable to delay disease progression or improve survival in mutant SOD1 mice (Liu *et al.* 2005). The overexpression of HSPB1 in mutant SOD1 mice only proved beneficial at an early stage of the disease, increasing motor neuron survival (Patel *et al.* 2008). However, the protective effect was not sustained; the overexpression of HSPB1 had no effect on late-stage disease progression. In contrast to the upregulation of individual chaperones, the upregulation of multiple chaperones has proved more successful in combating mutant SOD1 aggregation and toxicity *in vivo* (Kieran *et al.* 2004). The treatment of SOD1 G93A mice with arimoclomal, a drug that upregulates chaperones such as Hsp90, Hsp70 and DnaJ proteins by stabilising the binding of HSF1 to heat shock elements, delayed disease progression, with a decrease in ubiquitin positive aggregates in the spinal cord and an improvement in motor neuron survival at late stages of the disease. This was accompanied by a 22% increase in life-span (Kieran *et al.* 2004).

1.7.3 Mutations in molecular chaperones cause neurodegenerative diseases

Mutations in molecular chaperones cause inherited neurodegenerative diseases, highlighting their critical role in neuronal survival (Table 1.3). Interestingly, mutations in five members of the molecular chaperone family (Hsp60, DnaJC29, HSPB1, HSPB8 and DnaJB2) have been identified to cause motor neuron degeneration.

1.7.3.1 Hsp60

As discussed in section 1.2.2, hereditary spastic paraplegia is caused by the degeneration of upper motor neuron axons in the corticospinal tract, leading to progressive spasticity and weakness of the lower limbs. Two missense mutations in the mitochondrial chaperonin Hsp60 (V98I and Q461E) have been reported in autosomal dominant cases of the disease (Hansen *et al.* 2002, Bross *et al.* 2007). Hsp60 Q461E, complemented the deletion of GroEL in *E. coli*, however, the resultant colonies were consistently smaller than wild-type colonies and grew at a significantly slower rate at higher and lower temperatures (Hansen *et al.* 2002). These observations suggest that the substitution may compromise the activity of Hsp60. The V98I patient mutation was found to have a more severe effect on Hsp60 function. Hsp60 V98I was unable to support the growth of *E. coli* lacking GroEL (Bross *et al.* 2007). Furthermore, purified Hsp60 V98I displayed decreased ATPase activity and exhibited a reduced capacity to fold denatured malate dehydrogenase (Bross *et al.* 2007). The cellular consequences of impaired Hsp60 function have been investigated *in vivo*, using a heterozygous *Hsp60* knockout mouse (Magnoni *et al.* 2013). The heterozygous mice

developed progressive, late onset deficits in motor function. Morphological changes in mitochondria were observed, with a reduction in ATP synthesis. The reduction in ATP synthesis was attributed to lower levels of complex III, suggesting that Hsp60 plays an important role in respiratory chain complex assembly. Overall, this research suggests that the neurodegeneration process could be driven by Hsp60 haploinsufficiency rather than a dominant or dominant-negative effect of the mutant protein.

1.7.3.2 DnaJC29

Autosomal recessive spastic ataxia of Charlevoix-Saguenay (ARSACS) is an early onset neurodegenerative disease caused by the progressive loss of Purkinje cells in the cerebellum, followed by motor neurons in the spinal cord (Bouchard 1978). The disease is caused by mutations in DnaJC29 (sacsin), with over 170 mutations identified throughout the 520 kDa protein. Sacsin contains an N-terminal ubiquitin-like domain (UBL) followed by three large sacsin repeat regions, an XPCB domain, a C-terminal J domain and a HEPN domain. A full understanding of sacsin function is currently lacking, however, the identification of sacsin-interacting proteins suggests a role in protein quality control, with the ubiquitin-like domain and the XPCB domain binding to the proteasome and ubiquitin ligases, respectively (Parfitt *et al.* 2009, Greer *et al.* 2010). Sacsin is predominantly localised in the cytosol but also localises to mitochondria (Girard *et al.* 2012). Sacsin was shown to interact with dynamin-related protein 1 (DRP1), a GTPase that mediates mitochondrial fission (Girard *et al.* 2012). Interestingly, in patient fibroblasts, mitochondria appear overly fused, suggesting a role for sascin in mitochondrial fission (Girard *et al.* 2012). Impairments in mitochondrial fission are likely to lead to mitochondrial dysfunction, a common mechanism underlying motor neuron degeneration.

1.7.3.3 DNAJB2, HSPB1 and HSPB8

Mutations in *DNAJB2, HSPB1* and *HSPB8* are associated with dHMN and CMT2. The mechanisms by which mutations in these chaperones cause motor neuron degeneration are discussed in the following section.

Family	Chaperone	Inheritance	Disease	Reference
Hsp70	HSPA9 (Mortalin)	Dominant	Parkinson's disease	De Mena *et al.* 2009, Freimann *et al.* 2013
Hsp60	HSP60 (HSPD)	Dominant	Spastic paraplegia	Hansen *et al.* 2002, Bross *et al.* 2007
		Recessive	Hypomyelinating leukodystrophy	Magen *et al.* 2008
	CCT4	Recessive	Hereditary sensory neuropathy	Lee *et al.* 2003
	CCT5	Recessive	Sensory neuropathy with spastic paraplegia	Bouhouche *et al.* 2006, Lee *et al.* 2003
Hsp40 (DnaJ)	DNAJB2 (HSJ1)	Recessive	Distal hereditary motor neuropathy, Charcot Marie Tooth 2	Blumen *et al.* 2012, Gess *et al.* 2014
	DNAJB6 (MRJ)	Dominant	Limb-girdle muscular dystrophy	Harms *et al.* 2012, Sarparanta *et al.* 2012, Sato *et al.* 2013
	DNAJC3 (ERdj6)	Recessive	Diabetes and multisystemic neurodegeneration	Vilariño-Güell *et al.* 2014
	DNAJC5 (CSPα)	Dominant	Neuronal ceroid lipofusinosis	Benitez *et al.* 2011, Noskova *et al.* 2011
	DNAJC6 (Auxilin)	Recessive	Juvenile Parkinsonism	Edvardson *et al.* 2012, Köroğlu *et al.* 2013
	DNAJC13 (RME-8)	Dominant	Parkinson's disease	Vilariño-Güell *et al.* 2014
	DNAJC19 (TIM14)	Recessive	Dilated cardiomyopathy and cerebellar ataxia	Davey *et al.* 2006, Ojala *et al.* 2012
	DNAJC29 (Sacsin)	Recessive	Spastic ataxia of Charlevoix-Saguenay	Engert *et al.* 2000, Thiffault *et al.* 2013
Small Hsp	HSPB1 (Hsp27)	Dominant and recessive	Distal hereditary motor neuropathy, Charcot Marie Tooth 2	Evgrafov *et al.* 2004, Houlden *et al.* 2008, Ikeda *et al.* 2009
	HSPB3 (HspL27)	Dominant	Hereditary motor neuropathy	Kolb *et al.* 2010
	HSPB5 (αβ-crystallin)	Recessive	Infantile muscular dystrophy	Del Bigio *et al.* 2011
	HSPB8 (Hsp22)	Dominant	Distal hereditary motor neuropathy, Charcot Marie Tooth 2	Irobi *et al.* 2004
Chaperone co-factors	SIL1	Recessive	Cerebellar ataxia	Senderek *et al.* 2005
	VCP	Dominant	Amyotrophic lateral sclerosis	Johnson *et al.* 2010, Gonzalez-Perez *et al.* 2012
	BAG3	Dominant	Muscular dystrophy Giant axonal neuropathy	Selcen *et al.* 2009, Jaffer *et al.* 2012

Table 1.3 Molecular chaperones as causative genes in inherited neurodegenerative diseases

1.8 Impaired proteostasis in dHMN and CMT2

The identification of causative genes in dHMN and CMT2 has provided the foundations to explore the cellular mechanisms underlying motor neuron degeneration. The characterisation of mutations in *HSPB1, HSBP8, LRSAM1, BSCL2* and *DNAJB2* has implicated impaired proteostasis as a critical driving force in the pathogenesis of the disease.

1.8.1 HSPB1 and HSPB8

Mutations in HSPB1 (Hsp27) and HSPB8 (Hsp22) are typically associated with autosomal dominant forms of dHMN and CMT2 (Irobi *et al.* 2004, Evgrafov *et al.* 2004, James *et al.* 2008, Ikeda *et al.* 2009, Luigetti *et al.* 2010). The majority of mutations identified are missense mutations that lie in the α-crystallin domain (Carra *et al.* 2012). The mutations trigger Hsp27 or Hsp22 aggregate formation, thereby disrupting proteostasis. Proteostasis is further impaired through the co-aggregation of the wild-type counterpart, resulting in a loss of wild-type Hsp27 or Hsp22 chaperone activity (Carra *et al.* 2012). Accumulating evidence suggests that a loss of Hsp22 chaperone activity plays a central role in disease pathogenesis through a loss of protein quality control. Mutant Hsp22 exhibited a reduced ability to block mutant huntingtin and SOD1 aggregation in cells compared to the wild-type protein (Carra *et al.* 2005, Crippa *et al.* 2010). Mutant Hsp22 was also less effective at reducing the levels of high molecular weight aggregated protein in a cell model expressing mutant ataxin-3 (SCA3) (Carra *et al.* 2010). The loss of anti-aggregation function was confirmed in *Drosophila*; mutant Hsp22 was unable to protect against SCA3-mediated eye degeneration (Carra *et al.* 2010). Mutant Hsp22 showed a reduced binding affinity for its interacting partner Bag3 (Carra *et al.* 2010, Shemetov *et al.* 2011). Hsp22 interacts with Bag3 to target misfolded proteins for autophagy-mediated degradation (Carra *et al.* 2008). Whether the decreased binding affinity for Bag3 accounts for the impaired anti-aggregation function of the protein remains to be determined. However, an inability to target misfolded proteins for degradation, in addition to Hsp22 aggregate formation, is likely to overwhelm the protective capabilities of the protein quality control network, driving the collapse of proteostasis and motor neuron degeneration.

1.8.2 LRSAM1

The inability to target specific client proteins for degradation has also been identified as an underlying cause of CMT2 in patients with a mutation in *LRSAM1*. A 2bp insertion in *LRSAM1*, which encodes an E3 ubiquitin ligase, was identified in a family with autosomal dominant CMT2 (Weterman *et al.* 2012). The insertion resulted in a frameshift, with a L708R substitution and the introduction of a stop codon 28 bp downstream. Mutant

LRSAM1 expression levels were unaffected, however the E3 ubiquitin ligase activity of the protein was found to be impaired. In cells, the expression of mutant LRSAM1 led to the accumulation of TSG101, the only identified client of LRSAM1 to date (Weterman *et al.* 2012). Whether motor neuron degeneration is mediated by the accumulation of TG101 or another unidentified client remains to be determined, however the identification of *LRSAM1* as a causative gene highlights the importance of maintaining proteostasis for motor neuron survival.

1.8.3 BSCL2

Missense mutations in *BSCL2* have been reported to cause autosomal dominant cases of dHMN and CMT2. *BSCL2* encodes the ER transmembrane protein seipin. The mutations disrupt N-glycosylation motifs, preventing its correct folding and maturation (Windpassinger *et al.* 2004). The overexpression of mutant seipin in cells resulted in the accumulation of misfolded seipin in the ER and induced the upregulation of the UPR markers BiP and CHOP (Ito *et al.* 2008). The activation of the UPR in response to the accumulation of misfolded protein resulted in an increase in apoptotic cell death (Ito *et al.* 2008). The characterisation of BSCL2 mutants potentially links protein misfolding to motor neuron degeneration.

1.8.4 DnaJB2

Recently, mutations in *DNAJB2* have been identified in autosomal recessive cases of dHMN and CMT2 (Blumen *et al.* 2012, Gess *et al.* 2014), further supporting the important role of molecular chaperones and protein quality control in motor neuron survival. The identified mutations are discussed in more detail in Chapter 4.

DnaJB2 (HSJ1) is a type II DnaJ protein that is alternatively spliced to produce two isoforms with alternative C-termini (Cheetham *et al.* 1998). The two isoforms, HSJ1a and HSJ1b, are preferentially expressed in neurons and show distinct intracellular localisations (Cheetham *et al.* 1992, Chapple and Cheetham 2003). The shorter isoform, HSJ1a, is a 36 kDa protein that localises to the nucleus and the cytoplasm, whereas the longer HSJ1b isoform is a 42 kDa protein that localises to the cytoplasmic face of the ER by C-terminal geranylgeranylation (Chapple and Cheetham 2003). Both isoforms contain an N-terminal J domain, a client binding domain and two ubiquitin interacting motifs (UIMs) (Figure 1.11) (Chapple *et al.* 2004, Westhoff *et al.* 2005).

Both HSJ1 isoforms function to target misfolded proteins for proteasomal degradation (Westhoff *et al.* 2005, Howarth *et al.* 2007, Meimaridou *et al.* 2011, Novoselov *et al.* 2013).

The combination of a J domain, a client binding domain and UIMs enables HSJ1 to recognise misfolded, ubiquitylated client proteins and load them onto Hsp70, with subsequent delivery to the proteasome for degradation. Alternatively, HSJ1 can load non-ubiquitylated misfolded clients onto Hsp70 and subsequently promote their ubiquitylation by co-operating with E3 ubiquitin ligases. The binding of the UIMs to the generated ubiquitin chains enables HSJ1 to protect the client from de-ubiquitylation by ubiquitin hydrolases, ensuring that the signal for proteasomal degradation remains intact (Westhoff *et al.* 2005). The cytoplasmic localisation of HSJ1a enables the isoform to act as an escort factor, accompanying the client-bound Hsp70-E3 ubiquitin ligase complex to the proteasome. Interestingly, HSJ1a has been found to bind to the proteasome, suggesting a possible role in proteasomal docking (Westhoff *et al.* 2005).

HSJ1 has been demonstrated to be a potent modulator of protein aggregation in cell and mouse models of neurodegenerative diseases. The overexpression of HSJ1a was able to significantly reduce polyQ inclusion incidence in a cell model of HD (Westhoff *et al.* 2005). The anti-aggregation properties were specific to HSJ1a; HSJ1b was only able to reduce polyQ aggregation when it was released from the cytoplasmic face of the ER through the introduction of a mutation that prevented its C-terminal prenylation. The localisation of HSJ1a is therefore critical for its protective function against polyQ. The ability of HSJ1a to modulate polyQ aggregation was found to be both J domain and UIM dependent (Westhoff *et al.* 2005). PolyQ levels were increased upon proteasome inhibition, indicating that HSJ1a reduces polyQ inclusion formation *in vitro* by targeting the protein for proteasomal degradation. The overexpression of HSJ1a also reduced aggregate formation *in vivo*, in a R6/2 mouse model of HD (Labbadia *et al.* 2012). HSJ1a expression significantly reduced the level of aggregated mutant huntingtin in the brain, whilst increasing the levels of soluble protein. In contrast to the observations made *in vitro*, the mechanism of action did not rely on proteasomal degradation, instead relying on the association of HSJ1a with K63-linked ubiquitylated, higher order, detergent insoluble species, preventing their further nucleation. The reduction in aggregation was neuroprotective and led to an improvement in neurological performance of the R6/2 mice at a late stage of the disease (Labbadia *et al.* 2012).

The overexpression of HSJ1a was also shown to reduce the aggregation of SOD1 G93A in a cell model of ALS. HSJ1a stimulated the ubiquitylation and proteasomal degradation of SOD1 G93A, leading to a reduction in inclusion formation. The process was dependent on the J domain and functional UIMs (Novoselov *et al.* 2013). *In vivo*, the overexpression of HSJ1a was able to ameliorate late stage disease in a SOD1 G93A mouse model of ALS (Novoselov *et al.* 2013). HSJ1a reduced the levels of insoluble SOD1 G93A, leading to a significant improvement in neuromuscular function, with a preservation of muscle force, an

increase in motor unit number and enhanced motor neuron survival. Altered ubiquitin immunoreactivity was observed in the double transgenic mice, suggesting that ubiquitin modifications may be important for the observed improvements (Novoselov *et al.* 2013). The ability of HSJ1a to protect against mutant SOD1-mediated toxicity highlights the potential importance of HSJ1 for normal motor neuron function.

In contrast to cells models of HD and ALS, the overexpression of HSJ1a in a cell model of PD reduced mutant parkin aggregation in a manner solely dependent on the J domain (Rose *et al.* 2011). HSJ1a was therefore proposed to reduce mutant parkin aggregation by targeting the protein for refolding rather than for proteasomal degradation. HSJ1a was able to partially rescue the re-location of mutant parkin to damaged mitochondria, suggesting HSJ1a promoted a proportion of misfolded parkin to be refolded to a functionally active conformation (Rose *et al.* 2011).

The localisation of HSJ1b to the cytoplasmic face of the ER enables the isoform to function in ERAD, targeting misfolded ER membrane proteins with exposed cytoplasmic domains for ubiquitylation and subsequent proteasomal degradation (Chapple and Cheetham 2003, Westhoff *et al.* 2005). The overexpression of HSJ1b in cells reduced the levels of cystic fibrosis transmembrane conductance regulator (CFTR), a large membrane protein processed in the ER that this particularly prone to misfolding (Westhoff *et al.* 2005). The decline in CFTR levels was abolished upon proteasome inhibition, confirming that HSJ1b targets CFTR for ERAD (Westhoff *et al.* 2005). HSJ1b was also able to target the G-protein coupled receptor melanocortin-4 receptor (MC4R) for ERAD (Meimaridou *et al.* 2011). The two HSJ1 isoforms therefore both act to target misfolded proteins for degradation.

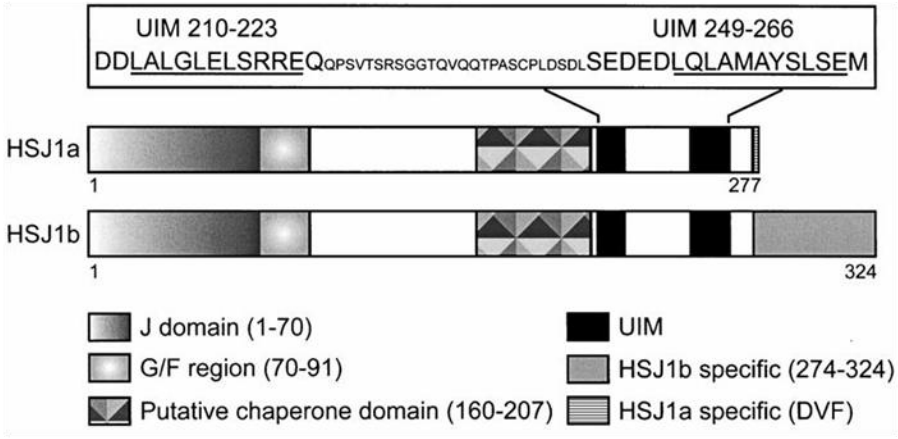

Figure 1.11 Domain composition of HSJ1a and HSJ1b. HSJ1 is alternatively spliced at the C-terminal to produce two isoforms, HSJ1a and HSJ1b. Both isoforms contain an N-terminal J domain, a GF region and two UIMs. Residues 160-207 are predicted to form a client binding domain. Figure from Chapple *et al.* 2004.

1.9 Aims

This Thesis describes investigations into the function of HSJ1 in motor neurons and probes the mechanisms by which loss of function mutations in *HSJ1* cause motor neuron degeneration. Specifically, I aimed to;

- Examine whether UIM1 of HSJ1a functions to bind to the UBL-containing protein ubiquilin-2, a protein recently implicated in ALS.
- Investigate the pathogenicity of a recently identified amino acid substitution in *HSJ1* in a family with CMT2.
- Characterise motor neuron survival in a *Hsj1* knockout mouse model and investigate the potential cellular mechanisms by which loss of function mutations in *HSJ1* cause dHMN and CMT2.

Chapter 2 – Materials and Methods

2.1 *In vitro* techniques

2.1.1 Molecular techniques

2.1.1.1 Plasmid transformation

10 ng of plasmid was added to a pre-chilled 1.5 mL eppendorf tube containing 25 µL of thawed JM109 competent cells (Promega). The tube was placed in a water bath at 42°C for 45 seconds before being chilled on ice for 1 minute. 500 µL of Luria-Bertani (LB) broth (Sigma) was then added to the eppendorf and the tube was placed in a shaker and incubated for 1 hour at 37°C. 100 µL of bacterial culture was then spread onto an ampicillin or kanamycin agar plate. Plates were incubated at 37°C overnight. The following day, 2-4 colonies were picked and used to inoculate either 5 mL (for miniprep) or 50 mL (for midiprep) of LB media with appropriate antibiotic selection (ampicillin (50 µg/mL) or kanamycin (10 µg/mL)). Cultures were grown overnight at 37°C with shaking.

2.1.1.2 Plasmid purification (Miniprep)

The miniprep was performed using a GenElute Plasmid Miniprep Kit (Sigma) according to the manufacturer's protocol. Briefly, 5 mL of bacterial culture was centrifuged at 13,000 x g for 2 minutes. The supernatant was removed and the pellet was resuspended in 200 µL of Resuspension solution. 200 µL of Lysis solution was added and the solution was mixed by inverting the tube 5 times before being centrifuged at 13,000 x g for 2 minutes. 350 µL of Neutralisation solution was added, the solution was mixed 5 times, then centrifuged for 10 minutes at 13,000 x g. Following centrifugation, the lysate was transferred to a binding column that had been equilibrated with 500 µL of Column Wash solution. The column was spun for 1 minute and the flow-through was discarded. 750 µL of Wash solution was added to the column; the column was centrifuged and the flow-through discarded. The column was spun for a further minute to dry the column and the column was subsequently transferred to a 1.5 mL eppendorf tube. 100 µL of ultra pure Milli-Q water was added to the column and was spun for 1 minute to elute the DNA. Plasmid concentration was measured on a NanoDrop ND-1000 spectrophotometer (Lab Tech).

2.1.1.3 Plasmid purification (Midiprep)

Midipreps were performed using a HighLink HiPure Midi Prep kit (Invitrogen) according to the manufacturer's protocol. Briefly, 50 mL of bacterial culture was centrifuged at 4,000 x g for 10 minutes. The supernatant was removed and the pellet was resuspended in 10 mL of

Resuspension solution (50 mM Tris-HCl, pH 8.0, 10 mM EDTA). 10 mL of Lysis solution (0.2 M NaOH, 1% SDS) was added and the solution was mixed by gently inverting the tube 5 times. After 5 minutes, 10 mL of Precipitation solution (3.1 M Potassium acetate, pH 5.5) was added; the solution was mixed and transferred to a filter column that had been equilibrated with 15 mL of Equilibration solution (0.1 M Sodium acetate, pH 5.0, 0.6 M NaCl, 0.15% Triton X-100). The lysate was allowed to pass through the filter by gravitational flow. The filter cartridge was then removed from the column, the column was washed with 20 mL of Wash solution (0.1 M Sodium acetate, pH 5.0, 825 mM NaCl) and the flow-through was discarded. 5 mL of Elution buffer (100 mM Tris-HCl, pH 8.5, 1.25 M NaCl) was added to the column and the eluted DNA was collected in a 15 mL falcon tube. The eluted DNA was incubated with 3.5 mL isopropanol for 2 minutes before being centrifuged at 4,000 x g for 30 minutes. The supernatant was removed and the pellet was resuspended in 3 mL 70% ethanol. Following a 10 minute centrifugation, the supernatant was removed and the pellet was air-dried for 10 minutes. The pellet was then resuspended in 100 µL of Milli-Q water. Plasmid concentration was measured on a NanoDrop ND-1000 spectrophotometer (Lab Tech).

2.1.1.4 Site directed mutagenesis

Site directed mutagenesis was performed using a QuikChange II kit (Stratagene). 5 µL of 10x Reaction buffer (100 mM KCl, 100 mM $(NH_4)_2SO_4$, 200 mM Tris-HCl, 20 mM $MgSO_4$, 1% Triton X-100, 1 mg/mL bovine serum albumin (BSA)), 125 ng of forward and reverse primers, 25 ng of DNA template, 1 µL dNTPs and 1 µL of PfuUltra HF DNA polymerase (2.5 U) was added to a 0.5 mL eppendorf tube and the reaction mixture was made up to 50 µL with Milli-Q water. The polymerase chain reaction (PCR) cycle was as follows; initial denaturation of 95°C for 3 minutes, followed by 18 cycles of 95°C for 30 seconds, 60°C for 1 minute and 68°C for 5 minutes. The PCR product was then incubated was 1.5 µL of DpnI (15 U) restriction enzyme for 1 hour at 37°C. 2.5 µL of the DpnI-treated DNA was added to a pre-chilled 1.5 mL eppendorf containing 50 µL of the XL1 Blue supercompetent cells. The mixture was then incubated on ice for 30 minutes then placed in a water bath set to 42°C for 45 seconds. The mixture was placed on ice for 1 minute, 500 µL of LB was added and the tubes were incubated at 37°C with shaking for 2 hours. Cells were then plated on the appropriate antibiotic plate and were left to grow overnight at 37°C. The following day 2-4 colonies were picked and used to inoculate a culture of LB containing the appropriate antibiotic. After a 16 hour incubation period, the DNA was isolated and purified before being sequenced.

Table 2.1 Primer sequences

Primer	Sequence 5'-3'
Untagged HSJ1 Y5C F	cggatccgatggcatcctactgcgagatcctaga
Untagged HSJ1 Y5C R	tctaggatctcgcagtaggatgccatcggatccg
Ubiquilin-2 P497H F	ggcccagtcacccacataggccccata
Ubiquilin-2 P497H R	tatggggcctatgtgggtgactgggcc
Ubiquilin-2 P497S F	ggcccagtcacctccataggccccata
Ubiquilin-2 P497S R	tatggggcctatggaggtgactgggcc
Ubiquilin-2 P506T F	ccataggccctatagtcacttttacccccataggc
Ubiquilin-2 P506T R	gcctatgggggtaaaagtgactatagggcctatgg
Ubiquilin-2 P509S F	cctatagtccctttacctccataggccccattgggc
Ubiquilin-2 P509S R	gcccaatggggcctatggaggtaaaagggactatagg
Ubiquilin-2 P525S F	ctggccctgcagccccctctggctccaccggctctgg
Ubiquilin-2 P525S R	ccagagccggtggagccagagggggctgcagggccag
oIM0872	aagttcatctgcaccaccg
oIM1416	tccttgaagaagatggtgcg
DloxR	gcactctactgacaaagttacagcctc
Int2F	ccttttactcatatccctggcacacc
Gx2478	cctgtgtttgagagactgctgcatagc

Table 2.2 Plasmid constructs

Vector	Insert	Tag	Resistance	Source
pCMV Tag 3A	HSJ1a WT HSJ1b WT HSJ1a H31Q HSJ1a ΔUIM HSJ1a ΔUIM1 HSJ1a ΔUIM2	N-terminal myc	Kanamycin	Professor Cheetham
pBSTR1	HSJ1a WT HSJ1b WT	Untagged	Ampicillin	Professor Cheetham
pBSTR1	HSJ1a Y5C HSJ1b Y5C	Untagged	Ampicillin	H.Smith This study
pCMV4	Ubiquilin-2 WT	N-terminal FLAG	Ampicillin	Addgene (8661)
pCMV4	Ubiquilin-2 P497H Ubiquilin-2 P497S Ubiquilin-2 P506T Ubiquilin-2 P509S Ubiquilin-2 P525S	N-terminal FLAG	Ampicillin	H.Smith This study
pEGFP-C3	LC3	N-terminal GFP	Kanamycin	Addgene (11546)

2.1.1.5 DNA sequencing

4 µL of sequencing buffer (200 mM TrisHCl pH 9.0, 5 mM $MgCl_2$), 4 µL Big Dye v3.1 (Life Technologies), 1 µL of 10 µM primer and 125 ng of DNA template was added to a 0.5 mL eppendorf tube on ice. The PCR was 30 cycles at 96°C for 30 seconds, 50°C for 15 seconds and 60°C for 4 minutes. The reaction mixture was cooled to 4°C and 26 µL of precipitation solution (95% ethanol, 3 M NaOAc pH5.2) was added. Following a 10 minute incubation on ice, the reaction mixture was centrifuged at 13,000 x g for 30 minutes. The supernatant was removed and 200 µL of 70% ethanol was added. The reaction mixture was centrifuged again at 13,000 x g for 10 minutes. The supernatant was removed and tubes were placed on a heating block set to 65°C for 3 minutes to dry off the remaining ethanol. 11 µL of formamide was added and the tubes were heated to 95°C for 10 minutes to denature the DNA. Samples were then transferred to a loading plate and samples were run on a 3730 DNA Analyser (Applied Biosystems). Sequences were aligned using BioEdit sequencing alignment software (Ibis Therapeutics).

2.1.2 Cell culture techniques

2.1.2.1 Reagents

All cell culture medium and transfection reagents were purchased from Invitrogen. 6 well plates, 96 well plates and T75 flasks were purchased from VWR and 8 well chamberslides were purchased from Thermo Fischer Scientific. Bafilomycin was purchased from Abcam and used at a concentration of 200 nM. Cycloheximide was purchased from Sigma and used at a concentration of 50 µg/mL. MG132 was purchased from Enzo Life Sciences and used at a concentration of 50 µM.

2.1.2.2 Cell culture of SK-N-SH cells

SK-N-SH neuroblastoma cells were obtained from European Collection of Cell Cultures (ECCAC). The cells were cultured in Dulbecco's modified Eagle's medium F12 with GlutaMAX (DMEM F-12) (Invitrogen), supplemented with 10% (v/v) fetal calf serum (FCS) (Invitrogen), 100 U/mL penicillin and 100 µg/mL streptomycin (Invitrogen). Cells were grown at 37°C in 5% CO_2. Cells were passaged when then reached 80-90% confluency. Cells were washed in Hank's Balanced Salt solution (HBSS) (Invitrogen), incubated with 1 mL of trypsin (Invitrogen) for 3 minutes, then resuspended in 9 mL of DMEM F-12. Cells were counted with a glass haemocytometer and 6 well plates were seeded at a density of $5x10^5$ cells per well and 8 well chamber slides were seeded at a density of $5x10^4$ cells per well. T75 flasks were seeded at a 1:4 ratio.

2.1.2.3 Transfection of 8 well chamberslides

SK-N-SH cells were transfected when they reached around 70% confluency using Lipofectamine™ and Plus™ reagents (Invitrogen). For each well, 200 ng of total DNA was added to 25 µL of DMEM F-12 serum free media (SFM) and 1 µL Plus. In a separate tube, 0.5 µL of Lipofectamine was added to 100 µL SFM. Both tubes were incubated at 22°C for 15 minutes. The tubes were subsequently mixed and incubated for a further 15 minutes. During this incubation period, cells were washed twice with HBSS. 100 µL of SFM was then added to the well. After 15 minutes, 125 µL of the mixture was added to the well. Following a 2 hour incubation at 37°C in 5% CO_2, the media was removed and replaced with DMEM F-12 with 10% FCS. Cells were then grown for a further 24 hours prior to fixation.

2.1.2.4 Transfection of 6 well plates

For the transfection of 6 well plates, 500 ng/well of plasmid was added to 100 µL/well of SFM and the total DNA was made up to 2000 ng using pCMV3 stuffer plasmid. 8 µL/well of Plus reagent was added and the mixture was incubated for 15 minutes at 22°C. For each transfection reaction, 4 µL of Lipofectamine was added to 100 µL SFM and incubated for 15 minutes. The two tubes were then mixed together and incubated for a further 15 minutes. During this incubation, SK-N-SH cells were washed twice in HBSS and 780 µL of SFM was added to each well. The transfection mixture was then added to the cells and incubated at 37°C in 5% CO_2 for 3 hours. The media was then removed and replaced with DMEM F-12 containing 10% FCS. Cells were grown for a further 24 hours before being treated or harvested.

2.1.2.5 Cell culture of human fibroblasts

Control fibroblasts were provided by Professor Paul Chapple (Queen Mary University of London) and patient fibroblasts were obtained from the UCL Institute of Neurology BioBank, with the permission of Professor Michaela Auer-Grumbach (Vienna) and approval by the UCL Institute of Neurology ethics committee. Fibroblasts were maintained in T75 flasks and grown in an incubator at 37°C and 5% CO_2. Both control and patient fibroblasts grew at comparable rates and were split on the same day when they reached 90% confluency. The media was removed from the T75 flask and the fibroblasts were washed with 10 mL Dulbecco's Phosphate-Buffered Saline (PBS) (Invitrogen). 1 mL of trypsin was added and the flask was placed back in to the incubator for 3 minutes. Fibroblasts were then resuspended in 9 mL of DMEM (high glucose, pyruvate) (Invitrogen) supplemented with 10% FCS, 100 U/mL penicillin and 100 µg/mL streptomycin, and were subsequently seeded

into 6 well plates or 8 well chamberslides. Fibroblasts were not grown beyond P15. Control and patient fibroblasts were passage matched for all experiments.

2.1.2.6 The knockdown of HSJ1 in control fibroblasts

An adeno-associated virus containing mIR30 shRNA against HSJ1 was provided by Professor James Uney (University of Bristol) at a titre of $2x10^{10}$ virus particles (VP)/mL. 50,000 control fibroblast cells were seeded per well of a 6 well plate. 24 hours post seeding, the virus was added directly to the well at the required multiplicity of infection (MOI). 24 hours post transduction, the media was removed and replaced with fresh DMEM (high glucose, pyruvate) supplemented with 10% FCS. Cells were harvested following a further 24 hour or 48 hour incubation period.

2.1.2.7 The restoration of HSJ1 in patient fibroblasts

Adeno-associated virus expressing either HSJ1a or HSJ1b was provided by Professor James Uney (University of Bristol) at a titre of $6x10^{10}$ VP/mL and $5x10^{9}$ VP/mL, respectively. 50,000 patient fibroblasts cells were seeded per well of a 6 well plate, with 10,000 patient fibroblast cells seeded per well of an 8 well chamberslide. 24 hours post seeding, the virus was added directly to the well at the required MOI. 24 hours post transduction, the media was removed and replaced with fresh DMEM (high glucose, pyruvate) supplemented with 10% FCS. Cells were harvested following a further 24 hour incubation period.

2.1.3 Protein based techniques

2.1.3.1 Preparation of cell lysates

6 well plates were placed on ice, the media from each well was removed and cells were washed twice with PBS (137 mM NaCl, 2.7 mM KCl, 8.1 mM Na_2HPO_4, 1.5 mM K_2HPO_4). Cells were then lysed with 200 µL RIPA buffer (50 mM Tris-HCl pH 7.4, 150 mM NaCl, 2 mM EDTA, 1% NP-40, 0.5% sodium deoxycholate, 0.1% SDS) containing 2% mammalian protease inhibitor cocktail (PIC) and, where appropriate, 5% phosphatase inhibitor (Sigma) for 10 minutes. Lysates were collected in a 1.5 mL eppendorf then sonicated for 10 seconds. The eppendorfs were then placed on ice for 30 seconds before being sonicated again for another 10 seconds. Following sonication, lysates were centrifuged at 4°C for 10 minutes at 13,000 x g. The supernatant was then removed and the protein concentration was determined using a bicinchroninic acid (BCA) Protein Assay kit (Pierce). 0, 0.125, 0.25, 0.5 and 1 mg/mL bovine serum albumin (BSA) was used as standards and 10 µL of each concentration was added in triplicate to a 96 well plate. 10 µL of cell lysate was added in triplicate to 3 separate wells of the plate. Reagent A was mixed with Reagent B in a 50:1 ratio and the

mixture was vortexed. 190 µL of the mixture was then added to each well. The wells were mixed by pipetting up and down 5 times using a multichannel pipette. The lid was placed over the plate and the plate was incubated for 30 minutes at 37°C. The absorbance was then measured on a spectrophotometer (Techan, SAFIRE) at 562 nm. The mean absorbance of the 3 wells was calculated and background readings were subtracted using the blank control (0 mg/mL BSA). A standard curve was then generated using the BSA standards and was used to calculate the protein concentration of the cell lysates.

2.1.3.2 Immunoprecipitation

24 hours post transfection, cells were placed on ice, the media was removed and the cells were washed twice in PBS. 500 µL of 1% n-Dodecyl-β-D-maltoside (DM) lysis buffer supplemented with 2% PIC was added to each well. After 10 minutes, cells were scrapped into a 1.5 mL eppendorf and sonicated briefly. 30 µL of lysate was removed to provide the input fraction. 400 µL of lysate was added to 50 µL of protein G magnetic Dynabeads (Invitrogen) that had been incubated overnight in 5% BSA, 0.02% Tween-20 in PBS. The lysate and beads were incubated with the appropriate antibody and the tubes were placed on a rotating wheel for 1 hour at room temperature. A Magnarack (Invitrogen) was used to remove the supernatant then the beads were washed 5 times in 1% DM lysis buffer with 0.02% Tween-20. 20 µL of 2x SDS loading buffer (10% SDS, 20% glycerol, 0.1% Bromophenol Blue, 0.5 M Tris HCl , pH 6.8, 2.5% β-mercaptoethanol) was added to the beads and the tubes were vortexed briefly before being boiled at 95°C for 3 minutes. The Magnarack was used to remove the beads and the sample was then loading onto a 10% poly-acrylamide gel.

2.1.3.3 SDS-PAGE

Samples were loaded onto a 10% or 12% resolving gel with a 4% stacking gel. Resolving gels were made with 1.5 mM Tris pH 8.8, 10-12% acrylamide, 0.1% SDS, 0.1% Ammonium persulphate (APS) and 0.05% TEMED. The 4% stacking gel was made from 0.5 mM Tris pH 6.8, 4% acrylamide, 0.1% SDS, 0.1% APS and 0.1% TEMED. Samples were run at 150 V with a Tris-glycine running buffer (25 mM Tris-HCl, 250 mM glycine and 0.1% SDS) until the blue bromophenol dye reached the bottom of the gel.

2.1.3.4 Western blot

Proteins were transferred to a nitrocellulose membrane using a semi-dry electrophoretic transfer unit (BioRad). The nitrocellulose membrane was sandwiched between blotting paper that had been soaked in transfer buffer containing 25 mM Tris, 192 mM Glycine, 0.01%

SDS and 20% methanol. The unit was run for 20 minutes at 15 V, 0.4 Amps. Transfer of the proteins was confirmed by staining with Ponceau S (Sigma). The membrane was blocked for 1 hour in 5% Marvel milk in 0.1% PBS Tween (blocking buffer). Subsequently the membrane was incubated overnight at 4°C with primary antibody diluted in blocking buffer (Table 2.3). The next day, the membrane was washed 3 times for 5 minutes in 0.1% PBS Tween before being incubated for 1 hour with the secondary antibody diluted in blocking buffer. Following a further 3 washes of 5 minutes each, immunostaining was detected using ECL Plus Chemiluminescence reagent (Amersham Biosciences), which was prepared by mixing 1 mL of reagent A with 25 µL of reagent B per membrane. Immunostaining was detected using X-ray film or a BioRad Chemidoc. For the detection of phosphorylated proteins, 5% BSA in TBS (50 mM Tris-HCl pH 7.6, 150 mM NaCl) with 0.1% Tween was used as the blocking buffer, with all wash steps performed using 0.1% TBS Tween.

2.1.3.5 Protein quantification using ImageJ

Protein quantification was performed using ImageJ (NIH). Protein levels were corrected for loading using β-actin or β-tubulin. Protein levels were then normalised as stated in the Figure legends. At least three biological replicates were performed for all experiments in which statistical significance was determined.

2.1.3.6 Proteasome activity assay

Proteasome activity was measured using a 20S Proteasome Assay kit (Millipore), according to the manufacturer's protocol. 10 µg of control and patient fibroblast cell lysate was added in triplicate to a 96 well black plate (Sigma). 10 µL of 10x Assay buffer and 10 µL of 500 µM MG132 was added to each well and the final volume was made up to 90 µL using Milli-Q water. The plate was incubated for 15 minutes at room temperature. During this incubation period, 10 µg of cell lysate was added in triplicate to separate wells. This time, only 10x Assay buffer was added and the final volume was made up to 90 µL with Milli-Q water. Following the pre-incubation period, 10 µL of 10 mM Proteasome Substrate was added to each well (apart from the blank controls) and the wells were mixed by pipetting up and down five times using a multichannel pipette. The plate was then incubated for 1 hour at 37°C. Fluorescence was measured on a spectrofluorometer (Techan, SAFIRE), using an excitation wavelength of 380 nm and an emission wavelength of 460 nm. The fluorescent intensity of the blank controls was averaged and subtracted from all readings. The average fluorescent intensity in the presence of MG132 was then subtracted from the readings in the absence of MG132, to give the proteasome-specific activity. The activity of the patient fibroblast cell lysate was then normalised to the activity of the control fibroblast cell lysate.

2.1.3.7 Immunocytochemistry

Cells were washed twice in PBS before being fixed in 4% paraformaldehyde (PFA) (TAAB Laboratories) for 10 mintutes. Cells were washed in PBS then permeabilised in 0.1% Triton-X for 10 minutes. Following three washes in PBS, cells were blocked for 1 hour in 3% BSA and 10% normal donkey serum in PBS. Primary antibodies were diluted in the blocking solution and cells were incubated overnight at 4°C (Table 2.3). Following three washes in PBS, cells were incubated with secondary antibodies, also diluted in blocking solution, for 1 hour at room temperature. Cells were washed in PBS then incubated for 5 minutes with 2 mg/mL 4',6-diamidino-2-phenylindole (DAPI) (Sigma) at a 1:5000 dilution. Once washed for a final time, the chamber was removed and a coverslip was mounted using Fluorescent Mounting Medium (DAKO).

2.1.3.8 Fluorescence microscopy

SK-N-SH cells transfected with GFP-Q103 or GFP-SOD1 G93A were visualised on a Nikon Eclipse 80i fluorescent microscope. Inclusion incidence was calculated by counting the number of transfected cells containing inclusions. GFP-Q103 inclusions appear as large circular structures whereas GFP-SOD1 G93A appears as perinuclear aggregates that are excluded from the nucleus (Chapter 4). In each condition, at least 100 transfected cells were counted. Three biological replicates were performed.

2.1.3.9 Confocal microscopy

Images were acquired on a Zeiss LSM 700 confocal microscope using 40x or 63x oil immersion objectives. The excitation/emission spectrum of the channels used was as follows; DAPI 364/475-525 nm, Cy2 488/505-530 nm and Cy3 543/560 nm. Images were exported from Zeiss 2009 software (Carl Zeiss) to Adobe Photoshop (Adobe) and then presented in Adobe Illustrator (Adobe).

2.1.4 Quantification of gene expression

2.1.4.1 RNA extraction

Total RNA extraction was performed using the RNeasy mini kit (Qiagen) following the manufacturer's protocol. Cells were placed on ice, the media was removed from each well and the cells were washed twice in PBS. 350 µL of Buffer RLT was then added to each well. Following a 10 minute incubation, a cell scrapper was used to collect the lysate in a 1.5 mL eppendorf. The lysate was homogenised by passing the lysate 10 times through a small 20-gauge needle. 1 volume of 70% ethanol was added and the lysate was mixed by pipetting up

and down 5 times. The lysate was then transferred to a RNeasy spin column and the tube was centrifuged for 20 seconds at 8000 x g. To digest DNase, 350 µL of Buffer RW1 was added to the column. The tube was centrifuged for 20 seconds at 8000 x g and the flow-through was discarded. 10 µL of DNase stock solution was added to 70 µL Buffer RDD and the solution was mixed gently by inverting the tube. 80 µL of the DNase solution was then added to the membrane of the column and was left for 15 minutes at room temperature. 350 µL of Buffer RW1 was added, the column was centrifuged for 20 seconds at 8000 x g and the flow-through was discarded. 500 µL of Buffer RPE was added and the column was centrifuged for 2 minutes at 8000 x g. The column was then transferred to a new 1.5 mL eppendorf, 50 µL of RNase free water was added and the tube was spun at 13,000 x g for 1 minute to elute the RNA. RNA concentration was measured on a NanoDrop ND-1000 spectrophotometer (Lab Tech).

2.1.4.2 cDNA synthesis

cDNA synthesis was performed using the SuperScript III First-strand synthesis system kit (Invitrogen). 5 µg of total RNA was added to a 0.5 mL eppendorf tube along with 1 µL 50 µM oligo$(dT)_{20}$, and 1 µL 10 mM dNTP, and the mixture was made up to 10 µL with DEPC-treated water. The mixture was incubated at 65°C for 5 minutes, then placed on ice for 1 minute. In a separate 0.5 mL eppendorf tube, 2 µL 10x RT buffer, 4 µL 25 mM $MgCl_2$, 2 µL 0.1 M DTT, 1 µL RNaseOUT (40 U/µL) and 1 µL SuperScript III RT (200 U/µL) was added. 10 µL of this mixture was then added to the RNA mixture and the eppendorf was incubated for 50 minutes at 50°C. The reaction was terminated by incubating the eppendorf at 85°C for 5 minutes. The reaction mixture was chilled on ice, then 1 µL of RNase H was added and the reaction mixture was then incubated at 37°C for 20 minutes. The cDNA synthesis reaction mixture was then stored at -20°C.

2.1.4.3 qPCR

50 ng of total cDNA, 200 nM forward primer, 200 nM reverse primer and 10 µL SYBR Green (Invitrogen) was added to a 96 well plate and the final volume was made up to 20 µL with Milli-Q water. Quantitative PCR was performed using an ABI Prism Real-time Sequence Detection System (Applied Biosciences) with 40 cycles at 95°C for 15 seconds then 60°C for 1 minute. Data was analysed using SDS 2.2.2 software (Applied Biosystems).

Table 2.3 Primary antibodies

Antibody	Host	Company	Dilutions
ATF6	Rabbit	Santa Cruz (22799)	WB 1:1000
β-actin	Mouse	Santa Cruz (47778)	WB 1:1000
BiP	Rabbit	Sigma (G8919)	WB 1:1000 ICC 1:750
β-tubulin	Mouse	Sigma (T4026)	WB 1:1000
β-III-tubulin	Mouse	Abcam (78078)	ICC 1:750
β-III-tubulin	Rabbit	Abcam (18207)	ICC 1:750
eIF2α	Rabbit	Cell Signalling (5324)	WB 1:1000
p-eIF2α	Rabbit	Sigma (SAB4504385)	WB 1:1000
FLAG	Rabbit	Sigma (M7425)	WB 1:500 ICC 1:200 IP 1:200
GADD34	Rabbit	Protein Tech (10449)	WB 1:1000
HSJ1	Sheep	In house (S653)	WB 1:1000 ICC 1:500
IRE1	Rabbit	Cell Signalling (3294)	WB 1:1000
p-IRE1	Rabbit	Novus Biologicals (NB100-2323)	WB 1:1000
LC3B	Rabbit	Cell Signalling (3868)	WB 1:1000
Myc	Mouse	Sigma (M4439)	WB 1:1000 ICC 1:200 IP 1:200
PERK	Rabbit	Cell Signalling (5683)	WB 1:1000
p-PERK	Rabbit	Cell Signalling (3179)	WB 1:1000
p62	Rabbit	Abcam (56416)	WB 1:1000 ICC 1:750
Ubiquitin	Rabbit	DAKO Z0458	WB 1:1000

Table 2.4 Secondary antibodies

Antibody	Host	Company	Dilutions
Anti-mouse IgG (H+L) Cy2 and Cy3	Donkey	Jackson Immunoresearch	1:200
Anti-rabbit IgG (H+L) Cy2 and Cy3	Donkey	Jackson Immunoresearch	1:200
Anti-sheep IgG (H+L) Cy2 and Cy3	Donkey	Jackson Immunoresearch	1:200
Anti-mouse IgG (H+L) peroxidise conjugated	Goat	Pierce	1:40,000
Anti-rabbit IgG (H+L) peroxidise conjugated	Goat	Pierce	1:40,000
Anti-sheep IgG (H+L) peroxidise conjugated	Goat	Piece	1;40,000

2.2 *In vivo* techniques

All procedures were conducted according to the Home Office (UK) regulations under the Animals (Scientific Procedures) Act of 1986 and with local UCL Institute of Neurology and UCL Institute of Ophthalmology ethic committee approval. Project licence number: 70/06976, personal licence number: 70/24130.

2.2.1 Animal maintenance

Transgenic Hb9:*GFP*$^{+/-}$ mice were purchased from the Jackson Laboratory (Strain: B6.Cg-Tg(Hlxb9-GFP)1Tmj/J, Stock number: 005029). The colony was maintained in a heterozygous state through breeding with C57BL/6 mice. Hb9:*GFP*$^{+/-}$ mice and the subsequent crosses were maintained at the Denny Brown Laboratories, UCL Institute of Neurology, London, UK. *Hsj1*$^{-/-}$ mice were previously obtained from GenOway (Wendy Mustill, UCL, Thesis) and were bred on a C57BL/6 background. *Hsj1*$^{-/-}$ and C57BL/6 wild-type mice were maintained at UCL Institute of Ophthalmology, London, UK. Mice were housed at 21°C ± 1°C with relative humidity 55% ± 10% and were maintained on a 12:12 light dark cycle with access to food and water *ad libitum*.

2.2.2 Genotyping

DNA was extracted from ear biopsies using the Wizard SV Genomic DNA purification kit (Promega). Each ear biopsy was placed in a 1.5 mL eppendorf tube and incubated overnight at 55°C with 100 µL Nuclei Lysis solution, 25 µL EDTA, 20 µL proteinase K and 5 µL RNase A solution. Following incubation, 250 µL of Wizard SV Lysis buffer was added to each eppendorf tube and the tube was briefly vortexed. The lysates was then transferred to a Wizard SV minicolumn. The columns were spun at 13,000 x g for 3 minutes. The flow-through liquid was discarded from the collection tube and samples were spun again at 13,000 x g for 1 minute. The flow-through liquid was discarded and 650 µL Column Wash solution was added to each column. Columns were spun for 1 minute and the liquid was discarded. This washing step was repeated 4 times. Following the last wash, the column was spun at 13,000 x g for 2 minutes to dry the column. Columns were then transferred to a 1.5 mL eppendorf and 100 µL of nuclease free water was added to each column. After a 2 minute incubation at room temperature, columns were spun at 12,000 x g for 1 minute. The column was then discarded and the purified DNA was stored at 4°C.

2.2.2.1 GFP PCR

2.5 µL of genomic DNA was added to 6.25 µL GoTaq (Promega), 1.5 µL 10 µM oIM0872 primer, 1.5 µL 10 µM oIM1416 primer and 1.25 µL Milli-Q water. The reaction cycle was

as follows; initial denaturation at 94°C for 2 minutes, followed by 30 cycles of 94°C for 30 seconds, 65°C for 30 seconds and 68°C for 2 minutes. The PCR product was then run on a 1% agarose gel and the DNA was visualised on a UV transilluminator. A band at 173 bp indicated the presence of the GFP transgene.

2.2.2.2 HSJ1 PCR

2.5 µL genomic DNA was added to 6.25 µL GoTaq, 0.6 µL 10 µM GX2478, 0.6 µL 10 µM Int2F, 1.2 µL 10 µM DloxP and 1.35 µL Milli-Q water. The reaction cycle was as follows; initial denaturation at 94°C for 5 minutes, followed by 40 cycles of 94°C for 30 seconds, 65°C for 30 seconds and 68°C for 90 seconds, with a final elongation step at 68°C for 8 minutes. PCR products were run on a 1% agarose gel and were visualised on a UV transilluminator. A PCR product at 850 bp indicates a $Hsj1^{+/+}$ genotype, whereas a band at 650 bp indicates a $Hsj1^{-/-}$ genotype. The presence of both bands indicates the mouse is a heterozygote.

2.2.3 Transcardial perfusion

Mice of the required age were terminally anaesthetised with an overdose of Euthasol (100 mg/kg), administered via an intraperitoneal injection. When the mouse became unresponsive to toe-pinch, a lateral incision was made above the abdomen and the rib cage was exposed. The rib cage was removed using sharp scissors, allowing access to the heart. Whilst holding the heart with forceps, a needle (attached to the perfusion pump via connective tubing) was inserted into the left ventricle. The right atrium was cut with scissors to create an outlet for the blood. 0.9% saline was then pumped through the mouse until all the blood had been drained from the body. At this point, the mouse was perfused with 40 mL 4% PFA. Following perfusion, the spinal cord was dissected and post-fixed overnight in 4% PFA at 4°C. The spinal cord was then cryoprotected in 30% sucrose in PBS for 24 hours.

2.2.4 The preparation of spinal cords for cryosectioning

The L2-L6 lumbar region of the spinal cord was dissected under a light dissecting microscope (Leica) (Figure 2). The lumbar region was then placed upright into a mould containing OCT mounting medium (CellPath). The base of the mould was then immersed in ice-cold acetone until the OCT mounting medium froze. Once the tissue had been frozen, samples were wrapped in foil and kept at -80°C.

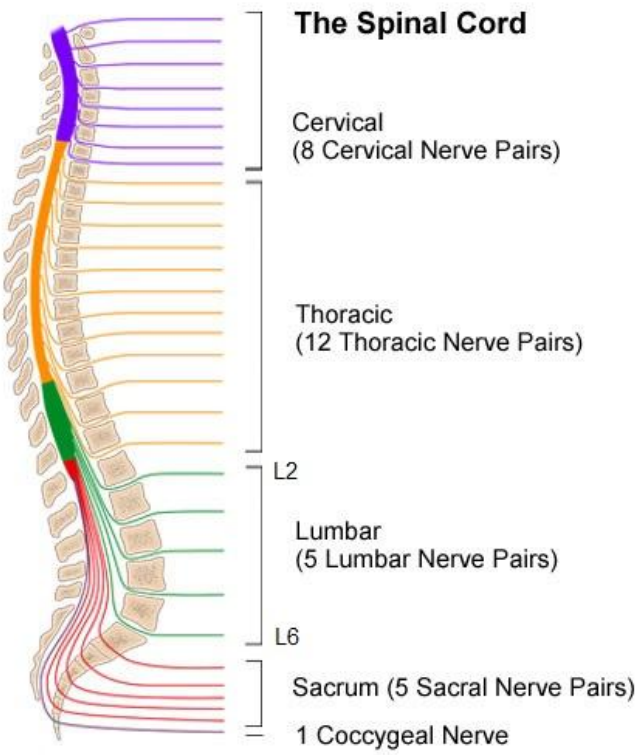

Figure 2: Diagram highlighting the lumbar region of the spinal cord. The enlarged lumbar region of the spinal cord is shown in green, with 5 pairs of lumbar nerves (L2-L6). Figure from uahealth.com.

2.2.5 Motor neuron counts

Spinal cords were sectioned into 20 µm slices on a cryostat (Leica) and mounted onto Superfrost Plus microscope slides (VWR). The slides were kept at -20°C until they were required. Slides were allowed to dry for 30 minutes upon removal from the freezer. Slides were immersed in PBS for 5 minutes before being immersed in 0.3% gallocyanine solution (Sigma) for 1.5 hours. The slides were then washed in increasing ethanol concentrations, with 5 minutes in 70% ethanol, 2 minutes in 70% ethanol, 2 minutes in 90% ethanol and 2 minutes in absolute ethanol. Slides were then transferred to HistoClear (National Diagnostics). Following a 5 minute incubation, slides were incubated in fresh HistoClear solution for a further 5 minutes. After this time, DPX mounting medium (Sigma) was placed on the slides and coverslips were added. Slides were wrapped in foil and allowed to dry overnight at room temperature. Gallocyanine-stained sections were visualised on a Nikon Eclipse 80i Light microscope. Motor neurons were counted based on established criteria. Only large, polygonal cells located in the ventral horns of the spinal cord with a darkly stained cytoplasm, a pale nucleus and a darkly stained nucleolus were counted. Motor neurons were counted in every 4^{th} consecutive section, in order to avoid counting the same motor neuron twice. At least 30 sections were counted per animal.

2.2.6 Immunohistochemistry

Slides were air dried at room temperature for 30 minutes. An ImmEdge hydrophobic pen (Vector Laboratories) was then used to draw a barrier around the sections. Slides were then washed in PBS for 5 minutes before being incubated with 0.2% Triton-X100 in PBS for 20 minutes. Sections were then blocked in 10% normal donkey serum in PBS and incubated overnight at 4°C with primary antibody diluted in blocking solution. Following overnight incubation, slides were washed 3 times for 5 minutes in PBS. Slides were then incubated with secondary antibody for 1 hour at room temperature before being washed 3 times for 5 minutes in PBS. Slides were finally mounted with coverslips using fluorescent mounting medium.

Chapter 3 – The potential interaction of HSJ1 with UBL proteins

3.1 Introduction

HSJ1a is a potent suppressor of protein aggregation and can significantly reduce inclusion incidence in cell models of HD, PD and ALS (Westhoff *et al.* 2005, Howarth *et al.* 2007, Rose *et al.* 2011, Novoselov *et al.* 2013). In cell models of ALS, the overexpression of HSJ1a reduced the aggregation of mutant SOD1, a protein commonly mutated in familial cases of the disease (Novoselov *et al.* 2013). In 2011, *ubiquilin-2* was identified as a novel causative gene in X-linked ALS (Deng *et al.* 2011). As with mutations in SOD1, mutations in ubiquilin-2 resulted in the aggregation of the protein, with the presence of cytoplasmic inclusions positive for ubiquilin-2 in the motor neurons of patient spinal cords (Deng *et al.* 2011). Interestingly, ubiquilin-2 has been identified as a component of cytoplasmic inclusions in ALS patients lacking mutations in ubiquilin-2, highlighting a potential role for ubiquilin-2 in the pathogenesis of ALS (Zhang *et al.* 2014). Based on the ability of HSJ1a to reduce the aggregation of ALS-associated proteins, I sought to examine whether HSJ1a could potentially modulate mutant ubiquilin-2 aggregation in cells.

Ubiquilin-2 is a member of the ubiquilin family. The human genome encodes four *ubiquilin* genes, each located on a different chromosome and exhibiting different patterns of expression. Ubiquilin-1 is ubiquitously expressed, with ubiquilin-2 and ubiquilin-4 expressed in most tissues. Ubiquilin-3 expression is more restricted and is only detected in the testis (Conklin *et al*. 2000). The four isoforms are highly conserved among mammals and share a high degree of sequence and domain homology. All isoforms contain an N-terminal ubiquitin-like (UBL) domain and a C-terminal ubiquitin-binding (UBA) domain. The UBL domain interacts with the proteasome, whereas the UBA domain binds to polyubiquitin, with a high affinity for both K48 and K63-linked ubiquitin chains (Kleijnen *et al.* 2000, Zhang *et al.* 2008). The presence of UBL and UBA domains enables the ubiquilins to act as shuttles, binding to ubiquitylated proteins and delivering them to the proteasome for degradation. The central region between the UBL and UBA domains is variable among the different isoforms. Unlike other ubiquilin proteins, the central region of ubiquilin-2 has a unique repeat region containing 12 PXX tandem repeats. All five patient mutations identified by Deng *et al.* (2011) involved the substitution of a proline residue in the PXX repeat region (Figure 3).

Figure 3 The functional domains of ubiquilin-2. Ubiquilin-2 contains an N-terminal ubiquitin-like domain (UBL), four heat shock-chaperonin binding motifs (STI1), 12 PXX repeats and a C-terminal ubiquitin binding domain (UBA). The ALS-linked mutations in the PXX region are highlighted. Figure from Deng *et al.* 2011.

To understand the role of ubiquilin-2 in ALS, research has focussed on characterising the function of ubiquilin-2 through the identification of specific binding partners. Recently, ubiquitin regulatory X domain-containing protein 8 (UBXD8) was shown to co-immunoprecipitate with ubiquilin-2, identifying the protein as an ubiquilin-2 binding partner (Xia *et al.* 2014). The binding affinity for UBXD8 was impaired in the presence of a truncated ubiquilin-2 protein lacking the PXX region and UBA domain, implying that ubiquilin-2 binds to UBXD8 via its C-terminal domains (Xia *et al.* 2014). UBXD8 is an ER transmembrane protein that mediates the translocation of ERAD substrates to the cytosol (Alexandru *et al.* 2008). An interaction between the two proteins suggests that ubiquilin-2 may function in ERAD, possibly delivering ERAD substrates to the proteasome upon their release from the ER. Indeed, the knockdown of ubiquilin-2 in HeLa cells impaired the degradation of α1-anti trypsin null Hong Kong mutant, a misfolded luminal ERAD substrate (Xia *et al.* 2014).

In addition to functioning in ERAD, accumulating evidence suggests that ubiquilin-2 plays a prominent role in autophagy. Ubiquilin-2 co-localised with autophagosomes in HeLa cells and co-immunoprecipitated with LC3 (N'diaye *et al.* 2009, Rothenberg *et al.* 2010). The interaction was dependent on the UBA domain of ubiquilin-2, however the binding to LC3 appeared to be indirect; a GST-pulldown assay failed to detect any strong binding between purified ubiquilin-2 and LC3 (Rothenberg *et al.* 2010). Ubiquilin-2 is degraded by autophagy; therefore the protein was proposed to act as a selective adaptor, recruiting ubiquitylated cargo into the autophagosome through an indirect interaction with LC3 (Rothenberg *et al.* 2010). The knockdown of ubiquilin-2 inhibited the degradation of autophagosomes, rendering cells more susceptible to death upon starvation (N'diaye *et al.*

2009). The impaired fusion of autophagosomes with autolysosomes suggests that ubiquilin-2 may have a broader function in autophagy, rather than simply acting as an adaptor protein.

Interestingly, HSJ1a has been identified as a binding partner of ubiquilin-1 (Heir *et al.* 2006). The binding was dependent on the UBL domain of ubiquilin-1 and the UIMs of HSJ1a (Heir *et al.* 2006). Considering the conservation of the UBL domain among the ubiquilin isoforms, the data presents the possibility that HSJ1a may also bind to ubiquilin-2, with both proteins potentially co-operating to target misfolded, ubiquitylated proteins for degradation. Interestingly, investigations into the anti-aggregation function of HSJ1a suggest that the protein may indeed co-operate with another protein to target misfolded substrates for degradation. Both UIM1 and UIM2 of HSJ1a are required to fully counteract polyQ aggregation (Labbadia *et al.* 2012), despite the fact that only UIM2 appears to bind to polyubiquitin chains with high affinity (Dr Sergey Novoselov, personal communications). The role of UIM1 in the anti-aggregation process is therefore unknown; however, it was hypothesised that UIM1 may function to bind to UBL-containing proteins. Based on these findings, the ability of HSJ1a to bind to ubiquilin-1 in a UIM-dependent manner and the association of both HSJ1 and ubiquilin-2 with motor neuron degeneration, I sought to test the hypothesis that ubiquilin-2 is a binding partner of HSJ1a. To test this hypothesis, the immunopurification and localisation of tagged ubiquilin-2 and tagged HSJ1a was assessed using SK-N-SH neuroblastoma cells. Binding between tagged ubiquilin-2 and tagged HSJ1a domain mutants was also examined. The ability of HSJ1a to bind to ubiquilin-2 mutants was also investigated, to examine if HSJ1a could potentially modulate mutant ubiquilin-2 aggregation in cells.

3.2 Results

3.2.1 HSJ1a co-localises and co-immunopurifies with ubiquilin-2

The cellular localisation of FLAG-tagged ubiquilin-2 (FLAG-ubiquilin-2) was examined by immunocytochemistry. SK-N-SH cells were transfected with FLAG-ubiquilin-2 and 24 hours post transfection, cells were fixed and immunostained with a FLAG antibody. FLAG-ubiquilin-2 appeared both diffuse in the cytoplasm and in multiple punctate structures, as previously described (Figure 3.1A) (Osaka *et al.* 2015, Xia *et al.* 2014, Rothenberg *et al.* 2010, N'diaye *et al.* 2009). The co-transfection of SK-N-SH cells with FLAG-ubiquilin-2 and myc-HSJ1a resulted in myc-HSJ1a being recruited to the FLAG-ubiquilin-2 punctate structures (Figure 3.1C). Myc-HSJ1a did not form punctate structures in the absence of FLAG-ubiquilin-2 (Figure 3.1B). The recruitment of HSJ1a to ubiquilin-2 puncta suggested that the two proteins might interact. To test this possibility, a co-immunopurification assay was performed. SK-N-SH cells were transfected with FLAG-ubiquilin-2 and myc-HSJ1a. 24 hours post transfection, cells were lysed and lysates were immunopurified for 1 hour with a FLAG, myc or IgG control antibody. Purified protein was then resolved by SDS-PAGE and Western blot analysis was performed using a FLAG or a HSJ1 antibody. A small proportion of myc-HSJ1a was detected in the FLAG purifications, suggesting myc-HSJ1a may bind to FLAG-ubiquilin-2 (Figure 3.1D). Myc-HSJ1a was not enriched with a control antibody (IgG), confirming the specificity of the interaction. Unfortunately, both a FLAG and ubiquilin-2 antibody were poor at detecting FLAG-ubiquilin-2 by Western blot. The efficiency of the FLAG-ubiquilin-2 immunopurification could therefore not be determined, along with the ability of anti-myc to co-immunopurify FLAG-ubiquilin-2 with myc-HSJ1a.

3.2.2 HSJ1a ΔUIM fails to co-localise and co-immunopurify with ubiquilin-2

The co-localisation and co-immunopurification of myc-HSJ1a and FLAG-ubiquilin-2 suggested that the two proteins interact. To examine whether the interaction was dependent on the UIMs of HSJ1a, the ability of anti-FLAG to co-immunopurify an HSJ1a mutant containing four amino acid substitutions that disrupts the function of both UIMs (myc-HSJ1a-ΔUIM-S219A/E222A/S262A/E265A) was assessed (Westhoff *et al.* 2005). SK-N-SH cells were transfected with FLAG-ubiquilin-2 and either wild-type myc-HSJ1a (WT) or myc-HSJ1a-ΔUIM (ΔUIM) and immunopurification of cell lysates was subsequently performed. Unlike myc-HSJ1a WT, anti-FLAG failed to immunopurify myc-HSJ1a-ΔUIM, suggesting that the binding of HSJ1a to ubiquilin-2 is dependent on the UIMs (Figure 3.2A). To confirm that FLAG-ubiquilin-2 lacks the ability to bind to myc-HSJ1a-ΔUIM, the localisation of the two proteins was examined by immunocytochemistry. FLAG-ubiquilin-2

and myc-HSJ1a-ΔUIM failed to co-localise (Figure 3.2B), supporting the notion that the binding between the two proteins is dependent on the UIMs of HSJ1a.

3.2.3 The binding of HSJ1a to ubiquilin-2 is dependent on UIM2

HSJ1 has two UIMs; to identify which UIM ubiquilin-2 binds to, the binding of FLAG-ubiquilin-2 to myc-HSJ1a mutants with either a functionally deficient UIM1 (myc-HSJ1a-ΔUIM1-S219A/E222A) or UIM2 (myc-HSJ1a-ΔUIM2-S262A/E265A) domain was probed (Westhoff *et al.* 2005). Anti-FLAG was able to immunopurify myc-HSJ1a-ΔUIM1 with FLAG-ubiquilin-2, but was unable to purify myc-HSJ1a-ΔUIM2 (Figure 3.3A). Consistent with this observation, myc-HSJ1a-ΔUIM1 retained the ability to be recruited to FLAG-ubiquilin-2 puncta, whereas myc-HSJ1a-ΔUIM2 showed no co-localisation with FLAG-ubiquilin-2 (Figure 3.3B). The binding between ubiquilin-2 and HSJ1a therefore appears to be dependent on UIM2.

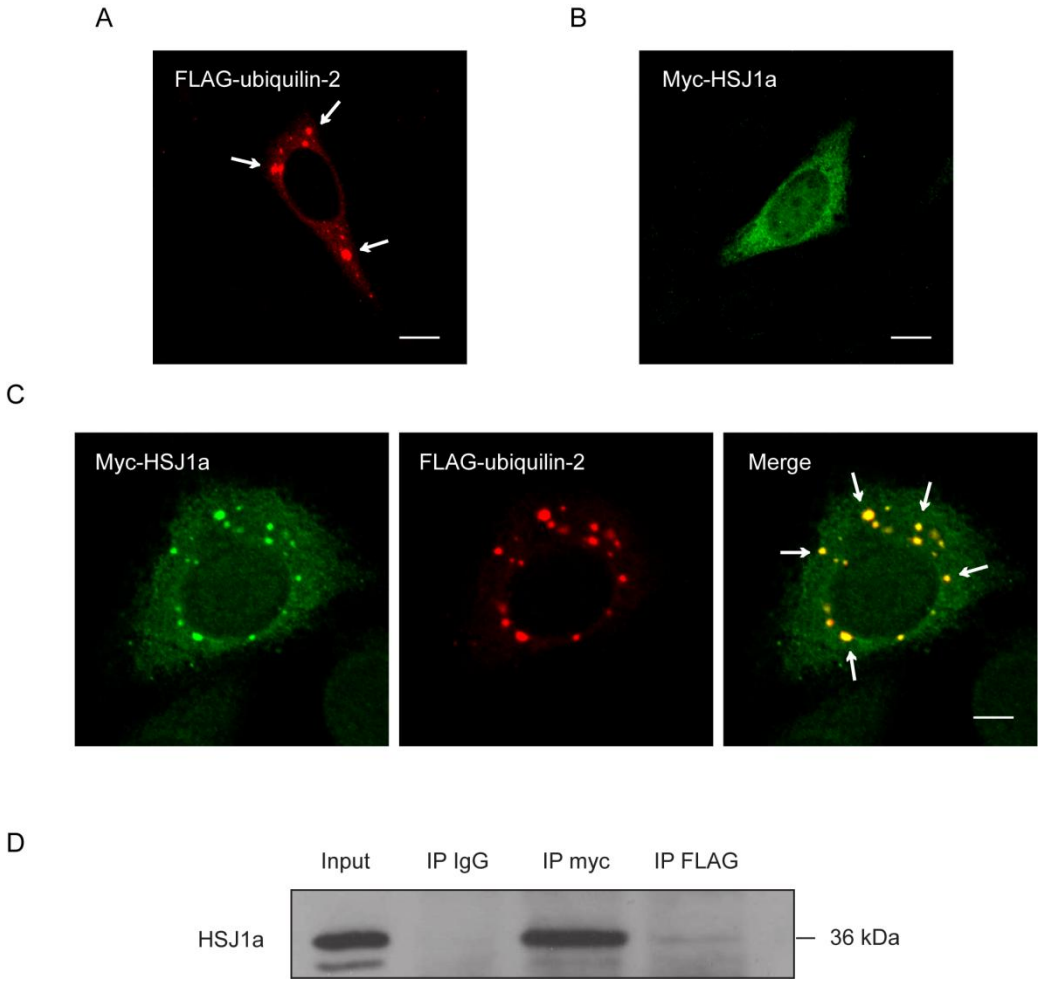

Figure 3.1 HSJ1a co-localises and co-immunopurifies with ubiquilin-2. A: SK-N-SH cells were transfected with FLAG-ubiquilin-2. 24 hours post transfection, cells were fixed in 4% PFA, permeabilised with 0.1% Triton-X100 and immunostained with a rabbit FLAG antibody at a dilution of 1:200 (Cy3, red). Cells were imaged on a Zeiss LSM 700 confocal microscope. Arrows highlight punctate structures. Scale bar, 10 µm (n=3). **B:** SK-N-SH cells were transfected with myc-HSJ1a. 24 hours post transfection, cells were fixed in 4% PFA, permeabilised with 0.1% Triton-X100 and immunostained with a sheep HSJ1 antibody at a dilution of 1:200 (Cy2, green). Cells were imaged on a Zeiss LSM 700 confocal microscope. Scale bar, 10 µm (n=3). **C:** SK-N-SH cells were transfected with FLAG-ubiquilin-2 and myc-HSJ1a. 24 hours post transfection, cells were fixed, immunostained and imaged as described above. Arrows highlight examples of punctate structures where the two proteins co-localise. Scale bar, 10 µm (n=3). **D:** SK-N-SH cells were transfected with FLAG-ubiquilin-2 and myc-HSJ1a. 24 hours post transfection, cells were lysed and lysates were incubated with protein G Dynabeads and either a FLAG, myc or IgG control antibody (1:200). After a one hour incubation on a rotating wheel, purified immuno-complexes were then resolved by SDS-PAGE and Western blot analysis was performed using a sheep HSJ1 antibody at a 1:1000 dilution (n=3).

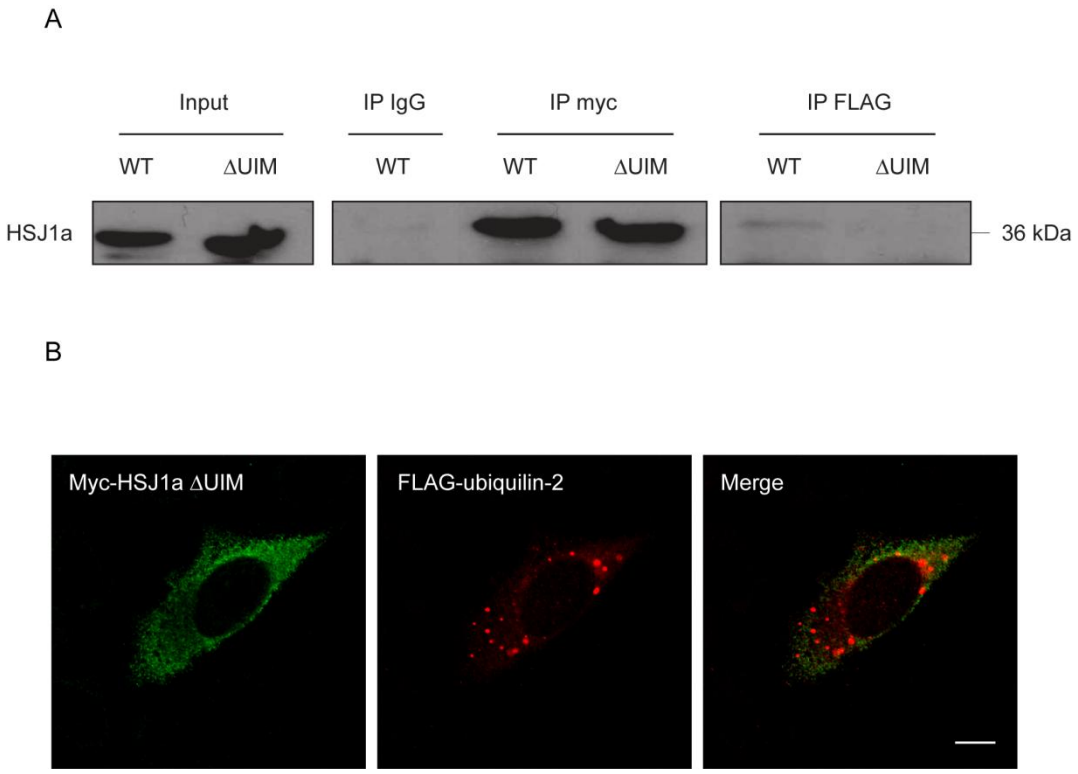

Figure 3.2 HSJ1a-ΔUIM fails to co-immunopurify and co-localise with ubiquilin-2. A: SK-N-SH cells were transfected with FLAG-ubiquilin-2 and either myc-HSJ1a (WT) or myc-HSJ1a-ΔUIM (ΔUIM). 24 hours post transfection, cell lysates were incubated with protein G Dynabeads and either a FLAG, myc or IgG control antibody (1:200). After a one hour incubation on a rotating wheel, purified immuno-complexes were resolved by SDS-PAGE and Western blot analysis was performed using a sheep HSJ1 antibody at a 1:1000 dilution. (n=3). **B:** SK-N-SH cells were transfected with FLAG-ubiquilin-2 and myc-HSJ1a-ΔUIM. Cells were subsequently fixed in 4% PFA, permeabilised in 0.1% Triton-X100 and immunostained with FLAG (Cy3, red) and HSJ1 antibodies (Cy2, green) at a dilution of 1:200. Cells were imaged on a Zeiss LSM 700 confocal microscope. Scale bar, 10 µm (n=3).

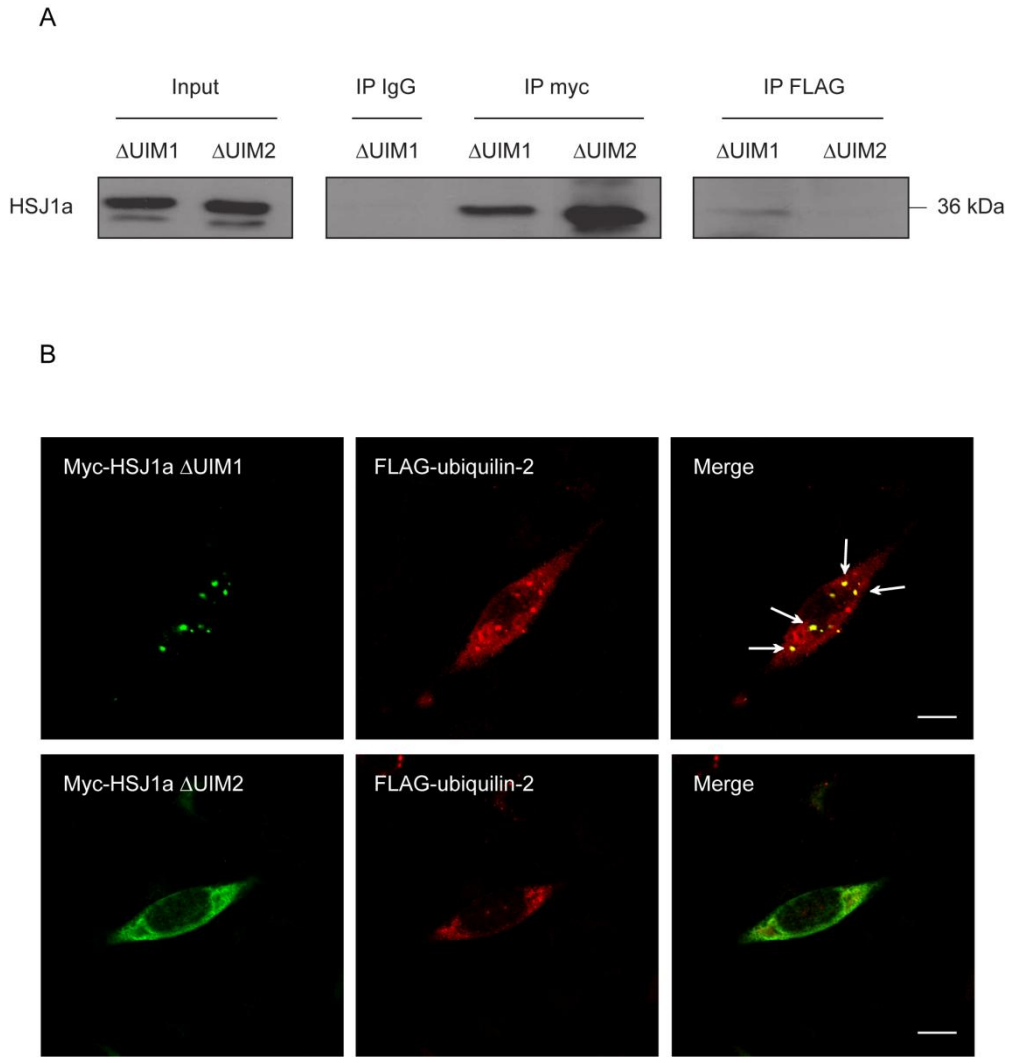

Figure 3.3 HSJ1a-ΔUIM2 fails to co-immunopurify and co-localise with ubiquilin-2. A: SK-N-SH cells were transfected with FLAG-ubiquilin-2 and either myc-HSJ1a-ΔUIM1 or myc-HSJ1a-ΔUIM2 mutants. 24 hours post transfection, cell lysates were incubated with protein G Dynabeads and either a FLAG, myc or IgG control antibody (1:200). After a one hour incubation on a rotating wheel, purified immuno-complexes were resolved by SDS-PAGE and Western blot analysis was performed using a sheep HSJ1 antibody at a 1:1000 dilution. (n=3) **B:** SK-N-SH cells were transfected with FLAG-ubiquilin-2 and either myc-HSJ1a-ΔUIM1 or myc-HSJ1a-ΔUIM2. Cells were subsequently fixed in 4% PFA, permeabilised in 0.1% Triton-X100 and immunostained with FLAG (Cy3, red) and HSJ1 antibodies (Cy2, green) at a dilution of 1:200. Cells were imaged on a Zeiss LSM 700 confocal microscope. Arrows highlight punctate structures where the two proteins co-localise. Scale bar, 10 μm (n=3).

3.2.4 Ubiquilin-2 localises to autophagosomes upon the induction of autophagy

Having established an interaction between HSJ1a and ubiquilin-2, I next sought to characterise the nature of the punctate structures that HSJ1a was recruited to. Previous studies showed that ubiquilin-2 puncta co-localise with the autophagosome marker, LC3 (N'diaye *et al.* 2009, Rothenberg *et al.* 2010). The localisation of LC3 in respect to ubiquilin-2 was therefore examined. SK-N-SH cells were transfected with FLAG-ubiquilin-2 and GFP-LC3 and were subsequently immunostained with a FLAG antibody. GFP-LC3 showed a diffuse distribution in both the cytoplasm and the nucleus. A small number of GFP positive punctate structures, indicative of autophagosomes, were observed, which appeared to co-localise with a small proportion of FLAG-ubiquilin-2 puncta (Figure 3.4). The majority of FLAG-ubiquilin-2 puncta, however, did not show co-localisation with GFP-LC3. To determine whether GFP-LC3 and FLAG-ubiquilin-2 co-localise upon the induction of autophagy, SK-N-SH cells transfected with FLAG-ubiquilin-2 and GFP-LC3 were starved of amino acids for 3 hours. Following starvation, multiple GFP positive punctate structures were observed, with extensive co-localisation with FLAG-ubiquilin-2 puncta (Figure 3.4). FLAG-ubiquilin-2 therefore shows increased localisation to autophagosomes upon the induction of autophagy.

3.2.5 HSJ1a co-immunopurifies with LC3 under basal conditions and upon the induction of autophagy

Ubiquilin-2 has been reported to co-immunoprecipitate with LC3, although the interaction appears to be indirect (Rothenberg *et al.* 2010). To investigate whether HSJ1a forms part of the complex that links ubiquilin-2 to LC3, the binding of HSJ1a to LC3 was examined. Considering that FLAG-ubiquilin-2 shows increased localisation to autophagosomes upon the induction of autophagy, the interaction between GFP-LC3 and myc-HSJ1a was examined in the absence and presence of amino acid starvation. SK-N-SH cells were transfected with GFP-LC3 and myc-HSJ1a. The transfected cells were then untreated or starved of amino acids for 3 hours. Cell lysates were subsequently immunopurified with a GFP or myc antibody. Purified protein was resolved by SDS-PAGE and the presence of GFP-LC3 in GFP and myc purifications was probed. GFP-LC3 co-immunopurified with myc-HSJ1a under basal conditions, suggesting that the proteins do indeed interact (Figure 3.5). GFP-LC3 also co-immunopurified with myc-HSJ1a upon the induction of autophagy. Upon the induction of autophagy, a faint band was detected beneath GFP-LC3 in both the GFP and myc purifications, corresponding in size to the autophagosome-associated isoform GFP-LC3-II. Neither GFP-LC3-I nor GFP-LC3-II was not enriched with an IgG antibody, confirming the specificity of the interaction.

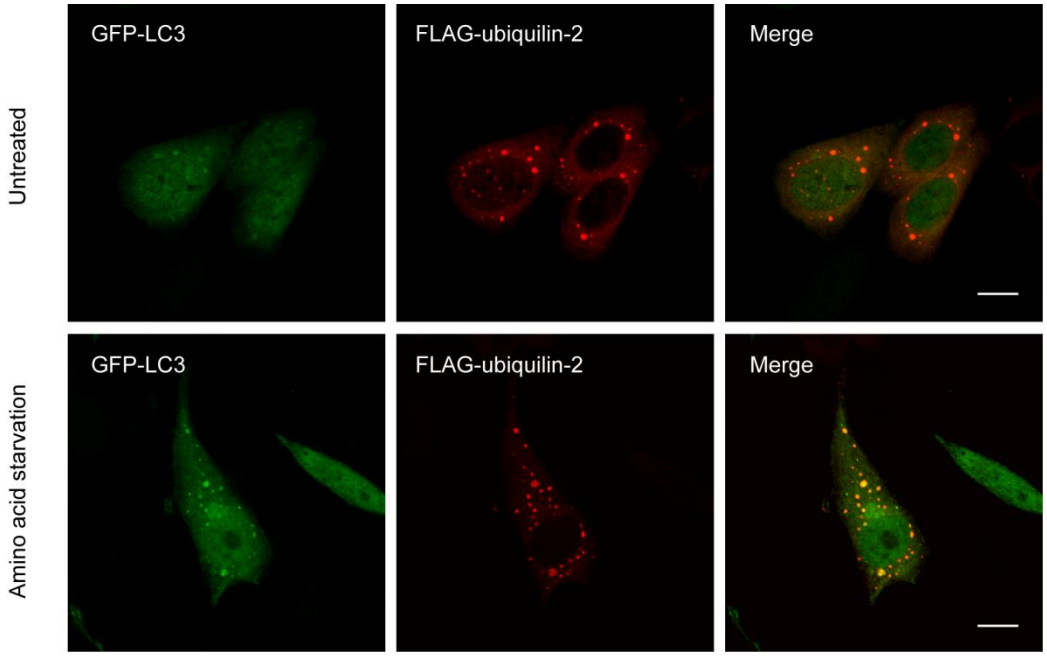

Figure 3.4 Ubiquilin-2 puncta co-localise with LC3 upon the induction of autophagy. SK-N-SH cells were transfected with FLAG-ubiquilin-2 and GFP-LC3. 24 hours post transfection, cells were untreated or incubated for 3 hours in HBSS culture medium that lacked amino acids. Following the incubation period, cells were fixed in 4% PFA, permeabilised with 0.1% Triton-X100 and immunostained with a FLAG antibody at a 1:200 dilution (GFP-LC3 green, FLAG-ubiquilin-2 red). Cells were imaged on a Zeiss LSM 700 confocal microscope. Scale bar, 10 µm (n=3).

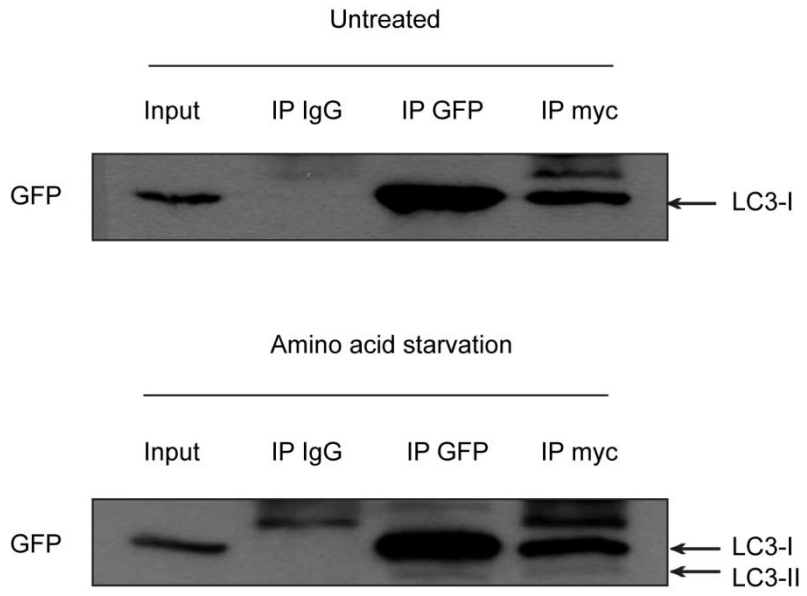

Figure 3.5 GFP-LC3 co-immunopurifies with HSJ1a. A: SK-N-SH cells were transfected with GFP-LC3 and myc-HSJ1a. 24 hours post transfection, cells were untreated or starved of amino acids for 3 hours in HBSS medium. Cells were lysed and lysates were incubated with protein G Dynabeads and either a GFP, myc, or IgG control antibody, all at a dilution of 1:200. After a one hour incubation on a rotating wheel, purifications were resolved by SDS-PAGE and Western blot analysis was performed using a mouse GFP antibody at a 1:1000 dilution (n=3).

3.2.6 Characterising ubiquilin-2 mutants

Five mutations in ubiquilin-2 were identified in families with X-linked ALS (Deng *et al.* 2011). I aimed to characterise the expression and localisation of the five ubiquilin-2 mutants and determine whether they retained the ability to bind to HSJ1a. The five patient mutations reported by Deng *et al.* (2011) (P497H, P497S, P506T, P509S and P525S) were introduced into the FLAG-ubiquilin-2 construct using site directed mutagenesis. To compare the expression levels of wild-type and mutant ubiquilin-2, SK-N-SH cells were transfected with either wild-type FLAG-ubiquilin-2 or one of the five FLAG-ubiquilin-2 mutants. 24 hours post transfection, cells were lysed and FLAG-ubiquilin-2 protein levels were determined by Western blot analysis. Although the signal was low, four of the FLAG-ubiquilin-2 mutants showed similar expression levels compared to wild-type FLAG-ubiquilin-2, with FLAG-ubiquilin-2 P509S showing slightly higher expression levels (Figure 3.6).

To characterise whether the patient mutations affected the localisation of ubiquilin-2, the localisation of the five ubiquilin-2 mutants was examined by immunocytochemistry. As with wild-type FLAG-ubiquilin-2, all five FLAG-ubiquilin-2 mutants appeared both diffuse in the cytoplasm and in multiple punctate structures (Figure 3.7). Interestingly, a proportion of these mutant FLAG-ubiquilin-2 punctate structures appeared larger than those observed with wild-type FLAG-ubiquilin-2. To investigate this observation in more detail, the number and size of puncta formed by wild-type and mutant FLAG-ubiquilin-2 was determined. There was no significant difference in the average number of puncta per cell; wild-type FLAG-ubiquilin-2 and mutant FLAG-ubiquilin-2 all exhibited an average of between 8 and 9 puncta per cell (Figure 3.8). However, three of the ubiquilin-2 mutants, FLAG-ubiquilin-2 P506T, P509S and P525S, displayed a significant increase in the average size of the puncta formed (Figure 3.9). Wild-type FLAG-ubiquilin-2 formed puncta with an average area of 127 nm^2, whereas FLAG-ubiquilin-2 P506T, P509S and P525S formed puncta with an average area of 159 nm^2, 149 nm^2 and 153 nm^2, respectively. FLAG-ubiquilin-2 P497H and FLAG-ubiquilin-2 P497S showed no significant difference in average puncta size when compared to the wild-type protein, with an average area of 138 nm^2 and 133 nm^2, respectively.

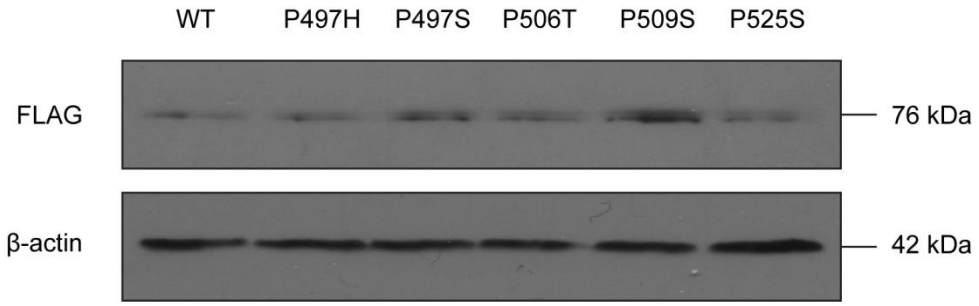

Figure 3.6 Protein expression levels of wild-type and mutant ubiquilin-2. SK-N-SH cells were transfected with either wild-type FLAG-ubiquilin-2 or FLAG-ubiquilin-2 P497H, P497S, P506T, P509S or P525S. 24 hours post transfection, cell lysates were resolved by SDS-PAGE and Western blot analysis was performed using a monoclonal mouse FLAG antibody (1:500). A monoclonal mouse β-actin antibody (1:5000) was used as a loading control (n=2).

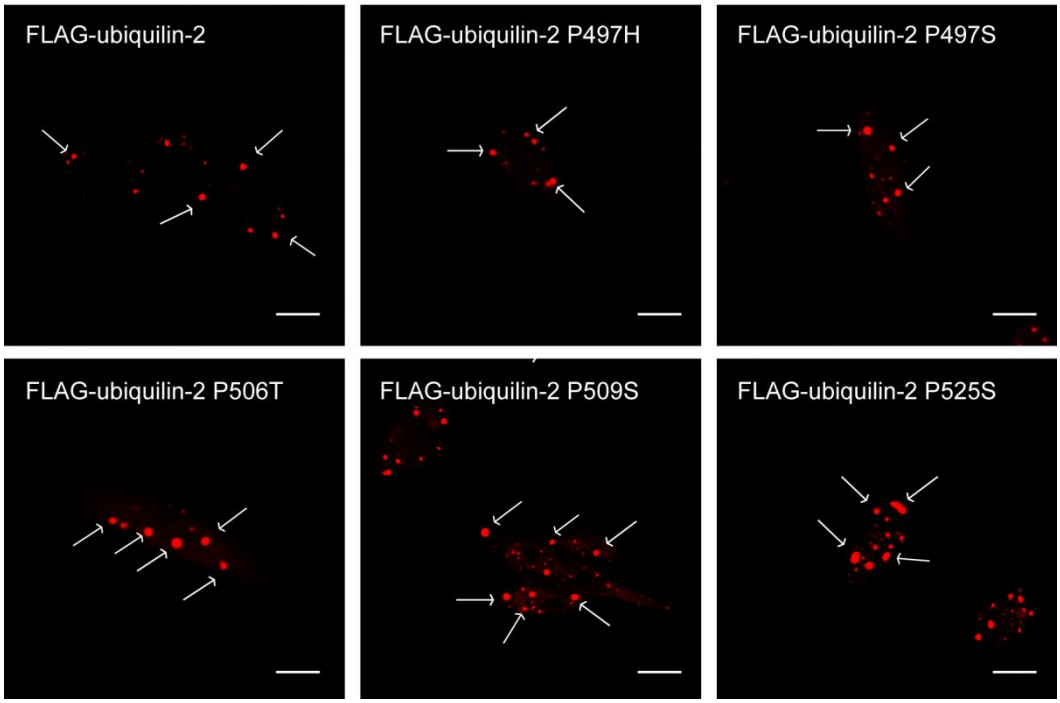

Figure 3.7 The localisation of ubiquilin-2 mutants. SK-N-SH cells were transfected with either wild-type FLAG-ubiquilin-2 or FLAG-ubiquilin-2 P497H, P497S, P506T, P509S or P525S. 24 hours post transfection, cells were fixed in 4% PFA, permeabilised in 0.1% Triton-X100 and immunostained with a rabbit FLAG (Cy3, red) antibody at a dilution of 1:200. Cells were imaged on a Zeiss LSM 700 confocal microscope. Arrows highlight examples of the punctate structures. Scale bar, 10 µm (n=3).

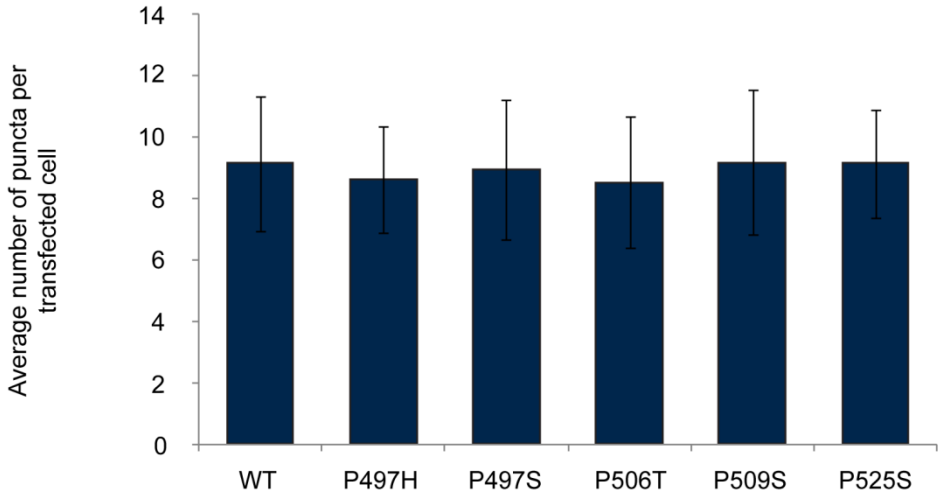

Figure 3.8 The average number of ubiquilin-2 puncta in transfected SK-N-SH cells. SK-N-SH cells were transfected with either wild-type FLAG-ubiquilin-2 or FLAG-ubiquilin-2 P497H, P497S, P506T, P509S or P525S. 24 hours post transfection, cells were fixed in 4% PFA, permeabilised in 0.1% Triton-X100 and immunostained with a rabbit FLAG (Cy3, red) antibody at a dilution of 1:200. The number of FLAG-ubiquilin-2 puncta was counted in at least 50 transfected cells per n using a Nikon Eclipse 80i Fluorescence microscope. Error bars represent ± SD (N.S one-way ANOVA, n=3).

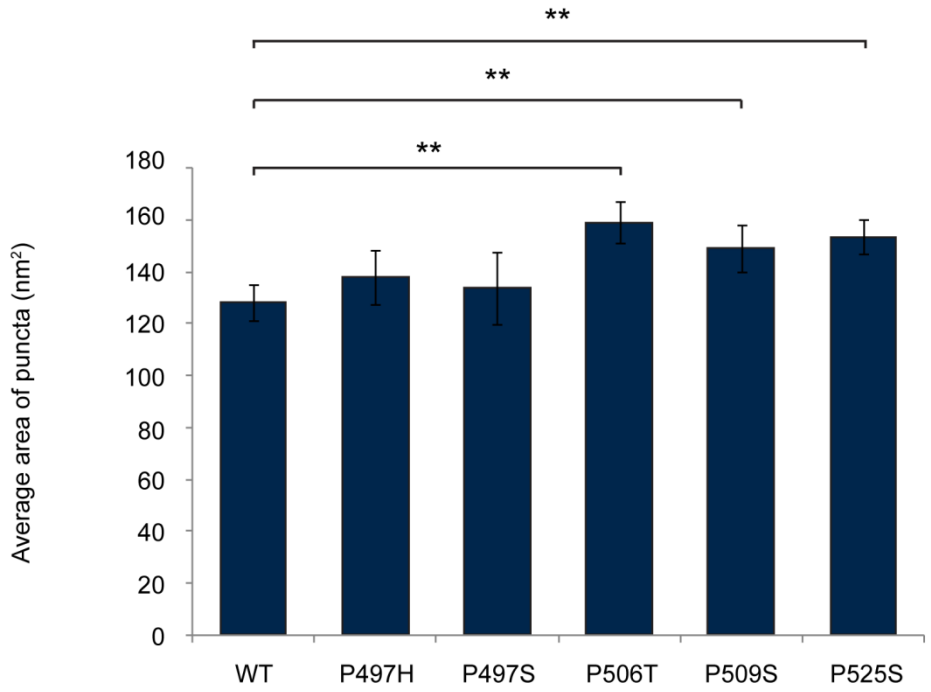

Figure 3.9 The average size of ubiquilin-2 puncta in transfected SK-N-SH cells. SK-N-SH cells were transfected with either wild-type FLAG-ubiquilin-2 or FLAG-ubiquilin-2 P497H, P497S, P506T, P509S or P525S. 24 hours post transfection, cells were fixed in 4% PFA, permeabilised in 0.1% Triton-X100 and immunostained with a rabbit FLAG (Cy3, red) antibody at a dilution of 1:200. Cells were imaged on a Zeiss LSM 700 confocal microscope. The average size of the puncta in a transfected cell was determined using ImageJ. Error bars represent ± SD (** $P < 0.01$, one-way ANOVA with post hoc Tukey test, n=3).

3.2.7 HSJ1a co-localises and co-immunopurifies with ubiquilin-2 mutants

To determine whether these patient mutations affected the binding of HSJ1a to ubiquilin-2, SK-N-SH cells were transfected with myc-HSJ1a and either wild-type or mutant FLAG-ubiquilin-2 and an immunopurification assay was performed. Myc-HSJ1a co-immunopurified with all five FLAG-ubiquilin-2 mutants and similar levels of myc-HSJ1a was purified in the presence of either wild-type or mutant FLAG-ubiquilin-2 (Figure 3.10).

To confirm the interaction between HSJ1a and mutant ubiquilin-2, SK-N-SH cells were transfected with myc-HSJ1a and one of the five FLAG-ubiquilin-2 mutants and their localisation was determined. As observed with wild-type FLAG-ubiquilin-2, myc-HSJ1a was recruited to the puncta structures formed by the FLAG-ubiquilin-2 mutants (Figure 3.11 and 3.12). Myc-HSJ1a was also recruited to the larger punctate structures formed by the mutants.

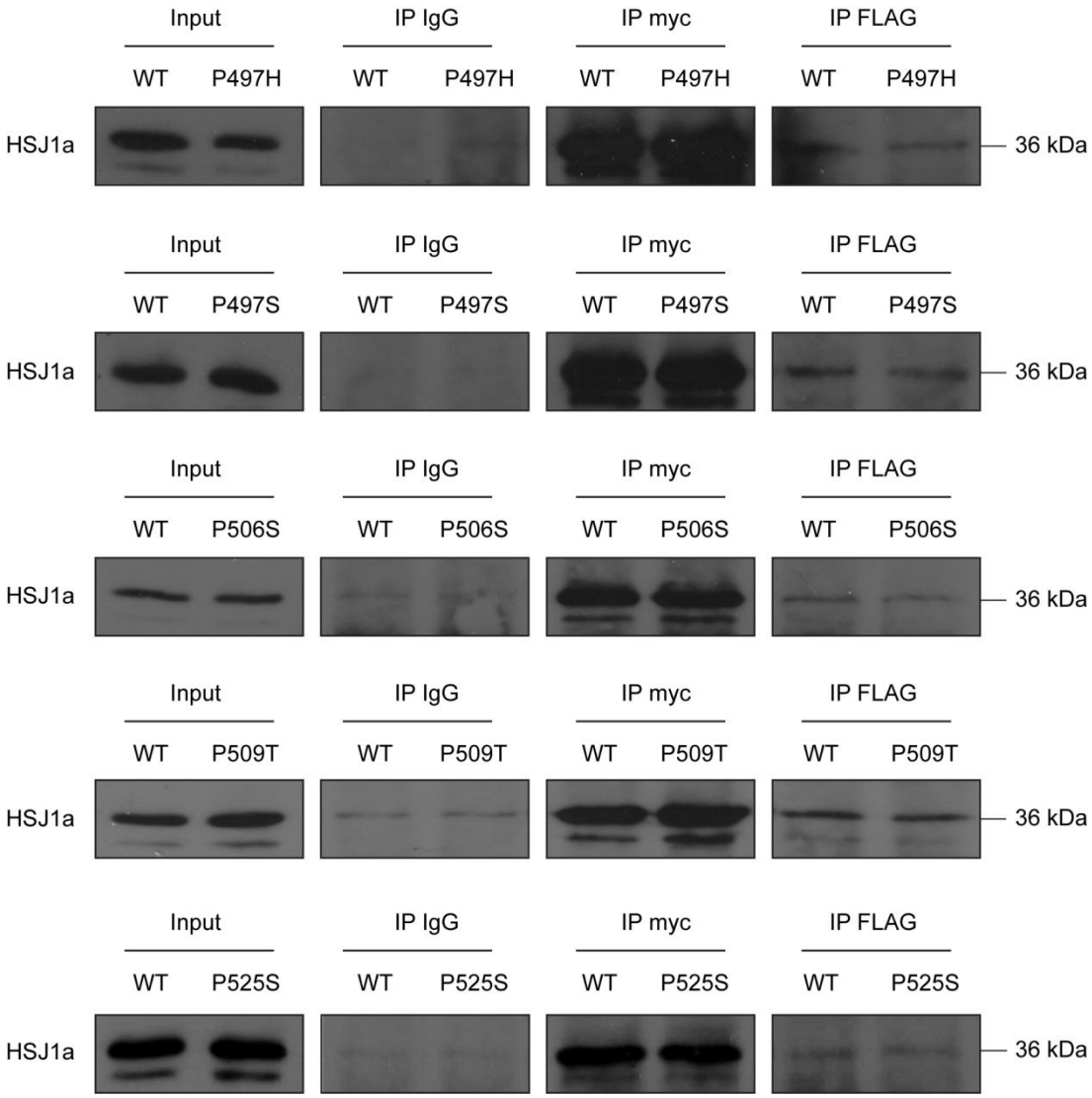

Figure 3.10 HSJ1a co-immunopurifies with all five ubiquilin-2 mutants. SK-N-SH cells were transfected with myc-HSJ1a and FLAG-ubiquilin-2 P497H, P497S, P506T, P509S or P525S. 24 hours post transfection, cell lysates were incubated with protein G Dynabeads and either a FLAG, myc or IgG control antibody (1:200). After a one hour incubation on a rotating wheel, purified immuno-complexes were resolved by SDS-PAGE and Western blot analysis was performed using a HSJ1 antibody at a 1:1000 dilution (n=3).

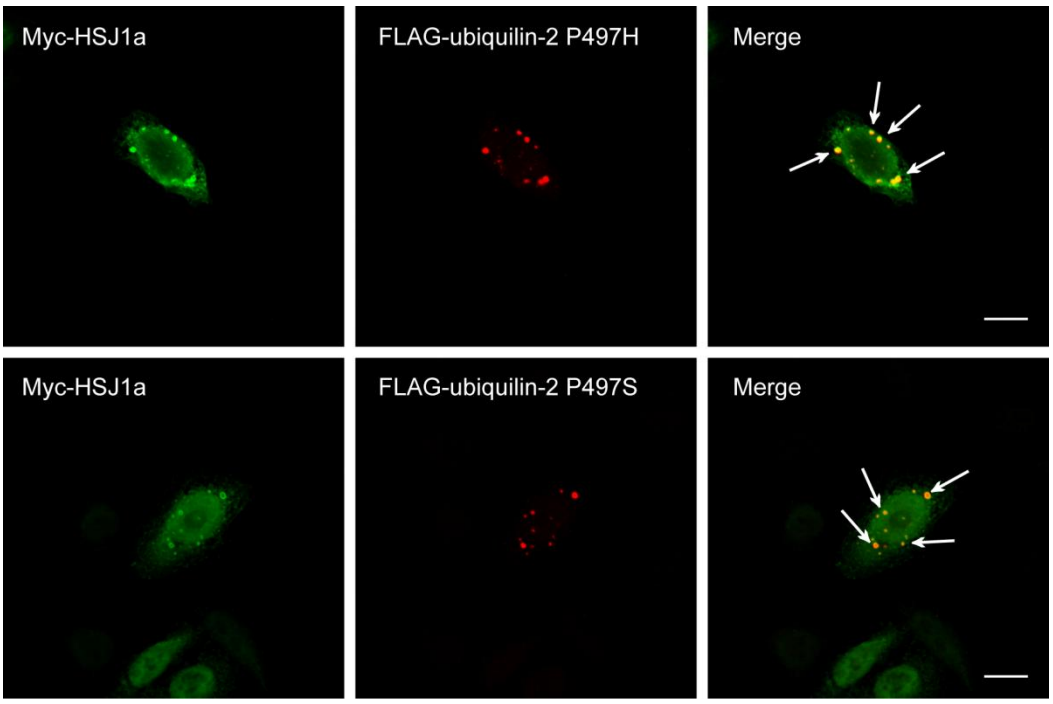

Figure 3.11 HSJ1a co-localises with mutant ubiquilin-2 puncta. SK-N-SH cells were transfected with myc-HSJ1a and FLAG-ubiquilin-2 P497H or P497S. 24 hours post transfection, cells were fixed in 4% PFA, permeabilised in 0.1% Triton-X100 and immunostained with a rabbit FLAG antibody (Cy3, red) and a sheep HSJ1 antibody (Cy2, green), both at a dilution of 1:200. Cells were imaged on a Zeiss LSM 700 confocal microscope. Arrows highlight punctate structures where the two proteins co-localise. Scale bar, 10 µm (n=3).

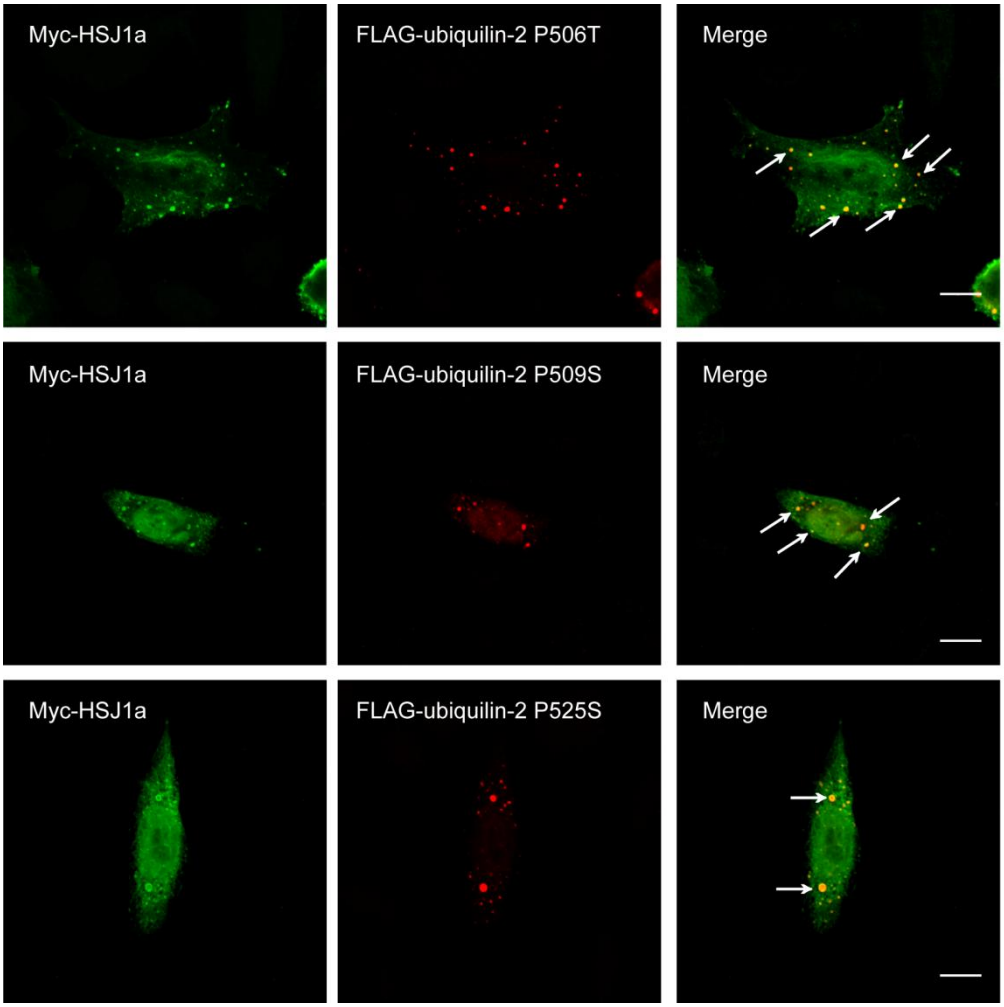

Figure 3.12 HSJ1a co-localises with mutant ubiquilin-2 puncta. SK-N-SH cells were transfected with myc-HSJ1a and FLAG-ubiquilin-2 P506T, P509S or P525S. 24 hours post transfection, cells were fixed in 4% PFA, permeabilised in 0.1% Triton-X100 and immunostained with a rabbit FLAG antibody (Cy3, red) and a sheep HSJ1 antibody (Cy2, green), both at a dilution of 1:200. Cells were imaged on a Zeiss LSM 700 confocal microscope. Arrows highlight puncta structures where the two proteins co-localise. Scale bar, 10 µm (n=3).

3.3 Discussion

HSJ1a has previously been identified to interact with the UBL-containing protein ubiquilin-1 (Heir *et al.* 2006). The interaction was dependent on the UBL domain of ubiquilin-1 and the UIMs of HSJ1a (Heir *et al.* 2006). Considering the conserved nature of the UBL domain among ubiquilin isoforms, the interaction raised the possibility that HSJ1a may also interact with ubiquilin-2, a protein recently associated with X-linked ALS (Deng *et al.* 2011). I therefore aimed to ascertain whether HSJ1a could interact with ubiquilin-2 and, if so, determine whether the interaction was dependent on the UIMs of HSJ1a. Furthermore, I aimed to investigate whether, like mutant SOD1, (Novoselov *et al.* 2013) HSJ1a could potentially suppress the aggregation of mutant ubiquilin-2 in a cell model of ALS.

The anti-aggregation function of HSJ1a towards polyQ was dependent on both UIM1 and UIM2, despite the fact that only UIM2 binds to polyubiquitin chains with high affinity (Dr Sergey Novoselov, personal communications). It was therefore hypothesised that UIM1 may function to bind to a UBL-containing protein. Considering that ubiquilin-2 also functions in protein degradation and that both HSJ1 and ubiquilin-2 are associated with motor neuron degeneration, ubiquilin-2 represented a possible candidate for potentially co-operating with HSJ1a to target misfolded, ubiquitylated proteins for degradation. The immunopurification and localisation data presented in this Chapter revealed that HSJ1a does indeed interact with ubiquilin-2; however, this interaction was not dependent on UIM1 of HSJ1a. The role of UIM1 in the anti-aggregation process therefore remains uncharacterised.

The binding of HSJ1a to ubiquilin-2 was dependent on UIM2 rather than UIM1. The inability of UIM1 to bind to ubiquilin-2 supports the notion that UIM1 and UIM2 of HSJ1a have distinct binding preferences. Interestingly, UIM1 and UIM2 of Eps15, a protein that functions in the sorting of substrates for endocytosis and lysosomal degradation, also display distinct binding properties, with UIM1 binding specifically to UBL proteins and UIM2 preferentially binding to polyubiquitin chains (Regan-Klapisz *et al.* 2005). The preference of Eps15 UIM2 for polyubiquitin chains was proposed to be mediated by the presence of a double-sided motif in UIM2, formed by key amino acids being repeated two residues along the UIM2 sequence (Hirano *et al.* 2006). The double-sided motif enables UIM2 to bind two ubiquitin molecules instead of one, enabling Eps15 UIM2 to bind to polyubiquitin chains with high affinity (Hirano *et al.* 2006). UIM2 of HSJ1a was also identified as a double-sided UIM (Hirano *et al.* 2006). The double-sided motif of HSJ1a UIM2, compared to the single-sided motif of HSJ1a UIM1, likely accounts for the observation that only UIM2 of HSJ1a binds strongly to polyubiquitin chains. It is therefore possible that the single or double-sided nature of the UIM accounts for the different binding properties of the two HSJ1a motifs.

Considering that UIM2 appears to be primed to bind to polyubiquitin chains, it is interesting to consider whether UIM2 mediates its interaction with ubiquilin-2 directly, via the UBL domain, or indirectly, via the ubiquitylated cargo bound to the UBA domain of ubiquilin-2. Direct binding of UIM2 to the UBL domain would suggest that, unlike UIM2 of Eps15, UIM2 of HSJ1a can bind to both polyubiquitin chains and UBL proteins. Determining the mode of interaction will therefore be important for clarifying the binding properties of HSJ1a UIM2. The dependence on either the UBL or UBA domain could be examined by assessing the ability of ubiquilin-2 mutants lacking the UBL or UBA domain to co-immunopurify and co-localise with HSJ1a.

Establishing the mode of interaction could provide insights into the function of HSJ1a binding. The indirect binding of ubiquilin-2 via the ubiquitylated cargo would suggest that HSJ1a functions to protect the chains from ubiquitin hydrolases, ensuring the efficient delivery of ubiquilin-2 substrates to the proteasome for degradation (Westhoff *et al.* 2005). Previous reports suggested that the direct binding of UIM-containing proteins to the UBL domain prevents the interaction of ubiquilin with the proteasome, diverting the cargo away from the degradation pathway (Heir *et al.* 2006). The direct binding of HSJ1a UIM2 to the UBL domain may therefore function to divert ubiquitylated cargo away from the proteasome, possible promoting autophagy-mediated degradation instead. However, HSJ1a itself has been shown to interact with the proteasome (Westhoff *et al.* 2005), therefore it is unclear whether the binding of HSJ1a to the UBL domain would alter the fate of the ubiquilin-2 cargo.

Endogenous and heterologously expressed ubiquilin-2 has been shown to adopt punctate structures in multiple neuronal cell types (N'diaye *et al.* 2009, Rothenberg *et al.* 2010, Osaka *et al.* 2015). The puncta have been found to co-localise with endogenous and GFP-LC3, suggesting that the structures represent autophagosomes (N'diaye *et al.* 2009, Rothenberg *et al.* 2010). Here, the transfection of FLAG-ubiquilin-2 in SK-N-SH cells also resulted in the formation of punctate structures; however, under basal conditions, the puncta showed limited co-localisation with GFP-LC3, which formed relatively few autophagosome structures in transfected cells. The majority of FLAG-ubiquilin-2 puncta do therefore not appear to represent autophagosomes. In transfected N2a and HeLa cells, ubiquilin-2 puncta showed co-localisation with optineurin, a protein proposed to function in endosome recycling and endocytic trafficking (Osaka *et al.* 2015, Nagabhushana *et al.* 2010). The co-localisation of the two proteins implied that ubiquilin-2 may be present in endosomes and indeed, ubiquilin-2 puncta co-localised with GFP-Rab11, a marker of recycling endosomes (Osaka *et al.* 2015). Interestingly, recycling endosomes have been demonstrated to contribute to autophagosome formation upon amino acid starvation (Longatti *et al.* 2012).

The incorporation of recycling endosomes into autophagosomes could explain the extensive co-localisation observed between GFP-LC3 and FLAG-ubiquilin-2 upon amino acid starvation. Such an observation has been previously reported. The co-localisation of ubiquilin-2 puncta with endogenous autophagosome markers such as LC3, p62 and ULK1 was substantially increased upon amino acid starvation (Osaka *et al.* 2015). The degree to which ubiquilin-2 co-localises with LC3 therefore appears to be dictated by the demand for autophagosome formation. This can vary in different cell types, possibly explaining why some cell types show greater co-localisation between LC3 and ubiquilin-2. It will be important in future studies to confirm the nature of the ubiquilin-2 puncta formed in SK-N-SH cells and determine whether they do indeed represent recycling endosomes.

In view of the co-localisation between GFP-LC3 and FLAG-ubiquilin-2 upon amino acid starvation, I sought to examine whether HSJ1a forms part of the complex that links ubiquilin-2 to LC3. LC3-interacting proteins have been identified to bind to LC3 via a LC3-interacting region (LIR), a motif with the consensus sequence of W/Y/FXXL/I/V (Ichimura *et al.* 2008). Interestingly, HSJ1 contains 8 such motifs (Figure 3.13), therefore, in theory; HSJ1 has the capabilities to bind directly to LC3. GFP-LC3 co-immunopurified with myc-HSJ1a under both basal conditions and upon amino acid starvation. Upon amino acid starvation, both GFP-LC3-I and GFP-LC3-II were immunopurified with myc-HSJ1a, although the levels of GFP-LC3-II immunopurified were substantially lower than the levels of GFP-LC3-I. HSJ1a therefore appears to interact with the cytosolic isoform LC3-I and the autophagosome-associated isoform LC3-II. It will be important to validate the interaction in the future, ideally using endogenous LC3, in order to verify that the interaction is not an artefact caused by the overexpression of the two proteins. The significance of HSJ1a binding to LC3-I is unclear, however, it could possibly indicate that HSJ1a is involved in the turnover of LC3-I. On the other hand, the binding of HSJ1a to LC3-II is an interesting concept. Binding to LC3-II would suggest that HSJ1a acts as a selective adaptor, recruiting ubiquitylated cargo into the autophagosome either through the direct binding of HSJ1a client proteins or, alternatively, though an interaction with ubiquilin-1 and ubiquilin-2, or other UBL proteins. To classify HSJ1a as an adaptor protein, the localisation of HSJ1a to autophagosomes would need to be established. Furthermore, it would be need to be shown that HSJ1a is degraded upon the induction of autophagy.

MASYYEILDVPRSASADDIKKAYRRKALQWHPDKNPDNKEFAEKKFKEVAEAYEVL
SDKHKREIYDRYGREGLTGTGTGPSRAEAGSGGPGFTFTFRSPEEVFREFFGSGDP
FAELFDDLGPFSELQNRGSRHSGPFFTFSSSFPGHSDFSSSSFSFSPGAGAFRSVS
TSTTFVQGRRITTRRIMENGQERVEVEEDGQLKSVTINGVPDDLALGLELSRREQQ
PSVTSRSGGTQVQQTPASCPLDSDLSEDEDLQLAMAYSLSEMEAAGKKPADVF

Figure 3.13 Predicted LC3-interacting regions (LIRs) in HSJ1a. LIRs with the consensus sequence W/Y/FXXL/I/V are highlighted in yellow. Where two LIRs overlap or where one LIR follows another, the second LIR is underlined.

Five mutations in ubiquilin-2 were initially reported by Deng *et al.* (2011) in families with X-linked ALS. Since this first report, other ubiquilin-2 patient mutations have been identified, with all mutations identified to date located in or around the PXX repeat region (Milliecamps *et al.* 2012, Gellera *et al.* 2013, Fahed *et al.* 2014). Investigations have focused on dissecting how mutations in the PXX repeat region cause motor neuron degeneration. One possible mechanism involves impaired proteostasis, with Deng *et al.* (2011) identifying that the ubiquilin-2 mutants have a reduced ability to target substrates to the proteasome for degradation. Furthermore, ubiquilin-2 mutants showed a reduced binding affinity for UBXD8, resulting in the accumulation of an ERAD reporter substrate (Xia *et al.* 2014). However, *in vivo* studies suggest that disease pathogenesis is driven by a toxic gain of function rather than a loss of function. Ubiquilin-2 knockout rats appeared healthy, with no observable phenotype, whereas transgenic rats overexpressing ubiquilin-2 P497H showed cognitive defects, with the progressive loss of neurons in the motor cortex (Wu *et al.* 2015). Prior to neuronal loss, ubiquilin-2 aggregates were observed, as seen in patient post mortem examinations (Deng *et al.* 2011). Ubiquilin-2 mutants were also shown to aggregate into cytoplasmic inclusions in transfected cells (Osaka *et al.* 2015, Xia *et al.* 2014). Here, I show that three of the ubiquilin-2 mutants, FLAG-ubiquilin-2 P506T, P509S and P525S form punctate structures that are significantly larger than those formed by wild-type ubiquilin-2. It is possible that the larger structures represent inclusions or potentially aggresomes, formed by the deposition of misfolded ubiquilin-2 protein. To determine whether the larger structures represent aggresomes, the localisation of mutant ubiquilin-2 puncta with aggresome markers could be examined. Aggresomes form at the microtubule-organising centre (MTOC), therefore a MTOC marker such as pericentrin could be used. Another characteristic feature of aggresomes is the deposition of intermediate filaments around the structure, therefore staining for an intermediate filament could provide another suitable marker.

HSJ1a retained the ability to bind to the ubiquilin-2 mutants and was recruited to both the small and large punctate structures. If the larger punctate structures do represent inclusions, it will be interesting to determine whether HSJ1a is able to bind mutant ubiquilin-2 as a client protein and reduce its aggregation either by promoting its refolding or degradation (Rose *et al.* 2011, Westhoff *et al.* 2005). Future studies should therefore focus on examining the effect of HSJ1a overexpression on mutant ubiquilin-2 protein levels as well as the effect on the number and size of mutant ubiquilin-2 punctate structures. The overexpression of HSJ1a in a mouse model of ALS protected motor neurons against SOD1 G93A-induced toxicity, reducing SOD1 G93A aggregation and resulting in an increase in motor unit number and an increase in motor neuron survival (Novoselov *et al.* 2013). It would be

interesting to determine whether HSJ1a can also protect motor neurons against ubiquilin-2 mediated toxicity. Such a protective response would further highlight the important role of HSJ1 in motor neuron survival.

Chapter 4 – Investigating the pathogenicity of HSJ1-Y5C

4.1 Introduction

dHMN and CMT2 are caused by the progressive degeneration of lower motor neurons. Clinically, there is significant overlap between dHMN and CMT2, with weakness and wasting of the lower limb muscles being the predominant phenotype of both diseases (Reilly *et al.* 2011, Rossor *et al.* 2012, Baets *et al.* 2014). The presence of sensory deficits, in addition to motor disturbances, differentiates CMT2 from dHMN. As discussed in Chapter 1, a range of causative genes for dHMN and CMT2 have been identified, with mutations in the same gene causing both phenotypes. Although the majority of disease-causing mutations are unsolved, novel causative genes are continuing to emerge. Recently, three mutations in *HSJ1* have been reported in two families with dHMN and one family with CMT2 (Blumen *et al.* 2012, Gess *et al.* 2014).

In 2012, Blumen *et al.* were the first group to report a mutation in *HSJ1* in three siblings with dHMN. The three siblings, from a consanguineous Jewish Moroccan family, reported symptom onset at 18, 23 and 20 years of age and initial symptoms were described as difficulties with walking, gait abnormalities and foot drop. At the time of presentation all three siblings showed progressive weakness, hypotonia and atrophy of the distal lower limbs. Plantar responses were flexor but ankle and knee jerk reflexes were absent. The distal hand muscles were unaffected. A follow up examination revealed severe distal weakness and atrophy, with swelling of the ankles and feet. The upper limbs were relatively spared although bicep and tricep jerks were absent. Nerve conductions studies revealed a normal median motor nerve velocity and no sensory deficits were recorded clinically or electrophysiologically.

Gess *et al.* (2014) identified a second mutation in *HSJ1* in two siblings with dHMN from a consanguineous Turkish family. As with the Moroccan family, symptom onset occurred in early adulthood, at 16 and 19 years of age. Initial symptoms were also described as difficulties with walking, with gait abnormalities and frequent stumbling. At the time of presentation the siblings exhibited mild atrophy of the peroneal and gastrocnemic muscles in the leg. In addition, mild bilateral paralysis of foot and toe dorsiflexion was observed. The siblings also presented with mild pareses of knee flexion. No sensory symptoms were observed and nerve conduction studies confirmed a lack of sensory involvement.

In both families, dHMN was associated with an autosomal recessive pattern of inheritance. In the Moroccan family, a homozygous c.352+1 G>A mutation was identified in *HSJ1*, abolishing the donor splice site of intron 5 (Blumen *et al.* 2012). The mutation led to

abnormal splicing events, with two additional *HSJ1* transcripts observed in patient fibroblasts. The additional transcripts retained either the partial or full sequence of intron 5, with both transcripts carrying a premature stop codon. At the protein level, patient fibroblasts showed reduced expression of HSJ1b, with no detectable levels of HSJ1a (Blumen *et al.* 2012). In the Turkish family, a homozygous c.229+1 G>A mutation was identified, abolishing the donor splice site of intron 4 (Gess *et al.* 2014). The mutation led to the abnormal splicing of *HSJ1*, with the retention of intron 4 in the transcript. Unlike *HSJ1* c.352+1 G>A, the correctly spliced transcript was absent from patient fibroblasts. At the protein level, patient fibroblasts showed no detectable levels of either HSJ1 isoform (Gess *et al.* 2014).

A third mutation in *HSJ1* was identified in two siblings with CMT2 (Gess *et al.* 2014). The two siblings, from an Austrian family, reported symptom onset at 30 and 23 years of age. Initial symptoms included an unstable gait and numbness of the distal lower limbs. At the time of presentation the two siblings showed peroneal and gastrocnemic muscle atrophy with a reduced sensation to touch. Incomplete paralysis of foot and toe dorsiflexion was also observed. Ankle and knee jerk reflexes were absent, as were reflexes of the upper limbs. Median motor nerve conduction velocities were normal in both siblings. Sensory nerve conduction studies were not performed, however the presence of sensory symptoms was indicative of CMT2 rather than dHMN. A comparison of the clinical phenotypes described for all three families is summarised in Table 4.

Whole-exome sequencing of the patients revealed the homozygous missense mutation c.14A>G in *HSJ1*, resulting in the substitution of a tyrosine for a cysteine at residue 5. As with the previous two *HSJ1* mutations, the third mutation also showed an autosomal recessive pattern of inheritance. Residue 5 of HSJ1 is located in the J domain and is highly conserved in HSJ1 orthologs across multiple species (Figure 4). The Y5C substitution was classified as disease-related by several different automatic algorithms, suggesting that residue 5 is critical for the structure and/or function of HSJ1.

Our lab was asked to investigate the pathogenicity of the c.14A>G substitution by Professor Michaela Auer-Grumbach (Vienna) who had identified the variant in her patients. For the mutation to be characterised as pathogenic, the substitution should confer a loss of function phenotype on HSJ1, as indicated by the recessive mode of inheritance. A loss of HSJ1 function may be driven by a reduction in protein levels, impaired activity or the mis-localisation of the protein. To determine whether the Y5C substitution does impart a loss of function phenotype on HSJ1, HSJ1-Y5C plasmids were created and the expression, function and localisation of HSJ1-Y5C was examined in SK-N-SH neuroblastoma cells.

	Family I (Moroccan)			Family II (Turkish)		Family III (Austrian)	
Patient	I	II	III	I	II	I	II
Age of onset (yrs)	18	23	20	16	19	30	23
Lower limb atrophy	Yes	Yes	Yes	Yes	Yes	Yes	Yes
Paralysis of foot and toe dorsiflexion	NR	NR	NR	Yes	Yes	Yes	Yes
Ankle and knee jerk reflexes	Absent	Absent	Absent	NR	NR	Absent	Absent
Biceps and triceps jerk reflexes	Absent	Absent	Absent	NR	NR	Absent	Absent
Knee flexion	NR	NR	NR	Reduced	Reduced	Reduced	Reduced
Sensory abnormalities	No	No	No	No	No	Yes	Yes

Table 4 A summary of the clinical phenotype of the patients from the three families with mutations in *HSJ1*. NR – not reported. (Blumen *et al.* 2012, Gess *et al.* 2014).

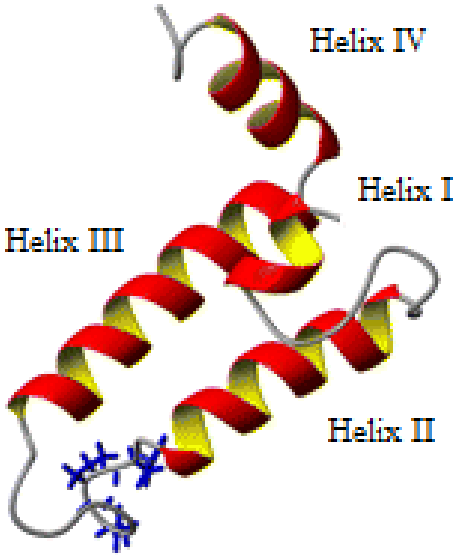

Homo sapiens	MASY**Y**EILDVPRSASADDIKKAYR
Mus musculus	MASY**Y**EILDVPRSASADDIKKAYR
Bos taurus	MASY**Y**EILDVPRSAFPDDIKKAYR
Danio rerio	MVDY**Y**DVLGVSRSASPDDIKKAYR
Drosophila melanogaster (MRJ)	MVDY**Y**KILDVSRSATDSEVKKAYR
Caenorhabditis elegans (DNJ-24)	EDSP**Y**ITLGISSTSDDVEIKKAYR
Saacharomyces cerevisiae (SIS1)	ETKL**Y**DLLGVSPSANEQELKKGYR
Eschericia coli (DNAJ)	KQDY**Y**EILGVSKTAEEREIRKAYK

Figure 4 The J domain structure of HSJ1 and the multiple sequence alignment of the region around Y5 of human HSJ1 and several orthologues. The structure of HSJ1's J domain. Y5 lies in helix I of the J domain, formed from residues 4-7. PBD: 1XBL. Y5, highlighted in red, is highly conserved across several orthologues.

4.2 Results

4.2.1 The Y5C substitution increases the turnover of HSJ1

Site directed mutagenesis was used to introduce the c.14A>G substitution into the cDNA of untagged HSJ1a and HSJ1b plasmids, generating HSJ1a-Y5C and HSJ1b-Y5C plasmids. To determine if the Y5C substitution affected the expression level of HSJ1a and HSJ1b, SK-N-SH neuroblastoma cells were transiently transfected with either a wild-type or mutant isoform of HSJ1. 24 hours post transfection, cells were lysed and the expression level of wild-type and mutant HSJ1 was compared by Western blot analysis. HSJ1 levels were corrected for loading using β-tubulin and the level of HSJ1a-Y5C and HSJ1b-Y5C was normalised to the expression of the corresponding wild-type isoform. Both HSJ1a-Y5C and HSJ1b-Y5C showed a significant reduction in expression levels compared to wild-type HSJ1a and HSJ1b (Figure 4.1). HSJ1a-Y5C showed a 37% reduction in expression levels compared to wild-type HSJ1a, with HSJ1b-Y5C showing a 48% reduction in expression levels compared to wild-type HSJ1b.

To determine if the reduction in expression levels was due to a shorter half-life of HSJ1-Y5C, the level of wild-type and mutant HSJ1 was compared following treatment with the protein synthesis inhibitor, cycloheximide. SK-N-SH cells were transfected with either a wild-type or mutant HSJ1 isoform then treated with 50 μM of cycloheximide for 0, 1, 2 or 4 hours. HSJ1 levels were then determined by Western blot analysis (Figure 4.2). The expression level of HSJ1 at each time point was corrected for loading using β-tubulin, then normalised to the level of HSJ1 at 0 hours. The percentage of HSJ1 remaining over time was then quantified. Both isoforms of wild-type HSJ1 showed no change in protein levels over the 4 hour treatment, suggesting that the heterologous protein is stable. In contrast, HSJ1a-Y5C and HSJ1b-Y5C showed a progressive decline in protein levels, initiating after 1 hour. At 2 hours, both HSJ1a-Y5C and HSJ1b-Y5C showed a 15% loss of protein, with a significant loss of 55% and 42%, respectively, observed at 4 hours. There was no significant difference in the rate of protein loss between the two mutant isoforms. The data therefore suggests that the Y5C substitution increases the turnover rate of HSJ1 compared to the wild-type protein.

4.2.2 HSJ1-Y5C is targeted to the proteasome for degradation

To establish whether HSJ1-Y5C was degraded by autophagy or the UPS, SK-N-SH cells transfected with either a wild-type or mutant HSJ1 isoform were treated for 4 hours with bafilomycin, to inhibit autophagy, or MG132, to inhibit the proteasome. HSJ1 protein levels were then determined by Western blot analysis. HSJ1 levels were corrected for loading then

normalised to the level of the corresponding wild-type HSJ1 isoform in untreated transfected cells. The reduced levels of both isoforms of HSJ1-Y5C could be partially restored following treatment with MG132 (Figure 4.3). The level of HSJ1a-Y5C increased by 19% over the 4 hour treatment with MG132, such that HSJ1a-Y5C was only 18% lower than wild-type HSJ1a at 4 hours, compared to the 37% reduction observed in untreated cells. Similarly, HSJ1b-Y5C levels increased by 26% in the presence of MG132, resulting in only a 20% reduction in protein levels compared to wild-type HSJ1b at 4 hours. Interestingly, both HSJ1a-Y5C and HSJ1b-Y5C levels were found to be further reduced in the presence of bafilomycin compared to untreated cells. HSJ1a-Y5C levels were reduced by an additional 12%, with HSJ1b-Y5C levels reduced by a further 11%. In the case of HSJ1a-Y5C, this decrease was found to be significant. No change in wild-type HSJ1 protein levels was observed in the presence of bafilomycin or MG132, in agreement with the cycloheximide data showing that the wild-type protein is stable. The results therefore confirm that both isoforms of HSJ1-Y5C are degraded at a higher rate than wild-type HSJ1 isoforms, with degradation being mediated by the proteasome.

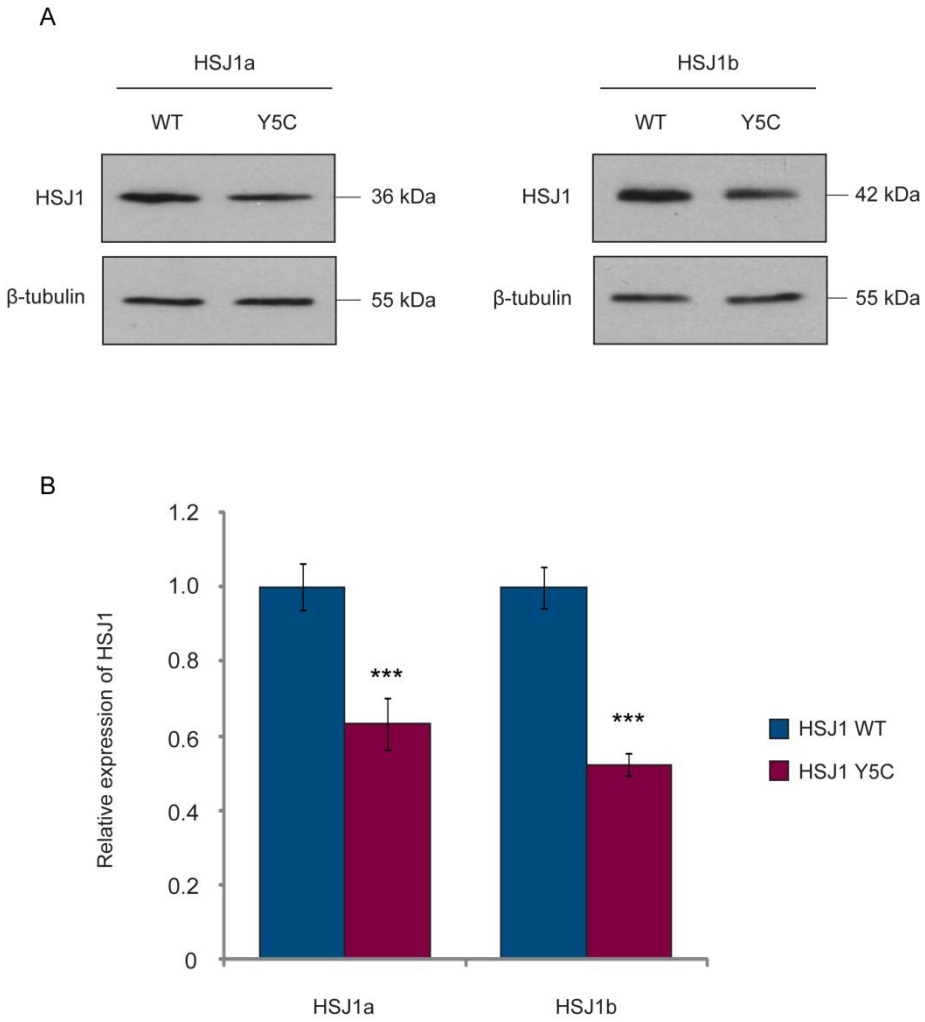

Figure 4.1 HSJ1-Y5C shows reduced expression levels compared to wild-type HSJ1. A: SK-N-SH cells were transfected with either a wild-type HSJ1 or HSJ1-Y5C isoform. 24 hours post transfection, cells were lysed and 15 µg of total protein was resolved by SDS-PAGE. Western blot analysis was performed using a polyclonal sheep HSJ1 antibody used at a dilution of 1:1000, and a monoclonal β-tubulin antibody used at 1:5000. **B:** Western blots of HSJ1 and β-tubulin were analysed using ImageJ. The level of HSJ1 was corrected for loading using β-tubulin. HSJ1a-Y5C and HSJ1b-Y5C levels were then normalised to the level of the wild-type HSJ1 isoform. Error bars represent ± SD (*** P <0.001, Student's t-test, n=3).

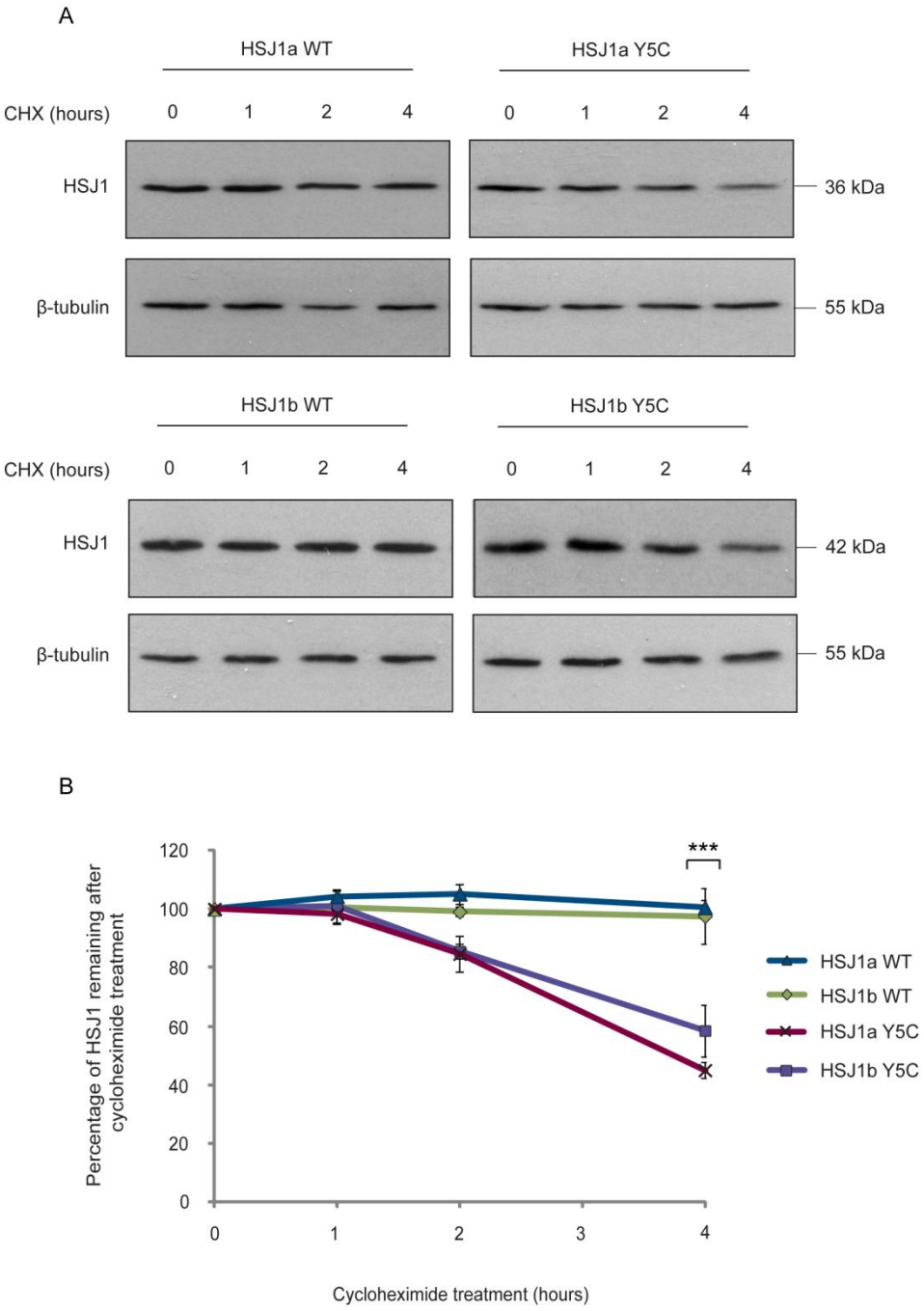

Figure 4.2 HSJ1-Y5C is degraded at a higher rate than wild-type HSJ1. A: SK-N-SH cells transfected with a wild-type or HSJ1-Y5C isoform were treated for 0, 1, 2 or 4 hours with 50 µg/mL cycloheximide. Samples were resolved by SDS-PAGE. Western blot analysis was performed using a polyclonal sheep HSJ1 antibody (1:1000) and a monoclonal β-tubulin antibody (1:5000). **B:** Western blots of HSJ1 and β-tubulin were analysed by ImageJ. The level of HSJ1 was corrected for β-tubulin and then normalised to the level of HSJ1 at 0 hours. The percentage of HSJ1 remaining over time was then quantified. Error bars represent ± SD (*** P <0.001, Student's t-test, n=3).

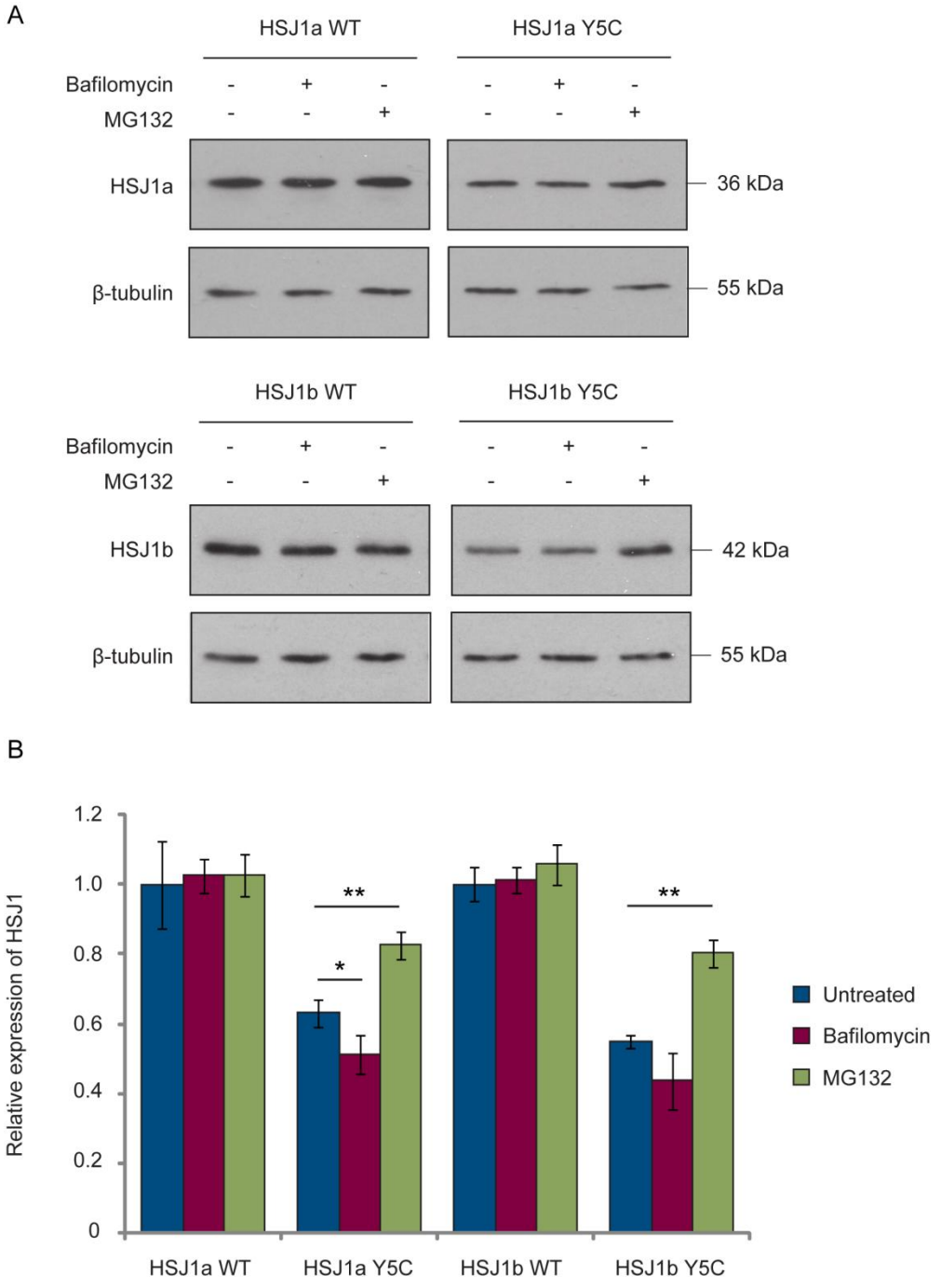

Figure 4.3 HSJ1-Y5C levels are partially restored in the presence of MG132. A: SK-N-SH cells were transfected with a wild-type HSJ1 or HSJ1-Y5C isoform. 24 hours post transfection, cells were either untreated or incubated with bafilomycin (200 nM) or MG132 (50 µM) for 4 hours. Cells were then harvested and 15 µg of total protein was resolved by SDS-PAGE. Western blot analysis was performed using a polyclonal sheep HSJ1 antibody (1:1000) and a monoclonal β-tubulin antibody (1:5000). **B:** Western blots were analysed using ImageJ. The level of HSJ1 was corrected for loading and then normalised to the level of wild-type HSJ1 in untreated transfected cells. Error bars represent ± SD (* P <0.05, ** P <0.01, one-way ANOVA with post hoc Tukey test, n=4).

4.2.3 HSJ1-Y5C retains its normal localisation

To examine the localisation of the remaining HSJ1-Y5C protein, SK-N-SH cells were transfected with wild-type or mutant HSJ1 and 24 hours post transfection cells were fixed and stained for HSJ1 (Figure 4.4). Although the fluorescent intensity was reduced, both mutant isoforms retained their normal localisation, with HSJ1a-Y5C appearing diffuse in the cytoplasm and the nucleus, and HSJ1b-Y5C displaying an ER staining pattern. The localisation of HSJ1b-Y5C to the cytoplasmic face of the ER was confirmed by its co-localisation with the ER chaperone, BiP (Chapple and Cheetham 2003). These results suggest that HSJ1-Y5C retains its normal localisation.

4.2.4 HSJ1a-Y5C retains its anti-aggregation function

Residue 5 of HSJ1 lies in helix I of the highly conserved J domain (Gao *et al.* 2012). To determine if the Y5C substitution affects the J domain activity of the remaining protein, the ability of HSJ1a-Y5C to target misfolded proteins for degradation, a process dependent on a functional J domain and UIMs, was assessed (Westhoff *et al.* 2005, Novoselov *et al.* 2013). SOD1 G93A and Q103 inclusion formation was examined in the presence of wild-type HSJ1a, HSJ1a-Y5C or the J domain mutant HSJ1a-H31Q. In order to accurately compare the ability of wild-type HSJ1a, HSJ1a-Y5C and HSJ1a-H31Q to reduce inclusion formation, it was important to avoid saturating amounts of HSJ1a in the assay. Titration curves were therefore generated in order to establish the amount of HSJ1a that gave a linear dose response. SK-N-SH cells were transfected with 50 ng of GFP-SOD1 G93A or GFP-Q103 and 0, 5, 15, 25, 50, 75 or 100 ng of wild-type HSJ1a. 24 hours post transfection, cells were fixed and the percentage of transfected cells containing inclusions was assessed as described in Chapter 2. For both GFP-SOD1 G93A and GFP-Q103 a significant linear decrease in the percentage of transfected cells containing inclusions was observed between 5 ng and 25 ng of HSJ1a, with the response plateauing between 30 ng and 100 ng (Figure 4.5). 15 ng of HSJ1a was therefore used in the assays. The transfection of SK-N-SH cells with GFP-SOD1 G93A resulted in 25.6% of transfected cells containing perinuclear inclusions (Figure 4.6). The co-transfection of GFP-SOD1 G93A with wild-type HSJ1a reduced the percentage of transfected cells containing inclusions from 25.6% to 16.4%, a reduction of 36% (as observed in Figure 4.5). In contrast, HSJ1a-H31Q was unable to significantly reduce inclusion incidence. HSJ1a-Y5C was found to be significantly more effective than HSJ1a-H31Q but less effective than wild-type HSJ1a, reducing inclusion incidence from 25.6% to 20.1%. This is a reduction of 22%, compared to 36% observed in the presence of wild-type HSJ1a. Similar results were observed for GFP-Q103 (Figure 4.7). The co-transfection of GFP-Q103 and wild-type HSJ1a reduced the percentage of cells containing inclusions from

33.7% to 18.8%, a reduction of 44%. As seen with GFP-SOD1 G93A, the reduction in inclusion incidence was abolished in the presence of HSJ1a-H31Q. HSJ1a-Y5C was able to significantly reduce the percentage of transfected cells containing inclusions from 33.7% to 23.2%. This reduction of 31% was significantly lower than the 44% reduction observed in the presence of wild-type HSJ1a. Overall, the data suggests that HSJ1a-Y5C retains some functionality.

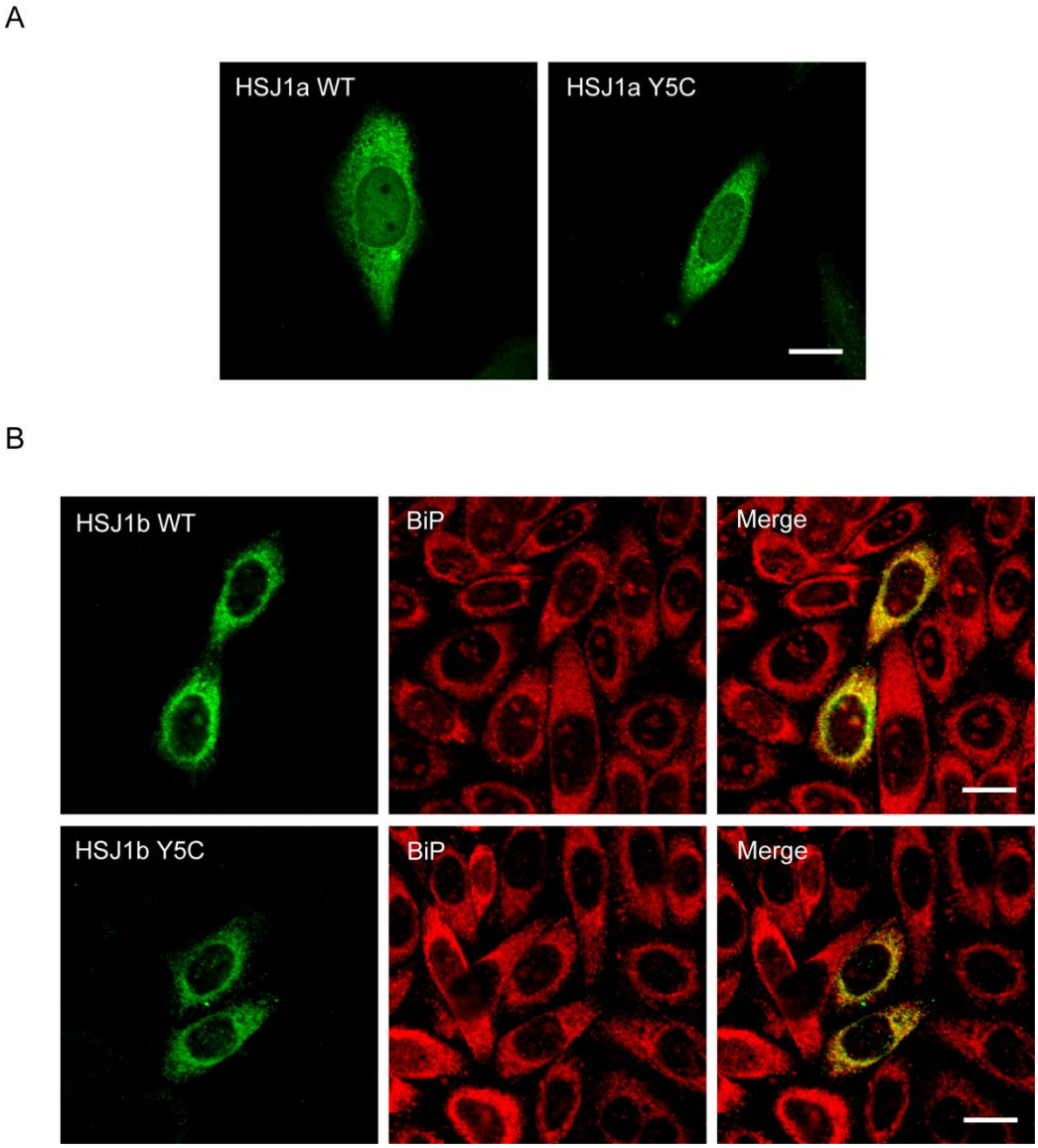

Figure 4.4 The Y5C substitution does not affect the localisation of HSJ1. A: SK-N-SH cells were transfected with wild-type HSJ1a or HSJ1a-Y5C. 24 hours post transfection, cells were fixed in 4% PFA and permeabilised in 0.1% Triton-X. Cells were immunostained with a sheep HSJ1 antibody (1:200) and cells were imaged using a Zeiss LSM 700 confocal microscope. Scale bar: 10 µm. **B:** SK-N-SH cells were transfected with wild-type HSJ1b or HSJ1b-Y5C. 24 hours post transfection, cells were fixed in 4% PFA and permeabilised in 0.1% Triton-X. Cells were immunostained with sheep HSJ1 antibody (1:200) (Cy2 green) and a rabbit BiP antibody (1:200) (Cy3 red). Cells were imaged using a Zeiss LSM 700 confocal microscope. Scale bar: 10 µm (n=3).

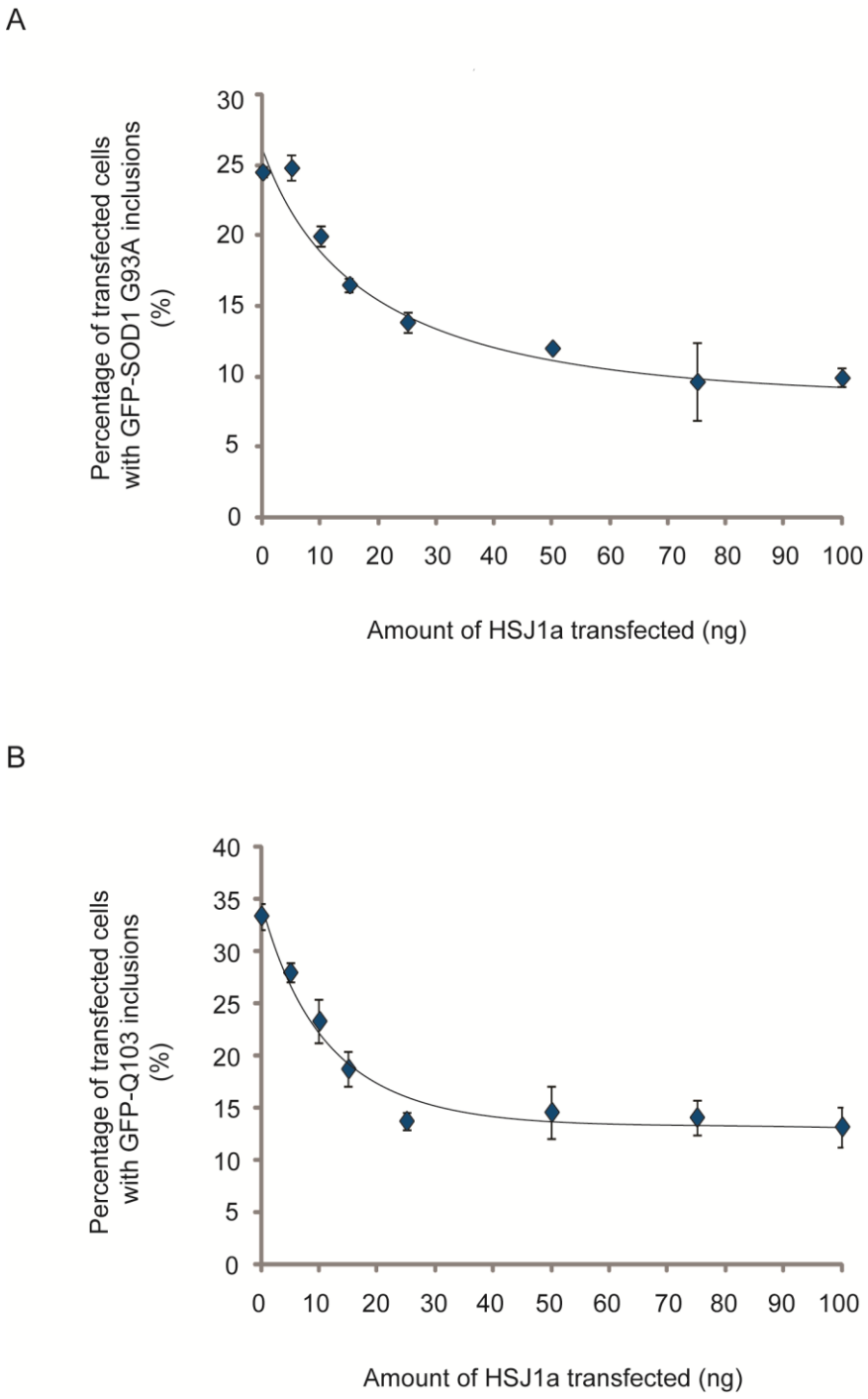

Figure 4.5 Titration curves demonstrate that wild-type HSJ1a reduces GFP-SOD1 G93A and GFP-Q103 inclusions formation in a concentration-dependent manner. SK-N-SH cells were transfected with 50 ng of GFP-SOD1 G93A (**A**) or GFP-Q103 (**B**) and 0, 5, 15, 25, 50, 75 or 100 ng of HSJ1a. 24 hours post transfection cells were fixed in 4% PFA. Cells were counted on a Nikon Eclipse 80i fluorescent light microscope. The number of transfected cells containing inclusions was divided by the total number of transfected cells and expressed as a percentage (n=3).

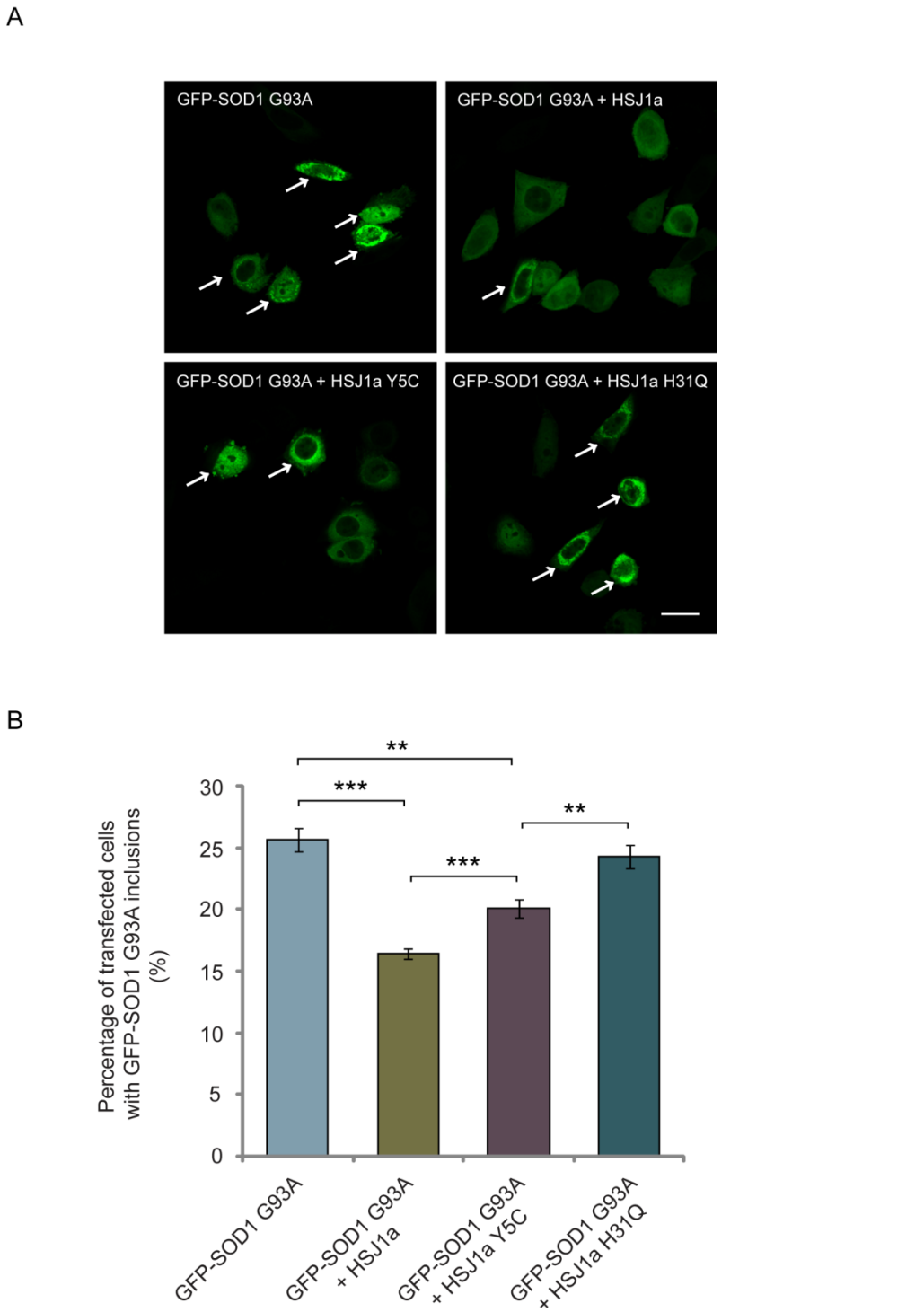

Figure 4.6 The effect of wild-type HSJ1a, HSJ1a-Y5C and HSJ1a-H31Q on GFP-SOD1 G93A inclusion formation. A: SK-N-SH cells were transfected with 50 ng of GFP-SOD1 G93A and 15 ng of wild-type HSJ1a, HSJ1a-Y5C or HSJ1a-H31Q. 24 hours post transfection, cells were fixed in 4% PFA. Representative images of GFP-SOD1 G93A inclusions in the absence or presence of wild-type HSJ1a, HSJ1a-Y5C or HSJ1a-H31Q. Images were taken on a Zeiss LSM 700 confocal microscope. Scale bar: 10 µm. **B:** The number of transfected cells containing inclusions was counted on a Nikon Eclipse 80i fluorescent light microscope and expressed as a percentage of the total number of transfected cells. Error bars represent ± SD. (** P <0.01, *** P < 0.001 Student's t-test, n=3).

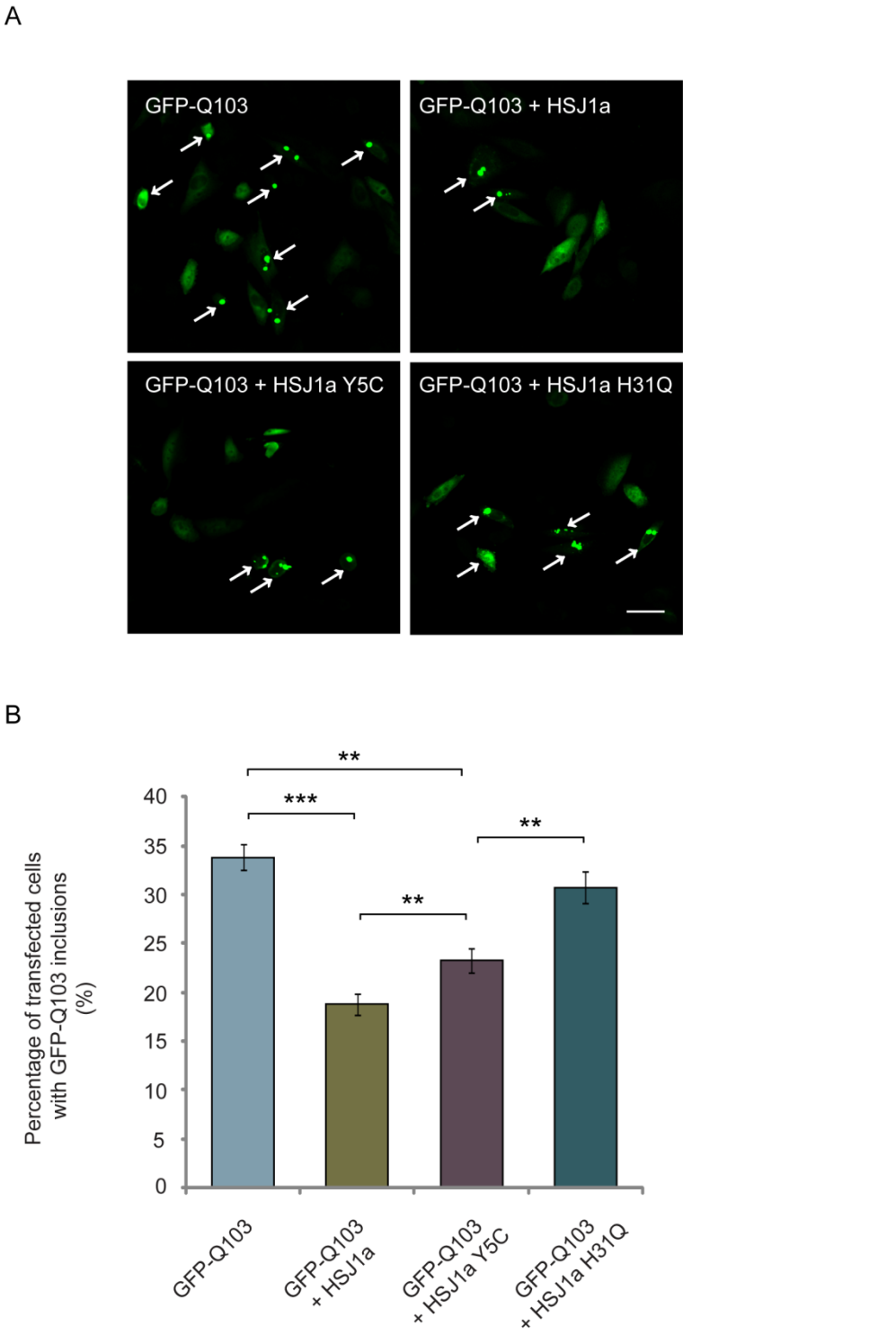

Figure 4.7 The effect of wild-type HSJ1a, HSJ1a-Y5C and HSJ1a-H31Q on GFP-Q103 inclusion formation. A: SK-N-SH cells were transfected with 50 ng of GFP-Q103 and 15 ng of wild-type HSJ1a, HSJ1a-Y5C or HSJ1a-H31Q. 24 hours post transfection, cells were fixed in 4% PFA. Representative images of GFP-Q103 inclusions in the absence or presence of wild-type HSJ1a, HSJ1a-Y5C or HSJ1a-H31Q. Images were taken on a Zeiss LSM 700 confocal microscope. Scale bar: 10 µm. B: The number of transfected cells containing inclusions was counted on a Nikon Eclipse 80i fluorescent light microscope and expressed as a percentage of the total number of transfected cells. Error bars represent ± SD (** P <0.01, *** P < 0.001 Student's t-test, n=3).

4.2.5 HSJ1a-Y5C retains the ability to interact with LC3

In the previous Chapter, HSJ1a was shown to co-immunopurify LC3, suggesting a potential interaction between the two proteins. As discussed in Chapter 3, it is possible that the interaction is direct, mediated by an LC3-interacting region (LIR) in HSJ1. Interestingly, one of the eight predicted LIR sequences in HSJ1 encompasses residues 5 to 8 (YXXL) (Figure 3.13). The Y5C substitution would be predicted to abolish the LIR sequence. To investigate whether residue 5 forms an LIR critical for LC3 binding, the ability of HSJ1a-Y5C to co-immunopurify LC3 was examined. A myc-HSJ1a-Y5C plasmid was generated using site directed mutagenesis. SK-N-SH cells were then transfected with GFP-LC3 and either wild-type myc-HSJ1a (WT) or myc-HSJ1a-Y5C (Y5C). 24 hours post transfection, cell lysates were immunopurified with a GFP, myc or IgG antibody. Purifications were then resolved by SDS-PAGE and Western blot analysis was performed with a GFP antibody. A 43 kDa band corresponding to GFP-LC3 was detected in both GFP and myc purifications (Figure 4.8). No band was detected in the IgG purifications, confirming the specificity of the interaction. GFP-LC3 was immunopurified in the presence of myc-HSJ1a or myc-HSJ1a-Y5C, suggesting that the Y5C substitution does not abolish the observed interaction between HSJ1a and LC3.

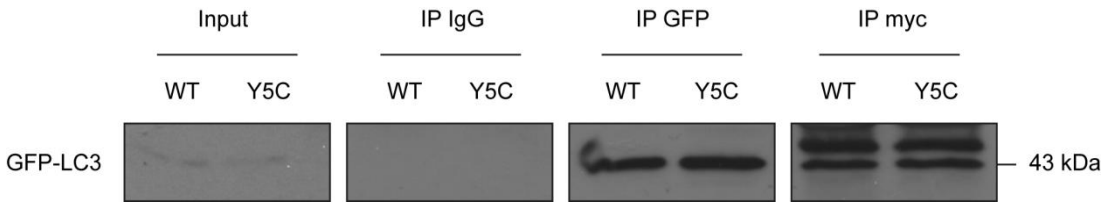

Figure 4.8 HSJ1a-Y5C retains the ability to interact with LC3. SK-N-SH cells were transfected with GFP-LC3 and either wild-type myc-HSJ1a (WT) or myc-HSJ1a-Y5C (Y5C). 24 hours post transfection, cell lysates were incubated with protein G Dynabeads and either a GFP, myc or IgG antibody (1:200). After a one hour incubation on a rotating wheel, purified immuno-complexes were resolved by SDS-PAGE and Western blot analysis was performed using a mouse monoclonal GFP antibody at a 1:1000 dilution (n=3).

4.3 Discussion

A c.14A>G homozygous variant was identified in *HSJ1* in two siblings with autosomal recessive CMT2. The mutation, resulting in a Y5C substitution at the protein level, was predicted to be disease-causing, however the pathogenicity of the mutation had not been confirmed. I sought to determine whether the Y5C substitution was indeed pathogenic.

The tyrosine residue in question lies in the first α-helix of HSJ1 (Gao *et al.* 2012). Interestingly, the multiple alignment of over 200 J domain sequences revealed that this residue in particular is one of a handful of amino acids that shows more than 90% sequence conservation across all three classes of DnaJ proteins (Hennessy *et al.* 2000). Such a high degree of sequence conservation indicates that the tyrosine residue is critical to the structure or function of the J domain. Based on the structural analysis of *E. coli* DnaJ, the conserved tyrosine residue was predicted to primarily adopt a structural role (Hennessy *et al.* 2000, Hennessy *et al.* 2005). The tyrosine side chain was found to project outwards from helix I; such an orientation was proposed to enable the aromatic ring to interact with residues in helix II, III and IV. The formation of inter-helix interactions is likely to be critical for ensuring the stability of the J domain structure.

The increased turnover of HSJ1-Y5C in SK-N-SH cells supports the hypothesis that the tyrosine residue is a key mediator of HSJ1 stability. The loss of the aromatic side chain may prevent the formation of the inter-helix interactions, destabilising the J domain structure and causing the unfolding and subsequent proteasomal degradation of HSJ1. The substitution to a cysteine may be particularly deleterious; its small side chain is unlikely to compensate for the large aromatic ring of the tyrosine residue. The increased turnover of HSJ1-Y5C results in a 37% and 48% decrease in HSJ1a-Y5C and HSJ1b-Y5C protein levels, respectively. As heterozygous carriers of the *HSJ1* splice site mutations are healthy, with no observable phenotype, 50% of HSJ1 protein levels appear to be sufficient for function (Blumen *et al.* 2012, Gess *et al.* 2014). As the reduction in HSJ1-Y5C levels is less than 50%, the reduced half-life of HSJ1-Y5C would not be expected to generate a loss of function phenotype. Considering the highly conserved nature of the residue and its proposed role in stabilising the J domain structure, it is somewhat surprising that the Y5C substitution does not have a more prominent effect on HSJ1 protein levels. However, it is possible that the reduction in HSJ1-Y5C is underestimated in this overexpression system. The high rate of HSJ1-Y5C protein synthesis may exceed the degradative capacity of the proteasome, leading to the accumulation of the protein. The observed HSJ1-Y5C protein levels may therefore not represent the true extent to which the substitution destabilises the protein.

Although the tyrosine residue is predicted to primarily adopt a structural role, it is possible that the residue has an indirect functional role, either by ensuring that the J domain is correctly orientated to interact with Hsp70 or by stabilising the binding of the two proteins. The functional impact of the Y5C substitution on J domain activity was assessed by examining the anti-aggregation function of HSJ1a-Y5C. HSJ1a-Y5C retained the ability to target misfolded proteins for degradation; however, compared to wild-type HSJ1a, HSJ1a-Y5C was 39% and 30% less effective at reducing GFP-SOD1 G93A and GFP-Q103 inclusion incidence, respectively. The 30-40% reduction in functionality correlates with the reduction in HSJ1a-Y5C expression levels. Considering that wild-type HSJ1a targets misfolded proteins for degradation in a concentration-dependent manner, the reduced ability to clear inclusions is likely due to the lower expression levels of HSJ1a-Y5C rather than an impairment in J domain activity. The retained functionality of HSJ1a-Y5C is consistent with previous mutagenesis studies. Nicoll *et al.* (2007) sought to examine the functional consequences of mutating some of the highly conserved J domain amino acids previously identified (Hennessy *et al.* 2000). The mutations were introduced into a range of chimeric proteins, generated by replacing the J domain of DnaJ with mammalian J domains, including that of HSJ1. Functionality was then assessed based on the ability to reverse the thermosensitivity of the mutant *E. coli* stain OD259, which lacks *dnaJ* and *cpbA*, a chaperone gene that can compensate for DnaJ. Tyrosine 5 of HSJ1 was mutated to alanine (referred to as Y7A based on the consensus sequence), generating a mutant HSJ1 chimeric protein. The mutant protein retained the ability to reverse the thermosensitivity of *E. coli* OD259, indicating that the chimeric HSJ1-Y5A protein was able to compensate for DnaJ and stimulate the ATPase activity of DnaK. The tyrosine residue does therefore not appear to play a critical role in J domain function, further supporting the hypothesis that the tyrosine residue adopts a structural role rather than a functional role.

Neither the reduction in protein levels nor the accompanied reduction in activity would be sufficient to confer a full loss of function phenotype on HSJ1. An alternative mechanism by which the Y5C substitution may confer a loss of function phenotype is through the mis-localisation of the protein, thereby preventing the interaction of HSJ1 with its clients. In SK-N-SH cells, HSJ1a-Y5C and HSJ1b-Y5C exhibited normal staining patterns, with HSJ1a-Y5C localised to the cytoplasm and the nucleus and HSJ1b-Y5C localised to the cytoplasmic face of the ER. In human retina, endogenous HSJ1a was found to localise to the axons of ganglia cells (Chapple and Cheetham 2003). It may therefore be worthwhile to examine the axonal localisation of HSJ1a-Y5C in cells that possess neuronal processes, such as NSC34, a motor neuron cell line. A loss of axonal localisation could account for the pathogenicity of the Y5C substitution. Interestingly, a loss of axonal localisation has been identified as an

underlying mechanism of disease pathogenesis in CMT2 caused by mutations in *GARS*. GARS, an essential enzyme that charges tRNA with cognate amino acids, localises to punctate structures within axons, enabling local translation (Antonellis *et al.* 2006). Patient mutations in GARS were found to prevent the axonal localisation of the protein when expressed in the motor neuron cell line MN-1 (Antonellis *et al.* 2006, Jordanova *et al.* 2006). The mis-localisation of the protein was proposed to prevent the local translation of axonal proteins, resulting in axonal dysfunction. An inability of HSJ1a-Y5C to interact with axonal client proteins could be a potential driving force behind axonal degeneration.

Of course, it is possible that the Y5C substitution impairs an uncharacterised function of HSJ1. In Chapter 3, a potential interaction between HSJ1a and LC3 was identified. Interestingly, residue 5 of HSJ1 forms a predicted LIR sequence that may mediate the binding to LC3. The Y5C substitution was predicted to abolish the LIR, potentially preventing the interaction between the two proteins. Although the precise function of HSJ1a binding to LC3 is unknown, an inability of HSJ1a to interact with LC3 could impair the function of HSJ1. The ability of HSJ1a to co-immunopurify LC3 was therefore assessed. HSJ1a-Y5C retained the ability to co-immunopurify LC3. Similar levels of GFP-LC3 co-immunopurified in the presence of wild-type myc-HSJ1a or myc-HSJ1a-Y5C, suggesting that the substitution does not impair the interaction with LC3. Of course, the level of wild-type and mutant HSJ1 immunopurified would need to be similar in order to support this hypothesis; however, the preliminary data does suggest that residue 5 does not form a critical LIR that mediates the interaction between HSJ1a and LC3.

Overall, the findings from this Chapter suggest that the Y5C substitution reduces the half-life of HSJ1, leading to a reduction in protein levels. However, the reduction in protein levels was not sufficient in itself to characterise the Y5C substitution as a pathogenic mutation. To determine whether the heterologous expression of HSJ1-Y5C affected the protein levels observed, the levels of endogenous HSJ1-Y5C was examined in patient fibroblasts. The result of the experiment and further investigations into the pathogenicity of the Y5C substitution, using patient fibroblasts as a cell model, are presented in the following Chapter.

Chapter 5 – Investigating HSJ1-Y5C in patient fibroblasts

5.1 Introduction

In the previous Chapter, the heterologous expression of HSJ1-Y5C in SK-N-SH neuroblastoma cells demonstrated that the Y5C substitution reduces the half-life of HSJ1, leading to a reduction in protein levels. The reduction in protein levels was not sufficient to characterise the substitution as a pathogenic loss of function mutation; however, the overexpression of HSJ1-Y5C may have led to protein loss being underestimated. I therefore aimed to further investigate the potential pathogenicity of the Y5C substitution by examining the levels of endogenous HSJ1-Y5C in patient fibroblasts.

Patient fibroblasts provide an advantage over the plasmid system in that they allow mutant proteins to be examined at their endogenous expression level, thereby avoiding artificial phenotypes caused by overexpression. Patient fibroblasts are therefore widely used to investigate the pathogenicity of novel mutations. They are particularly useful for examining mutations that are associated with an autosomal recessive pattern of inheritance, which typically confer a loss of function phenotype by significantly reducing the expression level of the mutant protein.

All recessive cases of dHMN and CMT2 identified to date (caused by mutations in *IGHMBP2, TRIM2, HINT1* and *HSJ1*) are associated with a loss of protein expression. Protein loss can be driven by nonsense-mediated decay (NMD) of the mRNA or post-translational degradation of the protein, depending on the type of mutation. Patient fibroblasts have been successfully utilised to determine the extent of protein loss and the mechanism by which protein loss occurs. In the case of IGHMBP2, both mechanisms of protein loss have been reported. In one family with CMT2, a homozygous c.449+1G>T donor splice site mutation was identified (Schottmann *et al.* 2015). The loss of the donor splice site led to the activation of a downstream cryptic donor splice site at c.449+101, resulting in 100 bp of intron 3 being retained in the transcript. The retained sequence contained a premature stop codon and the transcript was predicted to undergo NMD as neither full length or truncated IGHMBP2 protein was detected in patient fibroblasts (Schottmann *et al.* 2015). In another family with CMT2, the patient was identified as a compound heterozygote, with a 5' c.138T>A mutation and a 3' frameshift in the last exon of the gene (Cottenie *et al.* 2014). Both wild-type and mutant IGHMBP2 mRNA levels were comparable in the patient fibroblasts, indicating that the transcripts were not subject to NMD. IGHMBP2 protein levels were reduced by around 70%, implying that the mutant protein was being targeted for degradation.

In the case of TRIM2, NMD and post-translational degradation were found to operate respectively on each allele of the *TRIM2* gene. The CMT2 patient was a compound heterozygote, with a c.680A>T (E227V) missense mutation and a 1 bp deletion, leading to a frameshift with the introduction of a stop codon (c.1699delA, K567RfsX7) (Ylikalio *et al.* 2013). Allele specific qPCR using cDNA from patient fibroblasts revealed that cDNA derived from the deletion allele was only 7% of total TRIM2 cDNA, suggesting degradation through NMD. The TRIM2 cDNA in the patient fibroblasts therefore originated almost completely from the c.680A>T allele. Western blot analysis revealed that the fibroblasts were almost completely devoid of TRIM2 protein, with protein levels around 10% of control cells, indicating post-translational degradation of TRIM2 E227V.

In contrast to *IGHMBP2* and *TRIM2* mutations, all mutations identified in *HINT1* to date are missense mutations that cause the post-translational degradation of the protein (Zimon *et al.* 2012). qPCR using cDNA from 8 different patient lymphoblast cell lines revealed normal HINT1 mRNA levels, however negligible HINT1 proteins levels were detected. The treatment of patient lymphoblast cells with the proteasome inhibitor MG132 resulted in the accumulation of HINT1, confirming the degradation of the protein.

With respect to the two *HSJ1* splice site mutations, protein loss is likely to be driven by NMD, due to the inclusion of a premature stop codon in the transcript. Importantly, Blumen *et al.* (2012) and Gess *et al.* (2014) confirmed the presence of both HSJ1 isoforms in fibroblasts, enabling the pathogenicity of the two splice site mutations to be investigated. The expression of HSJ1 in fibroblasts and the previous cases whereby patient fibroblasts have been successfully utilised to examine recessively inherited mutations, suggests that patient fibroblasts could serve as a useful cellular model for investigating the pathogenicity of the Y5C substitution. The stability of endogenous HSJ1-Y5C was therefore examined in patient fibroblasts and the extent of protein loss was determined. Once altered HSJ1 expression was confirmed, I utilised the fibroblasts as a cellular model to study how the loss of HSJ1 protein might cause cellular dysfunction.

5.2 Results

5.2.1 HSJ1 levels are reduced in patient fibroblasts

The level of endogenous HSJ1 was examined in control and patient fibroblasts by Western blot analysis (Figure 5.1A). In control fibroblasts, both HSJ1a and HSJ1b bands were detected, at the expected size of 36 kDa and 42 kDa, respectively. HSJ1b was expressed at a higher level than HSJ1a, as previously reported (Blumen *et al.* 2012, Gess *et al.* 2014). In contrast to the control fibroblasts, patient fibroblasts showed a 95% reduction in HSJ1b levels, with no detectable levels of HSJ1a (Figure 5.1B). A loss of HSJ1 protein was also confirmed by immunocytochemistry. Control fibroblasts showed a modest immunofluorescent staining intensity for HSJ1, whereas HSJ1 staining was barely detectable in the patient fibroblasts (Figure 5.1C).

A loss of HSJ1 protein could be mediated at the mRNA or protein level. To distinguish between these possibilities, the effect of the c.14A>G Y5C substitution on the splicing and level of the HSJ1 transcript was investigated. RNA was extracted from both control and patient fibroblasts and was reverse transcribed to cDNA. PCR of the cDNA was performed using primers in exon 1 and 4 of the HSJ1 transcript, covering the c.14A>G substitution which lies in exon 2. Both control and patient samples showed a band at the expected size of 400 bp (Figure 5.2A). No other bands were present, suggesting that the c.14A>G substitution does not lead to a mis-splicing event in exons 1-4. HSJ1 transcript levels were also compared by qPCR using control and patient cDNA. No significant difference was observed in the levels of HSJ1 transcript (Figure 5.2B); therefore the loss of HSJ1 is likely to be mediated post-translationally.

To examine if HSJ1-Y5C is degraded by autophagy or the proteasome, control and patient fibroblasts were treated for 7 hours with 200 nM bafilomycin, to inhibit autophagy, or 50 µM MG132, to inhibit the proteasome. In the control fibroblasts, both HSJ1a and HSJ1b showed no change in protein levels over the 7 hour period, establishing that both endogenous HSJ1 isoforms are stable proteins with long half-lives (Figure 5.3), as observed with the heterologous protein (Chapter 4). In the patient fibroblasts, the levels of HSJ1b-Y5C increased 3 fold in the presence of MG132. HSJ1a-Y5C was not detectable in either untreated or treated samples. The data correlates with the observations made using the HSJ1-Y5C plasmids and establishes that endogenous HSJ1-Y5C is degraded by the proteasome. The Y5C substitution therefore reduces the half-life of HSJ1 protein such that only 5% remains in patient fibroblasts.

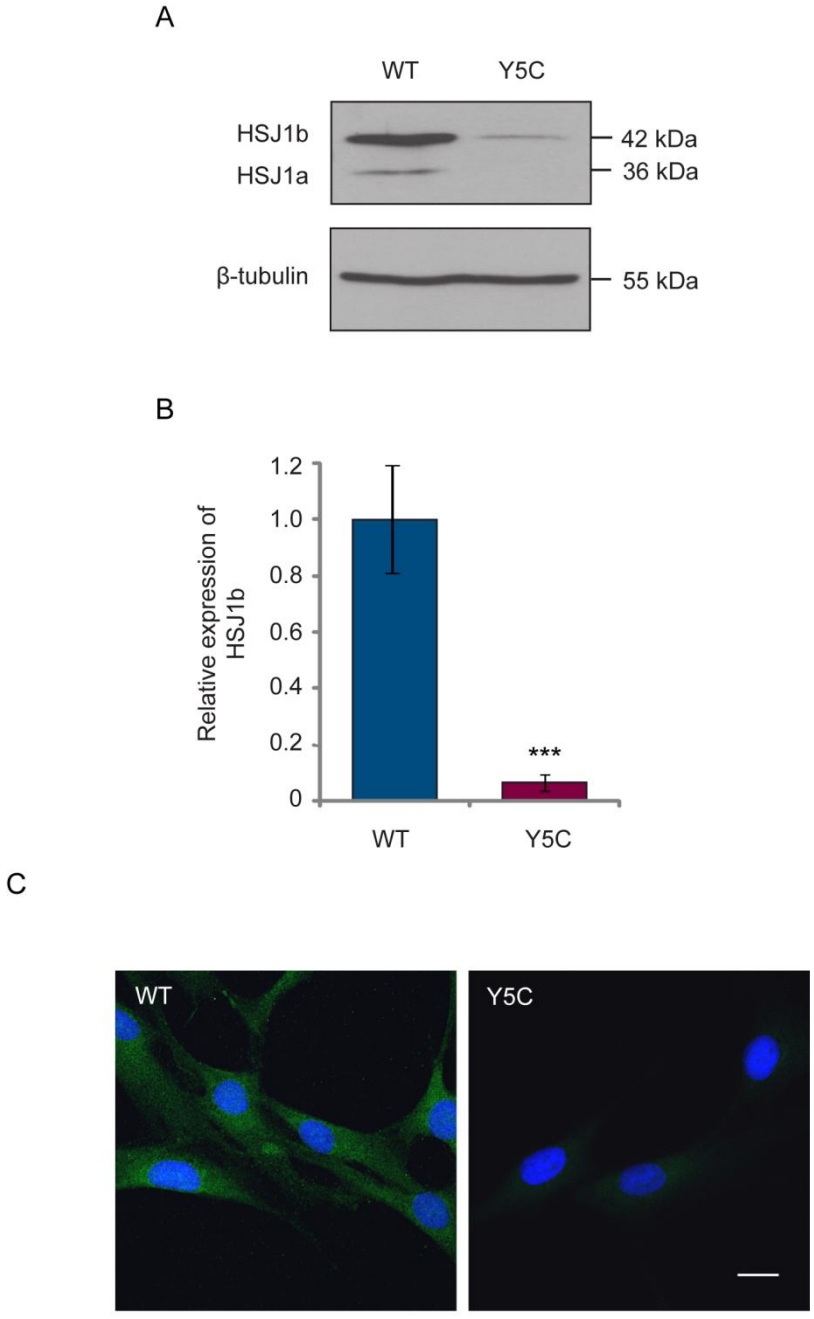

Figure 5.1 Patient fibroblasts show reduced expression of HSJ1. A: Control and patient fibroblasts were lysed and 40 µg of total protein was resolved by SDS-PAGE. Western blot analysis was performed using a polyclonal sheep HSJ1 antibody (1:1000) and a monoclonal β-tubulin antibody (1:5000). **B:** Western blots of HSJ1 and β-tubulin were analysed using ImageJ. The level of HSJ1b was corrected for loading using β-tubulin and normalised to the control sample. Error bars represent ± SD. (*** $P < 0.001$, Student's t-test, n=3). **C:** Control and patient fibroblasts were fixed in 4% PFA and permeabilised in 0.2% Triton-X. Cells were immunostained with sheep HSJ1 antibody (1:200), (Cy2 green) and DAPI. Cells were imaged using a Zeiss LSM 700 confocal microscope. Scale bar: 40 µm (n=3).

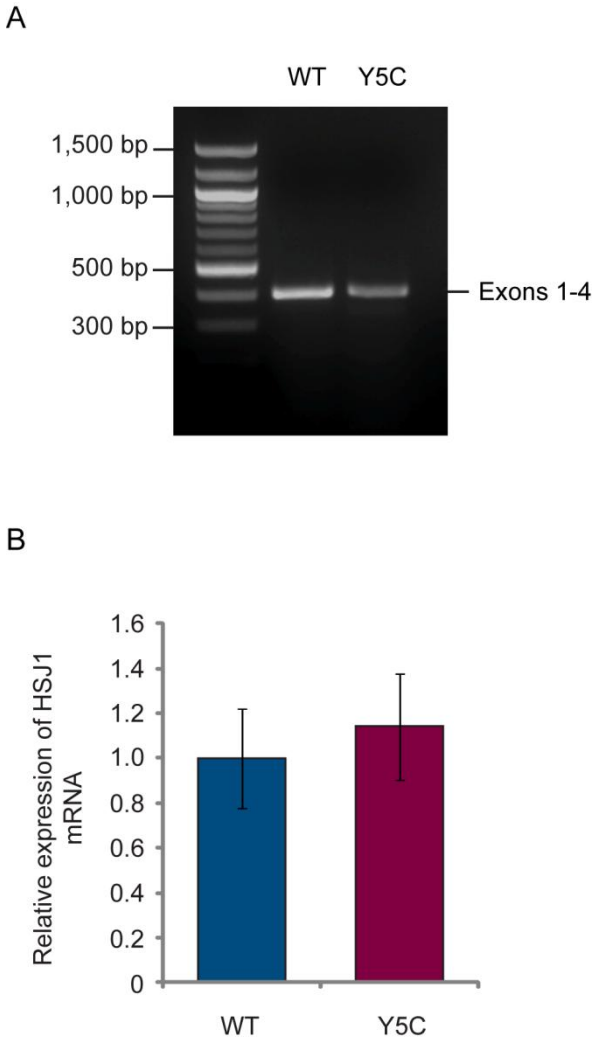

Figure 5.2 Patient fibroblasts show no defect in HSJ1 splicing and have similar levels of HSJ1 mRNA compared to control fibroblasts. A: RT-PCR of control and patient cDNA using primers in exons 1 and exons 4 of the *HSJ1* gene. Both the control and patient show a band at the expected size of 400 bp. **B:** qPCR of control and patient cDNA using primers in exon 5 of the *HSJ1* gene. The ribosomal housekeeping gene *RPL19* was used as an internal reference. Error bars represent ± SD (N.S Student's t-test, n=3).

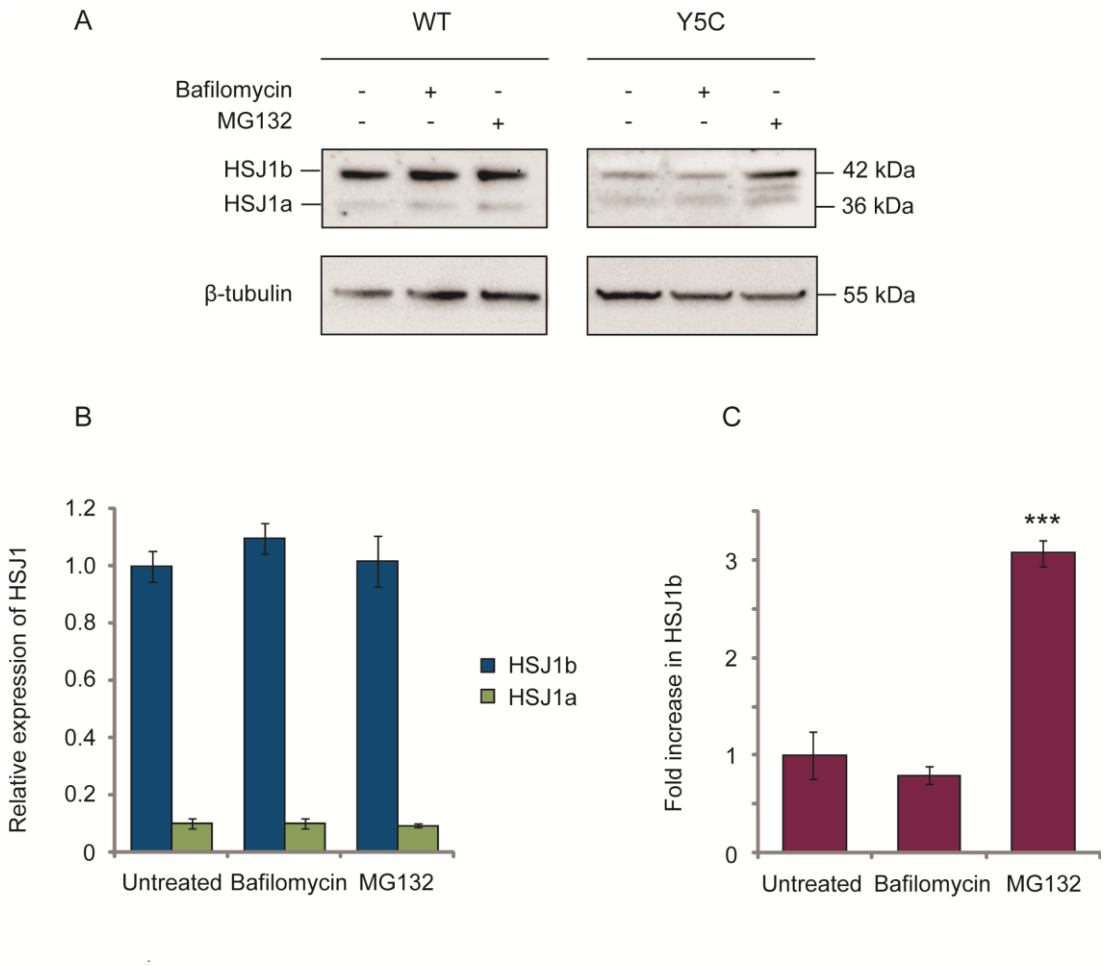

Figure 5.3 HSJ1-Y5C is degraded via the proteasome. A: Control and patient fibroblasts were untreated or treated for 7 hours with 200 nM bafilomycin or 50 µM MG132. Cells were then harvested and 40 µg of total protein was resolved by SDS-PAGE. Western blot analysis was performed using a polyclonal sheep HSJ1 antibody (1:1000) and a monoclonal β-tubulin antibody (1:5000). **B:** Western blots were analysed by ImageJ. The level of HSJ1a and HSJ1b in the control fibroblasts was corrected for loading and normalised to the untreated HSJ1b sample. Error bars represent ± SD (N.S, Student's t-test, n=3) **C:** The level of HSJ1b-Y5C in the patient fibroblasts was corrected for loading and normalised to the untreated HSJ1b-Y5C sample. Error bars represent ± SD (*** $P < 0.001$, Student's t-test, n=3).

5.2.2 Investigating the effect of the loss of HSJ1 on proteostasis in patient fibroblasts

Having established the Y5C substitution as a pathogenic loss of function mutation, I next sought to investigate whether the loss of HSJ1 affected the cellular function of the fibroblasts. I initially examined whether the loss of HSJ1 had any effect on proteostasis. Impaired proteostasis typically leads to the accumulation of misfolded proteins. These proteins are often ubiquitylated; therefore the levels of ubiquitylated protein can be used as a measure of the amount of misfolded protein present in the fibroblasts. Control and patient fibroblasts were either untreated or treated for 4 hours with the proteasome inhibitor MG132. Cell lysates were then analysed by Western blot and probed for polyubiquitin (Figure 5.4A). In the untreated control fibroblasts, a smear of high molecular weight ubiquitin immunoreactive species was observed, ranging in size from 60 kDa to 250 kDa. In the presence of MG132, the relative expression of ubiquitylated protein increased 2.7 fold (Figure 5.4B). There was no significant difference in the levels of ubiquitylated proteins in the untreated patient fibroblast sample. However, in the presence of MG132, the patient fibroblasts only displayed a 1.8 fold increase in ubiquitylated protein levels compared to the 2.7 fold increase observed for the control fibroblasts.

The activity of the proteasome contributes to the levels of ubiquitylated protein present in the cell; therefore the proteasome activity of control and patient fibroblasts was examined. Proteasome activity was assessed using an AMC tagged peptide substrate. Upon cleavage by the chymotrypsin-like activity of the proteasome, free AMC fluoresces, providing a direct measure of activity. Control and patient fibroblast lysates were incubated for 1 hour with the fluorogenic substrate. Fluorescent intensity was measured using a spectrofluorometer and the results were normalised to the control fibroblasts (Figure 5.5). The patient fibroblasts showed a significant 50% lower proteasome activity compared to control fibroblasts. The lower proteasome activity is likely to account for the smaller increase observed in ubiquitylation levels in patient fibroblasts in the presence of MG132.

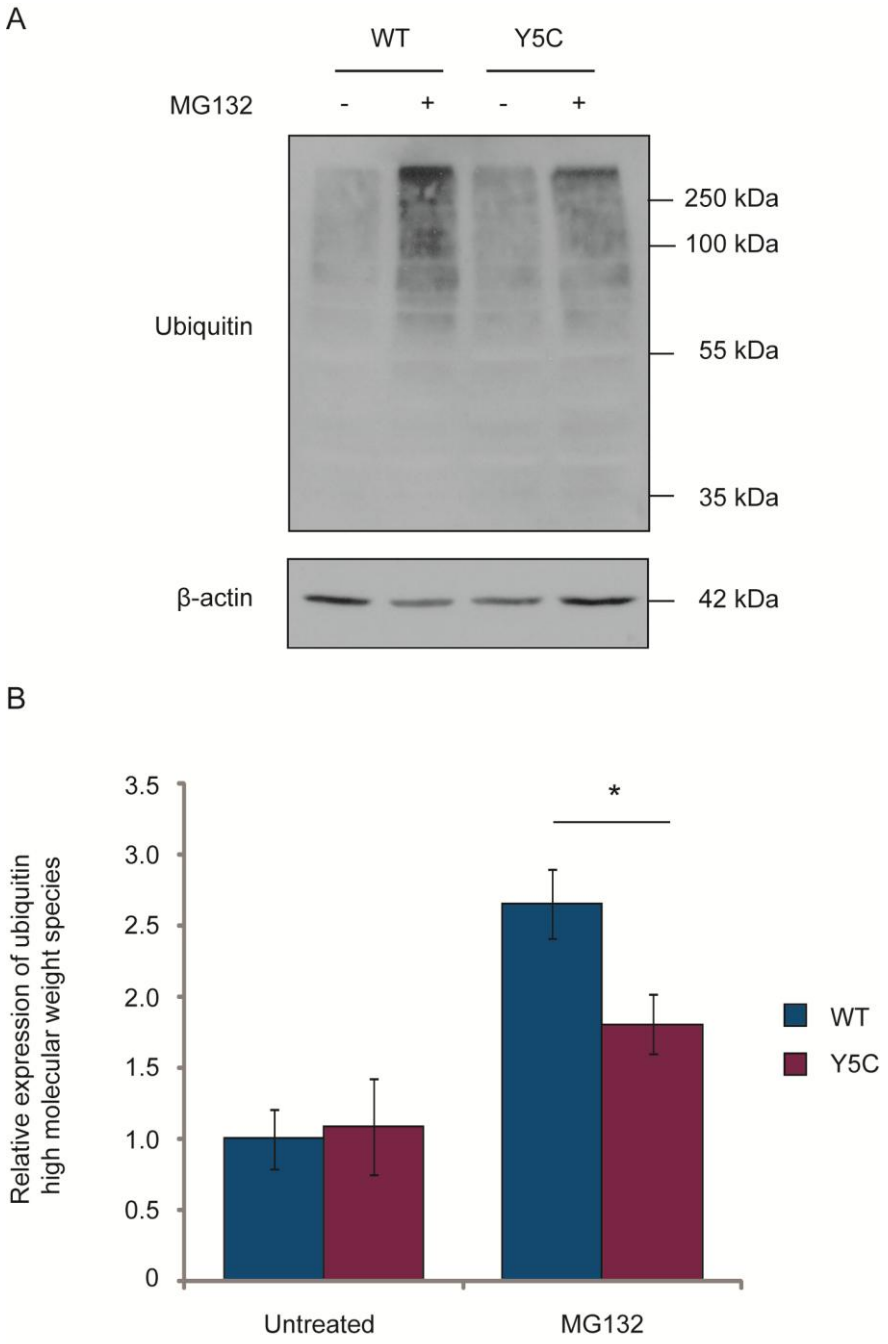

Figure 5.4 A comparison of the levels of ubiquitylated protein in control and patient fibroblasts. A: Control and patient fibroblasts were untreated or treated for 4 hours with 50 µM MG132. Cells were then harvested and 30 µg of total protein was resolved by SDS-PAGE. Membranes were boiled for 30 minutes after transfer then probed using a polyclonal rabbit ubiquitin antibody (1:1000) and a monoclonal β-tubulin antibody (1:5000). **B:** Blots were analysed using ImageJ. The level of ubiquitin species was corrected for loading using β-tubulin and normalised to the untreated control sample. Error bars represent ± SD. (* $P < 0.05$, Student's t-test, n=3).

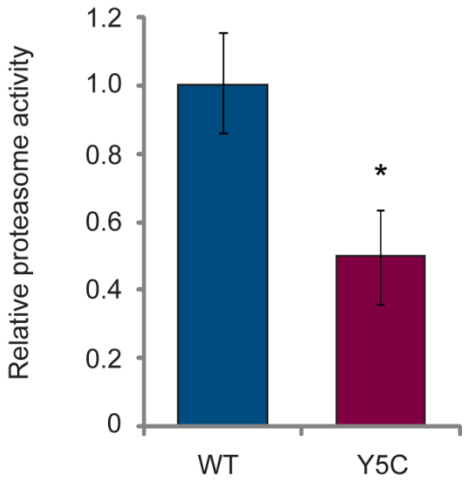

Figure 5.5 Patient fibroblasts have a lower proteasome activity compared to control fibroblasts. 20 µg of cell lysate from control and patient fibroblasts was incubated for 1 hour at 37 °C with 10 µM of the fluorogenic substrate AMC-LLVY. Fluorescence was then measured using a spectrofluorometer using an excitation of 380 nm and emission at 460 nm. Background readings were subtracted and the results were normalised to the activity of the control fibroblasts. Error bars represent ± SD. (* $P < 0.05$, Student's t-test, n=3).

5.2.3 Optimising the knockdown of HSJ1 in control fibroblasts

To establish if the reduced proteasome activity was due to the loss of HSJ1, I aimed to knockdown HSJ1 expression in the control fibroblasts to test if this could replicate the phenotype of the patient fibroblasts. To knockdown HSJ1, an adeno-associated virus (AAV) containing shRNA against HSJ1 was utilised (provided by Professor James Uney, University of Bristol). To determine the amount of virus particles required to sufficiently knockdown HSJ1, increasing amounts of virus particles per cell (the multiplicity of infection, MOI) were added to the control fibroblasts. 48 hours post infection, cells were harvested, lysed and proteins resolved by SDS-PAGE. The levels of HSJ1 were then determined by Western blot analysis, with protein levels normalised to the untreated sample (Figure 5.6A). MOIs of 5 and 10 had no significant effect on the levels of HSJ1b. An MOI of 20 lead to a 21% reduction in HSJ1b levels, with an MOI of 50 resulting in a 43% reduction in protein levels (Figure 5.6B). Increasing the MOI further to 75 or 100 had no effect on HSJ1b levels. Endogenous HSJ1 levels were established to be stable over a 7 hour period, as demonstrated in Figure 5.3. HSJ1 exhibits a long half-life; therefore the cells may require a longer incubation time to turnover HSJ1 and increase the level of knockdown. The two most effective MOIs, 20 and 50, were used to infect control fibroblasts and this time the incubation period was increased from 48 to 72 hours. HSJ1 levels were then determined by Western blot analysis (Figure 5.6C). The levels of HSJ1b correlated with the levels observed after a 48 hour incubation. The MOI of 20 and 50 reduced HSJ1b levels by 11% and 48%, respectively (Figure 5.6D). Therefore, increasing the incubation period did not improve on the level of HSJ1 knockdown.

5.2.4 Optimising the restoration of HSJ1 in patient fibroblasts

The knockdown of HSJ1 in control fibroblasts was not sufficient to effectively model the effect of the Y5C mutation (43% vs 95%); therefore an alternative approach to confirming whether proteasome activity is affected by the loss of HSJ1 was adopted. Proteasome activity would be analysed upon restoration of HSJ1 levels in the patient fibroblasts. To restore HSJ1 to its endogenous level, AAV expressing either HSJ1a or HSJ1b were utilised (provided by Professor James Uney, University of Bristol). Patient fibroblasts were infected with either the HSJ1a or HSJ1b virus at MOIs of 2, 5, 10 and 20. 48 hours after transduction, HSJ1 protein levels were determined by Western blot analysis and the level of HSJ1 protein was compared to the control fibroblasts. All four MOIs used for the HSJ1a virus resulted in high expression levels of HSJ1a, with the levels of HSJ1a increasing with an increasing MOI (Figure 5.7A). An MOI lower than 2 was therefore required to reach the levels of HSJ1a observed in the control fibroblasts. Patient fibroblasts were therefore infected with HSJ1a

virus at the lower MOIs of 1, 0.8, 0.6, 0.4 or 0.2. 48 hours post infection, HSJ1a levels were analysed by Western blot (Figure 5.7B). An MOI of 0.4 appeared to generate comparable HSJ1a levels with the control fibroblasts. For HSJ1b, an MOI of 5 appeared to correspond with the levels of endogenous HSJ1b in the control fibroblasts.

Although the required MOIs to match endogenous level had been determined, it was important to establish the transduction efficiencies at these MOIs to ascertain whether all cells were expressing similar levels of HSJ1. Patient fibroblasts transduced with HSJ1a at MOIs of 1, 0.8, 0.6, 0.4 and 0.2, or HSJ1b at MOIs of 20, 10, 5 and 2, were fixed in 4% PFA 48 hours post infection. Cells were stained for HSJ1 and DAPI and the number of transduced cells was calculated and expressed as a percentage of the total number of cells (Figure 5.7C). The transduction efficiency for HSJ1b was above 80% for all four MOIs. In contrast, the transduction efficiency for HSJ1a dropped with decreasing MOI. An MOI of 1, 0.8 and 0.6 displayed transduction efficiencies of 87%, 89% and 82% respectively. An MOI of 0.4 reduced the transduction efficiency to 51%, with an MOI of 0.2 reducing transduction efficiency even further, to 26%. Taking into account expression levels and transduction efficiency an MOI of 0.6 for HSJ1a and 5 for HSJ1b would be used in further experiments as this represented the best compromise for matching the level of HSJ1 in the majority of cells (Figure 5.8).

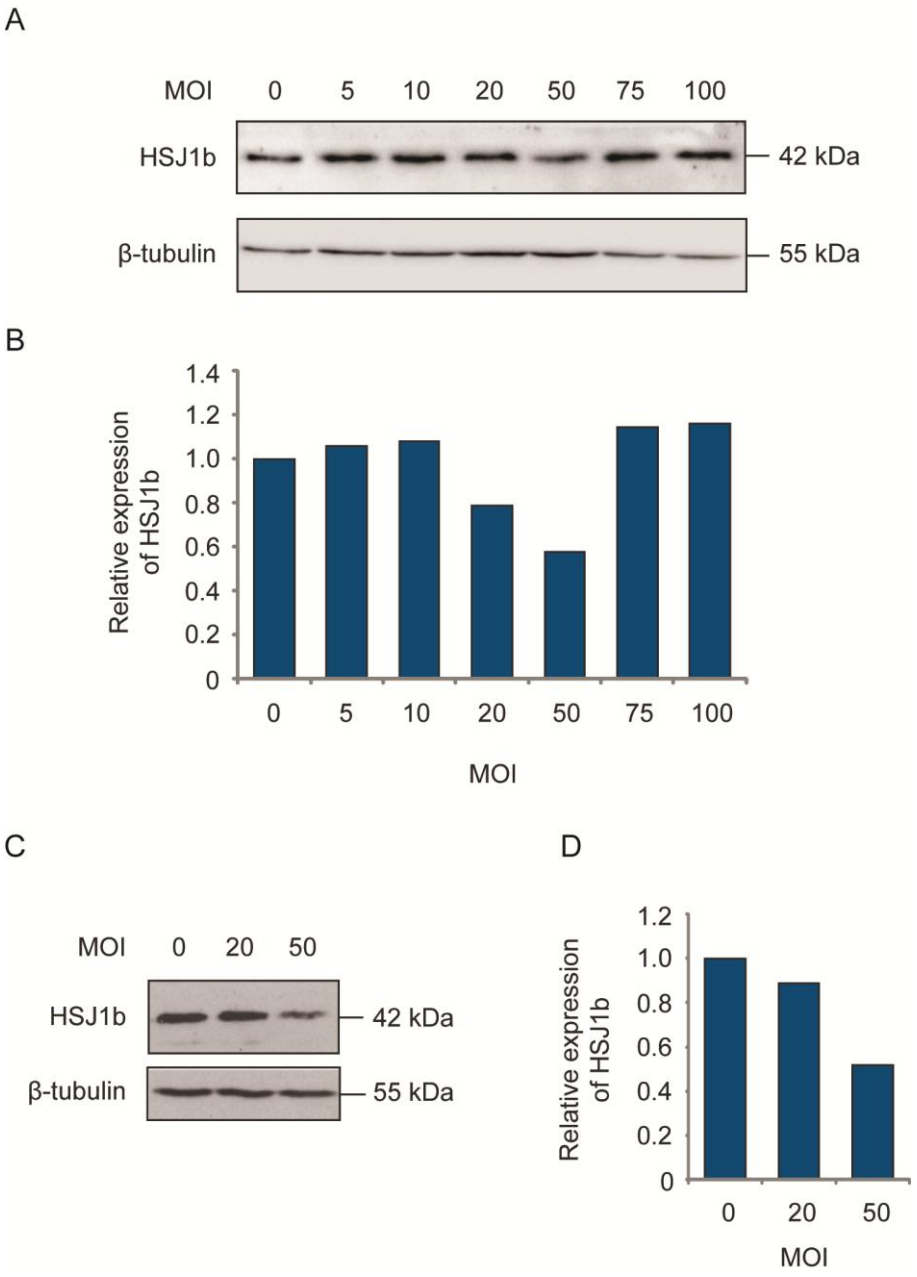

Figure 5.6 Optimising the knockdown of HSJ1 in control fibroblasts. A: Control fibroblasts were infected with an AAV containing shRNA against HSJ1 at increasing MOIs of 5, 10, 20, 50, 75 and 100. 48 hours post infection, 30 µg of total cell lysates were resolved by SDS-PAGE. Western blot analysis was performed using a polyclonal sheep HSJ1 antibody (1:1000) and a monoclonal β-tubulin antibody (1:5000). **B:** Western blots were analysed using ImageJ. The level of HSJ1b was corrected for loading using β-tubulin and normalised to the untreated sample. The graph shows an n of 1. **C:** Control fibroblasts were infected with the virus at an MOI of 20 or 50 and incubated for 72 hours. 30 µg of total cell lysates were then resolved by SDS-PAGE and analysed by Western blot and as described above. **D:** Graph shows normalised HSJ1b levels (n=1).

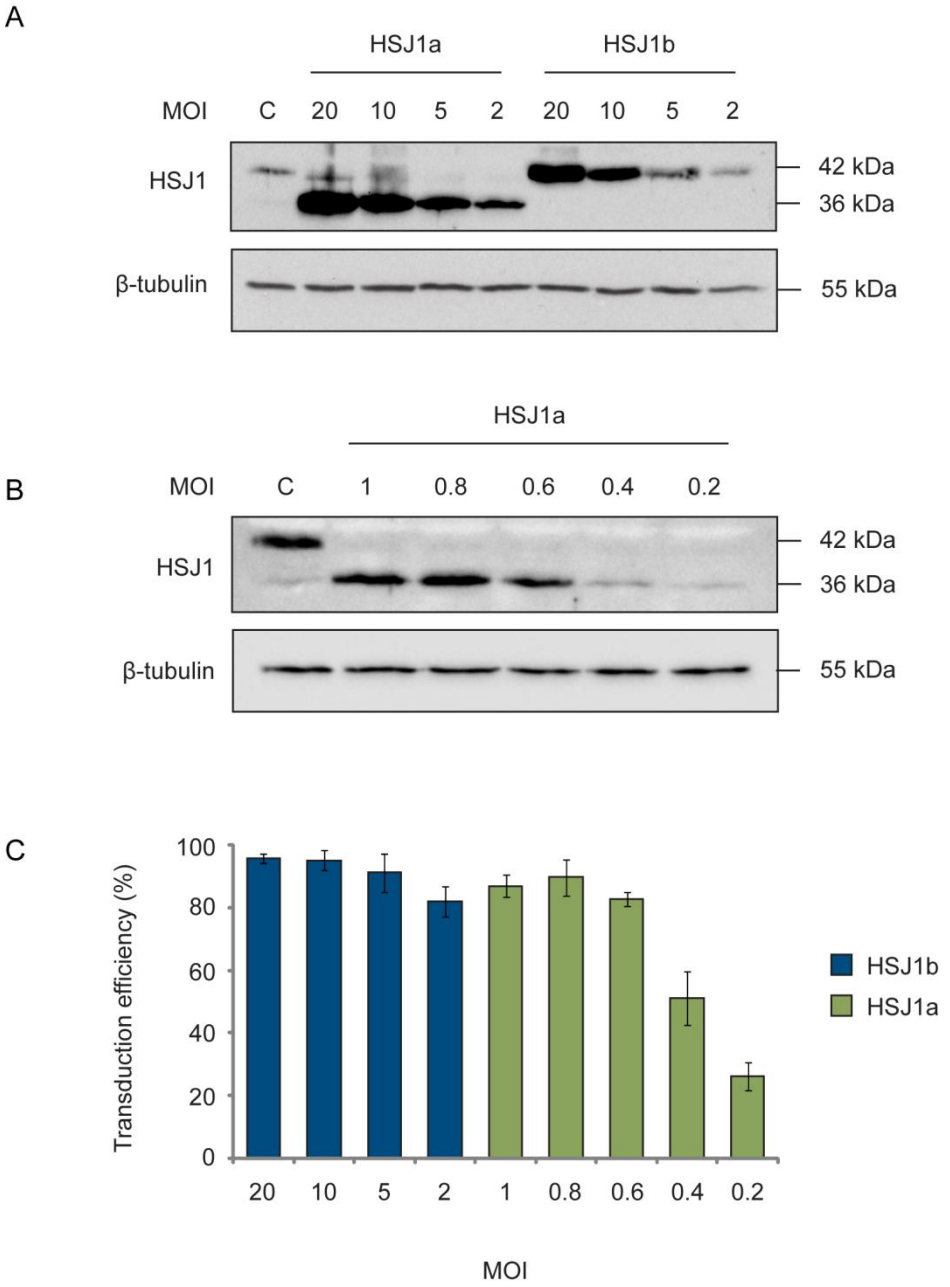

Figure 5.7 Optimising the rescue of HSJ1 levels in patient fibroblasts. A: Patient fibroblasts were infected with a virus containing either HSJ1a or HSJ1b at MOIs of 2, 5, 10 and 20. 48 hours post infection, 40 µg of total cell lysate was resolved by SDS-PAGE along with 40 µg of total cell lysate from untreated control fibroblasts (C). Membranes were probed for HSJ1 (1:1000) and β-tubulin (1:5000). **B:** Patient fibroblasts were infected with the HSJ1a virus at MOIs of 0.2, 0.4, 0.6, 0.8 and 1. 48 hours post infection, 40 µg of total cell lysate was resolved by SDS-PAGE along with 40 µg of total cell lysate from untreated control fibroblasts (C). Membranes were probed for HSJ1 (1:1000) and β-tubulin (1:5000). **C:** Patient fibroblasts were infected with the HSJ1b virus at MOIs of 20, 10, 5 and 2, or the HSJ1a virus at MOIs of 1, 0.8, 0.6, 0.4 and 0.2. 48 hours post transduction, cells were fixed in 4% PFA and stained for HSJ1 and DAPI. Transduction efficiency was calculated by counting the number of total cells and the number of transduced cells. The graph shows transduction efficiency ± SD (n=3).

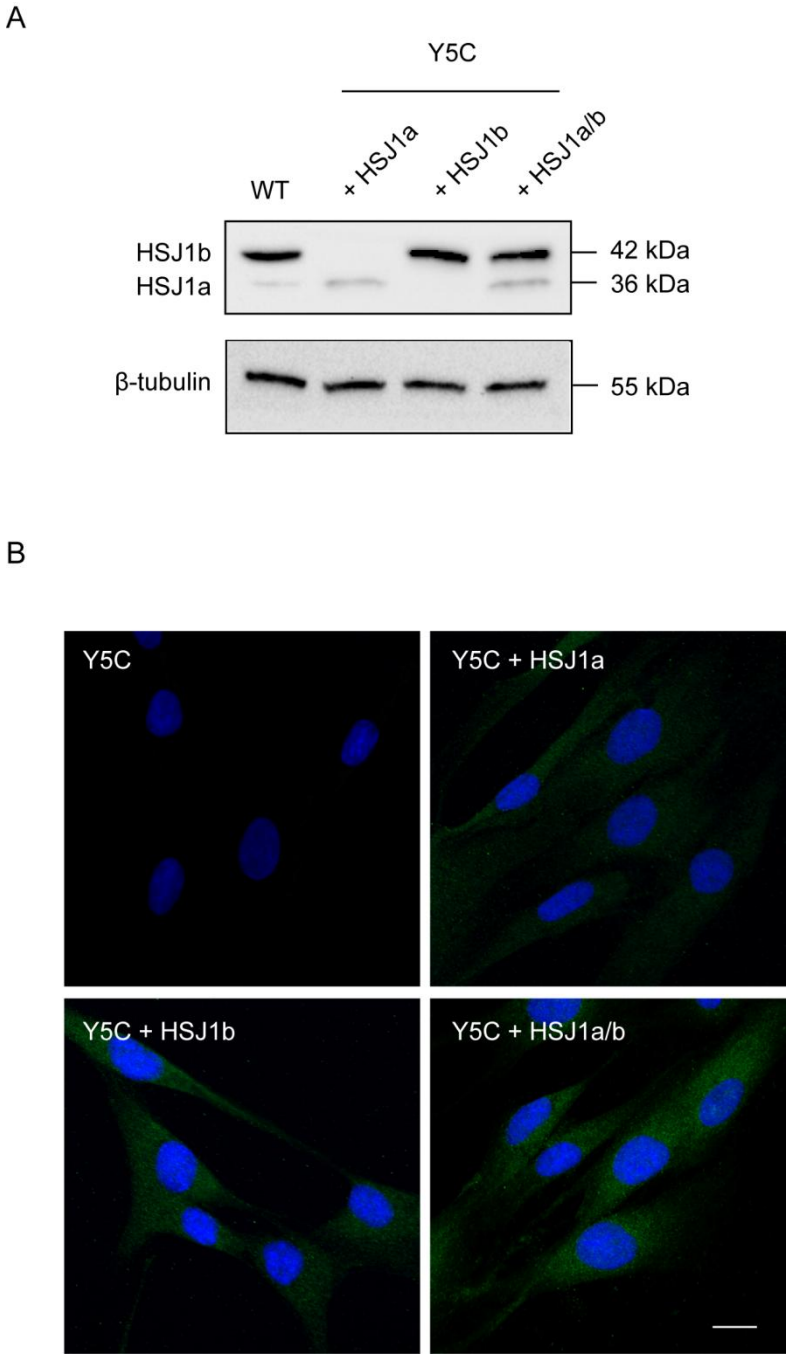

Figure 5.8 Optimised restoration of endogenous levels of HSJ1 in patient fibroblasts. **A:** Patient fibroblasts were infected with HSJ1a virus at an MOI of 0.6, or HSJ1b virus at an MOI of 5. One sample was infected with both viruses. 48 hours post transfection, 40 µg of cell lysate was resolved by SDS-PAGE, alongside 40 µg of cell lysate from untreated control fibroblasts. Western blots were probed using a polyclonal sheep HSJ1 antibody (1:1000) and a monoclonal mouse β-tubulin antibody (1:5000). **B:** Patient fibroblasts were untreated or infected with HSJ1a virus at an MOI of 0.6, or HSJ1b virus at an MOI of 5. One sample was infected with both viruses. 48 hours post infection, cells were fixed in 4% PFA and stained for HSJ1 (1:200) (Cy2 green) and DAPI (blue). Representative images were captured on a Zeiss LSM 700 confocal microscope. Scale bar: 40 µm (n=3).

5.2.5 The lower proteasome activity observed in patient fibroblasts is independent of the loss of HSJ1

To determine if the reduction in proteasome activity was due to a loss of HSJ1, the effect of restoring HSJ1 on proteasome activity was assessed. Patient fibroblasts were either untransduced, or transduced with HSJ1a, HSJ1b or both isoforms. 48 hours post transduction, cells were harvested and cell lysates were incubated for 1 hour with the flurogenic substrate AMC-LLVY. Fluorescent intensity was measured using a spectrofluorometer and the results were normalised to the untransduced patient fibroblast sample. The patient fibroblasts transduced with HSJ1 showed no significant difference in proteasome activity compared to the untransduced patient fibroblasts (Figure 5.9). Therefore, the loss of HSJ1 does not appear to account for the lower proteasome activity in the patient fibroblasts compared to the control fibroblasts.

The difference in proteasome activity between the two fibroblast lines makes it difficult to meaningfully compare the levels of ubiquitylated protein. Therefore in this instance, the effect of the loss of HSJ1 on ubiquitylated protein levels cannot be simply determined by a comparison with the control fibroblasts. Instead, the effect of restoring HSJ1 on ubiquitylated protein levels was examined. Patient fibroblasts were untransduced or transduced with HSJ1a, HSJ1b or both. 48 hours post transfection, cells were harvested and protein lysates were analysed by Western blot. Restoring HSJ1a had no significant effect on the levels of ubiquitylated protein (Figure 5.10). However, restoring HSJ1b resulted in a significant 1.9 fold increase in protein ubiquitylation. A 1.5 fold increase in protein ubiquitylation was observed in the presence of both isoforms, although this increase did not reach significance.

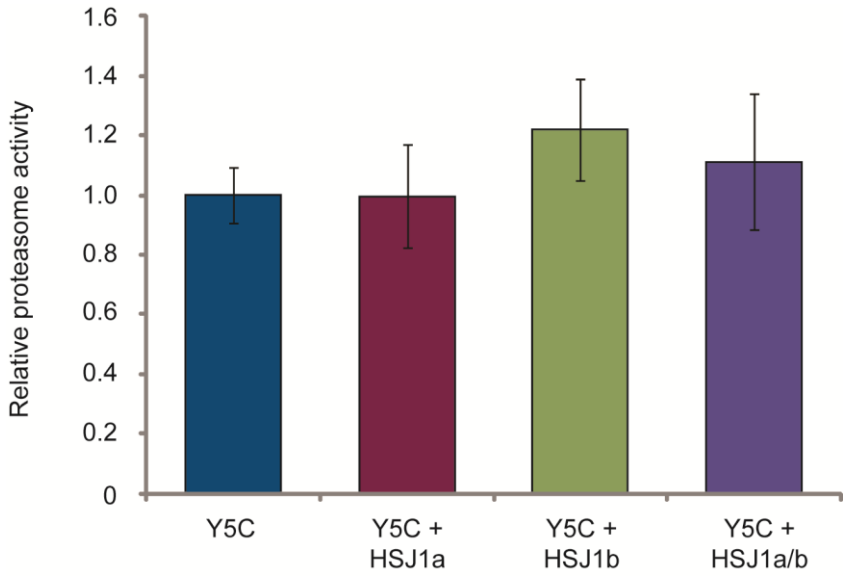

Figure 5.9 The restoration of HSJ1 in patient fibroblasts has no effect on proteasome activity. Patient fibroblasts were untransduced or transduced with the HSJ1a virus, HSJ1b virus or both. 48 hours post infection, 20 µg of cell lysate was incubated for 1 hour at 37 °C with 10 µM of the fluorogenic substrate AMC-LLVY. Fluorescence was then measured using a spectrofluorometer using an excitation of 380 nm and emission at 460 nm. Background readings were subtracted and the results were normalised to the activity of the untreated patient fibroblasts. Error bars represent ± SD (N.S, one-way ANOVA, n=3).

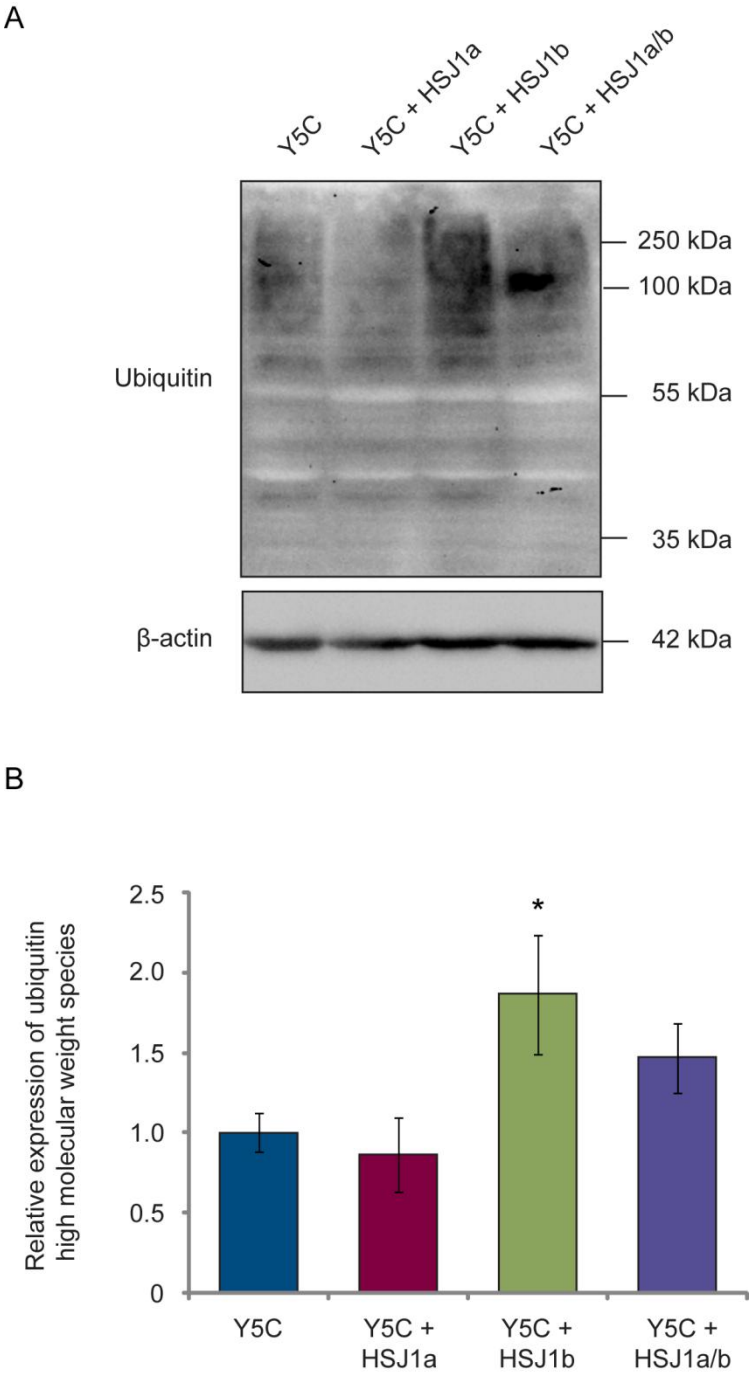

Figure 5.10 The restoration of HSJ1b in patient fibroblasts increases the level of ubiquitylated protein. A: Patient fibroblasts were untransduced or transduced with the HSJ1a or HSJ1b virus or both. 48 hours post infection, cells were harvested and 40 µg of total protein was resolved by SDS-PAGE. Membranes were boiled for 30 minutes after transfer then probed using a polyclonal rabbit ubiquitin antibody (1:1000) and a monoclonal β-tubulin antibody (1:5000). **B:** Blots were analysed by ImageJ. The level of ubiquitin species was corrected for β-tubulin and normalised to the untreated patient sample. Error bars represent ± SD. (* $P < 0.05$, one-way ANOVA with post hoc Tukey test, n=3).

5.2.6 The loss of HSJ1 does not activate the UPR in patient fibroblasts

The impairment of ERAD has been established to cause ER stress, resulting in the activation of the UPR. I aimed to examine the levels of UPR markers in control and patient fibroblasts in order to determine whether the loss of HSJ1b has any effect on the ERAD process. Cell lysates from control and patient fibroblasts were resolved by SDS-PAGE. Western blot analysis was performed using markers from all three branches of the UPR. The expression levels of IRE1, ATF6 and BiP were used to examine the IRE1 and ATF6 branches. Phosphorylated eIF2α and total eIF2α levels were used to examine the activation of the PERK branch. The control and patient fibroblasts showed no significant difference in the expression of UPR markers across all three branches (Figure 5.11). The UPR does therefore not appear to be activated in the HSJ1-Y5C patient fibroblasts.

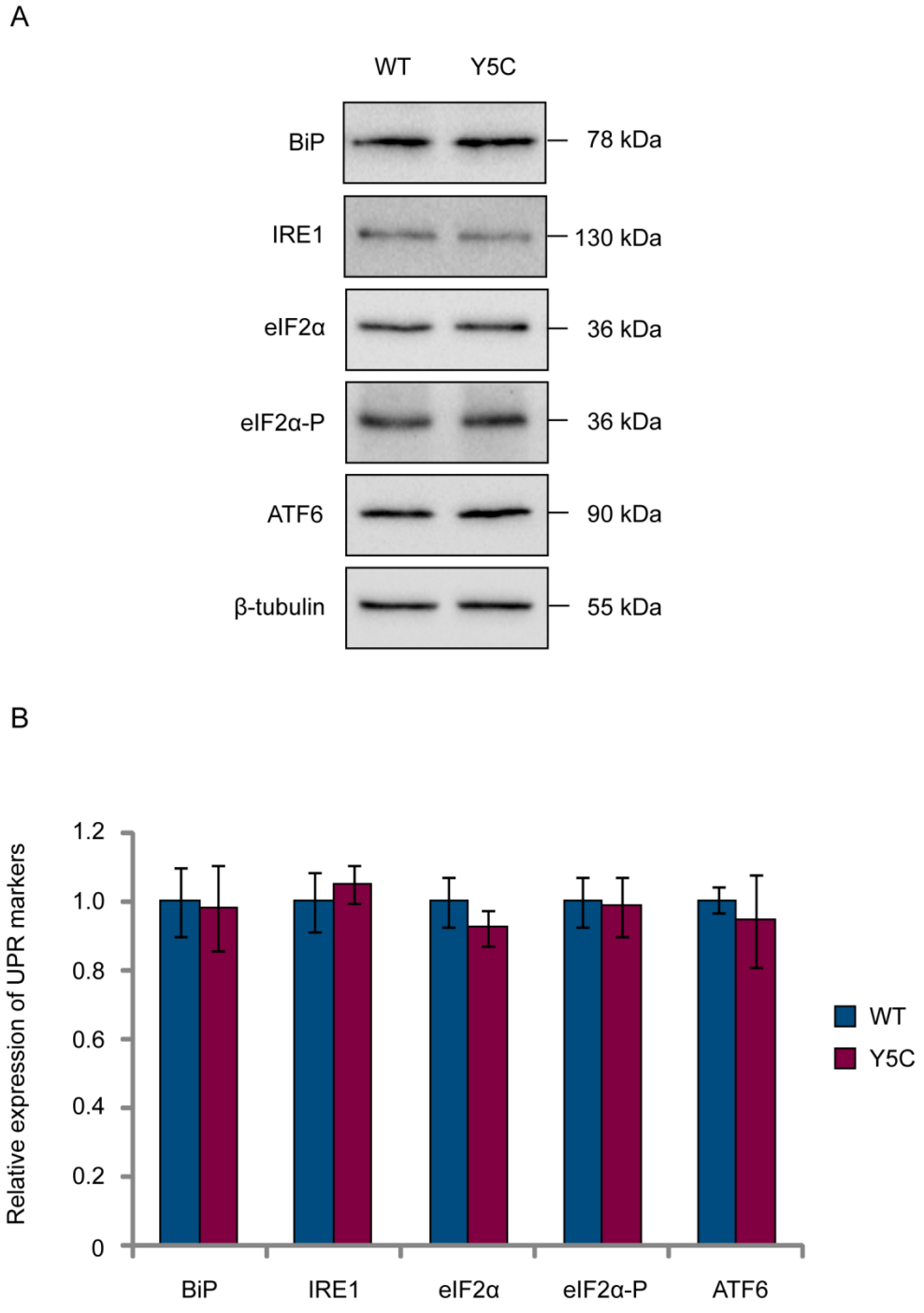

Figure 5.11 Control and patient fibroblasts show no difference in the expression levels of UPR markers. A: 30 µg of total cell lysate from control and patient fibroblasts was resolved by SDS-PAGE. Western blot analysis was performed using BiP, IRE1, eIF2α, eIF2α-P and ATF6 antibodies. All were polyclonal rabbit antibodies and used at a dilution of 1:1000. Mouse monoclonal β-tubulin was used as a loading control (1:5000). **B:** Western blots were analysed by ImageJ. The level of UPR marker was corrected for β-tubulin and normalised to the control fibroblasts. Error bars represent ± SD (N.S Student's t-test, n=4).

5.3 Discussion

The characterisation of heterologous HSJ1-Y5C expression described in Chapter 4 suggested that the Y5C substitution reduces the half-life of HSJ1, leading to a reduction in protein levels. The reduction in protein levels was less than 50%, therefore the Y5C substitution could not be characterised as a disease-causing mutation based on the plasmid data alone. I aimed to further investigate the potential pathogenicity of the Y5C substitution by examining the levels of endogenous HSJ1 in fibroblasts from one of the affected siblings. When compared to healthy control fibroblasts, patient fibroblasts showed a 95% reduction in HSJ1b levels, with no detectable HSJ1a. The reduction in HSJ1 was mediated by the proteasomal degradation of the protein, implying that the Y5C substitution reduces the half-life of HSJ1. This finding is consistent with the observations made in the previous chapter. Although both cell models identify the same mechanism underlying the reduction in protein levels, there is a disparity in the extent of the reduction. This disparity is likely due to differences in the rate of transcription. The overexpression of HSJ1-Y5C in SK-N-SH cells likely far exceeds the rate at which the protein can be degraded. The imbalance between protein synthesis and degradation is likely to cause HSJ1-Y5C to accumulate; the system would thereby underestimate the extent by which the Y5C substitution reduces the half-life of HSJ1.

Utilising the patient fibroblasts as a cellular model suggests that the Y5C substitution is indeed a disease-causing loss of function mutation. However, considering that only one control line and one patient line were used in this study, the results can only strongly support, not confirm, the pathogenicity of the Y5C substitution. It will be important to examine HSJ1 levels in multiple control lines and in patient fibroblasts from the second sibling, in order to confirm that the loss of HSJ1 is a valid phenotype of the Y5C substitution. Having supported the pathogenicity of the Y5C substitution, the three mutations identified in *HSJ1* to date can now be compared. It is interesting to note that the splice site mutations cause dHMN, whereas the missense mutation causes CMT2 (Blumen *et al.* 2012, Gess *et al.* 2014). It may be speculated that the difference in mutation accounts for the different clinical phenotypes, however; considering the small sample size this speculation may be somewhat premature. Also, in the case of HSPB1, HSPB8 and BSCL2, missense mutations have been identified to cause both dHMN and CMT2 (Irobi *et al.* 2004, Houlden *et al.* 2008, Ikeda *et al.* 2009, Evgrafov *et al.* 2012, Jerath *et al.* 2015). The identification of more mutations in *HSJ1* will clarify whether there is indeed any link between the type of mutation and the clinical presentation of the disease.

It is interesting to compare the extent of HSJ1 protein loss in the three fibroblast cell lines. The low expression of HSJ1a in fibroblasts resulted in HSJ1a levels being below the limits of detection in all three patient fibroblasts lines, therefore any difference in the remaining HSJ1a levels cannot be ascertained. However, the remaining levels of HSJ1b can be compared, with reported HSJ1b levels varying between patient mutations. The c.229+1G>A splice site mutation resulted in no detectable levels of HSJ1b (Gess *et al.* 2014), whereas the c.352+1G>A splice site mutation lead to a partial loss of HSJ1b, although this reduction was not quantified (Blumen *et al.* 2012). The Y5C mutation resulted in a 95% reduction in HSJ1b levels. The extent of HSJ1 protein loss did not appear to affect the disease phenotype at the time of examination; patients from all three families presented with similar clinical features and ages of disease onset (Table 4.1). However, an important caveat that needs to be considered when comparing the levels of remaining HSJ1 protein is that different antibodies were used to detect HSJ1. The commercial antibody used by Blumen *et al.* and Gess *et al.* generated a signal in *Hsj1*$^{-/-}$ spinal cords, suggesting that the antibody may detect another protein in addition to HSJ1 (Dr Sergey Novoselov, personal communications). It would therefore be interesting to examine the levels of HSJ1 in the two other patient fibroblast lines using the HSJ1 S653 antibody used in this study. If differences in the remaining HSJ1 protein levels were detected between the three patient fibroblast lines, it would be interesting to investigate whether the different levels of remaining HSJ1 protein had any effect on the progression of the disease or indeed the severity of the disease. Detailed clinical follow up examinations of patients from all three families could provide important insights into the pathological consequences of varying HSJ1 levels.

All three mutations are loss of function mutations; therefore HSJ1 function is clearly important for motor neuron survival. I aimed to investigate how the loss of HSJ1 leads to degeneration using the Y5C patient fibroblasts as a cellular model. I initially examined if the loss of HSJ1 chaperone activity had any effect on proteostasis by examining the levels of ubiquitylated protein. Control and patient fibroblasts exhibited similar levels of ubiquitylated protein under basal conditions. However, in the presence of MG132, patient fibroblasts showed a smaller accumulation of ubiquitylated protein. Proteasome activity was markedly reduced in patient fibroblasts, likely accounting for the lower accumulation of ubiquitylated protein upon proteasome inhibition. Unfortunately, the difference in proteasome activity in control and patient fibroblasts makes it difficult to compare the levels of ubiquitylated protein under basal conditions. The restoration of HSJ1 levels in the patient fibroblasts did not rescue proteasome activity, suggesting that the lower proteasome activity was independent of the loss of HSJ1. The activity of the proteasome is affected by aging. The comparison of fibroblasts from healthy individuals ranging in age from 20-82 years old

revealed a significant decrease in proteasome activity up to 50 years of age (Hwang *et al.* 2007). The reduction in proteasome activity correlated with a decrease in the expression of proteasome subunits. The control fibroblasts were from an adult donor of unknown age, whereas the patient fibroblasts were from a 38 year old. A difference in age could therefore potentially account for the lower activity observed in the patient fibroblasts. Further investigations into how the loss of HSJ1 affects proteostasis in patient fibroblasts may therefore require the use of age-matched controls, in order to control for variability in proteasome activity.

Factors such as age and gender could result in control and patient fibroblasts having substantially different phenotypes in addition to different genetic backgrounds. Such differences are likely to cause confounding effects and may lead to misleading phenotypic differences that are not associated with the disease-causing mutation. In order to avoid such confounding effects the generation of isogenic controls should be considered. Any observed phenotypic differences between the control and patient lines could then be fully attributed to the mutation. The generation of isogenic controls would require the correction of the c.14A>G substitution in patient fibroblasts. This could be achieved by targeted genome editing, a process that relies on the introduction of double-strand breaks at specific genomic loci and subsequent correction of the sequence. Double-strand breaks are generated using engineered nucleases such as zinc-finger nucleases (ZFN) and transcription activator-like effector nucleases (TALENs) (Bibikova *et al.* 2003, Christian *et al.* 2010). Both ZFN and TALENs consist of a DNA binding domain and a nuclease domain. The DNA binding domain can be designed specifically to bind to the required genomic sequence, targeting the action of the nuclease to the required location. ZFN and TALENs are usually delivered in AAVs along with single-strand DNA oligonucleotides that act as the correction template. Recently, clustered, regularly interspaced, short palindromic repeat system (CRISPR) technology has proved to be an easy and simple alternative to the use of ZFN and TALENs (Mali *et al.* 2013, Kim *et al.* 2014). Cells are transfected with vectors that encode the components required for CRISPR gene editing. The two components are Cas9, which cuts the DNA, and guide RNA, that directs Cas9 to the specific location where the break is to be made. Endogenous repair mechanisms then correct the sequence. The correction of the c.14A>G patient mutation using CRISPR technology would provide the most appropriate control to use in future investigations.

The restoration of HSJ1b in patient fibroblasts led to an increase in ubiquitylated protein. This result was somewhat expected, considering that the overexpression of HSJ1 has been previously shown to increase ubiquitylated protein levels (Westhoff *et al.* 2005, Howarth *et al.* 2007). Considering the role of HSJ1b in ERAD, two explanations for a possible reduction

in protein ubiquitylation in the absence of the protein may be hypothesised. Firstly, the loss of HSJ1b may favour the deubiquitylation of ERAD substrates by deubiquitinases (DUBs). Secondly, the loss of HSJ1b may prevent the targeting of client substrates for ubiquitylation and subsequent degradation. During ERAD, the substrate is retrotranslocated across the ER membrane to the cytoplasm (Brodsky 2012). As the substrate emerges on the cytosolic side, the substrate is ubiquitylated by a membrane-associated E3 ubiquitin ligase. In addition to acting as a signal to target the substrate for degradation, the ubiquitin modification also enables the engagement of the AAA ATPase VCP (Ye *et al.* 2001, Flierman *et al.* 2003). The ATPase activity of VCP provides the driving force to extract the ubiquitylated protein from the membrane (Ye *et al.* 2003). It is possible that HSJ1b utilises its client binding domain and UIMs to hold the ubiquitylated substrate after its release from the membrane. The ubiquitylated substrate can then be transferred to chaperones that transport the substrate to the proteasome for degradation. The binding of the UIMs may protect the ubiquitin chains from promiscuous DUB activity, many of which reside at the cytoplasmic face of the ER (Westhoff *et al.* 2005, Reyes-Turcu *et al.* 2009). Although their role in ERAD remains to be fully characterised, it is hypothesised that the action of DUBs allows remodelling of the ubiquitin chains (Liu *et al.* 2012). The remodelling of the ubiquitin chains is proposed to enable the selective recognition of the ubiquitylated substrate by the appropriate chaperone or shuttle factor. A loss of HSJ1b protein may therefore result in an increase in deubiquitylation, possibly preventing the recognition of the substrate by its interacting protein. The targeting of the substrate to the proteasome may therefore become inefficient, leading to an accumulation of misfolded protein. The restoration of HSJ1b could combat the counterproductive deubiquitylation of substrates, leading to an increase in protein ubiquitylation.

Alternatively, it may be speculated that an increase in ubiquitylation levels upon the restoration of HSJ1b suggests that the targeting of clients for ERAD may be impaired in the absence of the protein. HSJ1b can target CFTR and MC4R for proteasomal degradation (Westhoff *et al.* 2005, Meimaridou *et al.* 2011). Another DnaJ protein, DnaJB12, localises to the cytoplasmic face of the ER and was also shown to target CFTR for ERAD (Grove *et al.* 2012). Importantly, the effect of DnaJB12 depletion on CFTR degradation was also investigated (Grove *et al.* 2012). The knockdown of DnaJB12 by siRNA increased the half-life of CFTR, with an increase in the amount of plasma membrane localised CFTR. The depletion of DnaJB12 also increased the half-life of the mutant and permitted a small pool of CFTRΔF508 to escape from the ER. The data suggested that in the absence of DnaJB12, CFTR is partitioned into a folding pathway rather than a degradation pathway. A similar scenario may be occurring with HSJ1b. HSJ1b may target clients for ERAD. In the absence

of HSJ1b, the clients may be re-directed onto a folding pathway or could possibly be retained in the ER membrane. The restoration of HSJ1b would allow ERAD of the client to proceed, thereby promoting the ubiquitylation of the client and accounting for the increase in ubiquitylated protein levels. It would be interesting to determine whether the increase in ubiquitylation is driven by the ubiquitylation of a single substrate or group of proteins. The immunoprecipitation and subsequent mass spectrometry of ubiquitylated protein in the absence and presence of HSJ1b could enable HSJ1b ERAD clients to be identified.

Overall, examining if the loss of HSJ1 had any effect on proteostasis in patient fibroblasts has provided limited findings. The increase in protein ubiquitylation upon the restoration of HSJ1b suggests a possible impairment in the ubiquitylation and degradation of HSJ1b clients. The restoration of HSJ1a had no effect on protein ubiquitylation levels. However, the possible accumulation of HSJ1a clients in the absence of the protein cannot be ruled out. Endogenous HSJ1a levels in fibroblasts were lower than HSJ1b levels, as seen previously in both human and mouse brain and spinal cord tissue (Chapple and Cheetham 2003, Novoselov *et al.* 2013). The lower expression may result in a longer time period being required to restore the ubiquitylation of HSJ1a clients. It will be important to establish whether a reduction in protein ubiquitylation is indeed a valid phenotype of patient fibroblasts or whether the observation is an artefact of restoring HSJ1. Although further investigations using patient fibroblasts may be useful for dissecting how the loss of HSJ1 chaperone activity impacts proteostasis it is important to consider the possibility that fibroblasts may not express HSJ1 client proteins. The loss of HSJ1 leads to the selective degeneration of motor neurons; therefore HSJ1 clients may only be expressed in motor neurons, or alternatively, may be expressed at higher levels. For example, nerve biopsies from patients with *TRIM2* mutations revealed the accumulation of NFL in axons (Ylikalio *et al.* 2013). NFL is a client of the TRIM2 E3 ubiquitin ligase, however NFL is not expressed in fibroblasts and mutant TRIM2 was found to have no effect on other intermediate filaments (Ylikalio *et al.* 2013). The fibroblasts therefore did not provide an accurate representation of the phenotype occurring in affected neurons. Differences in gene expression between skin fibroblasts and motor neurons is a caveat that may limit the successful modelling of disease in a fibroblast model.

The validity of using fibroblasts as a cellular model to study neuronal diseases has indeed been questioned. Skin cells and neurons exhibit stark differences in architecture, function and gene expression. Cellular phenotypes observed in patient fibroblasts may therefore not represent the phenotype of the affected neurons. The ability to model disease in a relevant cell type has been revolutionised by the generation of induced pluripotent stem cells (iPSC) from patient fibroblasts (Takahashi *et al.* 2007). The transfection of patient fibroblasts with

the transcription factors Oct4, Sox2, c-Myc and Klf4 induces their reprogramming to a pluripotent state. The resulting iPSC have the capacity for self-renewal and can differentiate into all 3 embryonic germ layers. Motor neurons derived from iPSC have been established to possess many of the cellular and physiological characteristics of endogenous motor neurons, making them an excellent cellular model for studying motor neuron degeneration (Toma *et al.* 2015). iPSC-derived motor neurons have provided novel insights into disease pathogenesis, identifying abnormalities in electrophysiological properties as early events in both familial ALS and CMT2 (Devlin *et al.* 2015, Saporta *et al.* 2015). Motor neurons derived from patients with ALS and CMT2 both displayed hyperexcitability, followed by a progressive loss of action potential output and synaptic activity. A progressive decrease in voltage activated sodium and potassium currents was identified; implying that early dysfunction of ion channel activity may initiate the degenerative pathway. The generation of iPSC-derived motor neurons would provide a more physiologically relevant cellular model to probe how the loss of HSJ1 causes degeneration. Such a cell model would drastically increase the scope to investigate the underlying mechanism of disease, enabling the effect of the HSJ1 mutations on motor neuron size, shape, lifespan and electrophysiological properties to be examined in detail. These aspects could prove critical for establishing the timeframe of events and characterising early stages in the degeneration pathway. It would be interesting to generate motor neurons for all three HSJ1 patient mutations in order to compare whether the different mutations affect disease pathogenesis or whether they act via a universal mechanism. An iPSC disease model could be the key to unravelling the crucial role of HSJ1 in motor neurons and should be a priority for future studies.

Chapter 6 – Investigating motor neuron degeneration in *Hsj1* knockout mice

6.1 Introduction

Although the HSJ1-Y5C patient fibroblasts provided a valuable opportunity to examine the loss of HSJ1 protein, skin cells do not replicate the cellular environment of motor neurons, potentially limiting the ability of fibroblasts to reliably model the mechanisms that underlie disease pathogenesis. Mouse models provide an advantage over patient fibroblasts in that they enable patient mutations to be examined in the context of a relevant cell type. Indeed, characterising the phenotype of motor neurons in dHMN and CMT2 mouse models has provided novel insights into the cellular mechanisms that drive motor neuron degeneration.

A range of mouse models have been generated to study dHMN and CMT2. Patient mutations with autosomal dominant inheritance have been modelled through the knock-in or overexpression of the required gene, generating mice such as MFN2 R94W knock-in and Hsp27 S135F, Hsp22 K141N and GARS C201R transgenic overexpressors (Strickland *et al.* 2015, d'Ydewalle *et al.* 2011, Zhang *et al.* 2014, Seo *et al.* 2014). Patient mutations with autosomal recessive inheritance, such as those in *ATP7A*, *TRIM2* and *KIF1B*, have been modelled through the partial or complete knockout of the gene (Hodgkinson *et al.* 2015, Balastik *et al.* 2008, Zhao *et al.* 2000). The mouse models listed all exhibited progressive muscle weakness and atrophy, with reductions in grip strength, rotarod performance and muscle mass. Pathologically, the mice displayed a significant loss of motor neurons in the lumbar region of the spinal cord, along with the denervation of neuromuscular junctions. The mouse models generated therefore successfully recapitulate the clinical and pathological features of the human phenotype, making them an excellent tool for investigating disease pathogenesis.

All three patient mutations reported in *HSJ1* to date are loss of function mutations (Blumen *et al.* 2012, Gess *et al.* 2014, Chapter 5). As human HSJ1 shares 85% sequence identity with mouse Hsj1 (Figure 6), the *Hsj1* knockout mouse provides an excellent model system for examining the underlying mechanisms that compromise motor neuron function and cause disease. *Hsj1* knockout mice have previously been generated by the Cheetham laboratory (described in Wendy Mustill PhD Thesis, UCL), using the Cre/loxP system to delete exon 2 and 3 of *Hsj1* (Figure 6). The *Hsj1* knockout mice were then utilised to investigate whether Hsj1 exerts a protective effect against motor neuron degeneration in a mouse model of ALS (Wendy Mustill PhD Thesis, UCL). The loss of Hsj1 exacerbated disease pathogenesis in SOD1 G93A mice, with a further reduction in motor unit number and motor neuron counts compared to single transgenic mice. Interestingly, prior to the identification of HSJ1 patient

mutation in dHMN and CMT2, our lab found that the loss of *Hsj1* alone had detrimental effects on motor neuron survival. At 120 days, *Hsj1* knockout mice displayed a reduction in motor unit number and a reduction in the number of motor neurons present in the lumbar region of the spinal cord. To determine if the degeneration of motor neurons was progressive, motor neuron survival was examined at the earlier time point of P20. A reduction in motor neuron counts was also observed at this time point (Anna Gray, personal communications). Although the *Hsj1* knockout mice appear healthy, with no overt motor deficits, the degeneration of motor neurons is an encouraging sign that these mice can be used to successfully model the HSJ1 patient mutations and identify the underlying molecular mechanisms that drive the degeneration process.

The aim of this study was to confirm the loss of motor neurons in *Hsj1* knockout mice at P20 and establish whether the loss of motor neurons occurred during development or was due to post-natal degeneration. To assist the counting of motor neurons in *Hsj1* wild-type and knockout spinal cords, Hb9:*GFP* mice would be utilised. These mice express GFP under the motor neuron specific promoter, Hb9, driving GFP expression in the dendrites, axons and somas of motor neurons (Wichterle *et al.* 2002). Hb9:*GFP* mice have been used to successfully visualise motor neurons, providing a marker to monitor the differentiation of mouse embryonic stem cells to motor neurons and enabling the study of embryonic motor axon development in SMA mice (Karumbayaram *et al.* 2009, McGovern *et al.* 2008). Generating Hb9:*GFP-Hsj1*$^{+/+}$ and Hb9:*GFP-Hsj1*$^{-/-}$ mice should simplify the identification of motor neurons and increase the reliability of motor neuron counts. If motor neurons were degenerating post-natally, the timeframe of the degeneration process would be established. The cellular phenotype of motor neurons would then be characterised prior to cell death through Western blot analysis of spinal cord lysates and immunostaining of spinal cord sections, to identify cellular changes that may be associated with motor neuron degeneration in dHMN and CMT2.

A

```
HUMAN HSJ1    MASYYEILDVPRSASADDIKKAYRRKALQWHPDKNPDNKEFAEKKFKEVA 50
MOUSE HSJ1    MASYYEILDVPRSASPDDIKKAYRKKALQWHPDKNPDNKEFAEKKFKEVA 50
              **************.********:************************** 

HUMAN HSJ1    EAYEVLSDKHKREIYDRYGREGLTGTGTGPSRAEAGSGGPGFTFTFRSPE 100
MOUSE HSJ1    EAYEVLSDKHKREIYDRYGREGLTGAGSGPSRSETGGAGPGFTFTFRSPE 100
              ************************:*:****:*:*..************ 

HUMAN HSJ1    EVFREFFGSGDPFAELFDDLGPFSELQNRGSRHSGPFFTFSSSFPGHSDF 150
MOUSE HSJ1    EVFREFFGSGDPFSELFDDLGVFSELQNQGPRLTGPFFTFSSSFPANSDF 150
              ************:******* ******:*.* :***********.:*** 

HUMAN HSJ1    SSSSFSFSPGAGAFRSVSTSTTFVQGRRITTRRIMENGQERVEVEEDGQL 200
MOUSE HSJ1    SSSSFSFSPGAGAFRSVSTSTTFVQGRRITTRRIMENGQERVEVEEDGQL 200
              ************************************************** 

HUMAN HSJ1    KSVTINGVPDDLALGLELSRREQQPSVTSRSGGTQVQQTPASCPLDSDLS 250
MOUSE HSJ1    KSVSINGVPDDLALGLELSRREQQPSVAPGLGVMQVRPTSLSRPPDHDLS 250
              ***:************************:.  *  **: *. * * * *** 

HUMAN HSJ1    EDEDLQLAMAYSLSEMEAAGKKPAGGREAQHRRQGRPKAQHQDPGLGGTQ 300
MOUSE HSJ1    EDEDLQLAMAYSLSEMEAAGQKPAGGRGAQQRQHGQPKAQHRDLDVGGTH 300
              ********************:****** **:*::*:*****:* .:***: 

HUMAN HSJ1    EGARGEATKRSPSPEEKASRCLIL 324
MOUSE HSJ1    KSVRGEAAKLSPSSEEKASRCHIL 324
              :..****:* ***.******* ** 
```

B

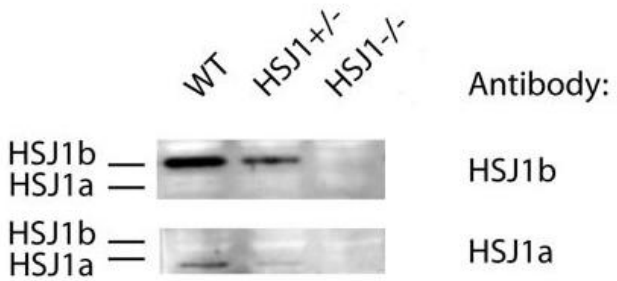

Figure 6 Sequence alignment of human and mouse HSJ1 and characterising the loss of Hsj1 in *Hsj1*$^{-/-}$ mice. A: The alignment of human and mouse HSJ1b protein sequences. Human and mouse HSJ1b share 85% sequence identity. B: The sheep polyclonal HSJ1 S653 antibody detects endogenous mouse Hsj1. Western blot analysis confirms the loss of both Hsj1 isoforms in *Hsj1*$^{-/-}$ mice (Figure from Wendy Mustill PhD Thesis, UCL).

6.2 Results

6.2.1 The generation of Hb9:*GFP*$^{+/-}$ *Hsj1*$^{+/+}$ and Hb9:*GFP*$^{+/-}$ *Hsj1*$^{-/-}$ mice

Hb9:*GFP*$^{+/-}$ mice were purchased from The Jackson Laboratory. They recommended that the strain should be maintained as hemizygotes, due to the high mortality of homozygous pups born to homozygous females. Hb9:*GFP*$^{+/-}$ mice were therefore maintained in a hemizygote state through crossings with C57BL/6 mice. In order to examine the effect of *Hsj1* knockout on motor neuron survival, both Hb9:*GFP*$^{+/-}$ *Hsj1*$^{+/+}$ and Hb9:*GFP*$^{+/-}$ *Hsj1*$^{-/-}$ double transgenic mice needed to be generated. Two rounds of breeding were therefore required. Firstly, Hb9:*GFP*$^{+/-}$ mice were crossed with *Hsj1*$^{-/-}$ mice to generate Hb9:*GFP*$^{+/-}$ and Hb9:*GFP*$^{-/-}$ mice heterozygous for *Hsj1*. Hb9:*GFP*$^{+/-}$ *Hsj1*$^{+/-}$ mice were then crossed with Hb9:*GFP*$^{-/-}$ *Hsj1*$^{+/-}$ littermates, generating Hb9:*GFP*$^{+/-}$ and Hb9:*GFP*$^{-/-}$ mice that were either *Hsj1* wild-type, *Hsj1* heterozygotes or *Hsj1* knockout. To ensure experimental animals had comparable genetic backgrounds, Hb9:*GFP*$^{+/-}$ *Hsj1*$^{+/+}$ and Hb9:*GFP*$^{+/-}$ *Hsj1*$^{-/-}$ mice needed to be generated in the same litter. The colony was therefore maintained through the crossing of Hb9:*GFP*$^{+/-}$ *Hsj1*$^{+/-}$ and Hb9:*GFP*$^{-/-}$ *Hsj1*$^{+/-}$ mice. Offspring were born at the expected Mendelian frequency and appeared healthy, with Hb9:*GFP*$^{+/-}$ *Hsj1*$^{-/-}$ mice indistinguishable from Hb9:*GFP*$^{+/-}$ *Hsj1*$^{+/+}$ littermate controls.

6.2.2 Characterising GFP expression in Hb9:*GFP*$^{+/-}$ *Hsj1*$^{+/+}$ mice

The expression of GFP under the control of the Hb9 promoter has been reported to be detectable between embryonic day 9.5 and post-natal day 10 (Jackson Laboratories). To determine the latest time point at which GFP expression could still be detected, the level of GFP in spinal cord lysates from Hb9:*GFP*$^{+/-}$ *Hsj1*$^{+/+}$ mice at P10, P15 and P20 was examined by Western blot analysis (Figure 6.1A). The levels of GFP were found to substantially decrease over time. GFP expression was reduced by 60% between P10 and P15. GFP levels were reduced by a further 32% between P15 and P20, resulting in P20 mice expressing 8% of the GFP levels observed at P10. To establish whether the reduction in GFP expression compromised the ability to visualise motor neurons, GFP fluorescence was examined at P10, P15 and P20. Hb9:*GFP*$^{+/-}$ *Hsj1*$^{+/+}$ mice of the required age were perfused and spinal sections were examined for GFP fluorescence on a Nikon Eclipse fluorescence light microscope. GFP positive motor neurons could be clearly visualised at both P10 and P15, although the fluorescent intensity was reduced at P15 (Figure 6.1B). In contrast, motor neurons could not be clearly distinguished at P20. The Hb9:*GFP*$^{+/-}$ mice could therefore only be used to count motor neurons in mice at or below the age of P15.

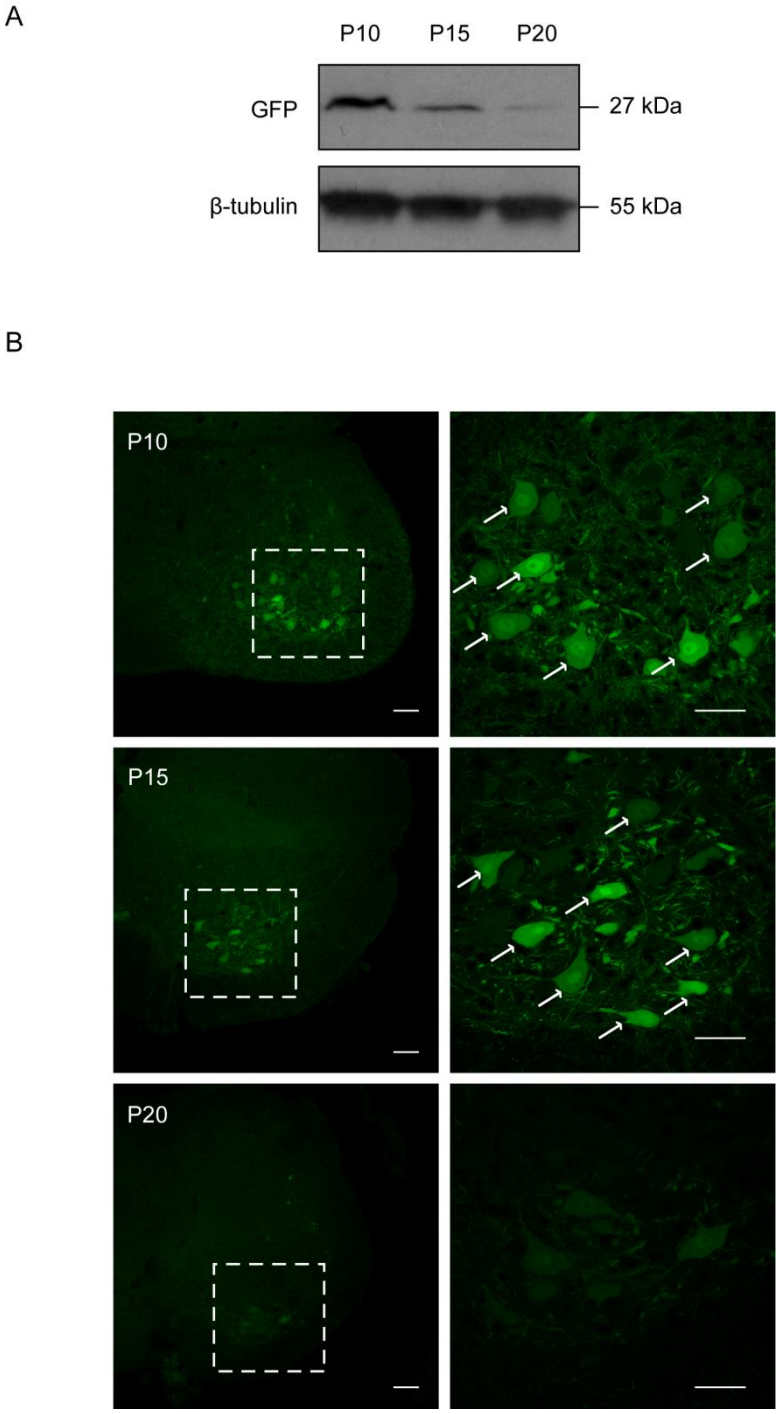

Figure 6.1 Characterising GFP expression in *GFP*$^{+/-}$ *Hsj1*$^{+/+}$ mice at P10, P15 and P20. **A:** 30 µg of spinal cord lysate from Hb9:*GFP*$^{+/-}$ *Hsj1*$^{+/+}$ mice at P10, P15 and P20 was resolved by SDS-PAGE. Western blot analysis was performed using a monoclonal rabbit GFP antibody (1:1000) and a monoclonal mouse β-tubulin antibody (1:5000). **B:** Hb9:*GFP*$^{+/-}$ *Hsj1*$^{+/+}$ mice at P10, P15 and P20 were transcardially perfused with 4% PFA. Spinal cords were dissected, post-fixed in 4% PFA overnight then cryoprotected in 30% sucrose. The lumbar region of the spinal cord was then sectioned into 20 µm slices. GFP fluorescence was visualised on a Nikon Eclipse 80i fluorescence light microscope. Scale bar, (left panel) 500 µm (right panel) 50 µm.

6.2.3 Hb9:*GFP*$^{+/-}$ *Hsj1*$^{+/+}$ and Hb9:*GFP*$^{+/-}$ *Hsj1*$^{-/-}$ mice show no difference in the number of motor neurons at P10 and P15

Motor neuron survival was examined in Hb9:*GFP*$^{+/-}$ *Hsj1*$^{+/+}$ and Hb9:*GFP*$^{+/-}$ *Hsj1*$^{-/-}$ mice at P10 and P15. Hb9:*GFP*$^{+/-}$ *Hsj1*$^{+/+}$ and Hb9:*GFP*$^{+/-}$ *Hsj1*$^{-/-}$ mice were perfused with 4% PFA at both time points. Spinal cords were then dissected, post fixed, cryoprotected and the lumbar region was subsequently cut into 20 µm sections. The Hb9:GFP positive motor neurons were easily visualised on a Nikon Eclipse fluorescence light microscope at 40X magnification. There were no obvious differences in Hb9:GFP positive motor neuron localisation, shape or size between Hb9:*GFP*$^{+/-}$ *Hsj1*$^{+/+}$ and Hb9:*GFP*$^{+/-}$ *Hsj1*$^{-/-}$ mice at P10 or P15 (Figure 6.2). GFP positive motor neurons located in the ventral horns were counted in every 4th consecutive spinal cord section, in order to avoid counting the same motor neuron twice. At least 30 sections were counted per animal and the average number of motor neurons per section was determined. At P10, Hb9:*GFP*$^{+/-}$ *Hsj1*$^{+/+}$ mice had an average of 19.7 ± 1.2 motor neurons per spinal cord section, compared to 19.5 ± 0.8 motor neurons observed in Hb9:*GFP*$^{+/-}$ *Hsj1*$^{-/-}$ mice (Figure 6.3). Similar counts were observed at P15; Hb9:*GFP*$^{+/-}$ *Hsj1*$^{+/+}$ mice had an average of 19.2 ± 0.6 motor neurons and Hb9:*GFP*$^{+/-}$ *Hsj1*$^{-/-}$ mice had an average of 19.1 ± 0.4 motor neurons per spinal cord section. Statistical analysis revealed no significant difference in the average number of motor neurons in Hb9:*GFP*$^{+/-}$ *Hsj1*$^{+/+}$ and Hb9:*GFP*$^{+/-}$ *Hsj1*$^{-/-}$ mice at both P10 and P15.

6.2.4 *Hsj1*$^{-/-}$ mice show a loss of motor neurons between P15 and P20

The loss of motor neurons in *Hsj1*$^{-/-}$ mice had been previously observed at P20 (Anna Gray unpublished observations). The motor neuron counts at P10 and P15 in the Hb9:*GFP*$^{+/-}$ mice therefore suggests that the loss may be occurring between P15 and P20. However, due to the reduction in GFP expression, the Hb9:*GFP*$^{+/-}$ mice could not be used to examine this possibility. To confirm whether the loss of motor neurons in *Hsj1*$^{-/-}$ mice is indeed occurring between P15 and P20, motor neurons were counted in the spinal cords of C57BL/6 wild-type mice and *Hsj1*$^{-/-}$ mice (congenic on the C57BL/6 background) using the Nissl stain gallocyanine (Figure 6.4). Gallocyanine is a basic dye that binds to negatively charged nucleic acids. Motor neurons have a high rate of protein synthesis and their cytoplasm contains high levels of RNA, concentrated in rough endoplasmic reticulum (RER). Gallocyanine therefore strongly stains the cytoplasm of motor neurons in a blue/purple colour, enabling their distinction from other neurons in the spinal cord. *Hsj1*$^{+/+}$ and *Hsj1*$^{-/-}$ mice were perfused at P15 and P20. Spinal cords were dissected and the lumbar region was sectioned into 20 µm slices. Spinal cord sections were stained with gallocyanine, as described in Chapter 2, and were then visualised on a Nikon Eclipse light microscope. Motor

neurons were counted based on established criteria (Zhao *et al.* 2011, Guo *et al.* 2013, Iguchi *et al.* 2013). Only large, polygonal neurons with a darkly stained cytoplasm, a pale nucleus and a large, darkly stained nucleolus were included. Following these criteria, motor neurons in the sciatic pool of the ventral horns were counted in every 4th consecutive spinal cord section. At least 30 sections were counted per animal and the average number of motor neurons per section was determined. At P15, *Hsj1*$^{+/+}$ and *Hsj1*$^{-/-}$ mice showed no significant difference in motor neuron counts (Figure 6.5). *Hsj1*$^{+/+}$ mice had an average of 21.5 ± 0.3 motor neurons per spinal cord section, with *Hsj1*$^{-/-}$ mice displaying an average of 21.6 ± 0.4 motor neurons. In contrast, at P20, *Hsj1*$^{-/-}$ mice exhibited an 11.6% reduction in motor neuron counts compared to *Hsj1*$^{+/+}$ mice. *Hsj1*$^{+/+}$ mice had an average of 21.8 ± 0.4 motor neurons, whereas *Hsj1*$^{-/-}$ mice had an average of 19.3 ± 0.2 motor neurons per spinal cord section. The 11.6% reduction was statistically significant ($P < 0.001$).

6.2.5 Motor neurons in *Hsj1*$^{-/-}$ mice show a reduction in area at P15 and P20

Large motor neurons are particularly vulnerable to degeneration (Saxena *et al.* 2009). To determine if large motor neurons are more susceptible to the loss of Hsj1, the average soma area of motor neurons in P15 and P20 *Hsj1*$^{+/+}$ and *Hsj1*$^{-/-}$ mice was analysed (Figure 6.6). Spinal sections were imaged on a Nikon Eclipse 80i light microscope. The area of motor neuron somas was then measured using ImageJ. *Hsj1*$^{+/+}$ motor neurons had an average soma area of 390 and 401 μm^2, at P15 and P20, respectively. *Hsj1*$^{-/-}$ mice displayed significantly smaller motor neurons at both time points, with an average soma area of 343 and 354 μm^2 at P15 and P20, respectively. There was no significant difference in the average soma size of *Hsj1*$^{-/-}$ motor neurons between P15 and P20.

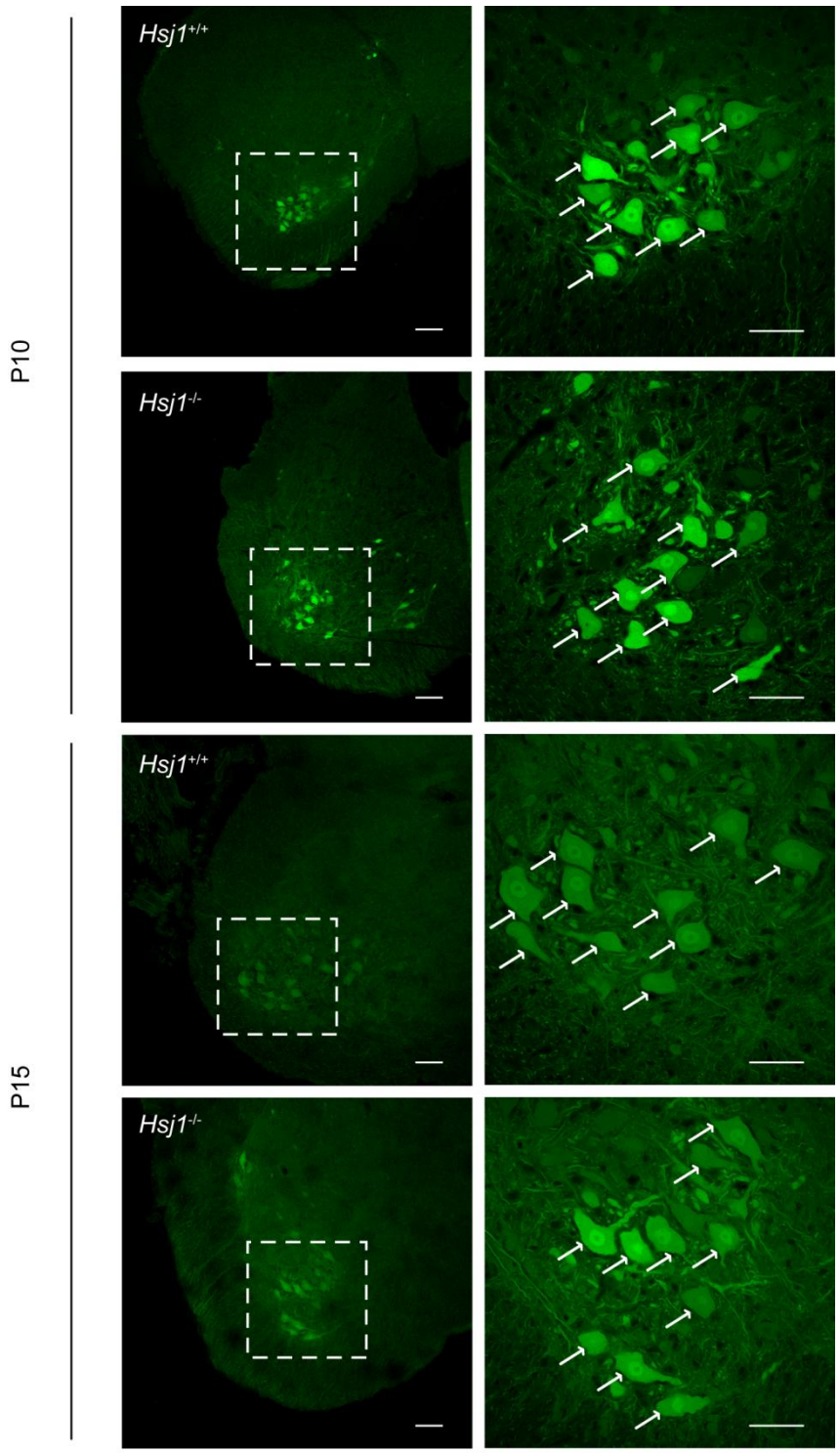

Figure 6.2 GFP positive motor neurons in *GFP*$^{+/-}$ *Hsj1*$^{+/+}$ and *GFP*$^{+/-}$ *Hsj1*$^{-/-}$ spinal cord sections at P10 and P15. Hb9:*GFP*$^{+/-}$ *Hsj1*$^{+/+}$ and Hb9:*GFP*$^{+/-}$ *Hsj1*$^{-/-}$ mice were perfused with 4% PFA at P10 and P15. Spinal cords were dissected, post-fixed in 4% PFA overnight then transferred to 30% sucrose. The lumbar region of the spinal cord was sectioned into 20 µm slices. Slides were mounted and imaged on a Zeiss LSM 700 confocal microscope. Arrows indicate GFP positive motor neurons. Scale bar, (left panel) 500 µm (right panel) 50 µm.

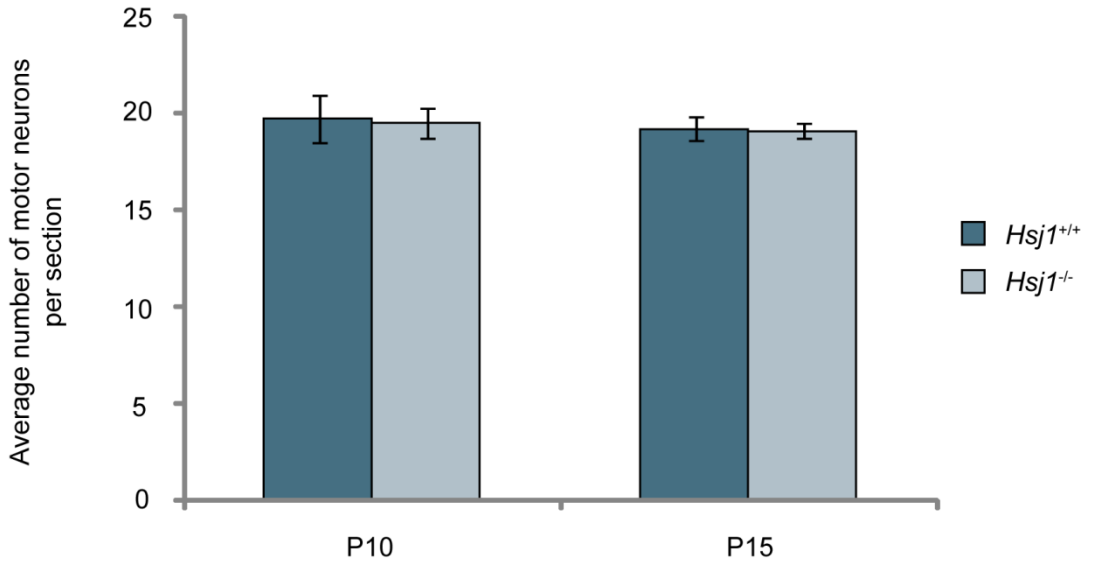

Figure 6.3 The average number of GFP positive motor neurons per spinal cord section in *GFP*$^{+/-}$ *Hsj1*$^{+/+}$ and *GFP*$^{+/-}$ *Hsj1*$^{-/-}$ mice. GFP positive motor neurons located in the sciatic pool of the ventral horns were counted on a Nikon Eclipse 80i fluorescence light microscope. Motor neurons were counted in every 4th consecutive section and at least 30 sections were counted per animal. The average number of motor neurons per section was calculated. Error bars represent ± SD (N.S, Student's t-test, n=4).

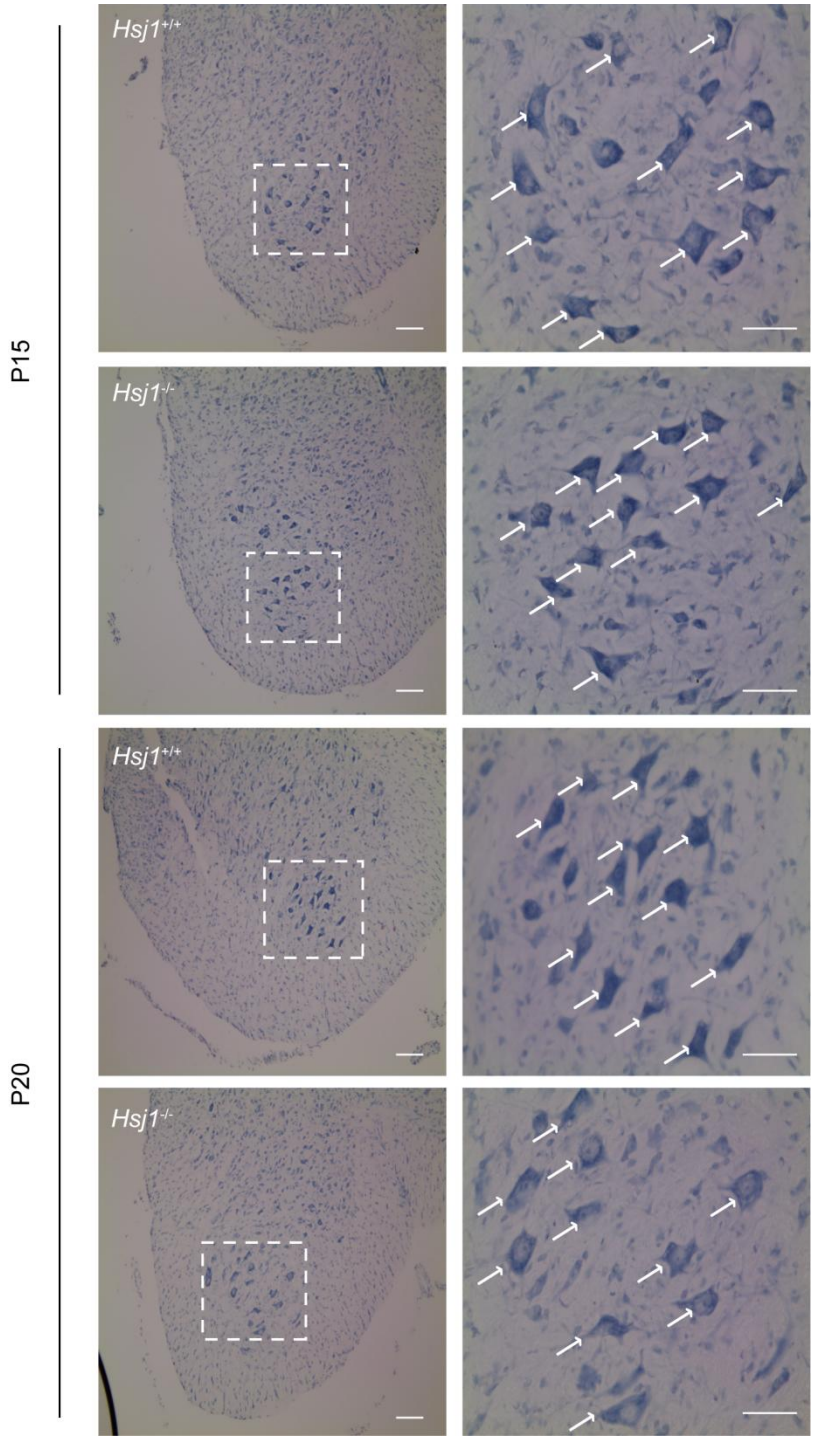

Figure 6.4 Staining of motor neurons with gallocyanine in *Hsj1*$^{+/+}$ and *Hsj1*$^{-/-}$ spinal cords at P15 and P20. *Hsj1*$^{+/+}$ and *Hsj1*$^{-/-}$ mice were perfused with 4% PFA at P15 and P20. Spinal cords were dissected, post-fixed in 4% PFA overnight, then cryoprotected in 30% sucrose. The lumbar region was sectioned into 20 µm sections. Slides were air-dried for 30 minutes then immersed in gallocyanine for 1 hour. Slides were then washed in increasing concentrations of ethanol before being immersed in Histoclear for 10 minutes. Slides were then mounted using DPX. Spinal cord sections were then imaged on a Nikon Eclipse 80i light microscope. Arrows indicate motor neurons. Scale bar, (left panel) 500 µm (right panel) 50 µm.

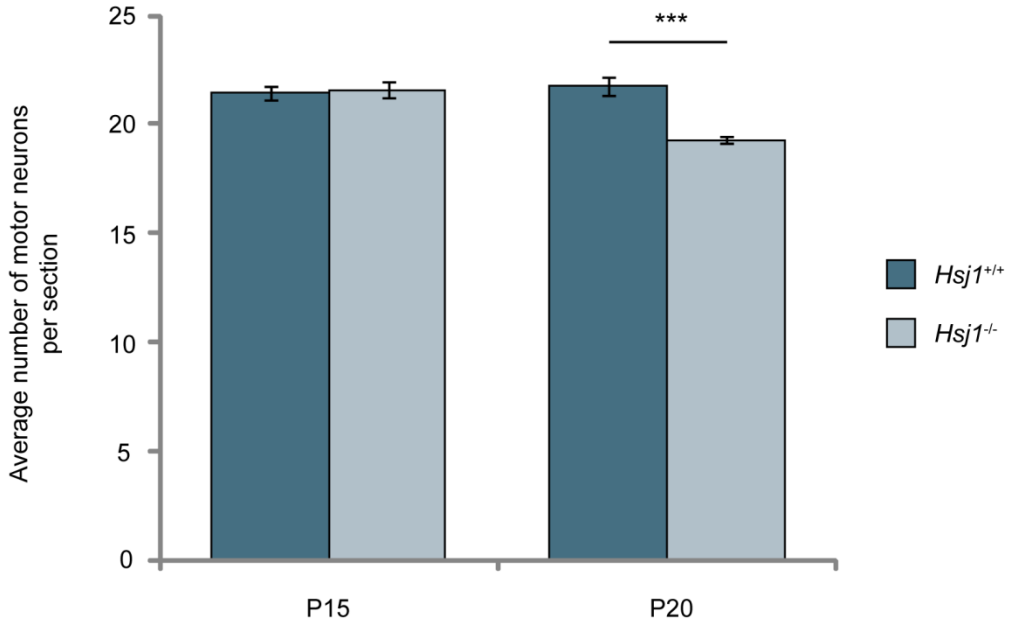

Figure 6.5 The average number of motor neurons per spinal cord section in *Hsj1*$^{+/+}$ and *Hsj1*$^{-/-}$ mice. Gallocyanine-stained motor neurons in the sciatic pool of the ventral horns were counted on a Nikon Eclipse 80i light microscope. Only large, polygonal neurons with a darkly stained cytoplasm, a pale nucleus and a darkly stained nucleolus were included in the counts. Motor neurons in every 4th consecutive spinal cord section were counted and at least 30 sections were counted per animal. Counts were expressed as the average number of motor neurons per spinal cord section. Error bars represent ± SD (*** P <0.001, Student's t-test, n=4).

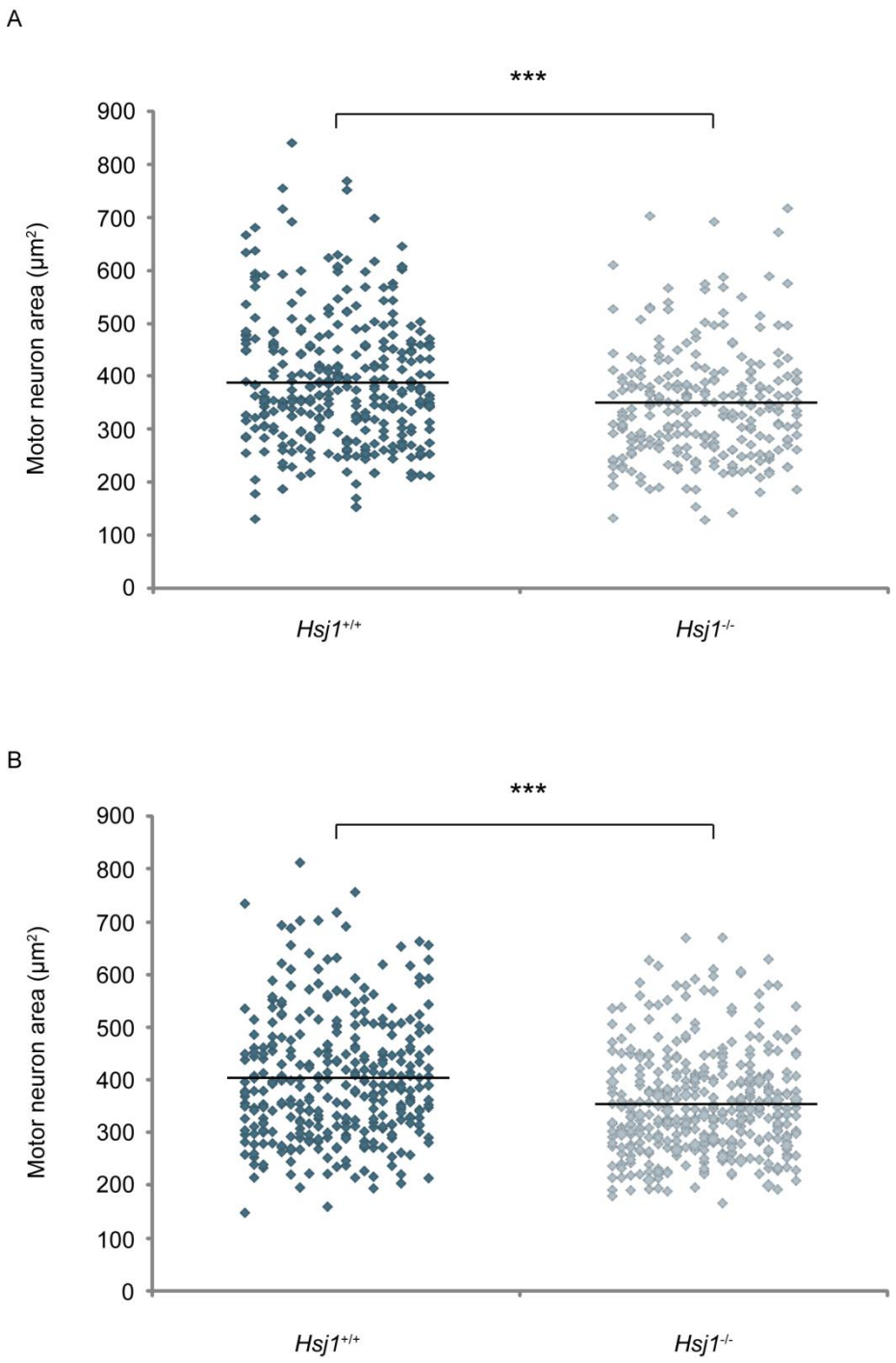

Figure 6.6 The average soma area of *Hsj1*$^{+/+}$ and *Hsj1*$^{-/-}$ motor neurons at P15 and P20. Gallocyanine-stained spinal cord sections from P15 and P20 *Hsj1*$^{+/+}$ and *Hsj1*$^{-/-}$ mice were imaged on a Nikon Eclipse 80i light microscope. The area of motor neuron somas was measured using ImageJ. At least 300 motor neurons were analysed in total at each time point, for each genotype. Each point represents the area of one motor neuron, with the bar representing the average soma area (*** P <0.001, Student's t-test, n=4).

6.2.6 *Hsj1*$^{-/-}$ spinal cords show increased levels of ubiquitylated protein

Having established that a proportion of motor neurons are lost in *Hsj1*$^{-/-}$ mice between P15 and P20, I sought to characterise the phenotype of motor neurons at P15, prior to cell death, in order to provide insights into the underlying mechanisms driving motor neuron degeneration. Data from Chapter 5 suggested that the loss of HSJ1 in patient fibroblasts may impair proteostasis through an inability to target client proteins for ubiquitylation. To examine whether this was a phenotype that also occurred *in vivo*, protein ubiquitylation levels in spinal cord lysates from P15 *Hsj1*$^{+/+}$ and *Hsj1*$^{-/-}$ mice were analysed (Figure 6.7). Spinal cord lysates were resolved by SDS-PAGE then probed for polyubiquitin by Western blot. The level of ubiquitylated protein was corrected for loading using β-actin then normalised to the *Hsj1*$^{+/+}$ sample. *Hsj1*$^{+/+}$ spinal cord lysates showed a smear of high molecular weight ubiquitin species, ranging in size from over 250 kDa to around 100 kDa. Spinal cord lysates from *Hsj1*$^{-/-}$ mice also showed a smear of high molecular weight ubiquitin species over the same size range. However, the expression level of ubiquitylated protein in *Hsj1*$^{-/-}$ spinal cords was 1.9 fold higher than the levels observed in *Hsj1*$^{+/+}$ spinal cords. This difference was statistically significant ($P < 0.001$).

6.2.7 The knockout of *Hsj1* does not compromise the activity of the proteasome

An increase in ubiquitylated protein in the *Hsj1*$^{-/-}$ spinal cords may be due to defects in protein degradation. To determine whether the activity of the proteasome is compromised by the knockout of *Hsj1*, proteasome activity was assessed in spinal cord lysates from P15 *Hsj1*$^{+/+}$ and *Hsj1*$^{-/-}$ mice. Spinal cord lysates were incubated for 1 hour with 10 μM of the fluorogenic substrate AMC-LLVY. Fluorescent intensity was measured using a spectrofluorometer. Background readings were subtracted and the activity of the proteasome was normalised to the *Hsj1*$^{+/+}$ sample. The *Hsj1*$^{+/+}$ and *Hsj1*$^{-/-}$ spinal cord lysates showed no significant difference in proteasome activity (Figure 6.8). The increase in ubiquitylated protein therefore does not appear to be a result of impaired proteasome function.

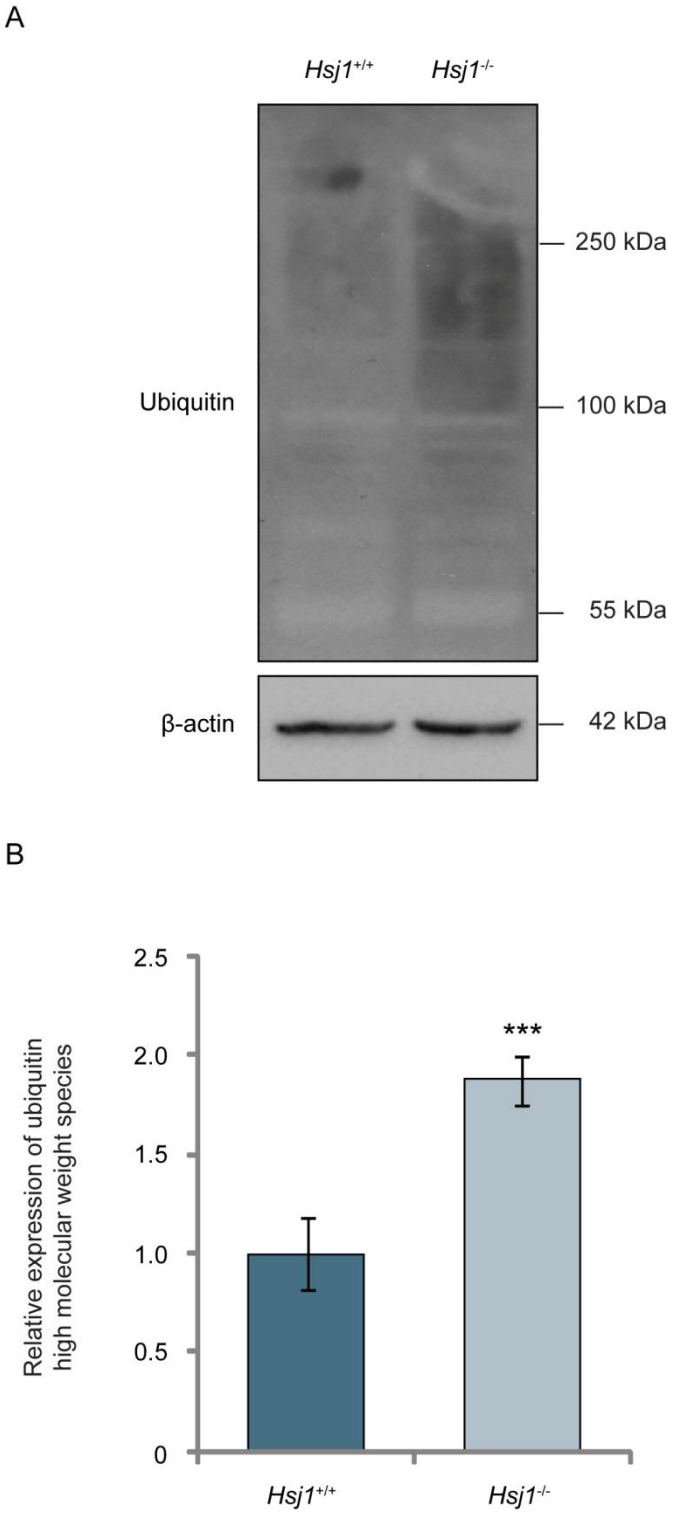

Figure 6.7 *Hsj1*$^{-/-}$ mice show an increase in ubiquitylated protein. A: 40 µg of spinal cord lysate from *Hsj1*$^{+/+}$ and *Hsj1*$^{-/-}$ mice at P15 was resolved by SDS-PAGE. Membranes were boiled for 30 minutes in Milli-Q water after transfer and then probed with a polyclonal poly-ubiquitin antibody (1:1000) and a monoclonal mouse β-actin antibody (1:5000). **B:** Western blots were analysed using ImageJ. The level of ubiquitylated protein was corrected for loading using β-actin and normalised to the level of ubiquitylated protein in *Hsj1*$^{+/+}$ spinal cords. Error bars represent ± SD (*** P <0.001, Student's t-test, n=4).

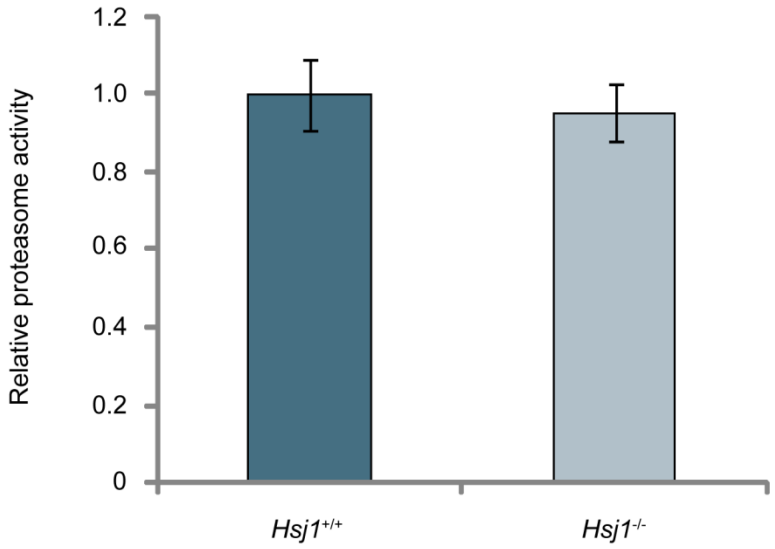

Figure 6.8 *Hsj1*$^{+/+}$ and *Hsj1*$^{-/-}$ spinal cords show no difference in proteasome activity. 30 µg of spinal cord lysate from *Hsj1*$^{+/+}$ and *Hsj1*$^{-/-}$ P15 mice was incubated with 10 µM AMC-LLVY for 1 hour at 37 °C. Fluorescence was then measured using a spectrofluorometer using an excitation wavelength of 380 nm and an emission wavelength of 460 nm. Background readings were subtracted and the results were normalised to the proteasome activity in *Hsj1*$^{+/+}$ spinal cords. Error bars represent ± SD (N.S, Student's t-test, n=4).

6.2.8 Autophagy is activated in P15 *Hsj1*$^{-/-}$ mice

Alternatively, an increase in ubiquitylated protein may be caused by a block in protein degradation mediated by autophagy. To examine this possibility, the level of the autophagosome marker, LC3-II, in spinal cord lysates was determined. Spinal cord lysates from P15 *Hsj1*$^{+/+}$ and *Hsj1*$^{-/-}$ mice were resolved by SDS-PAGE then probed for LC3 by Western blot. LC3-I and LC3-II isoforms were detected in both spinal cord lysates, at 18 and 16 kDa, respectively (Figure 6.9A). The level of each isoform was corrected for loading using β-actin then normalised to the level of LC3-I in *Hsj1*$^{+/+}$ spinal cord lysates. *Hsj1*$^{-/-}$ spinal cords showed a small reduction in LC3-I levels compared to wild-type spinal cords, although this difference was not significant. In contrast, LC3-II levels were found to be significantly different between *Hsj1*$^{+/+}$ and *Hsj1*$^{-/-}$ spinal cords. LC3-II was 2.4 fold higher than LC3-I in *Hsj1*$^{+/+}$ mice. In comparison, *Hsj1*$^{-/-}$ spinal cords showed a 0.8 fold higher level of LC3-II, with a 3.2 fold higher expression than *Hsj1*$^{+/+}$ LC3-I (Figure 6.9B).

The higher levels of LC3-II in *Hsj1*$^{-/-}$ mice may be due to an increase in autophagosome formation or a block in autophagosome degradation. The level of p62, a protein degraded by autophagy, was used to distinguish between these two possibilities. *Hsj1*$^{+/+}$ and *Hsj1*$^{-/-}$ spinal cord lysates were probed for p62 by Western blot analysis (Figure 6.10). Both wild-type and knockout spinal cords showed similar levels of p62, suggesting that the observed increase in LC3-II was due to an increase in autophagosome formation rather than a block in autophagosome degradation. To establish if the increase in autophagy was occurring in motor neurons, the number of autophagosomes present in the motor neurons of *Hsj1*$^{+/+}$ and *Hsj1*$^{-/-}$ spinal cord sections was compared using immunocytochemistry. The LC3 antibody used for Western blot was initially used to mark the autophagosomes; however, optimisation of the antibody for immunocytochemistry was unsuccessful. The p62 antibody used for Western blot was successfully optimised and was therefore used instead of the LC3 antibody. Spinal cord sections from P15 *Hsj1*$^{+/+}$ and *Hsj1*$^{-/-}$ mice were permeabilised with 0.2% Triton-X100, blocked for 1 hour, then immunostained for p62 and the neuronal marker β-III-tubulin. Z-stacks of the spinal cord sections were acquired using a Zeiss LSM 700 confocal microscope. Only β-III-tubulin positive, large, polygonal cells, in a location consistent with motor neurons were imaged. p62 appeared both diffuse in the cytoplasm and in multiple puncta structures (Figure 6.11). The number and size of p62 puncta in at least 30 motor neurons per animal were analysed using ImageJ, using maximum intensity projections. The number of p62 puncta per motor neuron were placed into 3 categories; <15, 15-30 and >30 puncta per cell (Bandyopadhyay *et al.* 2014). The number in each category was then expressed as a percentage of the total number of motor neurons analysed (Figure 6.12A). In *Hsj1*$^{+/+}$ spinal cords, 68% of motor neurons contained <15 p62 puncta, with 20%

of motor neurons containing between 15-30 puncta. A slight shift in the number of p62 puncta was observed in *Hsj1*$^{-/-}$ motor neurons. 64% of motor neurons contained <15 p62 puncta, with 25% of motor neurons containing 15-30 puncta. A 4% reduction in the percentage of motor neurons containing <15 p62 puncta is therefore accompanied by a 5% increase in the percentage of motor neurons containing between 15-30 puncta. The data suggests a possible increase in the number of p62 puncta in *Hsj1*$^{-/-}$ motor neurons, although the trend did not reach statistical significance. There was no significant difference in the percentage of motor neurons containing >30 p62 puncta in both *Hsj1*$^{+/+}$ and *Hsj1*$^{-/-}$ spinal cords. The p62 puncta present in *Hsj1*$^{-/-}$ motor neurons were found to be significantly smaller than p62 puncta observed in *Hsj1*$^{+/+}$ motor neurons (Figure 6.12B). p62 puncta had an average area of 780 nm^2 in *Hsj1*$^{+/+}$ motor neurons, compared to an area of 726 nm^2 in *Hsj1*$^{-/-}$ motor neurons. *Hsj1*$^{-/-}$ motor neurons therefore exhibit a subtle non-significant difference in the number of p62 puncta and a significant different in the size of the puncta.

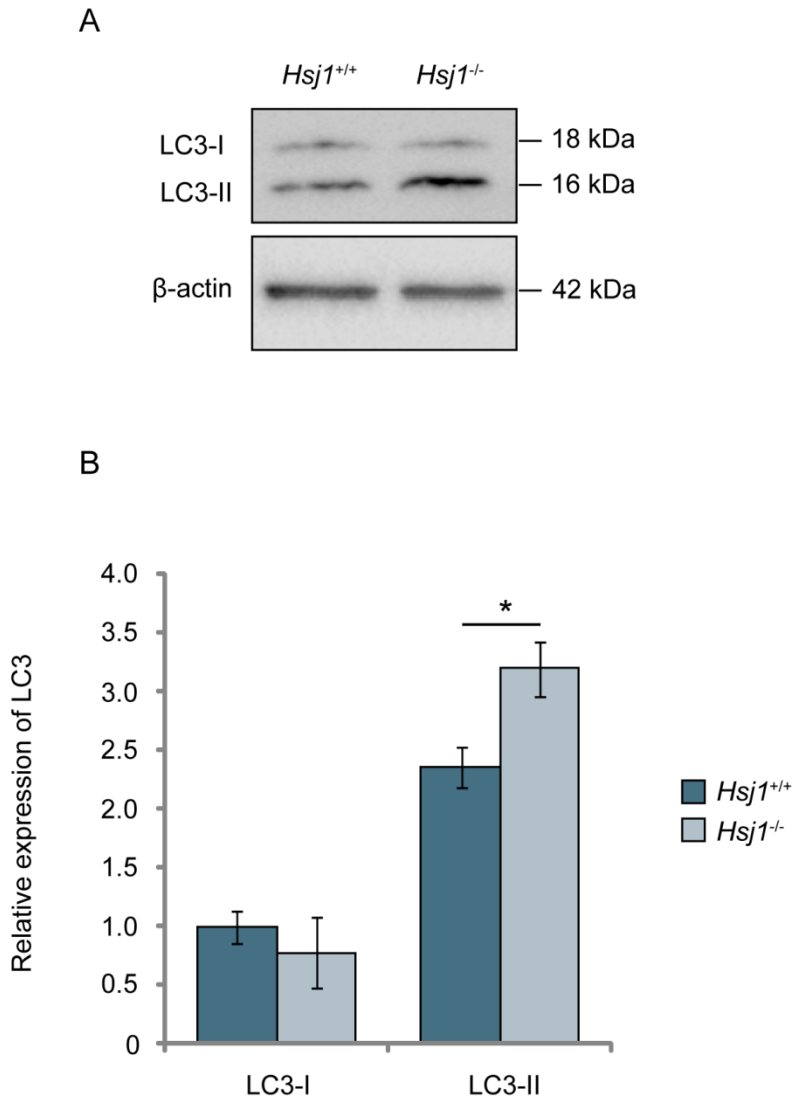

Figure 6.9 LC3 levels in *Hsj1*$^{+/+}$ and *Hsj1*$^{-/-}$ spinal cords. A: 30 µg of spinal cord lysate from *Hsj1*$^{+/+}$ and *Hsj1*$^{-/-}$ P15 mice was resolved by SDS-PAGE. Western blot analysis was performed using a polyclonal rabbit LC3 antibody (1:750) and a monoclonal mouse β-actin antibody (1:5000). **B:** Western blots were analysed using ImageJ. The level of each LC3 isoform was corrected for loading using β-actin before being normalised to the level of LC3-I in *Hsj1*$^{+/+}$ mice. Error bars represent ± SD (* P <0.05, Student's t-test, n=4).

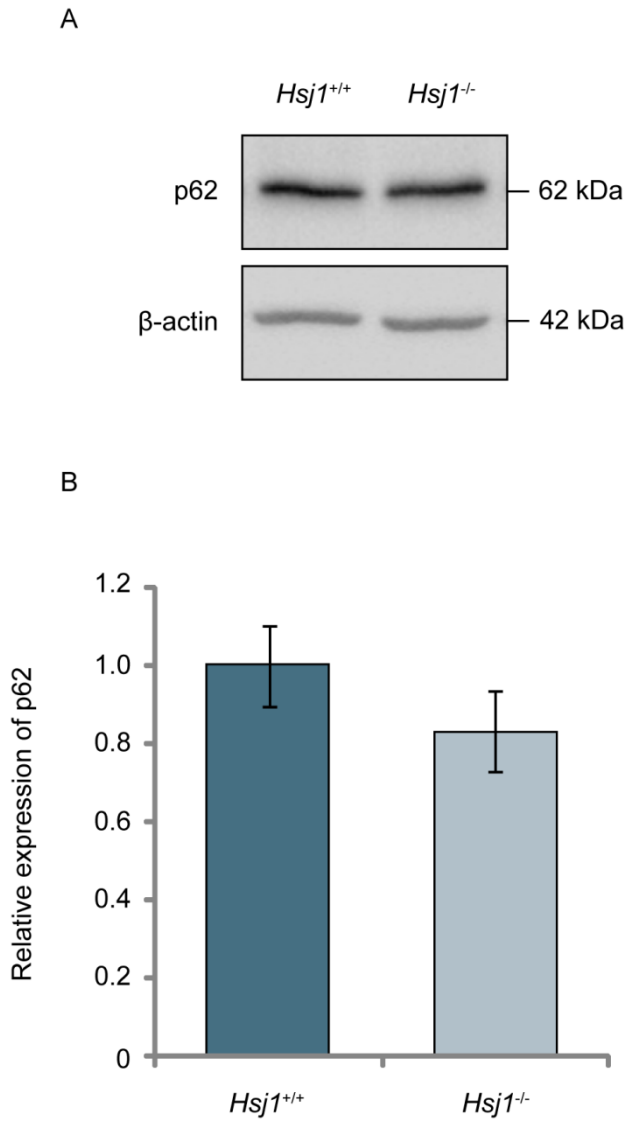

Figure 6.10 p62 levels in *Hsj1*$^{+/+}$ and *Hsj1*$^{-/-}$ spinal cords. A: 30 µg of spinal cord lysate from *Hsj1*$^{+/+}$ and *Hsj1*$^{-/-}$ P15 mice was resolved by SDS-PAGE. Western blot analysis was performed using a polyclonal rabbit p62 antibody (1:500) and a monoclonal mouse β-actin antibody (1:5000). **B:** Western blots were analysed using ImageJ. The level of p62 was corrected for loading using β-actin before being normalised to the level of p62 in *Hsj1*$^{+/+}$ mice. Error bars represent ± SD (N.S, Student's t-test, n=4).

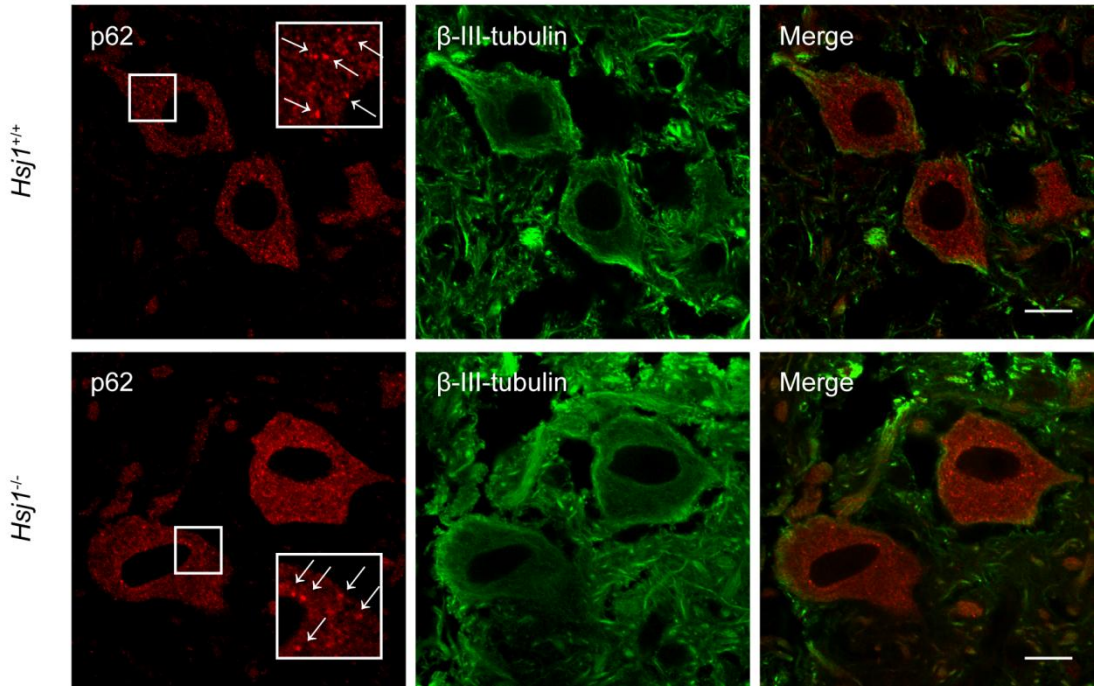

Figure 6.11 p62 localisation in *Hsj1*$^{+/+}$ and *Hsj1*$^{-/-}$ spinal cords. *Hsj1*$^{+/+}$ and *Hsj1*$^{-/-}$ P15 spinal cord sections were immunostained with a rabbit p62 antibody at a 1:200 dilution (Cy3, red) and a mouse β-III-tubulin antibody used at a 1:750 dilution (Cy2, green). Sections were imaged by Z-stack using a Zeiss LSM 700 confocal microscope. Only large, β-III-tubulin positive cells in a location consistent with motor neurons were imaged. Arrows highlight p62 puncta. Maximum intensity projections were generated and the number and size of p62 puncta was analysed using ImageJ. At least 30 motor neurons were analysed for each animal. Scale bar, 10 μm.

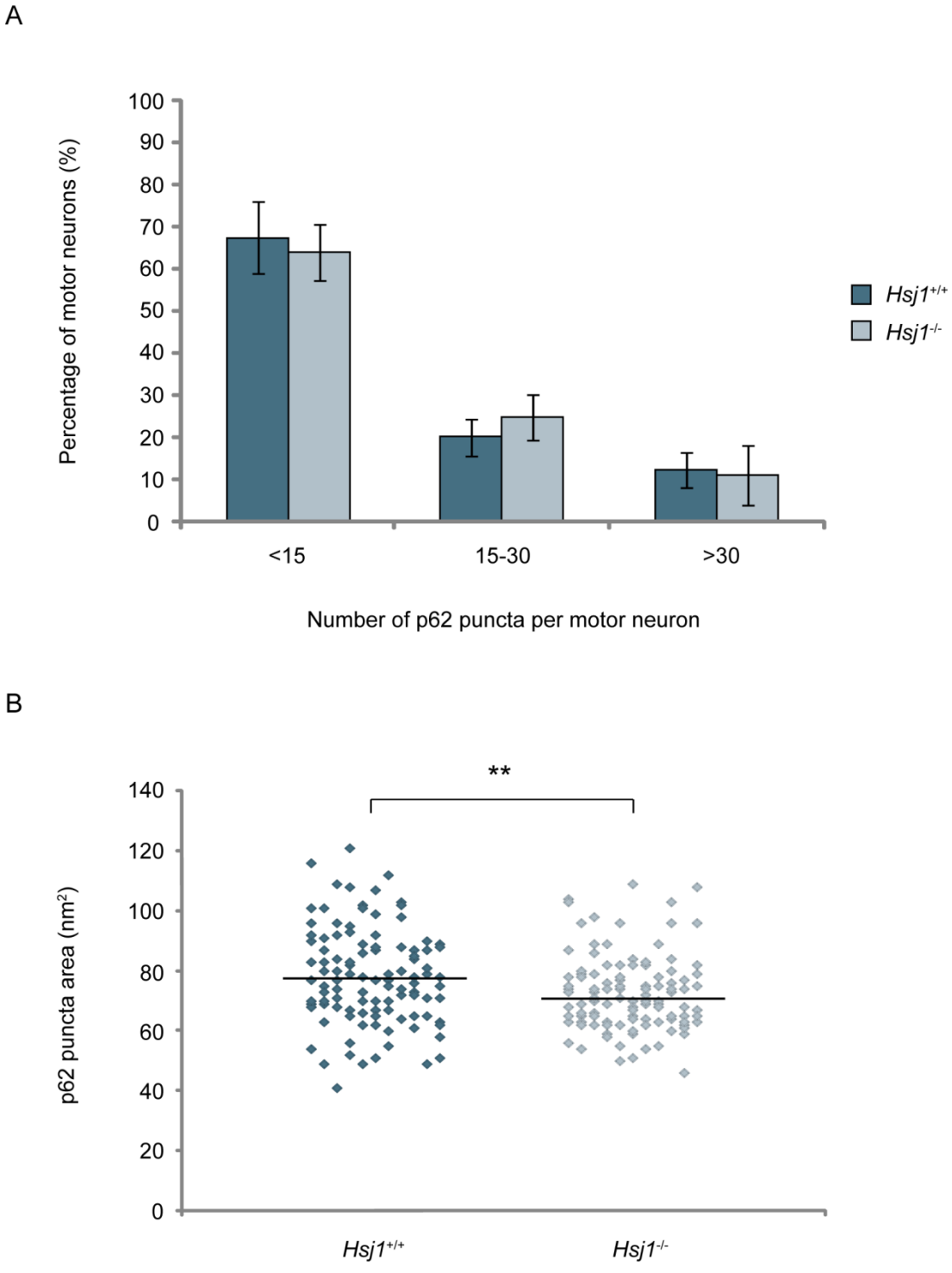

Figure 6.12 The number and size of p62 puncta in *Hsj1*$^{+/+}$ and *Hsj1*$^{-/-}$ motor neurons. A: The number of p62 puncta were counted in *Hsj1*$^{+/+}$ and *Hsj1*$^{-/-}$ motor neurons using ImageJ. The number of motor neurons that contained <15, 15-30 or >30 puncta were expressed as a percentage of the total number of cells analysed. (N.S, Student's t-test) **B:** The size of the p62 puncta was calculated using ImageJ. Each point represents the average area of p62 puncta in one motor neuron. The bar represent the average area of p62 puncta (** P <0.01, Student's t-test).

6.2.9 The presence of chromatolytic motor neurons in P15 *Hsj1*$^{-/-}$ spinal cords

Motor neuron counts at P15 and P20 established a timeframe during which motor neurons are lost in *Hsj1*$^{-/-}$ mice. Interestingly, a proportion of motor neurons showed signs of degeneration at P15. The majority of motor neurons in P15 *Hsj1*$^{-/-}$ spinal cords exhibited normal gallocyanine staining, with a darkly stained cytoplasm, a pale nucleus and a darkly stained nucleolus. However, some motor neurons showed abnormal staining; the dark gallocyanine stain only appeared at the periphery of the neuron, leaving a large unstained cytoplasm. In addition, the darkly stained nucleolus was displaced to the periphery of the neuron in these cells (Figure 6.13A). These observations are consistent with chromatolysis. Chromatolysis defines the dispersal and dissolution of Nissl bodies (RER) (Kusaka *et al.* 1988, Martin *et al.* 1999). To determine the proportion of chromatolytic neurons, the number of normal and abnormal motor neurons was counted based on the criteria described above. At P15 only 0.6% of motor neurons were chromatolytic in *Hsj1*$^{+/+}$ spinal cords. In contrast, 10% of motor neurons were chromatolytic in *Hsj1*$^{-/-}$ spinal cords (Figure 6.13B). At P20, comparable levels of chromatolytic motor neurons were observed, with 0.5% in *Hsj1*$^{+/+}$ and 0.8% in *Hsj1*$^{-/-}$ spinal cords. The increase in chromatolytic motor neurons in *Hsj1*$^{-/-}$ mice at P15 was found to be statistically significant. The 10% of chromatolytic motor neurons correlates closely with the 11.6% loss of motor neurons at P20. Considering the percentage of chromatolytic neurons returns to the wild-type level at P20, the chromatolytic neurons observed at P15 could represent the motor neurons that undergo cell death between P15 and P20.

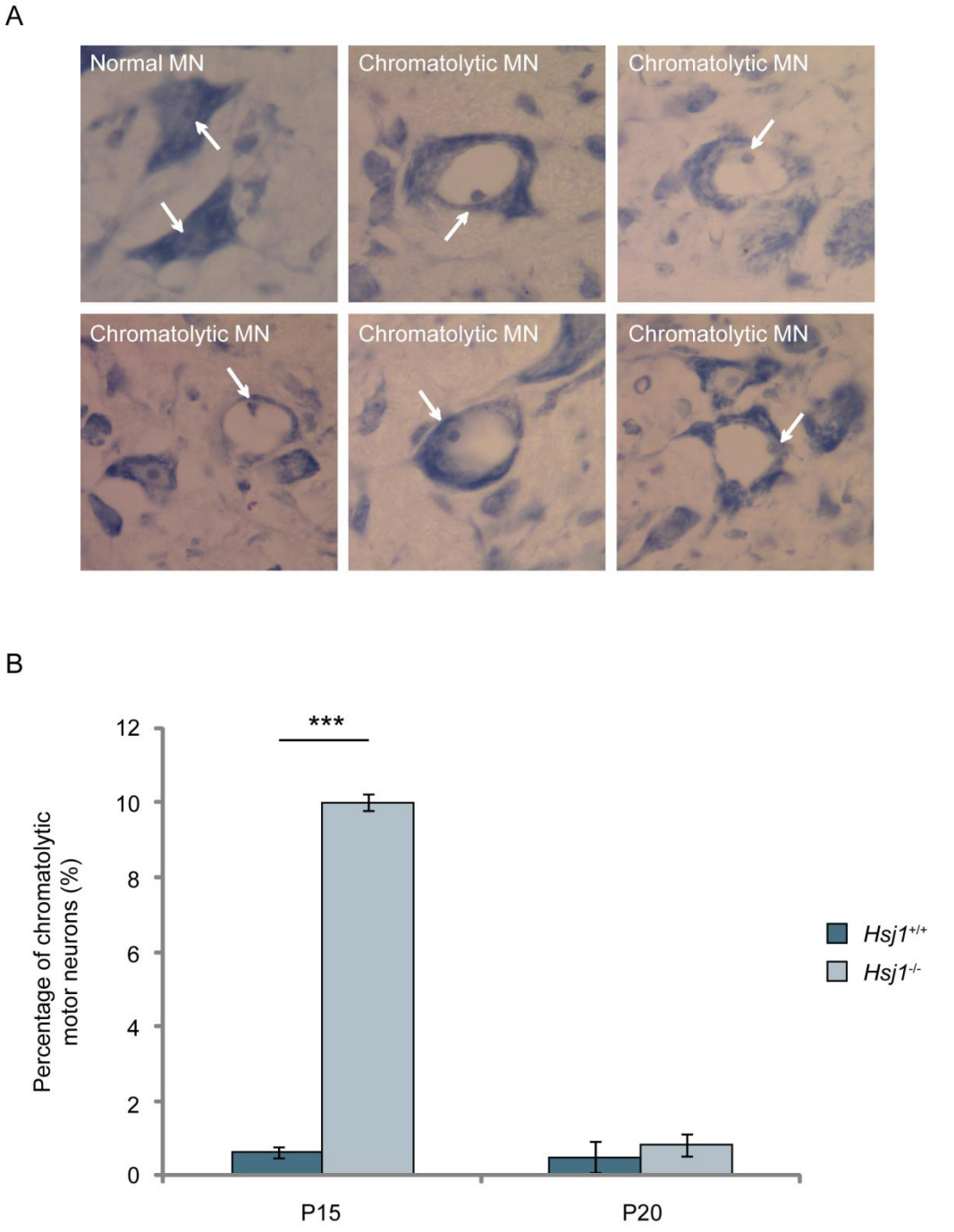

Figure 6.13 Chromatolytic motor neurons in *Hsj1*$^{-/-}$ spinal cord sections at P15. A: Gallocyanine-stained spinal cord sections were imaged on a Nikon Eclipse 80i light microscope. Normal motor neuron (MN) staining, darkly stained cytoplasm, pale nucleus and darkly stained central nucleolus. Chromatolytic MNs appear with a large pale cytoplasm with the dispersal of Nissl bodies to the periphery of the neuron and the displacement of the nucleolus (highlighted by arrow). **B:** The number of chromatolytic motor neurons was counted based on the above criteria and expressed as a percentage of the total number of cells counted. Motor neurons were counted in every 4th spinal cord section and at least 200 neurons were counted per animal. Error bars represent ± SD (*** P <0.001, Student's t-test, n=4).

6.2.10 The UPR is activated in *Hsj1*$^{-/-}$ mice at P10

The fragmentation and dissolution of RER has been reported to be a manifestation of chronic ER stress. To probe whether motor neurons in *Hsj1*$^{-/-}$ mice exhibit an ER stress response, the levels of UPR markers in P15 *Hsj1*$^{+/+}$ and *Hsj1*$^{-/-}$ spinal cord lysates was investigated. Considering that chromatolysis has already occurred at P15, spinal cord lysates from an earlier time point, P10, were also examined for UPR markers. P10 and P15 *Hsj1*$^{+/+}$ and *Hsj1*$^{-/-}$ spinal cord lysates were resolved by SDS-PAGE. Western blot analysis was performed using antibodies against components on the IRE1 branch (p-IRE1, IRE1 and BiP), the PERK branch (p-PERK, PERK, p-eIF2α, eIF2α and GADD34) and the ATF6 branch (ATF6 and ATF6 (N)). The level of UPR marker was corrected for loading with β-actin, then normalised to the level of UPR marker in *Hsj1*$^{+/+}$ spinal cord. At P10, both the IRE1 and PERK branches of the UPR appeared to be activated. The level of phosphorylated IRE1 was 3 fold higher in *Hsj1*$^{-/-}$ spinal cords, with total IRE1 levels also increased 1.6 fold. Phosphorylated PERK was 0.5 fold higher in the *Hsj1*$^{-/-}$ spinal cords, with total PERK, p-eIF2α and GADD34 showing a 1.8, 1.6 and 2 fold increase in expression levels, respectively (Figure 6.14). The total levels of eIF2α were unchanged in *Hsj1*$^{-/-}$ mice, as were the levels of full length ATF6, cleaved ATF6 and BiP. The increase in p-IRE1, IRE1, p-PERK, PERK, p-eIF2α and GADD34 were statistically significant. At P15, no signs of UPR activation were observed in *Hsj1*$^{-/-}$ spinal cords (Figure 6.15). The levels of UPR markers were comparable between both *Hsj1*$^{+/+}$ and *Hsj1*$^{-/-}$ mice.

To determine if the UPR was activated in motor neurons, I tried to examine the expression levels of UPR markers in the motor neurons of spinal cord sections by immunocytochemistry. Unfortunately, p-IRE1, p-PERK, p-eIF2α, eIF2α and ATF6 antibodies could not be optimised for immunocytochemistry. The BiP antibody did however produce a specific signal. P15 *Hsj1*$^{+/+}$ and *Hsj1*$^{-/-}$ spinal cord sections were therefore immunostained for BiP and the neuronal marker β-III-tubulin. Motor neurons were imaged on a Zeiss LSM 700 confocal microscope and the same settings were maintained when imaging both *Hsj1*$^{+/+}$ and *Hsj1*$^{-/-}$ sections. The fluorescent intensity of BiP staining appeared similar in both *Hsj1*$^{+/+}$ and *Hsj1*$^{-/-}$ motor neurons at P15 (Figure 6.15). The data therefore supports the Western blot data, suggesting that BiP is not upregulated in *Hsj1*$^{-/-}$ motor neurons.

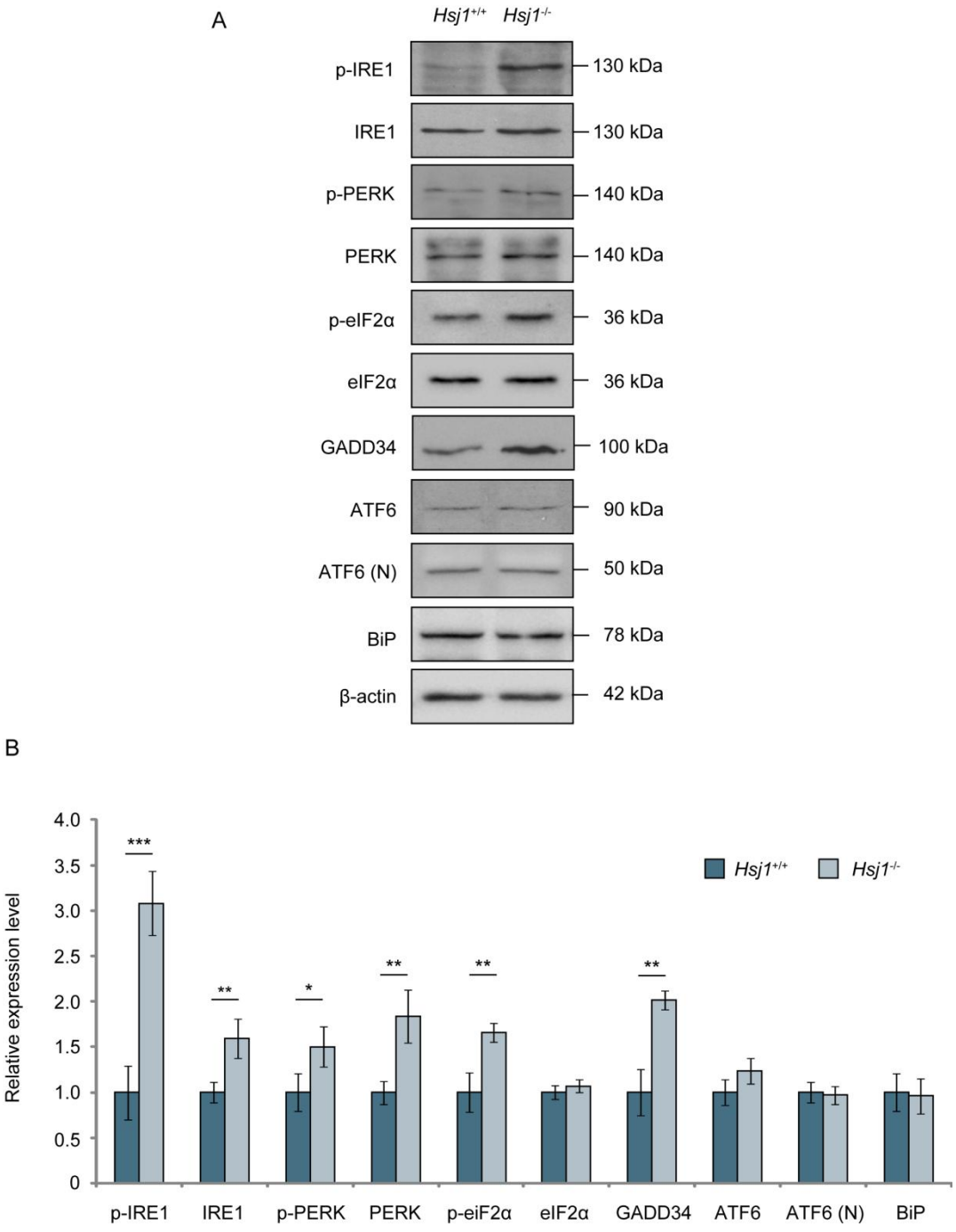

Figure 6.14 UPR markers in *Hsj1*$^{+/+}$ and *Hsj1*$^{-/-}$ spinal cords at P10. A: 30 µg of spinal cord lysate from *Hsj1*$^{+/+}$ and *Hsj1*$^{-/-}$ P10 mice was resolved by SDS-PAGE. Western blot analysis was performed using rabbit antibodies against p-IRE1, IRE1, p-PERK, PERK, p-eIF2α, eIF2α, GADD34, ATF6 and BiP, all used at a dilution of 1:1000, and a monoclonal mouse antibody against β-actin (1:5000). **B:** Western blots were analysed using ImageJ. The level of each UPR marker was corrected for loading using β-actin before being normalised to the level of the UPR marker in *Hsj1*$^{+/+}$ mice. Error bars represent ± SD (*** P <0.001, ** P <0.01, Student's t-test, n=4).

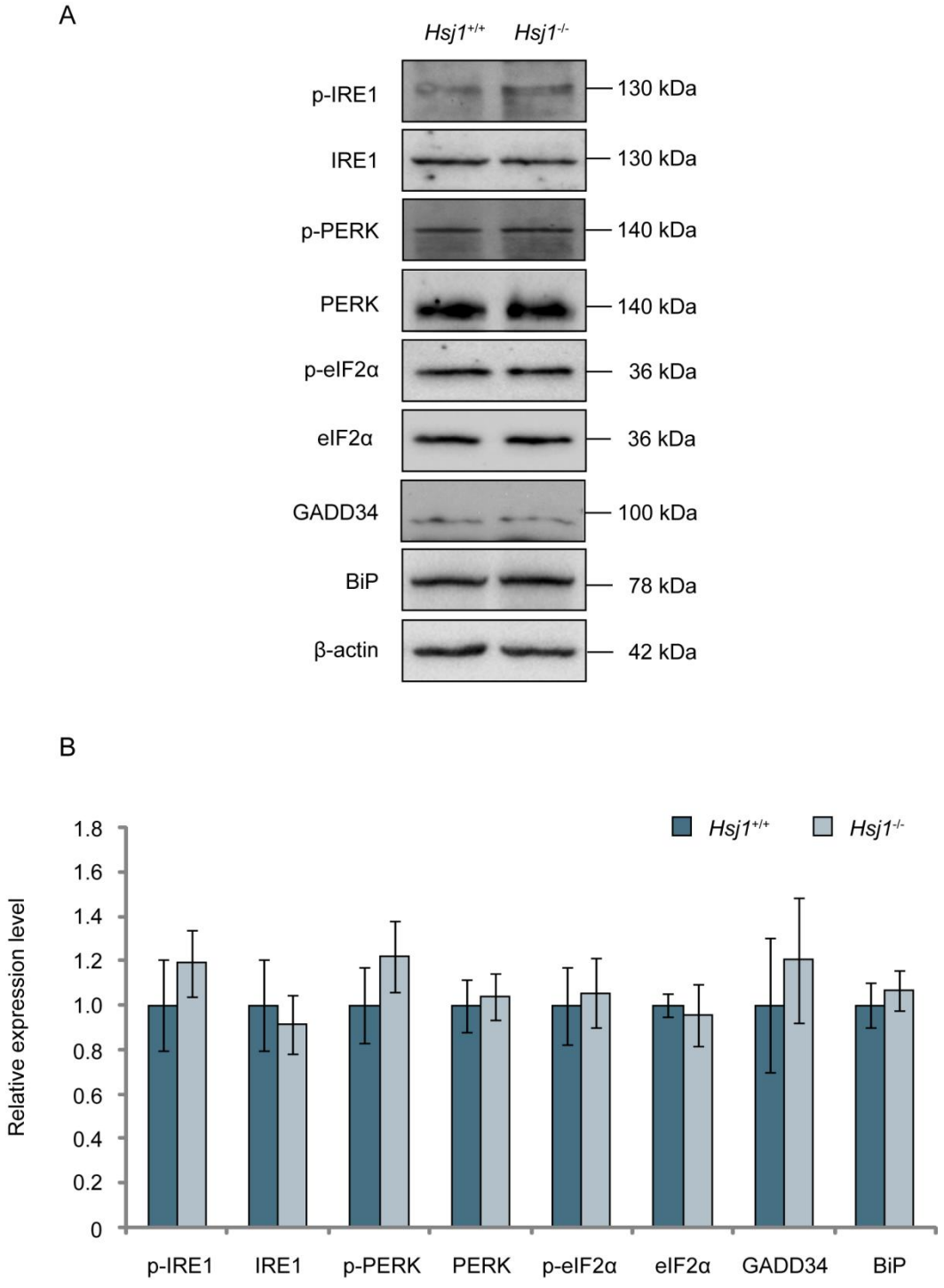

Figure 6.15 UPR markers in *Hsj1*$^{+/+}$ and *Hsj1*$^{-/-}$ spinal cords at P15. A: 30 µg of spinal cord lysate from *Hsj1*$^{+/+}$ and *Hsj1*$^{-/-}$ P15 mice was resolved by SDS-PAGE. Western blot analysis was performed using rabbit antibodies against p-IRE1, IRE1, p-PERK, PERK, p-eIF2α, eIF2α, GADD34, ATF6 and BiP, all used at a dilution of 1:1000, and a monoclonal mouse antibody against β-actin (1:5000). **B:** Western blots were analysed using ImageJ. The level of each UPR marker was corrected for loading using β-actin before being normalised to the level of the UPR marker in *Hsj1*$^{+/+}$ mice. Error bars represent ± SD (N.S, Student's t-test, n=4).

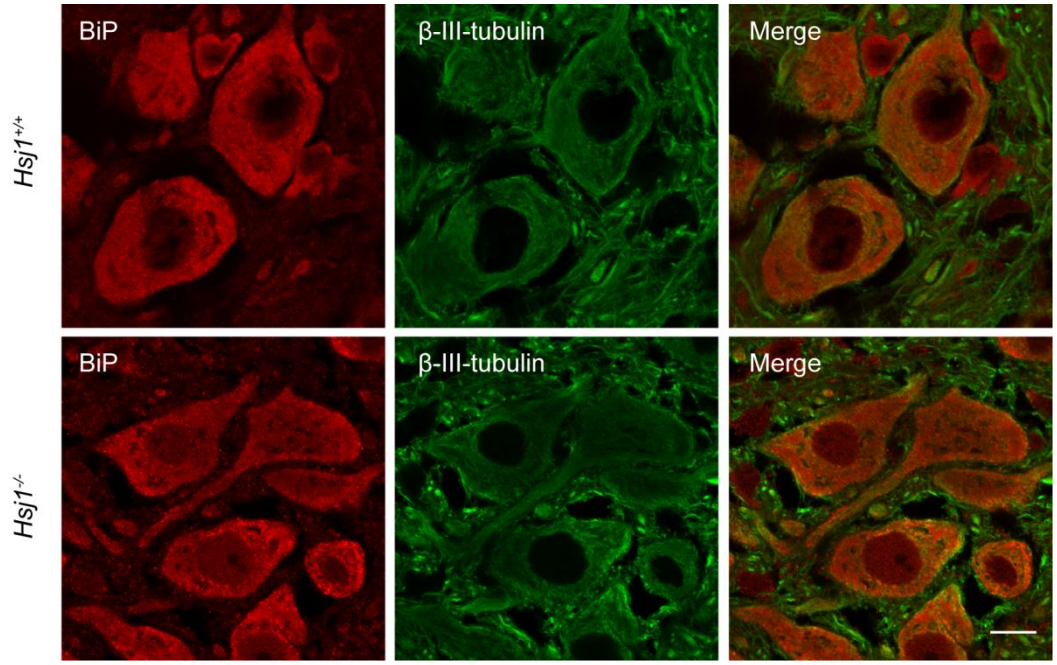

Figure 6.16 BiP staining in *Hsj1*$^{+/+}$ and *Hsj1*$^{-/-}$ motor neurons at P15. Spinal cord sections from *Hsj1*$^{+/+}$ and *Hsj1*$^{-/-}$ P15 mice were immunostained with a rabbit BiP antibody at a 1:750 dilution (Cy3 red) and a mouse β-III-tubulin antibody at a 1:750 dilution (Cy2 green). Sections were imaged on a Zeiss LSM 700 confocal microscope. Only large, β-III-tubulin positive cells in a location consistent with motor neurons were imaged. Settings were maintained during the imaging of the *Hsj1*$^{+/+}$ and *Hsj1*$^{-/-}$ motor neurons. Scale bar, 10 µm.

6.3 Discussion

Previous data from our lab identified a reduction in motor neuron counts in the spinal cords of both 120 day old and 20 day old *Hsj1*$^{-/-}$ mice (Wendy Mustill and Anna Gray). To confirm the loss of motor neurons at P20 and to establish whether motor neuron loss was occurring during development or postnatally, mice expressing GFP specifically in motor neurons were utilised to assist the counting process in *Hsj1*$^{+/+}$ and *Hsj1*$^{-/-}$ mice at P10, P15 and P20. Hb9:*GFP*$^{+/-}$ *Hsj1*$^{+/+}$ and Hb9:*GFP*$^{+/-}$ *Hsj1*$^{-/-}$ mice showed no difference in motor neuron counts at P10 and P15. The data therefore suggested that the loss of motor neurons occurs postnatally, between P15 and P20. Unfortunately, due to the loss of GFP expression between P15 and P20, Hb9:*GFP*$^{+/-}$ mice could not be used to quantify the number of motor neurons present at P20. Instead, the Nissl stain, gallocyanine, was used to count the motor neurons in the spinal cord sections of P15 and P20 *Hsj1*$^{+/+}$ and *Hsj1*$^{-/-}$ mice. *Hsj1*$^{-/-}$ mice revealed a significant 11.6% loss of motor neurons at P20. The loss of motor neurons therefore occurs after P15, as suggested by the data from the Hb9:*GFP*$^{+/-}$ mice.

The two methods of counting motor neurons yielded comparable results. Hb9:*GFP*$^{+/-}$ *Hsj1*$^{+/+}$ mice had an average of 19.5 motor neurons per spinal cord section at P15. At the same time point, *Hsj1*$^{+/+}$ spinal cords stained with gallocyanine displayed a slightly higher average, with 21.5 motor neurons per spinal cord section. The comparison of the two values suggests that, on average, two gallocyanine-stained cells per section may have been incorrectly identified as motor neurons. However, the error between the two values is subtle, and both values are consistent with published motor neuron counts from wild-type mice (Zhao *et al.* 2011, Guo *et al.* 2013, Iguchi *et al.* 2013). The concordance with published data suggests that the counts obtained from both Hb9:*GFP*$^{+/-}$ mice and through gallocyanine staining are reliable.

Motor neurons are classified into subtypes according to the contractile properties of the motor units they form. Motor neurons are classed as fast fatigable (FF), fast fatigue-resistant (FR) or slow fatigue-resistant (S). FF motor neurons are the largest, with more dendritic and axonal branches than the other two subtypes. FF motor neurons were identified as the first motor neurons to undergo degeneration in SOD1 G93A mice, followed by FR motor neurons (Frey *et al.* 2000). S motor neurons were relatively resistant to degeneration, remaining preserved until late stages of the disease. To examine whether FF motor neurons were particularly vulnerable to the loss of Hsj1, the average soma area of motor neurons in P15 and P20 *Hsj1*$^{+/+}$ and *Hsj1*$^{-/-}$ mice was measured. *Hsj1*$^{-/-}$ motor neurons were significantly smaller than *Hsj1*$^{+/+}$ motor neurons at both P15 and P20. *Hsj1*$^{-/-}$ motor neurons were reduced from an average size of 390 to 343 μm^2 at P15, with a reduction from 401 to 354 μm^2 at

P20. There was no significant difference in the area of *Hsj1*$^{-/-}$ motor neurons at P15 and P20. Cell shrinkage is a classical feature of degeneration and it is possible that the large motor neurons shrink prior to P15, before undergoing cell death. Alternatively, the smaller area may indicate a developmental failure (d'Errico *et al.* 2013). To clarify whether FF motor neurons are indeed susceptible to degeneration in this model, the number of FF motor neurons at P15 and P20 could be compared using a marker protein. Recently, the examination of gene expression profiles in vulnerable and resistant motor neurons revealed that matrix metalloproteinase-9 (MMP-9) was solely expressed in FF motor neurons (Kaplan *et al.* 2014). The immunostaining of MMP-9 could therefore be used to distinguish FF motor neurons from the other two subtypes.

Alternatively, the selective vulnerability of FF motor neurons could be investigated by assessing the number of FF motor units in leg muscles, such as the extensor digitorum longus (EDL) or tibialis anterior (TA) muscle. A reduction in motor unit number would indicate the loss of FF motor neurons. It would be interesting to assess FF motor unit number at P15, prior to the cell death. A reduction in motor unit number at P15 would support a 'dying-back' phenomenon, whereby denervation of the NMJ is the first pathological event to occur and is followed by the gradual degeneration of the neuron towards the cell body. Increasing experimental evidence suggests that motor neuron degeneration in ALS may proceed through a dying-back mechanism. Several studies in SOD1 G93A mice found that NMJ denervation occurs at an early stage of the disease, long before the loss of motor neuron cell bodies (Fischer *et al.* 2004, Rocha *et al.* 2014). Assessing motor unit number in *Hsj1*$^{-/-}$ mice could greatly enhance our understanding of the degeneration process and may pinpoint whether NMJ denervation is an early pathological event in disease progression.

At P15, 10% of *Hsj1*$^{-/-}$ motor neurons appeared chromatolytic, with the loss of Nissl bodies from the cytoplasm and the eccentric positioning of the nucleus and nucleolus. Chromatolysis has been reported to be induced by axonal injury, ischemia and neurotoxicity, and is a prominent pathological feature of neurodegenerative diseases such as ALS, SMA and AD (Wakayama *et al.* 1992, Sasaki *et al*. 2011, Tapia *et al.* 2012, Palanca *et al.* 2014). Chromatolysis is regarded as a sign of degeneration and is often followed by apoptosis (Martin *et al.* 1999). The 10% of chromatolytic motor neurons at P15 may therefore represent the motor neurons that are lost by P20.

The loss of Nissl bodies in the cytoplasm of chromatolytic neurons is caused by structural changes in the RER network. Electron microscopy of chromatolytic motor neurons in SOD1 G93A mice revealed extensive morphological alterations, with RER appearing collapsed,

fragmented and with the detachment of membrane-associated polyribosomes (Riancho *et al.* 2014). These structural changes compromise the ability of the ER to participate in active translation, thereby suppressing protein synthesis. The disruption of the RER network is proposed to be a manifestation of chronic ER stress. Chronic ER stress is an early pathological event observed in SOD1 G93A mice and precedes the appearance of chromatolytic motor neurons (Saxena *et al.* 2009, Riancho *et al.* 2014). The appearance of chromatolytic motor neurons in *Hsj1*$^{-/-}$ mice suggests that the loss of Hsj1 may result in ER stress. To probe this possibility, UPR markers were examined in spinal cord lysates from P10 and P15 mice. At P10, expression levels of phosphorylated PERK, total PERK, phosphorylated eIF2α and GADD34 were increased in *Hsj1*$^{-/-}$ spinal cords, indicating that the PERK branch of the UPR had been activated. The activation of the PERK branch can mediate a pro-survival or pro-apoptotic response. To determine which response is generated in *Hsj1*$^{-/-}$ spinal cords, the expression of ATF4 target genes should be examined. The upregulation of ER chaperones or ERAD components would indicate a protective response, whereas the upregulation of the transcription factor CHOP could indicate a pro-apoptotic response (Walter *et al.* 2011). In SOD1 G85R and G93A mouse models, the activation of the PERK branch appears to drive a protective response, promoting motor neuron survival. The hemizygous deletion of PERK in SOD1 G85R mice accelerated disease onset and shortened life span (Wang *et al.* 2011). The acceleration in disease was proposed to be caused by the loss of PERK-mediated inhibition of general translation, preventing the downregulation of SOD1 G85R synthesis. Indeed, sustaining eIF2α phosphorylation in mutant SOD1 mice delayed disease onset and prolonged lifespan (Wang *et al.* 2014). It is possible that the activation of the PERK branch is part of a protective adaptive response in *Hsj1*$^{-/-}$ mice.

It is interesting to note that in addition to phosphorylated PERK, total PERK, phosphorylated eIF2α and GADD34, expression levels of phosphorylated IRE1 and total IRE1 were also increased at P10. It will be important to clarify whether the IRE1 signalling pathway is active in future studies. To examine this possibility, the levels of spliced XBP-1 could be examined in *Hsj1*$^{-/-}$ spinal cords. The upregulation of both PERK and IRE1 themselves could indicate that UPR signalling is active prior to P10. Considering that chromatolysis is linked with chronic ER stress it would be important to establish the full time frame of UPR activation and determine whether UPR activation precedes the appearance of chromatolytic motor neurons.

Both the PERK and IRE1 branches of the UPR are capable of inducing ER stress-mediated cell death. How the two signalling pathways shift from a pro-survival to a pro-apoptotic response remains unclear. However, a recent study suggests that the temporal activation pattern of the two branches may contribute to cell fate decisions (Walter *et al.* 2015). Using

fluorescent cell reporters, XBP-1 splicing and ATF4 translation were monitored over time following tunicamycin treatment. The relative timing of IRE1 and PERK signalling differed between dying cells and those resistant to ER stress-induced death. In the IRE1 reporter cells, early onset and early attenuation in XBP-1 splicing was observed in cells resistant to death. In the PERK reporter cells, resistant cells showed a slow translation of ATF4 and a late re-initiation of general translation. Temporal differences in the relative dynamics of the signalling pathways therefore appear to dictate either a pro-survival or pro-apoptotic response.

Further investigations are required to elucidate whether UPR signalling drives motor neuron degeneration in *Hsj1*$^{-/-}$ mice. Although the UPR appears to be activated in spinal cords lysates, its occurrence in motor neurons needs to be confirmed. If the UPR is indeed activated in motor neurons it would be interesting to determine the proportion of motor neurons that show such activation. The global activation of the UPR could possibly suggest differential responses in vulnerable and resistant motor neurons. In resistant motor neurons the UPR may mediate a pro-survival response, whereas a pro-apoptotic response may occur in the vulnerable motor neurons. This selective vulnerability may be driven by differences in the temporal dynamics of IRE1 and PERK signalling pathways in different motor neurons (Walter *et al.* 2015). Alternatively, the UPR may be selectively activated in the 11.6% of motor neurons that degenerate. This is seen in SOD1 G93A mice (Saxena *et al.* 2009). Essentially all subtypes of motor neurons showed an increase in ubiquitin signal 25-30 days before the earliest denervation event occurs; however, an unfolded protein response was only initiated in the vulnerable FF motor neurons. A recent study sought to build on these findings and investigate the mechanism underlying motor neuron subtype-selective ER stress (Filézac de L'Etang *et al.* 2015). Using qPCR, gene expression profiles of ER resident proteins were examined in vulnerable and resistant motor neurons in wild-type mice, with the aim of characterising the molecular environment of the ER in the two motor neuron subtypes. ER resident proteins were found to be differentially expressed in FF and S motor neurons. Vulnerable FF motor neurons displayed 2-3 fold higher levels of transcripts belonging to the ERAD machinery and the ER stress sensors PERK, IRE1 and eIF2α. In contrast, resistant S motor neurons were enriched for transcripts encoding protein folding chaperones. An enhanced protein folding capacity of the ER therefore appears to confer S motor neurons resistant to the activation of the UPR.

It is interesting to contemplate whether the distinct molecular environment of the ER in FF motor neurons renders them particularly vulnerable to the loss of the ER-associated isoform, HSJ1b. High expression levels of ERAD machinery and ER stress sensors implies that FF motor neurons may be particularly prone or vulnerable to protein misfolding in the ER

(Filézac de L'Etang *et al.* 2015). FF motor neurons may therefore place high demands on the ERAD system to efficiently remove misfolded protein and maintain proteostasis in the ER. If the ERAD system is basally under considerable strain, the ER may be unable to tolerate impairments in the pathway. As discussed in previous chapters, HSJ1b functions to target misfolded clients for ERAD. Considering the apparent high rate of protein misfolding in FF motor neurons, HSJ1b may be required to target a larger number of proteins for degradation. If this were the case, the loss of HSJ1b could substantially increase the load of misfolded proteins in the ER of FF motor neurons, activating the unfolded protein response. The high level of misfolded protein could potentially overwhelm the protective capabilities of the UPR in 10% of FF motor neurons, triggering a pro-apoptotic response (Figure 6.17). To investigate the selective vulnerability of FF motor neurons further, it would be interesting to examine HSJ1 expression levels in motor neuron subtypes. The upregulation of HSJ1b in FF motor neurons, in addition to other ERAD components, would support the hypothesis that HSJ1b targets a larger number of proteins for degradation in FF motor neurons and therefore plays a more critical role in maintaining ER homeostasis. The differential demands on the ERAD machinery, and possible on HSJ1b itself, could account for the potential vulnerability of FF motor neurons to the loss of HSJ1b.

The activation of the UPR can most likely be attributed to the loss of the ER-associated isoform, HSJ1b, as discussed above. However, it cannot be ruled out that UPR activation lies downstream of the loss of the cytosolic isoform, HSJ1a. In SBMA mice, activation of the UPR was found to be downstream of protein misfolding in the cytosol (Montague *et al.* 2014). SBMA is caused by a polyglutamine expansion in the androgen receptor gene. The mutant androgen receptor aggregates into inclusions, preventing the binding of androgen ligand to the receptor and the subsequent translocation of the protein to the nucleus where it activates target genes. One of the target genes regulated by androgen receptor is the 2b isoform of sarco/endoplasmic reticulum calcium ATPase (SERCA2b) (Foradori *et al.* 2008). SERCA2b expression levels were reduced in cultured embryonic motor neurons from SBMA mice, resulting in the depletion of ER Ca^{2+} levels (Montague *et al.* 2014). The reduction in Ca^{2+} levels lead to ER stress, with UPR markers observed in cell culture and in the spinal cords of SBMA mice. The loss of both Hsj1 isoforms could therefore, in theory, contribute to UPR activation, through the accumulation of misfolded proteins in the ER or in the cytosol.

At P15, *Hsj1*$^{-/-}$ spinal cord lysates exhibited a 1.9 fold increase in the level of ubiquitylated protein. In addition, *Hsj1*$^{-/-}$ mice also displayed a significant increase in LC3-II levels. The levels of p62 remained unchanged, suggesting that the increase in LC3-II was caused by an increase in autophagosome formation rather than a block in autophagosome degradation.

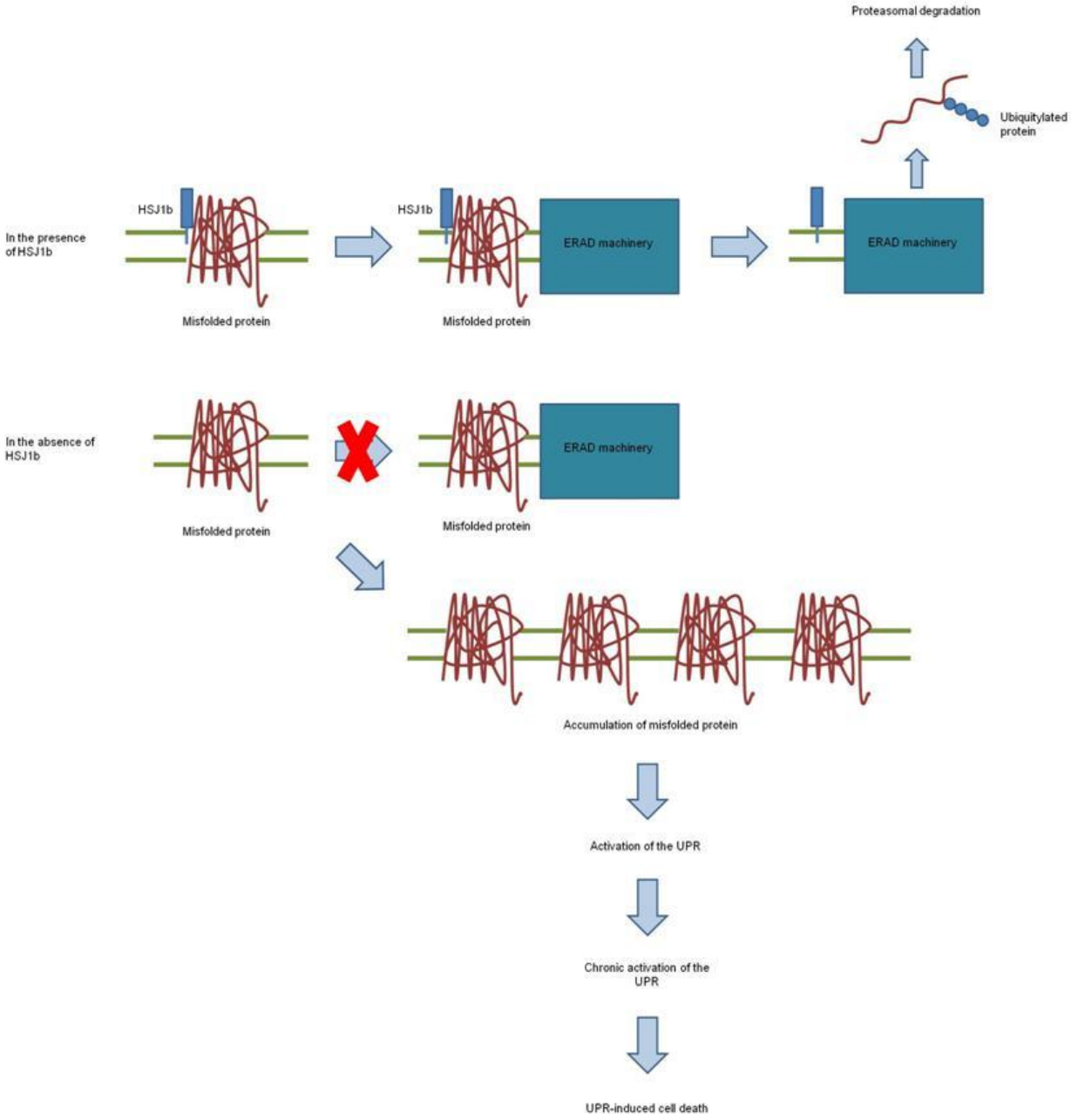

Figure 6.17 A potential model for how the loss of HSJ1 activates the UPR. HSJ1b binds to misfolded ER transmembrane proteins and targets them for ERAD. In the absence of HSJ1b, misfolded proteins fail to be targeted for ERAD, leading to their accumulation. In FF motor neurons, the load of misfolded proteins may be sufficient to activate the UPR. The high level of misfolded protein may overwhelm the protective capabilities of the UPR, resulting in a pro-apoptotic response being mediated.

The number of p62 puncta in *Hsj1*$^{+/+}$ motor neurons correlated with published p62 counts performed on the motor neurons of three month old wild-type mice (Bandyopadhyay *et al.* 2014). Interestingly, there was a subtle shift in the number of p62 puncta in the motor neurons of *Hsj1*$^{-/-}$ mice, with a 4% decrease in the percentage of motor neurons containing less than 15 puncta, and a 5% increase in the percentage of motor neurons containing 15-30 puncta. The shift did not reach statistical significance; however, considering the small change in percentage it may be worthwhile to increase the number of motor neurons analysed. Considering that both HSJ1a and HSJ1b target misfolded proteins for degradation, an increase in ubiquitylated protein and a rise in LC3-II levels could be attributed to the loss of either Hsj1 isoform. The ubiquitylated protein could represent misfolded and potentially aggregated Hsj1 client proteins, or alternatively, misfolded proteins retrotranslocated from the ER following an ER stress-induced UPR-mediated upregulation of ERAD. In both scenarios the increase in autophagy is likely to represent a protective response in an attempt to clear the misfolded proteins. It will be important to dissect the order in which the responses are observed in future studies. The activation of the UPR followed by an increase in ubiquitylated protein would support the hypothesis the accumulation of misfolded proteins in the ER caused by the loss of HSJ1b is the initiator of motor neuron degeneration. The accumulation of ubiquitylated protein followed by the activation of the UPR would establish HSJ1a as the critical isoform. Of course, the two mechanisms may not be mutually exclusive; the loss of both HSJ1 isoforms could contribute to disease pathogenesis. The use of mice expressing HSJ1a only (h*HSJ1a*$^{+/-}$: *Hsj1*$^{-/-}$) or HSJ1b only (h*HSJ1b*$^{+/-}$: *Hsj1*$^{-/-}$) generated by our lab will prove to be a particularly valuable tool for defining the role of each isoform in motor neurons and their respective importance in motor neuron survival. Preliminary data from the HSJ1a only and HSJ1b only mice suggests that the loss of the HSJ1b isoform drives motor neuron degeneration (Bernadett Kalmar unpublished observations). At 120 days, HSJ1a only mice exhibited a significant reduction in EDL motor units. No significant reduction in motor unit number was observed in the HSJ1b only mice. It would be interesting to build on these findings in the future and establish whether a loss of motor units in HSJ1a only mice is accompanied by a loss of motor neurons. A 10% loss of motor neurons in HSJ1a only mice would place ER stress at the centre of disease pathogenesis and would potentially help to identify critical client proteins.

Mouse models of dHMN and CMT2 have increased the scope to investigate the underlying mechanisms of motor neuron degeneration. Many of the models recapitulate the phenotype of the disease and have identified dysfunctions in a wide range of cellular processes. However, not all mouse models of dHMN and CMT2 display motor neuron deficits, as seen with the *Hsj1*$^{-/-}$ mice. LRSAM1 mutations are typically associated with autosomal dominant

CMT2; however, a mutation in *LRSAM1* was identified in one family with autosomal recessive CMT2, with the mutation causing a loss of function phenotype (Guernsey *et al.* 2010). *Lrsam1* knockout mice appear healthy and demonstrate largely normal neuromuscular performance (Bogdanik *et al.* 2013). Even though the mice did not show a motor deficit, the axons of *Lrsam1*$^{-/-}$ motor neurons were found to be more sensitive when challenged with the neurotoxic agent, acrylamide. Greater axonal degeneration was observed after acrylamide treatment, indicating that the loss of Lrsam1 compromised axonal homeostasis, making them more vulnerable to degeneration upon exposure to cell stress. It would be interesting to examine whether the exposure of *Hsj1*$^{-/-}$ mice to cell stress could exacerbate motor neuron degeneration. This could be achieved by examining axonal regeneration after sciatic nerve lesion. Impaired or delayed NMJ re-innervation could indicate that the loss of HSJ1 compromises the ability of motor neurons to restore homeostasis after exposure to cell stress. Conferring a vulnerability to cell stress could account for the lack of apparent motor deficits observed in both *Lrsam1*$^{-/-}$ and *Hsj1*$^{-/-}$ mice. Mouse motor neurons are unlikely to experience the same type, magnitude and frequency of stress compared to human motor neurons. However, there are other possible explanations for the disparity between the mouse and human phenotype. Differences in gene expression between mouse and human motor neurons could mask the deficiencies caused by the loss of Hsj1 in the mouse model. For example, mice may only express Hsj1 client proteins in 10% of motor neurons. Alternatively, mice may express a compensatory protein that is able to orchestrate the required functions normally mediated by Hsj1. Examining motor neuron degeneration on different genetic backgrounds could reveal a more pronounced phenotype. For example, GARS C201R mice exhibited a relative mild motor phenotype on a C3H genetic background; a more severe phenotype was observed on a C57BL/6 background (Achilli *et al.* 2009).

Overall, the results described in this Chapter identify UPR activation, an accumulation of ubiquitylated protein, an increase in autophagy and chromatolysis as key cellular events that occur prior to motor neuron cell death in *Hsj1*$^{-/-}$ mice. It will be important to expand on these findings in the future and characterise the degeneration process in detail. Identifying the cellular event that acts as the initial trigger for motor neuron dysfunction could enhance our outstanding of HSJ1 function and characterising motor neuron degeneration in HSJ1a only and HSJ1b only mice may establish whether one of the HSJ1 isoforms plays a more dominant role in motor neuron survival.

Chapter 7 – Discussion

Unravelling the genetic etiology of dHMN and CMT2 has provided fundamental insights into the cellular mechanisms that underlie motor neuron degeneration. Recently, mutations in the DnaJ protein, HSJ1, were reported in autosomal recessive cases of the disease (Blumen *et al.* 2012, Gess *et al.* 2014). The identification of *HSJ1* as a novel causative gene extends the number of causative genes with protein products that function in protein quality control, strengthening the concept that motor neurons are particularly vulnerable to impairments in proteostasis.

The protective role of HSJ1 in motor neurons is highlighted by the ability of the HSJ1a isoform to combat the aggregation of ALS-associated proteins in cell and mouse models of the disease (Novoselov *et al.* 2013, Jack Miller, MSc project, UCL). In Chapter 3, I propose that HSJ1a may also mediate a protective effect against mutant ubiquilin-2 aggregation. The data presented in Chapter 3 identifies ubiquilin-2, a protein recently implicated in ALS, as a novel binding partner of HSJ1a. The ability of HSJ1a to bind to ALS-linked ubiquilin-2 mutants suggests that HSJ1a overexpression could potentially modulate mutant ubiquilin-2 aggregation in cells. It will be important to build on these findings in future studies and determine whether HSJ1a represents a therapeutic target that could be used to delay motor neuron degeneration in ubiquilin-2 linked cases of ALS.

The protective role of HSJ1 in motor neurons is further highlighted by the loss of function phenotype underlying dHMN and CMT2. The data presented in Chapter 4 and Chapter 5 of this thesis extends the spectrum of HSJ1 patient mutations, characterising the recently identified HSJ1-Y5C substitution as a disease-causing loss of function mutation. All three patient mutations identified to date are therefore loss of function mutations. HSJ1 therefore appears critical for motor neuron survival.

Investigations using a *Hsj1* knockout mouse model place impairments in proteostasis at the centre of disease pathogenesis. Prior to motor neuron degeneration, *Hsj1*$^{-/-}$ mice exhibited an increase in ubiquitylated protein, an increase in autophagosome formation and activation of the IRE1 and PERK branches of the UPR. The activation of these cellular stress responses supports the hypothesis that the loss of HSJ1 leads to an increase in the levels of misfolded protein, potentially due to impairments in the targeting of proteins for degradation. It remains to be determined whether the accumulation of HSJ1a or HSJ1b client proteins is more detrimental to motor neurons. However, a number of observations suggest that the accumulation of HSJ1b client proteins may be more deleterious. Firstly, the higher expression levels of HSJ1b compared to HSJ1a in human fibroblasts and mouse brain and

spinal cord tissue implies that HSJ1b may play a more prominent role in protein clearance (Chapple and Cheetham 2003, Blumen *et al.* 2012). As such, the loss of HSJ1b would be expected to have a greater impact on proteostasis compared to the loss of HSJ1a. Secondly, only HSJ1a only mice displayed a reduction in EDL motor units; no reduction in EDL motor units was observed in HSJ1b only mice (Bernadett Kalmar, personal communications). Taking these observations into consideration, I propose a model that places the loss of the HSJ1b isoform at the centre of disease pathogenesis. Based on the increase in protein ubiquitylation upon the restoration of HSJ1b in patient fibroblasts, I propose a model whereby UPR activation in *Hsj1*$^{-/-}$ mice is driven by the inability to target HSJ1b misfolded clients for ubiquitylation, impairing the ERAD process and subsequently resulting in the accumulation of misfolded proteins in the ER. I hypothesise that the demand for HSJ1b-mediated ERAD in motor neurons overwhelms the ER with misfolded protein, leading to a vicious cycle that results in the collapse of ER proteostasis. I propose that the UPR is unable to compensate for the loss of HSJ1b and ultimately triggers UPR-induced cell death.

Of course, they are many aspects of the disease mechanism that require further investigation. The identification of endogenous HSJ1 client proteins could prove to be particularly informative; examining the levels of HSJ1 client proteins in the motor neurons of *Hsj1*$^{-/-}$ mice could help to ascertain whether the targeting of proteins for degradation is indeed impaired in the absence of HSJ1. Interestingly, the copper transporter ATP7A has recently been identified to interact with HSJ1 in a high-throughput proteomic study (Huttin *et al.* 2015, BioGRID, pre-publication). Mutations in *ATP7A* have been identified in patients with X-linked dHMN, highlighting its important role in motor neuron survival (Kennerson *et al.* 2010). As a membrane protein, ATP7A will be folded in the ER, potentially interacting with HSJ1b; therefore, ATP7A could represent a HSJ1b client protein. It will be interesting to determine whether the loss of HSJ1 has any effect on the folding or degradation of ATP7A. Such investigations could potentially implicate impaired copper homeostasis as a cause of motor neuron degeneration in this model.

Future investigations should also aim to identify and characterise motor neuron-specific HSJ1 clients or indeed HSJ1 client proteins that are expressed at high levels in motor neurons. Such investigations could provide important insights into why motor neurons are selectively vulnerable to the loss of HSJ1.

It is hoped that the generation of iPSC-derived motor neurons from patient fibroblasts will help to address the outstanding questions. Importantly, iPSC-derived motor neurons will mimic the human disease in relation to the fact that, unlike *Hsj1*$^{-/-}$ mice, motor neurons in this cell model will need to continually degrade HSJ1-Y5C protein. It will be interesting to

determine whether this additional demand on the UPS enables the cell model to more closely reflect the human disease and the extent of motor neuron degeneration. iPSC-derived motor neurons from the HSJ1-Y5C patients have now been generated by the lab and are currently being characterised.

Overall, the data presented in this Thesis builds on our understanding of the function of HSJ1 in motor neurons, highlighting its protective role and suitability as a therapeutic target in cases where motor neuron degeneration is driven by impairments in proteostasis.

References

Al-Chalabi, A., Calvo, A., Chio, A., Colville, S., Ellis, C. M., Hardiman, O., Heverin, M., Howard, R. S., Huisman, M. H., Keren, N., Leigh, P. N., Mazzini, L., Mora, G., Orrell, R. W., Rooney, J., Scott, K. M., Scotton, W. J., Seelen, M., Shaw, C. E., Sidle, K. S., Swingler, R., Tsuda, M., Veldink, J. H., Visser, A. E., van den Berg, L. H., Pearce, N. (2014). Analysis of amyotrophic lateral sclerosis as a multistep process: a population-based modelling study. *Lancet Neurol.* **13:** 1108-1113.

Alexandru, G., Graumann, J., Smith, G. T., Kolawa, N. J., Fang, R., & Deshaies, R. J. (2008). UBXD7 binds multiple ubiquitin ligases and implicates p97 in HIF1alpha turnover. *Cell* **134:** 804-816.

Anfinsen, C. B. (1973). Principles that govern the folding of protein chains. *Science* **181**: 223-230.

Antonellis, A., Ellsworth, R. E., Sambuughin, N., Puls, I., Abel, A., Lee-Lin, S. Q., Green, E.D. (2003). Glycyl tRNA synthetase mutations in Charcot-Marie-Tooth disease type 2D and distal spinal muscular atrophy type V. *Am. J. Hum. Genet.* **72:** 1293-1299.

Antonellis, A., Lee-Lin, S. Q., Wasterlain, A., Leo, P., Quezado, M., Goldfarb, L. G., Myung, K., Burgess, S., Fischbeck, K. H., Green, E. D. (2006). Functional analyses of glycyl-tRNA synthetase mutations suggest a key role for tRNA-charging enzymes in peripheral axons. *J. Neurosci*. **26:** 10397-10406.

Arrasate, M., Mitra, S., Schweitzer, E. S., Segal, M. R., & Finkbeiner, S. (2004). Inclusion body formation reduces levels of mutant huntingtin and the risk of neuronal death. *Nature* **431:** 805-810.

Auer-Grumbach, M., Olschewski, A., Papić, L., Kremer, H., McEntagart, M. E., Uhrig, S., Fischer, C., Fröhlich, E., Bálint, Z., Tang, B., Strohmaier, H., Lochmüller, H., Schlotter-Weigel, B., Senderek, J., Krebs, A., Dick, K. J., Petty, R., Longman, C., Anderson, N. E., Padberg, G. W., Schelhaas, H. J., van Ravenswaaij-Arts, C. M., Pieber, T. R., Crosby, A. H., Guelly, C. (2010). Alterations in the ankyrin domain of TRPV4 cause congenital distal SMA, scapuloperoneal SMA and HMSN2C. *Nat. Genet.* **42:** 160-164.

Auluck, P. K., Chan, H. Y., Trojanowski, J. Q., Lee, V. M., & Bonini, N. M. (2002). Chaperone suppression of alpha-synuclein toxicity in a Drosophila model for Parkinson's disease. *Science* **295:** 865-868.

Baets, J., De Jonghe, P., & Timmerman, V. (2014). Recent advances in Charcot-Marie-Tooth disease. *Curr. Opin. Neurol*. **27:** 532-540.

Balastik, M., Ferraguti, F., Pires-da Silva, A., Lee, T. H., Alvarez-Bolado, G., Lu, K. P., & Gruss, P. (2008). Deficiency in ubiquitin ligase TRIM2 causes accumulation of neurofilament light chain and neurodegeneration. *Proc. Natl. Acad. Sci. U S* A **105:** 12016-12021.

Baloh, R. H. (2008). Mitochondrial dynamics and peripheral neuropathy. *Neuroscientist* **14:** 12-18.

Bandyopadhyay, U., Nagy, M., Fenton, W.A., Horwich, A.L. (2014). Absence of lipofuscin in motor neurons of SOD1-linked ALS mice. *Proc. Natl. Acad. Sci. U S A* **111:** 11055-11060.

Benitez, B. A., Alvarado, D., Cai, Y., Mayo, K., Chakraverty, S., Norton, J., Morris, J. C., Sands, M. S., Goate, A., Cruchaga, C. (2011). Exome-sequencing confirms DNAJC5 mutations as cause of adult neuronal ceroid-lipofuscinosis. *PLoS One* **6:** e26741.

Bernassola, F., Karin, M., Ciechanover, A., & Melino, G. (2008). The HECT family of E3 ubiquitin ligases: multiple players in cancer development. *Cancer Cell* **14:** 10-21.

Bettens, K., Sleegers, K., & Van Broeckhoven, C. (2013). Genetic insights in Alzheimer's disease. *Lancet Neurol.* **12:** 92-104.

Bibikova, M., Beumer, K., Trautman, J. K., & Carroll, D. (2003). Enhancing gene targeting with designed zinc finger nucleases. *Science* **300:** 764.

Blumen, S. C., Astord, S., Robin, V., Vignaud, L., Toumi, N., Cieslik, A., Achiron, A., Carasso, R. L., Gurevich, M., Braverman, I., Blumen, N., Munich, A., Barkats, M., Viollet, L. (2012). A rare recessive distal hereditary motor neuropathy with HSJ1 chaperone mutation. *Ann. Neurol.* **71:** 509-519.

Bogdanik, L. P., Sleigh, J. N., Tian, C., Samuels, M. E., Bedard, K., Seburn, K. L., & Burgess, R. W. (2013). Loss of the E3 ubiquitin ligase LRSAM1 sensitizes peripheral axons to degeneration in a mouse model of Charcot-Marie-Tooth disease. *Dis. Model Mech.* **6:** 780-792.

Bouchard, J. P., Barbeau, A., Bouchard, R., & Bouchard, R. W. (1978). Autosomal recessive spastic ataxia of Charlevoix-Saguenay. *Can. J. Neurol. Sci.* **5:** 61-69.

Bouhouche, A., Benomar, A., Bouslam, N., Chkili, T., & Yahyaoui, M. (2006). Mutation in the epsilon subunit of the cytosolic chaperonin-containing t-complex peptide-1 (Cct5) gene causes autosomal recessive mutilating sensory neuropathy with spastic paraplegia. *J. Med. Genet.* **43:** 441-443.

Bozaykut, P., Ozer, N. K., & Karademir, B. (2014). Regulation of protein turnover by heat shock proteins. *Free Radic. Biol. Med.* **77:** 195-209.

Brennan, K. M., Bai, Y., & Shy, M. E. (2015). Demyelinating CMT-what's known, what's new and what's in store? *Neurosci. Lett.* **596:** 14-26.

Brodsky, J. L. (2012). Cleaning up: ER-associated degradation to the rescue. *Cell* **151:** 1163-1167.

Bross, P., Naundrup, S., Hansen, J., Nielsen, M. N., Christensen, J. H., Kruhøffer, M., Palmfeldt, J., Corydon, T. J., Gregersen, N., Ang, D., Georgopoulos, C., Nielsen, K. L. (2008). The Hsp60-(p.V98I) mutation associated with hereditary spastic paraplegia SPG13 compromises chaperonin function both in vitro and in vivo. *J. Biol. Chem.* **283:** 15694-15700.

Brownlees, J., Ackerley, S., Grierson, A. J., Jacobsen, N. J., Shea, K., Anderton, B. H., Leigh, P. N., Shaw, C. E., Miller, C. C. (2002). Charcot-Marie-Tooth disease neurofilament mutations disrupt neurofilament assembly and axonal transport. *Hum. Mol. Genet*. **11:** 2837-2844.

Burke, R. E., Levine, D. N., Tsairis, P., & Zajac, F. E. (1973). Physiological types and histochemical profiles in motor units of the cat gastrocnemius. *J. Physiol*. **234:** 723-748.

Carra, S., Crippa, V., Rusmini, P., Boncoraglio, A., Minoia, M., Giorgetti, E., Kampinga, H., Poletti, A. (2012). Alteration of protein folding and degradation in motor neuron diseases: Implications and protective functions of small heat shock proteins. *Prog. Neurobiol*. **97:** 83-100.

Carra, S., Seguin, S. J., Lambert, H., & Landry, J. (2008). HspB8 chaperone activity toward poly(Q)-containing proteins depends on its association with Bag3, a stimulator of macroautophagy. *J. Biol. Chem.* **283:** 1437-1444.

Carra, S., Sivilotti, M., Chávez Zobel, A. T., Lambert, H., & Landry, J. (2005). HspB8, a small heat shock protein mutated in human neuromuscular disorders, has in vivo chaperone activity in cultured cells. *Hum. Mol. Genet*. **14:** 1659-1669.

Cartoni, R., & Martinou, J. C. (2009). Role of mitofusin 2 mutations in the physiopathology of Charcot-Marie-Tooth disease type 2A. *Exp. Neurol.* **218:** 268-273.

Carvalho, P., Stanley, A. M., & Rapoport, T. A. (2010). Retrotranslocation of a misfolded luminal ER protein by the ubiquitin-ligase Hrd1p. *Cell* **143:** 579-591.

Chapple, J. P., & Cheetham, M. E. (2003). The chaperone environment at the cytoplasmic face of the endoplasmic reticulum can modulate rhodopsin processing and inclusion formation. *J. Biol. Chem*. **278:** 19087-19094.

Cheetham, M. E., Brion, J. P., & Anderton, B. H. (1992). Human homologues of the bacterial heat-shock protein DnaJ are preferentially expressed in neurons. *Biochem. J.* **284:** 469-476.

Cheetham, M. E., & Caplan, A. J. (1998). Structure, function and evolution of DnaJ: conservation and adaptation of chaperone function. *Cell Stress Chaperones* **3:** 28-36.

Chen, S., & Smith, D. F. (1998). Hop as an adaptor in the heat shock protein 70 (Hsp70) and hsp90 chaperone machinery. *J. Biol. Chem*. **273:** 35194-35200.

Christian, M., Cermak, T., Doyle, E. L., Schmidt, C., Zhang, F., Hummel, A., Bogdanove, A. J., Voytas, D. F. (2010). Targeting DNA double-strand breaks with TAL effector nucleases. *Genetics* **186:** 757-761.

Cleren, C., Calingasan, N. Y., Chen, J., & Beal, M. F. (2005). Celastrol protects against MPTP- and 3-nitropropionic acid-induced neurotoxicity. *J. Neurochem*. **94:** 995-1004.

Conklin, D., Holderman, S., Whitmore, T. E., Maurer, M., & Feldhaus, A. L. (2000). Molecular cloning, chromosome mapping and characterization of UBQLN3 a testis-specific gene that contains an ubiquitin-like domain. *Gene* **249:** 91-98.

Cottenie, E., Kochanski, A., Jordanova, A., Bansagi, B., Zimon, M., Horga, A., Jaunmuktane, Z., Saveri, P., Rasic, V. M., Baets, J., Bartsakoulia, M., Ploski, R., Teterycz, P., Nikolic, M., Quinlivan, R., Laura, M., Sweeney, M. G., Taroni, F., Lunn, M. P., Moroni, I., Gonzalez, M., Hanna, M. G., Bettencourt, C., Chabrol, E., Franke, A., von Au, K., Schilhabel, M., Kabzińska, D., Hausmanowa-Petrusewicz, I., Brandner, S., Lim, S. C., Song, H., Choi, B. O., Horvath, R., Chung, K. W., Zuchner, S., Pareyson, D., Harms, M., Reilly, M. M., Houlden, H. (2014). Truncating and missense mutations in IGHMBP2 cause Charcot-Marie Tooth disease type 2. *Am. J. Hum. Genet*. **95:** 590-601.

Crawford, T. O., & Pardo, C. A. (1996). The neurobiology of childhood spinal muscular atrophy. *Neurobiol. Dis.* **3:** 97-110.

Crippa, V., Sau, D., Rusmini, P., Boncoraglio, A., Onesto, E., Bolzoni, E., Galbiati, M., Fontana, E., Marino, M., Carra, S., Bendotti, C., De Biasi, S., Poletti, A. (2010). The small heat shock protein B8 (HspB8) promotes autophagic removal of misfolded proteins involved in amyotrophic lateral sclerosis (ALS). *Hum. Mol. Genet*. **19:** 3440-3456.

Cummings, C.J., Mancini, M.A., Antalffy, B., DeFranco, D.B., Orr, H.T., Zoghbi, H.Y. (1998). Chaperone suppression of aggregation and altered subcellular proteasome localization imply protein misfolding in SCA1. *Nat Genet.* **19:** 148-54.

d'Errico, P., Boido, M., Piras, A., Valsecchi, V., De Amicis, E., Locatelli, D., Capra, S., Vagni, F., Vercelli, A., Battaglia, G. (2013). Selective vulnerability of spinal and cortical motor neuron subpopulations in delta7 SMA mice. *PLoS One* **8:** e82654.

d'Ydewalle, C., Krishnan, J., Chiheb, D. M., Van Damme, P., Irobi, J., Kozikowski, A. P., Vanden Berghe, P., Timmerman, V., Robberecht, W., Van Den Bosch, L. (2011). HDAC6 inhibitors reverse axonal loss in a mouse model of mutant HSPB1-induced Charcot-Marie-Tooth disease. *Nat. Med*. **17:** 968-974.

Davey, K. M., Parboosingh, J. S., McLeod, D. R., Chan, A., Casey, R., Ferreira, P., Snyder, F. F., Bridge, P. J., Bernier, F. P. (2006). Mutation of DNAJC19, a human homologue of yeast inner mitochondrial membrane co-chaperones, causes DCMA syndrome, a novel autosomal recessive Barth syndrome-like condition. *J. Med. Genet.* **43:** 385-393.

de Brito, O. M., & Scorrano, L. (2008). Mitofusin 2 tethers endoplasmic reticulum to mitochondria. *Nature* **456:** 605-610.

de Brito, O. M., & Scorrano, L. (2010). An intimate liaison: spatial organization of the endoplasmic reticulum-mitochondria relationship. *EMBO J.* **29:** 2715-2723.

De Mena, L., Coto, E., Sánchez-Ferrero, E., Ribacoba, R., Guisasola, L. M., Salvador, C., Blázquez, M., Alvarez, V. (2009). Mutational screening of the mortalin gene (HSPA9) in Parkinson's disease. *J. Neural. Transm*. **116:** 1289-1293.

Deegan, S., Saveljeva, S., Gorman, A. M., & Samali, A. (2013). Stress-induced self-cannibalism: on the regulation of autophagy by endoplasmic reticulum stress. *Cell Mol. Life Sci.* **70:** 2425-2441.

Del Bigio, M. R., Chudley, A. E., Sarnat, H. B., Campbell, C., Goobie, S., Chodirker, B. N., & Selcen, D. (2011). Infantile muscular dystrophy in Canadian aboriginals is an αB-crystallinopathy. *Ann. Neurol*. **69:** 866-871.

Del Monte, F., & Agnetti, G. (2014). Protein post-translational modifications and misfolding: new concepts in heart failure. *Proteomics Clin. Appl*. **8:** 534-542.

Deng, H. X., Chen, W., Hong, S. T., Boycott, K. M., Gorrie, G. H., Siddique, N., Yang, Y., Fecto, F., Shi, Y., Zhai, H., Jiang, H., Hirano, M., Rampersaud, E., Jansen, G. H., Donkervoort, S., Bigio, E. H., Brooks, B. R., Ajroud, K., Sufit, R. L., Haines, J. L., Mugnaini, E., Pericak-Vance, M. A., Siddique, T. (2011). Mutations in UBQLN2 cause dominant X-linked juvenile and adult-onset ALS and ALS/dementia. *Nature* **477:** 211-215.

Deng, H. X., Klein, C. J., Yan, J., Shi, Y., Wu, Y., Fecto, F., Yau, H. J., Yang, Y., Zhai, H., Siddique, N., Hedley-Whyte, E. T., Delong, R., Martina, M., Dyck, P. J., Siddique, T. (2010). Scapuloperoneal spinal muscular atrophy and CMT2C are allelic disorders caused by alterations in TRPV4. *Nat. Genet*. **42:** 165-169.

Deshaies, R. J., & Joazeiro, C. A. (2009). RING domain E3 ubiquitin ligases. *Annu. Rev. Biochem*. **78:** 399-434.

Devlin, A. C., Burr, K., Borooah, S., Foster, J. D., Cleary, E. M., Geti, I., Vallier, L., Shaw, C. E., Chandran, S., Miles, G. B. (2015). Human iPSC-derived motoneurons harbouring TARDBP or C9ORF72 ALS mutations are dysfunctional despite maintaining viability. *Nat. Commun*. **6:** 5999.

DiFiglia, M., Sapp, E., Chase, K. O., Davies, S. W., Bates, G. P., Vonsattel, J. P., & Aronin, N. (1997). Aggregation of huntingtin in neuronal intranuclear inclusions and dystrophic neurites in brain. *Science* **277:** 1990-1993.

Drew, A. P., Blair, I. P., & Nicholson, G. A. (2011). Molecular genetics and mechanisms of disease in distal hereditary motor neuropathies: insights directing future genetic studies. *Curr. Mol. Med*. **11:** 650-665.

Edvardson, S., Cinnamon, Y., Ta-Shma, A., Shaag, A., Yim, Y. I., Zenvirt, S., Jalas, C., Lesage, S., Brice, A., Taraboulos, A., Kaestner, K. H., Greene, L. E., Elpeleg, O. (2012). A deleterious mutation in DNAJC6 encoding the neuronal-specific clathrin-uncoating co-chaperone auxilin, is associated with juvenile parkinsonism. *PLoS One* **7:** e36458.

El-Abassi, R., England, J. D., & Carter, G. T. (2014). Charcot-Marie-Tooth disease: an overview of genotypes, phenotypes, and clinical management strategies. *PM. R*. **6:** 342-355.

Ellis, J. (1987). Proteins as molecular chaperones. *Nature* **328:** 378-379.

Engert, J. C., Bérubé, P., Mercier, J., Doré, C., Lepage, P., Ge, B., Bouchard, J. P., Mathieu, J., Melançon, S. B., Schalling, M., Lander, E. S., Morgan, K., Hudson, T. J., Richter, A. (2000). ARSACS, a spastic ataxia common in northeastern Québec, is caused by mutations in a new gene encoding an 11.5-kb ORF. *Nat. Genet*. **24:** 120-125.

Evgrafov, O. V., Mersiyanova, I., Irobi, J., Van Den Bosch, L., Dierick, I., Leung, C. L., Schagina, O., Verpoorten, N., Van Impe, K., Fedotov, V., Dadali, E., Auer-Grumbach, M., Windpassinger, C., Wagner, K., Mitrovic, Z., Hilton-Jones, D., Talbot, K., Martin, J. J., Vasserman, N., Tverskaya, S., Polyakov, A., Liem, R. K., Gettemans, J., Robberecht, W., De Jonghe, P., Timmerman, V. (2004). Mutant small heat-shock protein 27 causes axonal Charcot-Marie-Tooth disease and distal hereditary motor neuropathy. *Nat. Genet.* **36:** 602-606.

Fahed, A. C., McDonough, B., Gouvion, C. M., Newell, K. L., Dure, L. S., Bebin, M., Bick, A. G., Seidman, J. G., Harter, D. H., Seidman, C. E. (2014). UBQLN2 mutation causing heterogeneous X-linked dominant neurodegeneration. *Ann. Neurol*. **75:** 793-798.

Fecto, F., Shi, Y., Huda, R., Martina, M., Siddique, T., & Deng, H. X. (2011). Mutant TRPV4-mediated toxicity is linked to increased constitutive function in axonal neuropathies. *J. Biol. Chem.* **286:** 17281-17291.

Filézac de L'Etang, A., Maharjan, N., Cordeiro Braña, M., Ruegsegger, C., Rehmann, R., Goswami, A., Roos, A., Troost, D., Schneider, B. L., Weis, J., Saxena, S. (2015). Marinesco-Sjögren syndrome protein SIL1 regulates motor neuron subtype-selective ER stress in ALS. *Nat. Neurosci*. **18:** 227-238.

Fink, J. K. (2014). Hereditary spastic paraplegia: clinical principles and genetic advances. *Semin. Neurol*. **34:** 293-305.

Fischer, L.R., Culver, D.G., Tennant, P., Davis, A.A., Wang, M., Castellano-Sanchez, A., Khan, J., Polak, M.A., Glass, J.D. (2004). Amyotrophic lateral sclerosis is a distal axonopathy: evidence in mice and man. *Exp. Neurol*. **185:** 232-240.

Flierman, D., Ye, Y., Dai, M., Chau, V., & Rapoport, T. A. (2003). Polyubiquitin serves as a recognition signal, rather than a ratcheting molecule, during retrotranslocation of proteins across the endoplasmic reticulum membrane. *J. Biol. Chem*. **278:** 34774-34782.

Foradori, C. D., & Handa, R. J. (2008). Living or dying in three quarter time: neonatal orchestration of hippocampal cell death pathways by androgens and excitatory GABA. *Exp. Neurol.* **213:** 1-6.

Freimann, K., Zschiedrich, K., Brüggemann, N., Grünewald, A., Pawlack, H., Hagenah, J., Lohmann, K., Klein, C., Westenberger, A. (2013). Mortalin mutations are not a frequent cause of early-onset Parkinson disease. *Neurobiol. Aging* **34:** e2619-2620.

Frey, D., Schneider, C., Xu, L., Borg, J., Spooren, W., Caroni, P. (2000). Early and selective loss of neuromuscular synapse subtypes with low sprouting competence in motoneuron diseases. *J. Neurosci*. **20:** 2534-2542.

Gao, X. C., Zhou, C. J., Zhou, Z. R., Wu, M., Cao, C. Y., & Hu, H. Y. (2012). The C-terminal helices of heat shock protein 70 are essential for J-domain binding and ATPase activation. *J. Biol. Chem*. **287:** 6044-6052.

Gassler, C. S., Wiederkehr, T., Brehmer, D., Bukau, B., & Mayer, M. P. (2001). Bag-1M accelerates nucleotide release for human Hsc70 and Hsp70 and can act concentration-dependent as positive and negative cofactor. *J. Biol. Chem*. **276:** 32538-32544.

Gellera, C., Tiloca, C., Del Bo, R., Corrado, L., Pensato, V., Agostini, J., Cereda, C., Ratti, A., Castellotti, B., Corti, S., Bagarotti, A., Cagnin, A., Milani, P., Gabelli, C., Riboldi, G., Mazzini, L., Sorarù, G., D'Alfonso, S., Taroni, F., Comi, G. P., Ticozzi, N., Silani, V. (2013). Ubiquilin 2 mutations in Italian patients with amyotrophic lateral sclerosis and frontotemporal dementia. *J. Neurol. Neurosurg. Psychiatry* **84:** 183-187.

Gentil, B. J., & Cooper, L. (2012). Molecular basis of axonal dysfunction and traffic impairments in CMT. *Brain Res. Bull*. **88:** 444-453.

Gess, B., Auer-Grumbach, M., Schirmacher, A., Strom, T., Zitzelsberger, M., Rudnik-Schöneborn, S., Röhr, D., Halfter, H., Young, P., Senderek, J. (2014). HSJ1-related hereditary neuropathies: novel mutations and extended clinical spectrum. *Neurology* **83:** 1726-1732.

Gillette, T. G., Kumar, B., Thompson, D., Slaughter, C. A., & DeMartino, G. N. (2008). Differential roles of the COOH termini of AAA subunits of PA700 (19 S regulator) in asymmetric assembly and activation of the 26 S proteasome. *J. Biol. Chem.* **283:** 31813-31822.

Girard, M., Larivière, R., Parfitt, D. A., Deane, E. C., Gaudet, R., Nossova, N., Blondeau, F., Prenosil, G., Vermeulen, E. G., Duchen, M. R., Richter, A., Shoubridge, E. A., Gehring, K., McKinney, R. A., Brais, B., Chapple, J. P., McPherson, P. S. (2012). Mitochondrial dysfunction and Purkinje cell loss in autosomal recessive spastic ataxia of Charlevoix-Saguenay (ARSACS). *Proc. Natl. Acad. Sci. U S A* **109:** 1661-1666.

Goedert, M., & Crowther, R. A. (1989). Amyloid plaques, neurofibrillary tangles and their relevance for the study of Alzheimer's disease. *Neurobiol. Aging* **10:** 405-406.

Goldstein, L. S. (2012). Axonal transport and neurodegenerative disease: can we see the elephant? *Prog. Neurobiol*. **99:** 186-190.

González-Pérez, P., Cirulli, E. T., Drory, V. E., Dabby, R., Nisipeanu, P., Carasso, R. L., Sadeh, M., Fox, A., Festoff, B. W., Sapp, P. C., McKenna-Yasek, D., Goldstein, D. B., Brown, R. H., Blumen, S. C. (2012). Novel mutation in VCP gene causes atypical amyotrophic lateral sclerosis. *Neurology* **79:** 2201-2208.

Grohmann, K., Schuelke, M., Diers, A., Hoffmann, K., Lucke, B., Adams, C., Bertini, E., Leonhardt-Horti, H., Muntoni, F., Ouvrier, R., Pfeufer, A., Rossi, R., Van Maldergem, L., Wilmshurst, J. M., Wienker, T. F., Sendtner, M., Rudnik-Schöneborn, S., Zerres, K., Hübner, C. (2001). Mutations in the gene encoding immunoglobulin mu-binding protein 2 cause spinal muscular atrophy with respiratory distress type 1. *Nat. Genet*. **29:** 75-77.

Grove, D.E., Fan, C.Y., Ren, H.Y., Cyr, D.M. (2011). The endoplasmic reticulum-associated Hsp40 DNAJB12 and Hsc70 cooperate to facilitate RMA1 E3-dependent degradation of nascent CFTRDeltaF508. *Mol. Biol. Cell* **22:** 301-314.

Gu, Z. C., & Enenkel, C. (2014). Proteasome assembly. *Cell Mol. Life Sci*. **71:** 4729-4745.

Guenther, U. P., Handoko, L., Laggerbauer, B., Jablonka, S., Chari, A., Alzheimer, M., Ohmer, J., Plöttner, O., Gehring, N., Sickmann, A., von Au, K., Schuelke, M., Fischer, U. (2009). IGHMBP2 is a ribosome-associated helicase inactive in the neuromuscular disorder distal SMA type 1 (DSMA1). *Hum. Mol. Genet*. **18:** 1288-1300.

Guenther, U. P., Varon, R., Schlicke, M., Dutrannoy, V., Volk, A., Hübner, C., von Au, K., Schuelke, M. (2007). Clinical and mutational profile in spinal muscular atrophy with respiratory distress (SMARD): defining novel phenotypes through hierarchical cluster analysis. *Hum. Mutat*. **28:** 808-815.

Guo, J., Qiu, W., Soh, S.L., Wei, S., Radda, G.K., Ong, W.Y., Pang, Z.P., Han, W. (2013). Motor neuron degeneration in a mouse model of seipinopathy. *Cell Death Dis.* **7:** e535.

Hageman, J., Rujano, M. A., van Waarde, M. A., Kakkar, V., Dirks, R. P., Govorukhina, N., Oosterveld-Hut, H. M., Lubsen, N. H., Kampinga, H. H. (2010). A DNAJB chaperone subfamily with HDAC-dependent activities suppresses toxic protein aggregation. *Mol. Cell* **37:** 355-369.

Hamilton, G., & Gillingwater, T. H. (2013). Spinal muscular atrophy: going beyond the motor neuron. *Trends Mol. Med*. **19:** 40-50.

Hansen, J. J., Dürr, A., Cournu-Rebeix, I., Georgopoulos, C., Ang, D., Nielsen, M. N., Davoine, C. S., Brice, A., Fontaine, B., Gregersen, N., Bross, P. (2002). Hereditary spastic paraplegia SPG13 is associated with a mutation in the gene encoding the mitochondrial chaperonin Hsp60. *Am. J. Hum. Genet*. **70:** 1328-1332.

Harding, A. E., & Thomas, P. K. (1980). The clinical features of hereditary motor and sensory neuropathy types I and II. *Brain* **103:** 259-280.

Hardy, J. A., & Higgins, G. A. (1992). Alzheimer's disease: the amyloid cascade hypothesis. *Science* **256:** 184-185.

Harms, M. B., Sommerville, R. B., Allred, P., Bell, S., Ma, D., Cooper, P., Lopate, G., Pestronk, A., Weihl, C. C., Baloh, R. H. (2012). Exome sequencing reveals DNAJB6 mutations in dominantly-inherited myopathy. *Ann. Neurol*. **71:** 407-416.

Hartl, F. U., Bracher, A., & Hayer-Hartl, M. (2011). Molecular chaperones in protein folding and proteostasis. *Nature* **475:** 324-332.

Hartl, F. U., & Hayer-Hartl, M. (2009). Converging concepts of protein folding in vitro and in vivo. *Nat. Struct. Mol. Biol*. **16:** 574-581.

Heir, R., Ablasou, C., Dumontier, E., Elliott, M., Fagotto-Kaufmann, C., & Bedford, F. K. (2006). The UBL domain of PLIC-1 regulates aggresome formation. *EMBO Rep*. **7:** 1252-1258.

Hennessy, F., Boshoff, A., & Blatch, G. L. (2005). Rational mutagenesis of a 40 kDa heat shock protein from Agrobacterium tumefaciens identifies amino acid residues critical to its in vivo function. *Int. J. Biochem. Cell Biol*. **37:** 177-191.

Hennessy, F., Cheetham, M. E., Dirr, H. W., & Blatch, G. L. (2000). Analysis of the levels of conservation of the J domain among the various types of DnaJ-like proteins. Cell Stress *Chaperones* **5:** 347-358.

Hipp, M. S., Park, S. H., & Hartl, F. U. (2014). Proteostasis impairment in protein-misfolding and -aggregation diseases. *Trends Cell. Biol*. **24:** 506-514.

Hirano, S., Kawasaki, M., Ura, H., Kato, R., Raiborg, C., Stenmark, H., & Wakatsuki, S. (2006). Double-sided ubiquitin binding of Hrs-UIM in endosomal protein sorting. *Nat. Struct. Mol. Biol.* **13:** 272-277.

Hodgkinson, V. L., Dale, J. M., Garcia, M. L., Weisman, G. A., Lee, J., Gitlin, J. D., & Petris, M. J. (2015). X-linked spinal muscular atrophy in mice caused by autonomous loss of ATP7A in the motor neuron. *J. Pathol*. **236:** 241-250.

Horwich, A. L., Fenton, W. A., Chapman, E., & Farr, G. W. (2007). Two families of chaperonin: physiology and mechanism. *Annu. Rev. Cell Dev. Biol.* **23:** 115-145.

Houlden, H., Laura, M., Wavrant-De Vrièze, F., Blake, J., Wood, N., & Reilly, M. M. (2008). Mutations in the HSP27 (HSPB1) gene cause dominant, recessive, and sporadic distal HMN/CMT type 2. *Neurology* **71:** 1660-1668.

Howarth, J. L., Kelly, S., Keasey, M. P., Glover, C. P., Lee, Y. B., Mitrophanous, K., Chapple, J. P., Gallo, J. M., Cheetham, M. E., Uney, J. B. (2007). Hsp40 molecules that target to the ubiquitin-proteasome system decrease inclusion formation in models of polyglutamine disease. *Mol. Ther*. **15:** 1100-1105.

Huang, C., Cheng, H., Hao, S., Zhou, H., Zhang, X., Gao, J., Sun, Q. H., Hu, H., Wang, C. C. (2006). Heat shock protein 70 inhibits alpha-synuclein fibril formation via interactions with diverse intermediates. *J. Mol. Biol*. **364:** 323-336.

Hwang, J. S., Chang, I., & Kim, S. (2007). Age-associated decrease in proteasome content and activities in human dermal fibroblasts: restoration of normal level of proteasome subunits reduces aging markers in fibroblasts from elderly persons. *J. Gerontol. A. Biol. Sci. Med. Sci.* **62:** 490-499.

Ichimura, Y., Kumanomidou, T., Sou, Y. S., Mizushima, T., Ezaki, J., Ueno, T., Kominami, E., Yamane, T., Tanaka, K., Komatsu, M. (2008). Structural basis for sorting mechanism of p62 in selective autophagy. *J. Biol. Chem*. **283:** 22847-22857.

Iguchi, Y., Katsuno, M., Niwa, J., Takagi, S., Ishigaki, S., Ikenaka, K., Kawai, K., Watanabe, H., Yamanaka, K., Takahashi, R., Misawa, H., Sasaki, S., Tanaka, F., Sobue, G. (2013). Loss of TDP-43 causes age-dependent progressive motor neuron degeneration. *Brain* **136:** 1371-1382.

Ikeda, Y., Abe, A., Ishida, C., Takahashi, K., Hayasaka, K., & Yamada, M. (2009). A clinical phenotype of distal hereditary motor neuronopathy type II with a novel HSPB1 mutation. *J. Neurol. Sci.* **277:** 9-12.

Inobe, T., & Matouschek, A. (2014). Paradigms of protein degradation by the proteasome. *Curr. Opin. Struct. Biol*. **24:** 156-164.

Irobi, J., Van Impe, K., Seeman, P., Jordanova, A., Dierick, I., Verpoorten, N., Michalik, A., De Vriendt, E., Jacobs, A., Van Gerwen, V., Vennekens, K., Mazanec, R., Tournev, I., Hilton-Jones, D., Talbot, K., Kremensky, I., Van Den Bosch, L., Robberecht, W., Van Vandekerckhove, J., Van Broeckhoven, C., Gettemans, J., De Jonghe, P., Timmerman, V. (2004). Hot-spot residue in small heat-shock protein 22 causes distal motor neuropathy. *Nat. Genet*. **36:** 597-601.

Ito, D., Fujisawa, T., Iida, H., & Suzuki, N. (2008). Characterization of seipin/BSCL2, a protein associated with spastic paraplegia 17. *Neurobiol. Dis*. **31:** 266-277.

Jaffer, F., Murphy, S. M., Scoto, M., Healy, E., Rossor, A. M., Brandner, S., Phadke, R., Selcen, D., Jungbluth, H., Muntoni, F., Reilly, M. M. (2012). BAG3 mutations: another cause of giant axonal neuropathy. *J. Peripher. Nerv. Syst.* **17:** 210-216.

Jerath, N. U., & Shy, M. E. (2015). Hereditary motor and sensory neuropathies: Understanding molecular pathogenesis could lead to future treatment strategies. *Biochim. Biophys. Acta.* **1852:** 667-678.

Johansen, T., & Lamark, T. (2011). Selective autophagy mediated by autophagic adapter proteins. *Autophagy* **7:** 279-296.

Johnson, J. O., Mandrioli, J., Benatar, M., Abramzon, Y., Van Deerlin, V. M., Trojanowski, J. Q., Gibbs, J. R., Brunetti, M., Gronka, S., Wuu, J., Ding, J., McCluskey, L., Martinez-Lage, M., Falcone, D., Hernandez, D. G., Arepalli, S., Chong, S., Schymick, J. C., Rothstein, J., Landi, F., Wang, Y. D., Calvo, A., Mora, G., Sabatelli, M., Monsurrò, M. R., Battistini, S., Salvi, F., Spataro, R., Sola, P., Borghero, G., Galassi, G., Scholz, S. W.,Taylor, J. P., Restagno, G., Chiò, A., Traynor, B. J. (2010). Exome sequencing reveals VCP mutations as a cause of familial ALS. *Neuron* **68:** 857-864.

Jordanova, A., Irobi, J., Thomas, F. P., Van Dijck, P., Meerschaert, K., Dewil, M., Dierick, I., Jacobs, A., De Vriendt, E., Guergueltcheva, V., Rao, C. V., Tournev, I., Gondim, F. A., D'Hooghe, M., Van Gerwen, V., Callaerts, P., Van Den Bosch, L., Timmermans, J. P., Robberecht, W., Gettemans, J., Thevelein, J. M., De Jonghe, P., Kremensky, I., Timmerman, V. (2006). Disrupted function and axonal distribution of mutant tyrosyl-tRNA synthetase in dominant intermediate Charcot-Marie-Tooth neuropathy. *Nat. Genet*. **38:** 197-202.

Kalia, L. V., & Lang, A. E. (2015). Parkinson's disease. *Lancet* **6736:** 61393-3.

Kampinga, H. H., & Craig, E. A. (2010). The HSP70 chaperone machinery: J proteins as drivers of functional specificity. *Nat. Rev. Mol. Cell. Biol*. **11:** 579-592.

Kampinga, H. H., Hageman, J., Vos, M. J., Kubota, H., Tanguay, R. M., Bruford, E. A., Cheetham, M. E., Chen, B., Hightower, L. E. (2009). Guidelines for the nomenclature of the human heat shock proteins. *Cell Stress Chaperones* **14:** 105-111.

Kaplan, A., Spiller, K. J., Towne, C., Kanning, K. C., Choe, G. T., Geber, A., Akay, T., Aebischer, P., Henderson, C. E. (2014). Neuronal matrix metalloproteinase-9 is a determinant of selective neurodegeneration. *Neuron* **81:** 333-348.

Karumbayaram, S., Kelly, T. K., Paucar, A. A., Roe, A. J., Umbach, J. A., Charles, A., Goldman, S. A., Kornblum, H. I., Wiedau-Pazos, M. (2009). Human embryonic stem cell-derived motor neurons expressing SOD1 mutants exhibit typical signs of motor neuron degeneration linked to ALS. *Dis. Model Mech.* **2:** 189-195.

Kennerson, M. L., Nicholson, G. A., Kaler, S. G., Kowalski, B., Mercer, J. F., Tang, J., Llanos, R. M., Chu, S., Takata, R. I., Speck-Martins, C. E., Baets, J., Almeida-Souza, L., Fischer, D., Timmerman, V., Taylor, P. E., Scherer, S. S., Ferguson, T. A., Bird, T. D., De Jonghe, P., Feely, S. M., Shy, M. E., Garbern, J. Y. (2010). Missense mutations in the copper transporter gene ATP7A cause X-linked distal hereditary motor neuropathy. *Am. J. Hum. Genet*. **86:** 343-352.

Kieran, D., Kalmar, B., Dick, J. R., Riddoch-Contreras, J., Burnstock, G., & Greensmith, L. (2004). Treatment with arimoclomol, a coinducer of heat shock proteins, delays disease progression in ALS mice. *Nat. Med*. **10:** 402-405.

Kiernan, M. C., Vucic, S., Cheah, B. C., Turner, M. R., Eisen, A., Hardiman, O., Burrell, J., Zoing, M. C. (2011). Amyotrophic lateral sclerosis. *Lancet* **377:** 942-955.

Kim, B. E., Nevitt, T., & Thiele, D. J. (2008). Mechanisms for copper acquisition, distribution and regulation. *Nat. Chem. Biol*. **4:** 176-185.

Kim, H., & Kim, J. S. (2014). A guide to genome engineering with programmable nucleases. *Nat. Rev. Genet*. **15:** 321-334.

Kim, J., & Guan, K. L. (2011). Regulation of the autophagy initiating kinase ULK1 by nutrients: roles of mTORC1 and AMPK. *Cell Cycle* **10:** 1337-1338.

Kim, Y. E., Hipp, M. S., Bracher, A., Hayer-Hartl, M., & Hartl, F. U. (2013). Molecular chaperone functions in protein folding and proteostasis. *Annu. Rev. Biochem*. **82:** 323-355.

Kleijnen, M. F., Shih, A. H., Zhou, P., Kumar, S., Soccio, R. E., Kedersha, N. L., Gill, G., Howley, P. M. (2000). The hPLIC proteins may provide a link between the ubiquitination machinery and the proteasome. *Mol. Cell* **6:** 409-419.

Klucken, J., Shin, Y., Masliah, E., Hyman, B. T., & McLean, P. J. (2004). Hsp70 Reduces alpha-Synuclein Aggregation and Toxicity. *J. Biol. Chem*. **279:** 25497-25502.

Kolb, S. J., Snyder, P. J., Poi, E. J., Renard, E. A., Bartlett, A., Gu, S., Sutton, S., Arnold, W. D., Freimer, M. L., Lawson, V. H., Kissel, J. T., Prior, T. W. (2010). Mutant small heat shock protein B3 causes motor neuropathy: utility of a candidate gene approach. *Neurology* **74:** 502-506.

Komander, D. (2009). The emerging complexity of protein ubiquitination. *Biochem. Soc. Trans.* **37:** 937-953.

Komander, D., & Rape, M. (2012). The ubiquitin code. *Annu. Rev. Biochem*. **81:** 203-229.

Kosmaoglou, M., Schwarz, N., Bett, J. S., & Cheetham, M. E. (2008). Molecular chaperones and photoreceptor function. *Prog. Retin. Eye Res*. **27:** 434-449.

Kuffler, S. W., Hunt, C. C., & Quilliam, J. P. (1951). Function of medullated small-nerve fibers in mammalian ventral roots; efferent muscle spindle innervation. *J. Neurophysiol*. **14:** 29-54.

Kusmierczyk, A. R., & Martin, J. (2001). Chaperonins--keeping a lid on folding proteins. *FEBS Lett.* **505:** 343-347.

Köroğlu, Ç., Baysal, L., Cetinkaya, M., Karasoy, H., & Tolun, A. (2013). DNAJC6 is responsible for juvenile parkinsonism with phenotypic variability. *Parkinsonism Relat. Disord.* **19:** 320-324.

La Fontaine, S., & Mercer, J. F. (2007). Trafficking of the copper-ATPases, ATP7A and ATP7B: role in copper homeostasis. *Arch. Biochem. Biophys*. **463:** 149-167.

Labbadia, J., Novoselov, S. S., Bett, J. S., Weiss, A., Paganetti, P., Bates, G. P., & Cheetham, M. E. (2012). Suppression of protein aggregation by chaperone modification of high molecular weight complexes. *Brain* **135:** 1180-1196.

Lander, G. C., Estrin, E., Matyskiela, M. E., Bashore, C., Nogales, E., & Martin, A. (2012). Complete subunit architecture of the proteasome regulatory particle. *Nature* **482:** 186-191.

Landouré, G., Zdebik, A. A., Martinez, T. L., Burnett, B. G., Stanescu, H. C., Inada, H., Shi, Y., Taye, A. A., Kong, L., Munns, C. H., Choo, S. S., Phelps, C. B., Paudel, R., Houlden, H., Ludlow, C. L., Caterina, M. J., Gaudet, R., Kleta, R., Fischbeck, K. H., Sumner, C. J. (2010). Mutations in TRPV4 cause Charcot-Marie-Tooth disease type 2C. *Nat. Genet*. **42:** 170-174.

Latour, P., Thauvin-Robinet, C., Baudelet-Méry, C., Soichot, P., Cusin, V., Faivre, L., Locatelli, M. C., Mayençon, M., Sarcey, A., Broussolle, E., Camu, W., David, A., Rousson, R. (2010). A major determinant for binding and aminoacylation of tRNA(Ala) in cytoplasmic Alanyl-tRNA synthetase is mutated in dominant axonal Charcot-Marie-Tooth disease. *Am. J. Hum. Genet*. **86:** 77-82.

Lee, M. J., Lee, J. H., & Rubinsztein, D. C. (2013). Tau degradation: the ubiquitin-proteasome system versus the autophagy-lysosome system. *Prog. Neurobiol*. **105:** 49-59.

Lee, M. J., Stephenson, D. A., Groves, M. J., Sweeney, M. G., Davis, M. B., An, S. F., Houlden, H., Salih, M. A., Timmerman, V., de Jonghe, P., Auer-Grumbach, M., Di Maria, E., Scaravilli, F., Wood, N. W., Reilly, M. M. (2003). Hereditary sensory neuropathy is caused by a mutation in the delta subunit of the cytosolic chaperonin-containing t-complex peptide-1 (Cct4) gene. *Hum. Mol. Genet.* **12:** 1917-1925.

Lefebvre, S., Bürglen, L., Reboullet, S., Clermont, O., Burlet, P., Viollet, L., Benichou, B., Cruaud, C., Millasseau, P., Zeviani, M. (1995). Identification and characterization of a spinal muscular atrophy-determining gene. *Cell* **80:** 155-165.

Li, D. K., Tisdale, S., Lotti, F., & Pellizzoni, L. (2014). SMN control of RNP assembly: from post-transcriptional gene regulation to motor neuron disease. *Semin. Cell Dev. Biol*. **32:** 22-29.

Liberek, K., Marszalek, J., Ang, D., Georgopoulos, C., & Zylicz, M. (1991). Escherichia coli DnaJ and GrpE heat shock proteins jointly stimulate ATPase activity of DnaK. *Proc. Natl. Acad. Sci. U S A* **88:** 2874-2878.

Lim, J., & Yue, Z. (2015). Neuronal aggregates: formation, clearance, and spreading. *Dev. Cell* **32:** 491-501.

Liu, J., Shinobu, L. A., Ward, C. M., Young, D., & Cleveland, D. W. (2005). Elevation of the Hsp70 chaperone does not effect toxicity in mouse models of familial amyotrophic lateral sclerosis. *J. Neurochem*. **93:** 875-882.

Liu, Y., Ye, Y. (2012). Roles of p97-associated deubiquitinases in protein quality control at the endoplasmic reticulum. *Curr. Protein Pept. Sci*. **13:** 436-446.

Lo Giudice, T., Lombardi, F., Santorelli, F. M., Kawarai, T., & Orlacchio, A. (2014). Hereditary spastic paraplegia: clinical-genetic characteristics and evolving molecular mechanisms. Exp. Neurol. **261:** 518-539.

Lodish, H., Berk, A., Zipursky, S.L., et al. (2000). Molecular Cell Biology. 4th edition. W. H. Freeman (New York).

Longatti, A., & Tooze, S. A. (2012). Recycling endosomes contribute to autophagosome formation. *Autophagy* **8:** 1682-1683.

Magen, D., Georgopoulos, C., Bross, P., Ang, D., Segev, Y., Goldsher, D., Nemirovski, A., Shahar, E., Ravid, S., Luder, A., Heno, B., Gershoni-Baruch, R., Skorecki, K., Mandel, H. (2008). Mitochondrial hsp60 chaperonopathy causes an autosomal-recessive neurodegenerative disorder linked to brain hypomyelination and leukodystrophy. *Am. J. Hum. Genet.* **83:** 30-42.

Magnoni, R., Palmfeldt, J., Christensen, J. H., Sand, M., Maltecca, F., Corydon, T. J., West, M., Casari, G., Bross, P. (2013). Late onset motoneuron disorder caused by mitochondrial Hsp60 chaperone deficiency in mice. *Neurobiol. Dis*. **54:** 12-23.

Mali, P., Yang, L., Esvelt, K. M., Aach, J., Guell, M., DiCarlo, J. E., Norville, J. E., Church, G. M. (2013). RNA-guided human genome engineering via Cas9. *Science* **339:** 823-826.

Mariño, G., Niso-Santano, M., Baehrecke, E. H., & Kroemer, G. (2014). Self-consumption: the interplay of autophagy and apoptosis. *Nat. Rev. Mol. Cell Biol.* **15:** 81-94.

Martin, L. J. (1999). Neuronal death in amyotrophic lateral sclerosis is apoptosis: possible contribution of a programmed cell death mechanism. *J. Neuropathol. Exp. Neurol*. **58:** 459-471.

Matus, S., Glimcher, L. H., & Hetz, C. (2011). Protein folding stress in neurodegenerative diseases: a glimpse into the ER. *Curr. Opin. Cell Biol*. **23:** 239-252.

Mayer, M. P. (2010). Gymnastics of molecular chaperones. *Mol. Cell* **39:** 321-331.

McCray, B. A., Skordalakes, E., & Taylor, J. P. (2010). Disease mutations in Rab7 result in unregulated nucleotide exchange and inappropriate activation. *Hum. Mol. Genet*. **19:** 1033-1047.

McGovern, V. L., Gavrilina, T. O., Beattie, C. E., & Burghes, A. H. (2008). Embryonic motor axon development in the severe SMA mouse. *Hum. Mol. Genet*. **17:** 2900-2909.

McMillan, D. R., Xiao, X., Shao, L., Graves, K., & Benjamin, I. J. (1998). Targeted disruption of heat shock transcription factor 1 abolishes thermotolerance and protection against heat-inducible apoptosis. *J. Biol. Chem*. **273:** 7523-7528.

Meimaridou, E., Gooljar, S. B., Ramnarace, N., Anthonypillai, L., Clark, A. J., & Chapple, J. P. (2011). The cytosolic chaperone Hsc70 promotes traffic to the cell surface of intracellular retained melanocortin-4 receptor mutants. *Mol. Endocrinol*. **25:** 1650-1660.

Metzger, M. B., Hristova, V. A., & Weissman, A. M. (2012). HECT and RING finger families of E3 ubiquitin ligases at a glance. *J. Cell Sci*. **125:** 531-537.

Millecamps, S., Corcia, P., Cazeneuve, C., Boillée, S., Seilhean, D., Danel-Brunaud, V., Vandenberghe, N., Pradat, P. F., Le Forestier, N., Lacomblez, L., Bruneteau, G., Camu, W., Brice, A., Meininger, V., LeGuern, E., Salachas, F. (2012). Mutations in UBQLN2 are rare in French amyotrophic lateral sclerosis. *Neurobiol. Aging* **33:** e831-833.

Misko, A., Jiang, S., Wegorzewska, I., Milbrandt, J., & Baloh, R. H. (2010). Mitofusin 2 is necessary for transport of axonal mitochondria and interacts with the Miro/Milton complex. *J. Neurosci*. **30:** 4232-4240.

Mizushima, N. (2011). Autophagy in protein and organelle turnover. *Cold Spring Harb. Symp. Quant. Biol*. **76:** 397-402.

Montague, K., Malik, B., Gray, A. L., La Spada, A. R., Hanna, M. G., Szabadkai, G., & Greensmith, L. (2014). Endoplasmic reticulum stress in spinal and bulbar muscular atrophy: a potential target for therapy. *Brain* **137:** 1894-1906.

Morimoto, R. I. (2011). The heat shock response: systems biology of proteotoxic stress in aging and disease. *Cold Spring Harb. Symp. Quant. Biol*. **76:** 91-99.

Mukherjee, A., Morales-Scheihing, D., Butler, P. C., & Soto, C. (2015). Type 2 diabetes as a protein misfolding disease. Trends Mol Med. [Epub doi:10.1016/j.molmed.2015.04.005].

Murphy, S. M., Laura, M., Fawcett, K., Pandraud, A., Liu, Y. T., Davidson, G. L., Rossor, A. M., Polke, J. M., Castleman, V., Manji, H., Lunn, M. P., Bull, K., Ramdharry, G., Davis, M., Blake, J. C., Houlden, H., Reilly, M. M. (2012). Charcot-Marie-Tooth disease: frequency of genetic subtypes and guidelines for genetic testing. *J. Neurol. Neurosurg. Psychiatry* **83:** 706-710.

N'Diaye, E. N., Kajihara, K. K., Hsieh, I., Morisaki, H., Debnath, J., & Brown, E. J. (2009). PLIC proteins or ubiquilins regulate autophagy-dependent cell survival during nutrient starvation. *EMBO Rep*. **10:** 173-179.

Nagabhushana, A., Chalasani, M. L., Jain, N., Radha, V., Rangaraj, N., Balasubramanian, D., & Swarup, G. (2010). Regulation of endocytic trafficking of transferrin receptor by optineurin and its impairment by a glaucoma-associated mutant. *BMC Cell Biol*. **11:** 4.

Nicoll, W. S., Botha, M., McNamara, C., Schlange, M., Pesce, E. R., Boshoff, A., Ludewig, M. H., Zimmermann, R., Cheetham, M. E., Chapple, J. P., Blatch, G. L. (2007). Cytosolic and ER J-domains of mammalian and parasitic origin can functionally interact with DnaK. *Int. J. Biochem. Cell Biol*. **39:** 736-751.

Niemann, A., Wagner, K. M., Ruegg, M., & Suter, U. (2009). GDAP1 mutations differ in their effects on mitochondrial dynamics and apoptosis depending on the mode of inheritance. *Neurobiol. Dis*. **36:** 509-520.

Nosková, L., Stránecký, V., Hartmannová, H., Přistoupilová, A., Barešová, V., Ivánek, R., Hůlková, H., Jahnová, H., van der Zee, J., Staropoli, J. F., Sims, K. B., Tyynelä, J., Van Broeckhoven, C., Nijssen, P. C., Mole, S. E., Elleder, M., Kmoch, S. (2011). Mutations in DNAJC5, encoding cysteine-string protein alpha, cause autosomal-dominant adult-onset neuronal ceroid lipofuscinosis. *Am. J. Hum. Genet*. **89:** 241-252.

Novoselov, S. S., Mustill, W. J., Gray, A. L., Dick, J. R., Kanuga, N., Kalmar, B., Greensmith, L., Cheetham, M. E. (2013). Molecular chaperone mediated late-stage neuroprotection in the SOD1(G93A) mouse model of amyotrophic lateral sclerosis. *PLoS One* **8:** e73944.

Ojala, T., Polinati, P., Manninen, T., Hiippala, A., Rajantie, J., Karikoski, R., Suomalainen, A., Tyni, T. (2012). New mutation of mitochondrial DNAJC19 causing dilated and noncompaction cardiomyopathy, anemia, ataxia, and male genital anomalies. *Pediatr. Res*. **72:** 432-437.

Olzmann, J. A., Kopito, R. R., & Christianson, J. C. (2013). The mammalian endoplasmic reticulum-associated degradation system. *Cold Spring Harb. Perspect. Biol*. **5:** a013185.

Osaka, M., Ito, D., Yagi, T., Nihei, Y., & Suzuki, N. (2015). Evidence of a link between ubiquilin 2 and optineurin in amyotrophic lateral sclerosis. *Hum. Mol. Genet*. **24:** 1617-1629.

Palanca, A., Casafont, I., Berciano, M. T., & Lafarga, M. (2014). Reactive nucleolar and Cajal body responses to proteasome inhibition in sensory ganglion neurons. *Biochim. Biophys. Acta*. **1842:** 848-859.

Parfitt, D. A., Michael, G. J., Vermeulen, E. G., Prodromou, N. V., Webb, T. R., Gallo, J. M., Cheetham, M. E., Nicoll, W. S., Blatch, G. L., Chapple, J. P. (2009). The ataxia protein sacsin is a functional co-chaperone that protects against polyglutamine-expanded ataxin-1. *Hum. Mol. Genet*. **18:** 1556-1565.

Patel, Y. J., Payne Smith, M. D., de Belleroche, J., & Latchman, D. S. (2005). Hsp27 and Hsp70 administered in combination have a potent protective effect against FALS-associated SOD1-mutant-induced cell death in mammalian neuronal cells. *Brain Res. Mol. Brain Res*. **134:** 256-274.

Pearl, L. H., & Prodromou, C. (2006). Structure and mechanism of the Hsp90 molecular chaperone machinery. *Annu. Rev. Biochem*. **75:** 271-294.

Puls, I., Jonnakuty, C., LaMonte, B. H., Holzbaur, E. L., Tokito, M., Mann, E., Floeter, M. K., Bidus, K., Drayna, D., Oh, S. J., Brown, R. H., Ludlow, C. L., Fischbeck, K. H. (2003). Mutant dynactin in motor neuron disease. *Nat. Genet*. **33:** 455-456.

Purves, D., Augustine, G.J., Fitzpatrick, D., *et al.* (2001). Neuroscience. 2nd edition. Sinauer Associates, Sunderland (MA).

Puthalakath, H., O'Reilly, L. A., Gunn, P., Lee, L., Kelly, P. N., Huntington, N. D., Hughes, P. D., Michalak, E. M., McKimm-Breschkin, J., Motoyama, N., Gotoh, T., Akira, S., Bouillet, P., Strasser, A. (2007). ER stress triggers apoptosis by activating BH3-only protein Bim. *Cell* **129:** 1337-1349.

Regan-Klapisz, E., Sorokina, I., Voortman, J., de Keizer, P., Roovers, R. C., Verheesen, P., Urbé, S., Fallon, L., Fon, E. A., Verkleij, A., Benmerah, A., van Bergen en Henegouwen, P. M. (2005). Ubiquilin recruits Eps15 into ubiquitin-rich cytoplasmic aggregates via a UIM-UBL interaction. *J. Cell Sci.* **118:** 4437-4450.

Reilly, M. M., Murphy, S. M., & Laurá, M. (2011). Charcot-Marie-Tooth disease. *J. Peripher. Nerv. Syst.* **16:** 1-14.

Renton, A. E., Chiò, A., & Traynor, B. J. (2014). State of play in amyotrophic lateral sclerosis genetics. *Nat. Neurosci*. **17:** 17-23.

Reyes-Turcu, F. E., & Wilkinson, K. D. (2009). Polyubiquitin binding and disassembly by deubiquitinating enzymes. *Chem. Rev*. **109:** 1495-1508.

Riancho, J., Ruiz-Soto, M., Villagrá, N. T., Berciano, J., Berciano, M. T., & Lafarga, M. (2014). Compensatory Motor Neuron Response to Chromatolysis in the Murine hSOD1(G93A) Model of Amyotrophic Lateral Sclerosis. *Front. Cell. Neurosci*. **8:** 346.

Rocha, M. C., Pousinha, P. A., Correia, A. M., Sebastião, A. M., & Ribeiro, J. A. (2013). Early changes of neuromuscular transmission in the SOD1(G93A) mice model of ALS start long before motor symptoms onset. *PLoS One* **8:** e73846.

Rose, J. M., Novoselov, S. S., Robinson, P. A., & Cheetham, M. E. (2011). Molecular chaperone-mediated rescue of mitophagy by a Parkin RING1 domain mutant. *Hum. Mol. Genet.* **20:** 16-27.

Rosen, D. R., Siddique, T., Patterson, D., Figlewicz, D. A., Sapp, P., Hentati, A., Donaldson, D., Goto, J., O'Regan, J. P., Deng, H. X. (1993). Mutations in Cu/Zn superoxide dismutase gene are associated with familial amyotrophic lateral sclerosis. *Nature* **362:** 59-62.

Ross, C. A., & Pickart, C. M. (2004). The ubiquitin-proteasome pathway in Parkinson's disease and other neurodegenerative diseases. *Trends Cell Biol*. **14:** 703-711.

Rossor, A. M., Kalmar, B., Greensmith, L., & Reilly, M. M. (2012). The distal hereditary motor neuropathies. J. *Neurol. Neurosurg. Psychiatry* **83:** 6-14.

Rossor, A. M., Polke, J. M., Houlden, H., & Reilly, M. M. (2013). Clinical implications of genetic advances in Charcot-Marie-Tooth disease. *Nat. Rev. Neurol*. **9:** 562-571.

Rothenberg, C., Srinivasan, D., Mah, L., Kaushik, S., Peterhoff, C. M., Ugolino, J., Fang, S., Cuervo, A. M., Nixon, R. A., Monteiro, M. J. (2010). Ubiquilin functions in autophagy and is degraded by chaperone-mediated autophagy. *Hum. Mol. Genet.* **19:** 3219-3232.

Rubinsztein, D. C., Shpilka, T., & Elazar, Z. (2012). Mechanisms of autophagosome biogenesis. *Curr. Biol*. **22:** 29-34.

Ruggiano, A., Foresti, O., & Carvalho, P. (2014). Quality control: ER-associated degradation: protein quality control and beyond. *J. Cell Biol*. **204:** 869-879.

Saporta, A. S., Sottile, S. L., Miller, L. J., Feely, S. M., Siskind, C. E., & Shy, M. E. (2011). Charcot-Marie-Tooth disease subtypes and genetic testing strategies. *Ann. Neurol*. **69:** 22-33.

Saporta, M. A., Dang, V., Volfson, D., Zou, B., Xie, X. S., Adebola, A., Liem, R. K., Shy, M., Dimos, J. T. (2015). Axonal Charcot-Marie-Tooth disease patient-derived motor neurons demonstrate disease-specific phenotypes including abnormal electrophysiological properties. *Exp. Neurol.* **263:** 190-199.

Sarparanta, J., Jonson, P. H., Golzio, C., Sandell, S., Luque, H., Screen, M., McDonald, K., Stajich, J. M., Mahjneh, I., Vihola, A., Raheem, O., Penttilä, S., Lehtinen, S., Huovinen, S., Palmio, J., Tasca, G., Ricci, E., Hackman, P., Hauser, M., Katsanis, N., Udd, B. (2012). Mutations affecting the cytoplasmic functions of the co-chaperone DNAJB6 cause limb-girdle muscular dystrophy. *Nat. Genet.* **44:** 450-455.

Sasaki, S. (2011). Autophagy in spinal cord motor neurons in sporadic amyotrophic lateral sclerosis. *J. Neuropathol. Exp. Neurol*. **70:** 349-359.

Sato, T., Hayashi, Y. K., Oya, Y., Kondo, T., Sugie, K., Kaneda, D., Houzen, H., Yabe, I., Sasaki, H., Noguchi, S., Nonaka, I., Osawa, M., Nishino, I. (2013). DNAJB6 myopathy in an Asian cohort and cytoplasmic/nuclear inclusions. *Neuromuscul. Disord.* **23:** 269-276.

Saxena, S., Cabuy, E., & Caroni, P. (2009). A role for motoneuron subtype-selective ER stress in disease manifestations of FALS mice. *Nat. Neurosci*. **12:** 627-636.

Scheufler, C., Brinker, A., Bourenkov, G., Pegoraro, S., Moroder, L., Bartunik, H., Hartl, F. U., Moarefi, I. (2000). Structure of TPR domain-peptide complexes: critical elements in the assembly of the Hsp70-Hsp90 multichaperone machine. *Cell* **101:** 199-210.

Schottmann, G., Jungbluth, H., Schara, U., Knierim, E., Morales Gonzalez, S., Gill, E., Seifert, F., Norwood, F., Deshpande, C., von Au, K., Schuelke, M., Senderek, J. (2015). Recessive truncating IGHMBP2 mutations presenting as axonal sensorimotor neuropathy. *Neurology* **84:** 523-531.

Schäfer, A., & Wolf, D. H. (2009). Sec61p is part of the endoplasmic reticulum-associated degradation machinery. *EMBO J*. **28:** 2874-2884.

Scorrano, L. (2013). Keeping mitochondria in shape: a matter of life and death. *Eur. J. Clin. Invest.* **43:** 886-893.

Selcen, D., Muntoni, F., Burton, B. K., Pegoraro, E., Sewry, C., Bite, A. V., & Engel, A. G. (2009). Mutation in BAG3 causes severe dominant childhood muscular dystrophy. *Ann. Neurol.* **65:** 83-89.

Senderek, J., Krieger, M., Stendel, C., Bergmann, C., Moser, M., Breitbach-Faller, N., Rudnik-Schöneborn, S., Blaschek, A., Wolf, N. I., Harting, I., North, K., Smith, J., Muntoni, F., Brockington, M., Quijano-Roy, S., Renault, F., Herrmann, R., Hendershot, L. M., Schröder, J. M., Lochmüller, H., Topaloglu, H., Voit, T., Weis, J., Ebinger, F., Zerres, K. (2005). Mutations in SIL1 cause Marinesco-Sjögren syndrome, a cerebellar ataxia with cataract and myopathy. *Nat. Genet*. **37:** 1312-1314.

Seo, A. J., Shin, Y. H., Lee, S. J., Kim, D., Park, B. S., Kim, S., Choi, K. H., Jeong, N. Y., Park, C., Jang, J. Y., Huh, Y., Jung, J. (2014). A novel adenoviral vector-mediated mouse model of Charcot-Marie-Tooth type 2D (CMT2D). *J. Mol. Histol.* **45:** 121-128.

Sharp, P. S., Akbar, M. T., Bouri, S., Senda, A., Joshi, K., Chen, H. J., Latchman, D. S., Wells, D. J., de Belleroche, J. (2008). Protective effects of heat shock protein 27 in a model of ALS occur in the early stages of disease progression. *Neurobiol. Dis*. **30:** 42-55.

Shemetov, A. A., & Gusev, N. B. (2011). Biochemical characterization of small heat shock protein HspB8 (Hsp22)-Bag3 interaction. *Arch. Biochem. Biophys*. **513:** 1-9.

Sheng, Z.H. (2014). Mitochondrial trafficking and anchoring in neurons: New insight and implications. *J. Cell Biol.* **204:** 1087-1098.

Shi, Y., Mosser, D. D., & Morimoto, R. I. (1998). Molecular chaperones as HSF1-specific transcriptional repressors. *Genes Dev*. **12:** 654-666.

Smith, D. M., Chang, S. C., Park, S., Finley, D., Cheng, Y., & Goldberg, A. L. (2007). Docking of the proteasomal ATPases' carboxyl termini in the 20S proteasome's alpha ring opens the gate for substrate entry. *Mol. Cell* **27:** 731-744.

Soto, C., & Estrada, L. D. (2008). Protein misfolding and neurodegeneration. *Arch. Neurol*. **65:** 184-189.

Spillantini, M. G., Crowther, R. A., Jakes, R., Hasegawa, M., & Goedert, M. (1998). alpha-Synuclein in filamentous inclusions of Lewy bodies from Parkinson's disease and dementia with lewy bodies. *Proc. Natl. Acad. Sci. U S A* **95:** 6469-6473.

Stolz, A., Hilt, W., Buchberger, A., & Wolf, D. H. (2011). Cdc48: a power machine in protein degradation. *Trends Biochem. Sci*. **36:** 515-523.

Strickland, A. V., Rebelo, A. P., Zhang, F., Price, J., Bolon, B., Silva, J. P., Wen, R., Züchner, S. (2014). Characterization of the mitofusin 2 R94W mutation in a knock-in mouse model. *J. Peripher. Nerv. Syst.* **19:** 152-164.

Szegezdi, E., Logue, S. E., Gorman, A. M., & Samali, A. (2006). Mediators of endoplasmic reticulum stress-induced apoptosis. *EMBO Rep*. **7:** 880-885.

Takahashi, K., Tanabe, K., Ohnuki, M., Narita, M., Ichisaka, T., Tomoda, K., Yamanaka, S. (2007). Induction of pluripotent stem cells from adult human fibroblasts by defined factors. *Cell* 2007 **131:** 861-872.

Takamori, M. (2012). Structure of the neuromuscular junction: function and cooperative mechanisms in the synapse. *Ann. N. Y. Acad. Sci*. **1274:** 14-23.

Takeuchi, H., Kobayashi, Y., Yoshihara, T., Niwa, J., Doyu, M., Ohtsuka, K., & Sobue, G. (2002). Hsp70 and Hsp40 improve neurite outgrowth and suppress intracytoplasmic aggregate formation in cultured neuronal cells expressing mutant SOD1.

Talbot, K. (2009). Motor neuron disease: the bare essentials. *Pract. Neurol*. **9:** 303-309.

Tapia, O., Bengoechea, R., Palanca, A., Arteaga, R., Val-Bernal, J. F., Tizzano, E. F., Berciano, M. T., Lafarga, M. (2012). Reorganization of Cajal bodies and nucleolar targeting of coilin in motor neurons of type I spinal muscular atrophy. *Histochem. Cell Biol.* **5:** 657-667.

Tazir, M., Hamadouche, T., Nouioua, S., Mathis, S., & Vallat, J. M. (2014). Hereditary motor and sensory neuropathies or Charcot-Marie-Tooth diseases: an update. *J. Neurol. Sci.* **347:** 14-22.

Thiffault, I., Dicaire, M. J., Tetreault, M., Huang, K. N., Demers-Lamarche, J., Bernard, G., Duquette, A., Larivière, R., Gehring, K., Montpetit, A., McPherson, P. S., Richter, A., Montermini, L., Mercier, J., Mitchell, G. A., Dupré, N., Prévost, C., Bouchard, J. P., Mathieu, J., Brais, B. (2013). Diversity of ARSACS mutations in French-Canadians. *Can. J. Neurol. Sci.* **40:** 61-66.

Thrower, J. S., Hoffman, L., Rechsteiner, M., & Pickart, C. M. (2000). Recognition of the polyubiquitin proteolytic signal. *EMBO J*. **19:** 94-102.

Toma, J. S., Shettar, B. C., Chipman, P. H., Pinto, D. M., Borowska, J. P., Ichida, J. K., Fawcett, J. P., Zhang, Y., Eggan, K., Rafuse, V. F. (2015). Motoneurons derived from induced pluripotent stem cells develop mature phenotypes typical of endogenous spinal motoneurons. *J. Neurosci*. **35:** 1291-1306.

Tomko, R. J., Funakoshi, M., Schneider, K., Wang, J., & Hochstrasser, M. (2010). Heterohexameric ring arrangement of the eukaryotic proteasomal ATPases: implications for proteasome structure and assembly. *Mol. Cell* **38:** 393-403.

Vallat, J. M., Mathis, S., & Funalot, B. (2013). The various Charcot-Marie-Tooth diseases. *Curr. Opin. Neurol*. **26:** 473-480.

Verhoeven, K., Claeys, K. G., Züchner, S., Schröder, J. M., Weis, J., Ceuterick, C., Jordanova, A., Nelis, E., De Vriendt, E., Van Hul, M., Seeman, P., Mazanec, R., Saifi, G. M., Szigeti, K., Mancias, P., Butler, I. J., Kochanski, A., Ryniewicz, B., De Bleecker, J., Van den Bergh, P., Verellen, C., Van Coster, R., Goemans, N., Auer-Grumbach, M., Robberecht, W., Milic Rasic, V., Nevo, Y., Tournev, I., Guergueltcheva, V., Roelens, F., Vieregge, P., Vinci, P., Moreno, M. T., Christen, H. J., Shy, M. E., Lupski, J. R., Vance, J. M., De Jonghe, P., Timmerman, V. (2006). MFN2 mutation distribution and genotype/phenotype correlation in Charcot-Marie-Tooth type 2. *Brain* **129:** 2093-2102.

Verma, R., Aravind, L., Oania, R., McDonald, W. H., Yates, J. R., Koonin, E. V., & Deshaies, R. J. (2002). Role of Rpn11 metalloprotease in deubiquitination and degradation by the 26S proteasome. *Science* **298:** 611-615.

Vihervaara, A., & Sistonen, L. (2014). HSF1 at a glance. *J. Cell Sci*. **127:** 261-266.

Vilariño-Güell, C., Rajput, A., Milnerwood, A. J., Shah, B., Szu-Tu, C., Trinh, J., Yu, I., Encarnacion, M., Munsie, L. N., Tapia, L., Gustavsson, E. K., Chou, P., Tatarnikov, I., Evans, D. M., Pishotta, F. T., Volta, M., Beccano-Kelly, D., Thompson, C., Lin, M. K., Sherman, H. E., Han, H. J., Guenther, B. L., Wasserman, W. W., Bernard, V., Ross, C. J., Appel-Cresswell, S., Stoessl, A. J., Robinson, C. A., Dickson, D. W., Ross, O. A., Wszolek, Z. K., Aasly, J. O., Wu, R. M., Hentati, F., Gibson, R. A., McPherson, P. S., Girard, M., Rajput, M., Rajput, A. H., Farrer, M. J. (2014). DNAJC13 mutations in Parkinson disease. *Hum. Mol. Genet*. **23:** 1794-1801.

Vos, M. J., Zijlstra, M. P., Kanon, B., van Waarde-Verhagen, M. A., Brunt, E. R., Oosterveld-Hut, H. M., Carra, S., Sibon, O. C., Kampinga, H. H. (2010). HSPB7 is the most potent polyQ aggregation suppressor within the HSPB family of molecular chaperones. *Hum. Mol. Genet*. **19:** 4677-4693.

Wakayama, I. (1992). Morphometry of spinal motor neurons in amyotrophic lateral sclerosis with special reference to chromatolysis and intracytoplasmic inclusion bodies. Brain Res. **586:** 12-18.

Walker, F. O. (2007). Huntington's disease. *Lancet* **369:** 218-228.

Wallen, R. C., & Antonellis, A. (2013). To charge or not to charge: mechanistic insights into neuropathy-associated tRNA synthetase mutations. *Curr. Opin. Genet. Dev*. **23:** 302-309.

Walsh, D. M., Klyubin, I., Fadeeva, J. V., Cullen, W. K., Anwyl, R., Wolfe, M. S., Selkoe, D. J. (2002). Naturally secreted oligomers of amyloid beta protein potently inhibit hippocampal long-term potentiation in vivo. *Nature* **416:** 535-539.

Walter, F., Schmid, J., Düssmann, H., Concannon, C. G., & Prehn, J. H. (2015). Imaging of single cell responses to ER stress indicates that the relative dynamics of IRE1/XBP1 and PERK/ATF4 signalling rather than a switch between signalling branches determine cell survival. *Cell Death Differ*. [Epub doi:10.1038/cdd.2014.241].

Walter, P., & Ron, D. (2011). The unfolded protein response: from stress pathway to homeostatic regulation. *Science* **334:** 1081-1086.

Wang, L., Popko, B., Roos, R.P. (2011). The unfolded protein response in familial amyotrophic lateral sclerosis. *Hum. Mol. Genet*. **20:** 1008-1015.

Wang, M., & Kaufman, R. J. (2014). The impact of the endoplasmic reticulum protein-folding environment on cancer development. *Nat. Rev. Cancer* **14:** 581-597.

Westhoff, B., Chapple, J.P. van der Spuy, J., Höhfeld, J., Cheetham, M.E. (2005). HSJ1 is a neuronal shuttling factor for the sorting of chaperone clients to the proteasome. *Curr Biol*. **15:** 1058-1064.

Weterman, M. A., Sorrentino, V., Kasher, P. R., Jakobs, M. E., van Engelen, B. G., Fluiter, K., de Wissel, M. B., Sizarov, A., Nürnberg, G., Nürnberg, P., Zelcer, N., Schelhaas, H. J., Baas, F. (2012). A frameshift mutation in LRSAM1 is responsible for a dominant hereditary polyneuropathy. *Hum. Mol. Genet*. **21:** 358-370.

Windpassinger, C., Auer-Grumbach, M., Irobi, J., Patel, H., Petek, E., Hörl, G., Malli, R., Reed, J. A., Dierick, I., Verpoorten, N., Warner, T. T., Proukakis, C., Van den Bergh, P., Verellen, C., Van Maldergem, L., Merlini, L., De Jonghe, P., Timmerman, V., Crosby, A. H., Wagner, K. (2004). Heterozygous missense mutations in BSCL2 are associated with distal hereditary motor neuropathy and Silver syndrome. *Nat. Genet*. **36:** 271-276.

Winner, B., Jappelli, R., Maji, S. K., Desplats, P. A., Boyer, L., Aigner, S., Hetzer, C., Loher, T., Vilar, M., Campioni, S., Tzitzilonis, C., Soragni, A., Jessberger, S., Mira, H., Consiglio, A., Pham, E., Masliah, E., Gage, F. H., Riek, R. (2011). In vivo demonstration that alpha-synuclein oligomers are toxic. *Proc. Natl. Acad. Sci. U S A* **108:** 4194-4199.

Wu, Q., Liu, M., Huang, C., Liu, X., Huang, B., Li, N., Zhou, H., Xia, X. G. (2015). Pathogenic Ubqln2 gains toxic properties to induce neuron death. *Acta Neuropathol*. **129:** 417-428.

Xia, Y., Yan, L. H., Huang, B., Liu, M., Liu, X., & Huang, C. (2014). Pathogenic mutation of UBQLN2 impairs its interaction with UBXD8 and disrupts endoplasmic reticulum-associated protein degradation. *J. Neurochem*. **129:** 99-106.

Ye, Y., Meyer, H. H., & Rapoport, T. A. (2001). The AAA ATPase Cdc48/p97 and its partners transport proteins from the ER into the cytosol. *Nature* **414:** 652-656.

Ye, Y., Meyer, H. H., & Rapoport, T. A. (2003). Function of the p97-Ufd1-Npl4 complex in retrotranslocation from the ER to the cytosol: dual recognition of nonubiquitinated polypeptide segments and polyubiquitin chains. *J. Cell Biol*. **162:** 71-84.

Ylikallio, E., Pöyhönen, R., Zimon, M., De Vriendt, E., Hilander, T., Paetau, A., Jordanova, A., Lönnqvist, T., Tyynismaa, H. (2013). Deficiency of the E3 ubiquitin ligase TRIM2 in early-onset axonal neuropathy. *Hum. Mol. Genet*. **22:** 2975-2983.

Yébenes, H., Mesa, P., Muñoz, I. G., Montoya, G., & Valpuesta, J. M. (2011). Chaperonins: two rings for folding. *Trends Biochem. Sci*. **36:** 424-432.

Zhai, J., Lin, H., Julien, J. P., & Schlaepfer, W. W. (2007). Disruption of neurofilament network with aggregation of light neurofilament protein: a common pathway leading to motor neuron degeneration due to Charcot-Marie-Tooth disease-linked mutations in NFL and HSPB1. *Hum. Mol. Genet*. **16:** 3103-3116.

Zhang, D., Raasi, S., & Fushman, D. (2008). Affinity makes the difference: nonselective interaction of the UBA domain of Ubiquilin-1 with monomeric ubiquitin and polyubiquitin chains. *J. Mol. Biol*. **377:** 162-180.

Zhang, K. Y., Yang, S., Warraich, S. T., & Blair, I. P. (2014). Ubiquilin 2: a component of the ubiquitin-proteasome system with an emerging role in neurodegeneration. *Int. J. Biochem. Cell Biol*. **50:** 123-126.

Zhang, R., Zhang, F., Li, X., Huang, S., Zi, X., Liu, T., Liu, S., Xia, K., Pan, Q., Tang, B. (2014). A novel transgenic mouse model of Chinese Charcot-Marie-Tooth disease type 2L. *Neural Regen. Res.* **9:** 413-419.

Zhao, C., Takita, J., Tanaka, Y., Setou, M., Nakagawa, T., Takeda, S., Yang, H. W., Terada, S., Nakata, T., Takei, Y., Saito, M., Tsuji, S., Hayashi, Y., Hirokawa, N. (2001). Charcot-Marie-Tooth disease type 2A caused by mutation in a microtubule motor KIF1Bbeta. *Cell* **105:** 587-597.

Zhao, W., Varghese, M., Yemul, S., Pan, Y., Cheng, A., Marano, P., Hassan, S., Vempati, P., Chen, F., Qian, X., Pasinetti, G.M. (2011). Peroxisome proliferator activator receptor gamma coactivator-1alpha (PGC-1α) improves motor performance and survival in a mouse model of amyotrophic lateral sclerosis. *Mol. Neurodegener*. **19:** 51.

Zimoń, M., Baets, J., Almeida-Souza, L., De Vriendt, E., Nikodinovic, J., Parman, Y., Battaloğlu, E., Matur, Z., Guergueltcheva, V., Tournev, I., Auer-Grumbach, M., De Rijk, P., Petersen, B. S., Müller, T., Fransen, E., Van Damme, P., Löscher, W. N., Barišić, N., Mitrovic, Z., Previtali, S. C., Topaloğlu, H., Bernert, G., Beleza-Meireles, A., Todorovic, S., Savic-Pavicevic, D., Ishpekova, B., Lechner, S., Peeters, K., Ooms, T., Hahn, A. F., Züchner, S., Timmerman, V., Van Dijck, P., Rasic, V. M., Janecke, A. R., De Jonghe, P., Jordanova, A. (2012). Loss-of-function mutations in HINT1 cause axonal neuropathy with neuromyotonia. *Nat. Genet*. **44:** 1080-1083.

Zou, J., Guo, Y., Guettouche, T., Smith, D. F., & Voellmy, R. (1998). Repression of heat shock transcription factor HSF1 activation by HSP90 (HSP90 complex) that forms a stress-sensitive complex with HSF1. *Cell* **94:** 471-480.